Finite Element Modeling of Delamination in Advanced Composite Beams and Plates using one-and two-dimensional Finite Elements based on the Refined Zigzag Theory

A. Eijo
E. Oñate
S. Oller

Monograph CIMNE Nº-149, October 2014

Finite Element Modeling of Delamination in Advanced Composite Beams and Plates using one-and two-dimensional Finite Elements based on the Refined Zigzag Theory

A. Eijo
E. Oñate
S. Oller

Monograph CIMNE Nº-149, October 2014

International Center for Numerical Methods in Engineering
Gran Capitán s/n, 08034 Barcelona, Spain

INTERNATIONAL CENTER FOR NUMERICAL METHODS IN ENGINEERING
Edificio C1, Campus Norte UPC
Gran Capitán s/n
08034 Barcelona, Spain
www.cimne.com

First edition: October 2014

FINITE ELEMENT MODELING OF DELAMINATION IN ADVANCED COMPOSIT BEAMS AND PLATES USING ONE-AND-TWO-DIMENSIONAL FINITE ELEMENTS BASED ON THE REFINED ZIGZAG THEORY
Monograph CIMNE M149

ISBN: 978-84-943307-1-1
Depósito legal: B-23557-2014

To my mother and my wife

Acknowledgments

It gives me pleasure to acknowledge to my supervisor Eugenio Oñate for giving me the opportunity to develop my thesis at the International Center for Numerical Methods in Engineering (CIMNE). I further want to thank him for guidance and scientific support, which considerably contributed to the success of my work.

My special acknowledgment to my second supervisor Sergio Oller who gave me continues support and advices through my thesis with patience and knowledge. It was a pleasure to work with his assistance.

I wish to express my sincere appreciation to Omar Faure for believing in me and giving me the confidence to start this doctoral journey. Furthermore, thanks for all his rewarding and helpful advices.

I am grateful to CIMNE, the Polytechnic University of Catalonia (UPC) and the Ministry of Education of Spain for their financial support which made this work possible.

My most sincere gratitude to all my colleges at CIMNE and the RMEE department of the UPC. Particularly many thanks to Enrique Ortega for his appreciated recommendations on the writing and edition of this document.

Special thanks to my mother Mari for her numerous sacrifices. She always tried to make everything possible and impossible to build a better future for me. This led me to be the person I am now.

Above all I would like to thank my wife Ana for her love and constant support during these hard years. But most of all, thank you for being my “compañera de la vida”.

Abstract

Although laminated materials have been used for decades, their employment has increased nowadays in the last years as a result of the gained confidence of the industry on these materials. This has provided the scientific community many reasons to dedicate considerable amount of time and efforts to address a better understanding of their mechanical behavior. With this objective both, experimental and numerical simulation have been working together to give response to a variety of problems related with these materials.

Regarding numerical simulation, a correct modeling of the kinematics of laminated materials is essential to capture the real behavior of the structure. Moreover, once the kinematics of the structure has been accurately predicted other non-linear phenomena such as damage and/or plasticity process could be also studied.

In consequence, in order to contribute to the constant development of simpler and more efficient numerical tools to model laminated materials, a numerical method for modeling mode II/III delamination in advanced composite materials using one- and two-dimensional finite elements is proposed in this work. In addition, two finite elements base on a zigzag theory for simulating highly heterogeneous multilayered beams and plates structures are developed here.

The document is written based on results of four papers published in indexed journals. Copies of all these papers are included in Appendix. The main body of this thesis is constituted by Chapters 2 to 4. Chapter 2 deals with the numerical treatment of laminated beams and plates. Chapter 3 presents the formulation of the LRZ beam and the QLRZ plate finite elements based on the Refined Zigzag Theory. Finally, the main contribution of this thesis, the LRZ/QLRZ delamination model, is developed in Chapter 4.

Resumen

Aunque los materiales laminados se han utilizado durante décadas, su uso ha aumentado en los últimos años como resultado de una mayor confianza por parte de la industria. Esto ha proporcionado a la comunidad científica muchas razones para dedicar una considerable cantidad de tiempo y esfuerzos en aras de una mejor comprensión de su comportamiento mecánico. Con este objetivo tanto la simulación experimental como numérica han estado trabajando juntos para dar respuesta a una variedad de problemas relacionados con estos materiales.

En cuanto a la simulación numérica, un correcto modelado de la cinemática de los materiales laminados es esencial para capturar el comportamiento real de la estructura. Por otra parte, una vez que la cinemática de la estructura se ha predicho con precisión otros fenómenos no lineales como los proceso de daño y/o plasticidad podrían ser también estudiados.

En consecuencia, con el fin de contribuir al constante desarrollo de herramientas numéricas más simples y eficaces para modelar materiales laminados, un método numérico para el modelado de la delaminación (modo II/III) en materiales compuestos avanzados utilizando elementos finitos de una y dos dimensiones es propuesto en este trabajo. Además, dos elementos finitos para la simulación de vigas y placas de varias capas altamente heterogéneos son desarrollados aquí.

El documento está escrito en base a los resultados de cuatro artículos publicados en revistas indexadas. Copias de estos artículos se incluyen en el Apéndice. El cuerpo principal de esta tesis está constituido por los Capítulos 2-4. El Capítulo 2 aborda el tratamiento numérico de vigas y placas laminadas. El capítulo 3 presenta la formulación de los elementos finitos de viga LRZ y placa QLRZ basados en la Teoría Zigzag Refinada. Finalmente, la principal contribución de esta tesis, el modelo de delaminación LRZ/QLRZ, se desarrolla en el capítulo 4.

Contents

1 Introduction

A laminated material is an orderly stacking of a finite number of relatively thin layers perfectly linked together, designed for achieving, among other properties, improved strength, stability, energy absorption and resistance to fatigue and correction. Nowadays, the varieties of materials to be combined available on the market and the different techniques of manufacturing made their design extremely customizable according to the needs, which is the key attribute.

Laminated or multilayered materials have a multitude of applications in a diversity of sectors. Aviation, astronautics, automotive, marine, civil engineering, sports equipment, musical instruments and information technology are a sample of them. Laminated materials are present in our daily life. For example, the modern windshields (Figure 1.1a), which generally consist of a sandwich of glass sheets with a plastic layer between them. Ballistic glasses (Figure 1.1b) are a special multilayered material, which are usually constructed by an alternation of plastic sheets and hard and soft glass layers that make the laminate stronger and more elastic. A very important laminated material in the electronic industry is the Printed Circuit Board (PCB) (Figure 1.2), which is a stacking of prepregs and copper layers. Laminated wood beams are also a multilayered material commonly used in civil engineering. These are constructed by stacking up wood plies bonded by adhesives. A special case of multilayered laminates are the sandwich-structured materials, which consist of two thin but stiff skins and a lightweight but thick core between them (Figure 1.3). One of the most interesting multilayered materials are the advanced composites (Figure 1.4). These are widely employed in many high-performance applications where conventional materials cannot be used. Each layer of these laminates consists of a composite material known as fiber-reinforced polymer (FRP), which is made of continuous fibers surrounded by a polymeric matrix.

a) b)

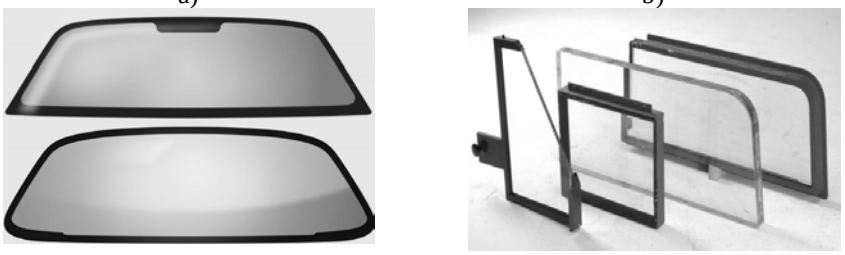

Figure 1.1 – Modern windshields for automobiles (a) (From: http://www.titanmotorsports.com) and ballistic glasses for windshields (b) (From: http://www.miller-holzwarthinc.com/).

Figure 1.2 – Printed circuit board. From: http://www.clarydon.com/.

a) b) c)

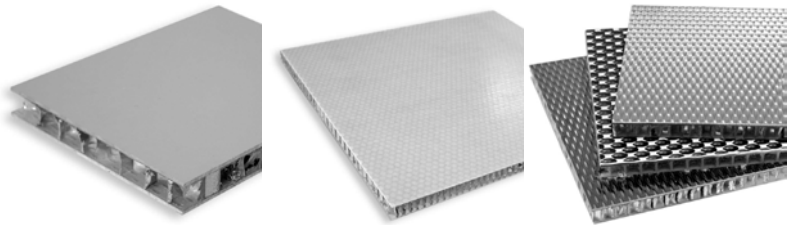

Figure 1.3 – Sandwich laminated formed by an aluminium honeycomb as core with skins of aluminium (a), fiber-glass composites (b) and fiber-carbon composites (c). From: http://www.cel.eu/.

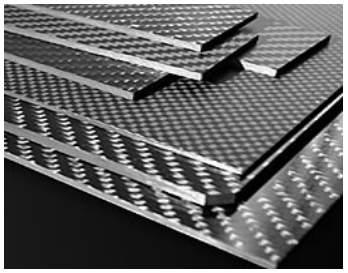

Figure 1.4 – Advanced composites of carbon fibers (CFRP). From: http://www.zero-carbon.com.

Although laminated materials have been used for decades, their employment has increased nowadays in the last years as a result of the gained confidence of the industry on these materials. This has provided the scientific community many reasons to dedicate considerable amount of time and efforts to address a better understanding of their mechanical behavior. With this objective both, experimental and numerical simulation have been working together to give response to a variety of problems related with these materials.

Regarding numerical simulation, the subject covered in this work, a correct modeling of the kinematics of laminated materials is essential to capture the real behavior of the structure. Moreover, once the kinematics has been accurately predicted other phenomena such as damage process could be also studied.

In order to correctly predict the kinematics of complex structures, 3D finite elements analysis can be the best alternative. However, the simulation of large multilayered structures with many plies can be unaffordable with 3D analyses because of the excessive computational cost, especially when non-linear studies are required. In addition, the discretization of very thin layers can lead to highly distorted elements carrying numerical issues.

These difficulties made the simpler models [1, 2], such as the Equivalent Single Layer (ESL) or the Layer-Wise (LW), a proper alternative to model multilayered laminates. In ESL theories governing equations are written for the whole plate, which leads to a constant number of variables through the thickness. This characteristic makes ESL models very efficient. However, they suffer from limitations to correctly simulate the kinematics of highly heterogeneous laminates.

Unlike ESL theories, LW models define each layer as an independent laminate which implies that the number of variables dependent on the number of analysis layers. Although LW theories accurately describe the behavior of multilayered laminates with independence of the level of transverse heterogeneity, they may result unattractive for simulating large laminated structures with many plies.

A good compromise between the accuracy of LW models and the computational efficiency of ESL models are the Zigzag theories (ZZT). ZZT models are a special case of LW models where the number of unknowns is independent of the number of analysis layer.

Among many other, the Refined Zigzag Theory (RZT) developed by Tessler et al. [3, 4] is a simple, efficient and robust ZZT theory to be considered for developing numerical tools able to simulate multilayered laminated materials.

According to the fracture process of advanced composites materials, different failure mechanisms can occur. These can be grouped into intra- and inter-laminar fracture modes, depending where the failure occurs: within or between the layers. The fiber fracture, the matrix cracking and the fiber-matrix shear failure (debonding) are distinguished as intra-laminar failure modes since they occur within the layer. Delamination, i.e. the relative displacement between neighboring layers, is a common inter-laminar failure mode that once it has been occurred the load carrying capacity of the composite member could be considerately reduced. Furthermore, this phenomenon may take place suddenly without any notice. These characteristics made delamination a really dangerous failure mechanism in advanced composite materials.

During the design phases of composite laminates, may be important to know how the global response of the structure is affected by delamination. For this purpose, the numerical simulation results very helpful.

Numerical techniques based on the linear elastic fracture mechanics (LEFM), the cohesive zone models (CZM) or the continuum damage mechanics (CDM) are usually applied for simulating delamination in a variety of engineering problems. Some applications examples are the skin-stiffness debonding [5] (CZM), the ply drop-off test [6] (CDM), the skin-core delamination and sub-laminate buckling [7] (LEFM) and the delamination in low-energy impact [8] (CZM). In these problems, the structures are discretized by means of 3D finite elements [6], by a combination between 3D elements and interface elements [8] or by employing shell elements and interface elements [5]. Although a detailed discretization of the structure is needed to accurately capture mix-mode delamination process in complex studies, simpler structural discretization may be enough for simulating delamination in cases where the opening mode (mode I) could be neglected. For instance, such case is found in low energy impact analyses, where fracture mode I appears usually after the shear modes (mode II and mode III) when the impact energy is considerably increased [8]. Thus, numerical methods based on a simpler discretization can be an acceptable approximation for modeling cases where delamination process is governed by the shear modes.

1.1 Objectives

This research aims at contributing to the development of simpler and more efficient numerical tools for simulating laminated materials.

Thus, this thesis is focused on two topics: the modeling of the kinematics of multilayered beam and plate structures (i) and the simulation of delamination in advanced composite materials (ii). At point (i), robust, efficient and effective finite elements are looked for. Regarding to point (ii), a simple delamination model that only uses reduced model to discretize the laminate is desired.

The main goals of this thesis are:

- The development of a numerical method based on one- and two-dimensional finite elements for simulating delamination processes (mode II and mode III) in beams and plates of advanced composite materials.

- The development of one- and two-dimensional finite elements based on the RZT theory in order to simulate the lineal behavior of highly heterogeneous multilayered beams and plates.

1.2 Organization

In order to achieve the objectives listed above, this work is structured as follows:

- Chapter 2 deals with the numerical treatment of laminated beams and plates. A review of more common reduced models employed to simulate multilayered beam/plate structures is presented first. Then, a complete description of the RZT plate theory used for developing the beam (LRZ) and plate (QLRZ) finite elements is given. Furthermore, the influence on the zigzag in-plane displacement of both, the transverse anisotropy and the span-to-thickness ratio is analyzed. In the second part of the Chapter, the failure mechanisms in advanced composite materials are dealt. In particular, special attention is given to the delamination process. Moreover, the most common numerical methods to model the failure mechanisms are presented.

- Chapter 3 presents the formulation of the LRZ beam and the QLRZ plate finite elements. The performance of these elements is studied through several numerical examples. Verification and convergence analyses are also performed. Furthermore, the problem of shear locking and the techniques employed to overcome it are addressed.

- Chapter 4 proposes the numerical model based on the LRZ and QLRZ finite element to model delamination process in advanced composite materials. A description about the isotropic damage model used for managing the onset and growth of delamination is also given. In addition, the modified Newton-Raphson scheme and the implicit integration algorithm used for solving the non-linear problem are presented. The performance of the method is analyzed by different numerical examples. The potential of this method to simulate multi-delamination is also investigated. Moreover, the limitations of the model due to the LRZ/QLRZ kinematics are also studied.

- Chapter 5 summarizes the main achievements of this work and gives some aspects which deserve future attention.

- Appendix includes copies of all four papers on which this document is based.

2 Numerical treatment of laminated beam/plate structures

In the first part of this Chapter, a review of reduced models for modeling multilayered beams and plates is presented. Furthermore, the Refined Zigzag Plate Theory (RZT) proposed by Tessler et al. [4] is fully described. Then, the influence on the zigzag in-plane displacement of the material transverse anisotropy and the laminate span-to-thickness ratio is studied.

The second part is focused on advanced composite materials and their failure mechanisms. In particular, special attention is given to the inter-laminar damage or delamination. Moreover, usual damage models to simulate intra- and inter-laminar failure modes are treated.

2.1 Multilayered beam/plate theories

The most precise technique for simulating laminated structures are the micro-models, where 3D finite elements are used for discretizing not only each ply but also the constituents within layer or even the interface between them. Although macroscopic approach at layer level could be considered, i.e. the constituents are not discretized, simulation of large laminated structures with many of plies can be unaffordable with 3D analyses due to the excessive computational cost, especially for non-linear analyses. In addition, the discretization of very thin layers can lead to highly distorted elements carrying numerical issues.

Multi-scale approaches [9, 10] can be also used to model multilayered materials. In this method a macroscopic model is used to obtain the global response of the structure whereas the material behavior is solved with a microscopic model. Basically, the macro-model transfers the structural deformation field onto the micro-model as boundary conditions. Then, within the micro-scale, the material response is evaluated and transferred back to the macroscopic model as a constitutive law.

Subsequently the structural equilibrium is found in the macro-scale and a new deformation field is computed and so forth. The simulation of large structures having complex geometries by means of this method results computationally unattractive.

Thus, simpler and more efficient techniques than that above-mentioned are required for modeling laminated structures. 3D descriptions can be reduced to 2D models by introducing hypotheses on the displacements or/and on the stresses field, since laminate thickness is at least one order of magnitude lower than in-plane dimensions.

However, in order to develop precise reduced models, the through-thickness discontinuity of mechanical properties within a laminated material has to be accounted for. From a qualitative point of view, the influence of the transverse anisotropy on the thickness distribution of the displacement and stress fields is schematized in Figure 2.1.

The in-plane displacement, outlined in Figure 2.1a, could exhibit abrupt changes of their slope along the thickness direction at each interface because large differences on the transverse shear properties between layers exist. This slope change leads to an in-plane displacement with zigzag pattern whose amplitude and shape depend not only on the transverse anisotropy but also on the laminate span-to-thickness ratio, as discussed in Section 2.1.4. Furthermore, all displacements are continuous along the thickness.

Although in-plane stresses can be discontinuous at each interface (Figure 2.1b), transverse stresses must be continuous for equilibrium reasons (Figure 2.1c). However, like in-plane displacement, the first derivatives along z are discontinuous at each interface.

As a result, it is desirable that multilayered models satisfy the following two conditions: zigzag pattern of in-plane displacements (ZZ condition) and the continuity of transverse stresses along the thickness direction (TC condition) [11].

Many 2D approaches have been developed and improved since 19th century [12]. In order to facilitate their classification, they could be distinguished according what type of unknown variables is chosen (i) and how these variables are described (ii). At point (i), displacements are defined as variable in the so-called “displacement-based theories” (DB) whereas stresses are employed in “stress-based theories” (SB). In case of both, the displacement and the stress are considered as

unknown, a "mixed[1] approach" (MB) is obtained. Regarding to point (ii), unknowns could be described by means of Equivalent Single Layer (ESL) or Layer-Wise (LW) descriptions.

In ESL description, governing equations are written for the whole plate, i.e. unknown variables are not defined for each layer but for the whole laminate. Thus, the number of variables is independent of the number of analysis layers.

On the contrary, each layer is treated as an independent plate in LW description, assuming separate displacement/stress field within each ply. In other words, governing equations are written for each layer. Moreover, in order to enforce compatibility conditions at the interface between layers, interface constraints on displacements and transverse stresses are required. Hence, the number of variables is dependent on the number of analysis layers.

A special case of LW models where the number of unknowns is independent of the number of analysis layer are the Zigzag theory (ZZT).

Useful overviews of available theories for modeling laminated plate structures have been written by Carrera [1] and Reddy [2].

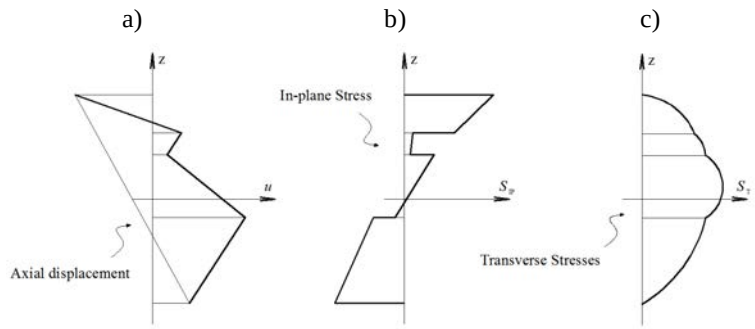

Figure 2.1 – Continuous zigzag in-plane displacement a), discontinuous in-plane stresses b), and continuous transverse stresses c).

2.1.1 Equivalent Single Layer models

Displacement-based models with ESL description (DB-ESL) have been widely developed for decades. An interesting review of DB-ESL models has been written by Wanji et al. [13].

The most basic DB-ESL model is the Classical theory (CT) [12, 14], which propose that transversal sections remain plane and normal to the reference surface

[1] Mixed approaches can be distinguished between full or partial models. In full mixed approaches all stresses are considered as variable whereas in partial mixed approach only the transverse shear stresses are accounted for.

after deformation, i.e. transverse shear strains are postulated to be negligible with respect to other strains. Because of these assumptions, the CT theory is limited to thin beams/plates where transverse shear effects can be neglected. In addition, this model despises the transverse normal deformation. The CT plate theory has only 5 unknown variables. Classical beam and plate models are also known as Euler-Bernoulli and Kirchhoff theories, respectively.

An improvement of the CT model are the First Order Shear Deformation theory (FSDT) [15-17], which enhance the CT kinematics by adding shear effects. This model establishes that transversal sections remain plane but not necessarily normal to the axis after deformation. Therefore, the transverse shear strain is defined constant through the thickness but not zero as in the CT theory. Like the CT model, strain along the thickness is not accounted for. Also, the plate FSDT contains only 5 unknown variables. However, in order to accurately compute transverse shear stresses, a shear correction factor[2] is required. FSDT beam and plate models are also known as Timoshenko and Reissner-Mindlin theories, respectively.

Although CT and FSDT theories are excellent alternatives to accurately model homogenous thin and thick structures, respectively, they gives poor predictions when applied to laminated structures having high level of transverse anisotropy. The cause is found in the linear thickness distribution of the axial displacement, which does not match the ZZ pattern schematized in Figure 2.1a.

FSDT theory can be improved by adding high-order terms of thickness coordinate z to the in-plane and transverse displacement fields. These improvements are known as High Order Shear Deformation theories (HSDTs).

One of first HSDTs model, where only the in-plane displacements are improved by a third-order polynomial, has been proposed by Reddy [18]. This model proposes a constant distribution of the transverse displacement.

Usually, both, the in-plane and the transverse displacement fields are defined by means of third-order polynomials [19]. However, it is also possible to find HSDTs models where fifth- and ninth-order polynomials are employed to describe the displacement field [20].

One advantage of HSDTs theories is that no shear correction factor is needed. Furthermore, those HSDTs models where a high-order description of the transverse displacement is used allow obtaining better through-thickness distribution of the transverse stresses.

[2] This factor is equal to 5/6 for homogeneous rectangular transversal sections.

With the aim to accurately satisfy the continuity of the transverse stresses along the thickness, mixed formulations should be employed.

For instance, Auricchio et al. [21] have proposed a partially mixed-based ESL model (MB-ESL) where the transverse shear stresses are a priori defined by means of the equilibrium equations assuming piecewise quadratic functions. Furthermore, the displacement field is described by the FSTD kinematics. Although the thickness distribution of transverse shear stresses is well predicted, the axial displacement does not match the ZZ form because of the linear FSTD kinematic.

Another way to achieve through-thickness continuity of the transverse stresses is by integrating a posteriori of the equilibrium equations[3]. However, the accuracy of this method depends on how precise the displacement field is modeled. A comprehensive analysis of the available techniques for computing transverse stresses in multilayered plates has been presented by Carrera [22].

Summarizing, although the TC condition could be satisfied by some ESL models, any of them is able to capture the zigzag shape of in-plane displacements.

2.1.2 Layer-Wise models

A LW description of the in-plane displacement is an accurate alternative to fulfill the ZZ condition. Displacement-based LW models (DB-LW) employs ESL theories, such as the CT, FSDT and HSDTs, to describe the displacement field of each layer.

Some DB-ESL and DB-LW models have been evaluated and compared by Reddy and Robbins [23].

Although the ZZ condition is satisfied by DB-LW models the TC condition is not fulfilled unless appropriate interface constraints are considered. For example, Robbins and Reddy [24] have improved a DB-LW theory by assuming a piecewise continuous distribution of the transverse strain, which allows to compute the inter-laminar continuity of transverse stresses.

Models that accurately fulfill the ZZ and TC conditions are those in which both, the displacement and the stress field are described by means of LW description. These models are known as mixed-based LW models (MB-LW).

Among many works related with MB-LW theories, readers are referred to Carrera's papers [25, 26] to go deeper on these models.

[3] The equilibrium equations for computing "a posteriori" the transverse shear stresses are defined by $\mathrm{div}[\boldsymbol{\sigma}] = 0$, where $\boldsymbol{\sigma}$ is the stresses tensor.

Although LW theories accurately fulfill both, the ZZ and the TC condition, the number of unknown variables is proportional to the number of analysis layers. As a result, these models yield not only a high level of accuracy but also an amount of unknown variables similar to the 3D analysis. For this reason, LW models may result unattractive for simulating large laminated structures with many plies. Therefore, these models should be employed to analyze complex problems where other less expensive approaches fail to give realistic predictions.

2.1.3 Zigzag models

A good compromise between the accuracy of MB-LW theories and the computational efficiency of DB-ESL models are the ZZT theories. One of the most important advantages of these theories is that the number of kinematics unknowns is independent of the number of analysis layers.

In ZZT models the in-plane displacement is defined by a superposition of a piecewise continuous function, called zigzag function henceforth, over a linear, quadratic, cubic or even higher order displacement field. The zigzag functions allow these models to reproduce the abrupt change in the slope of the in-plane displacement at each interface, as shown in Figure 2.1a. Moreover, in order to fulfill the TC condition and to reduce the number of unknown variables, constraint equations at the interface between layers must be enforced.

One of first attempt to refine an ESL model by means a zigzag function has proposed by Murakami [27]. In this model, the FSDT kinematics is enhanced by adding a piecewise linear zigzag function. It is important to remark that the slope of the Murakami's zigzag function is defined positive for odd layers and negative for even plies, which implies that the shape of this function depends on the stacking sequence of the laminate only. Then, Murakami et al. [28] have also proposed an improvement of a high-order ESL theory.

It should be mentioned that approaches where the displacement field is improved by means of the Murakami's zigzag function are unable to a priori satisfy the TC condition.

In order to provide the through-thickness continuity of the transverse shear stress, Carrera [29] has developed a refined FSDT plate model based on Murakami's concepts [27]. In Carrera's model the TC condition is fulfilled a priori by assuming a piecewise quadratic function and a set of equilibrium conditions at each interface.

Demasi [30] has investigated the numerical performance of Murakami's zigzag function by means of FEM analysis.

At around the same period Murakami was developing his refined FSDT model [27], Di Sciuva [31] was working in his ZZT model. He proposed a refinement of the FSDT theory by adding a linear zigzag function also. However, the transverse shear strain is defined as a kinematic variable instead of a bending rotation as in the FSDT model. Moreover, in order to compute the zigzag function, constant shear stresses along the thickness are enforced, which is a very strict constraint for simulating multilayered materials.

Furthermore, Di Sciuva [32] and Cho et al. [33] have independently provided a refinement of a third-order ESL models by adding a linear zigzag function.

Many ZZT theories, including those mentioned above, require C^1-continuity when solved via finite element analysis, which implies a disadvantage versus simpler C^0-continuity theories, such as the FSDT model.

In order to overcome this drawback, Averill [34] formulated a refined linear zigzag theory where the FSDT model is used as its baseline. Then, the FSTD kinematics variables, i.e. the deflection, the axial displacements and the bending rotation, are considered as unknowns together with a kinematics variable associated with the zigzag function. All these variables can be interpolated with C^0-continuious polynomials. Moreover, the through-thickness continuity of the transverse shear stress is enforced using a penalty method. A cubic zigzag model was also provided by Averill et al. [35]. Although C^0-continuity is achieved, Averill's theories suffer from their inability to model correctly clamped boundary conditions.

With the goal to avoid these shortcomings and propose an amiable theory to formulate robust C^0-continuity finite element, Tessler et al. [3, 4, 36, 37] have developed the Refined ZigZag Theory (RZT). The plate[4] RZT theory proposed by Tessler et al. [36] is described below in next section.

The RZT displacement field is defined by a superposition of a linear zigzag function over the FSDT kinematics. In these models, constraint conditions on the distribution of the zigzag functions are imposed, which leads to a constant piecewise distribution of transverse shear stress along the thickness. However, the TC condition of transverse shear stresses could be computed a posterior by using equilibrium equations [38, 39]. This post-process gives accurate results because the zigzag in-plane displacements are correctly predicted. On the other hand, transverse normal strain is despised. The RZT kinematics variables are the displacements and the bending rotations of the FSDT theory together with a variable associated with the zigzag function. The key attributes of the RZT are, first, the zigzag function

[4] The beam RZT displacement field is easy obtained from the plate RZT theory by neglecting the in-plane transverse displacement *v*.

vanishes at the top and bottom surfaces of the laminate section. Second, it does not require full transverse shear stress continuity across the thickness coordinates. Third, in order to formulate finite elements, C^0 continuous polynomials are needed for discretizing the kinematic variables. Fourth, all boundary conditions can be effectively simulated. Finally, the zigzag function is defined as a function of the transverse shear modulus of each layer, which results useful in non-linear material analysis [40, 41].

The simplicity, efficiency and effectiveness of the RZT theory allowed develop in this thesis two robust C^0 continuous finite elements for simulating multilayered beams [38] and plates [39]. The formulation of these elements is presented in Chapter 3. Simultaneously, Gherlone et al. [42] and Versino et al. [43] have also formulated beam and plate finite elements based on the RZT theory.

Recently, Barut et al. [44] have extended the RZT plate theory [4] for taking into consideration the transverse normal strain. In this model, the in-plane displacement consist of a piecewise quadratic function, whereas a quadratic polynomial is used for describing the transverse displacement component. Based on this extended RZT model, Barut et al. [45] have formulated a C^0 continuous triangular plate element.

2.1.3.1 Refined zigzag theory (RZT)

Let us consider a laminated plate of uniform thickness h formed by N orthotropic layers of thickness h^k (k = 1, 2, … , N). The orthogonal Cartesian coordinates system (x,y,z) is employed as reference coordinates. The ordered pair (x,y) is set as the in-plane coordinates whereas z denotes the thickness coordinate which ranges from $-h/2$ and $+h/2$. The in-plane reference surface is placed at the middle plane for z = 0.0.

The displacement field in the RZT plate theory is written as

$$\begin{aligned} u^k(x,y,z) &= u_0(x,y) - z\cdot\theta_x(x,y) + \bar{u}^k(x,y,z) \\ v^k(x,y,z) &= v_0(x,y) - z\cdot\theta_y(x,y) + \bar{v}^k(x,y,z) \\ w\,(x,y) &= w_0(x,y) \end{aligned} \qquad 2.1$$

where the axial displacement zigzag function $\bar{u}^k$ and $\bar{v}^k$ are defined as

$$\begin{aligned} \bar{u}^k &= \phi_x^k(z)\cdot\psi_x(x,y) \\ \bar{v}^k &= \phi_y^k(z)\cdot\psi_y(x,y) \end{aligned} \qquad 2.2$$

and superscript k indicates quantities within the kth layer. The uniform axial displacements along the coordinate directions x and y are denoted by u_0 and v_0, respectively; θ_x and θ_y represent the average bending rotation of the transverse normal about the negative y and positive x directions; and w_0 is the uniform transverse deflection. $\phi_i^k \left(i = x, y\right)$ denote the known piecewise linear *zigzag function*, and ψ_i is a primary kinematics variable defining the amplitude of the zigzag function. Summarizing, the unknown variables are

$$\mathbf{a} = \begin{bmatrix} u_0 & v_0 & w_0 & \theta_x & \theta_y & \psi_x & \psi_y \end{bmatrix}^T \tag{2.3}$$

where the uniform displacement u_0, v_0 and w_0, and the bending rotation θ_x and θ_y are derivate from the FSDT theory, where the ψ_i variables are associated with the added displacement zigzag functions $\overline{u}^k$ and $\overline{v}^k$.

The in-plane (ε_p^k) and transverse shear (ε_t^k) strains are defined as

$$\boldsymbol{\varepsilon}_p^k = \begin{bmatrix} \varepsilon_x \\ \varepsilon_y \\ \gamma_{xy} \end{bmatrix}^k = \begin{bmatrix} \dfrac{\partial u_0}{\partial x} - z\dfrac{\partial \theta_x}{\partial x} + \phi_x^k(z)\dfrac{\partial \psi_x}{\partial x} \\ \dfrac{\partial v_0}{\partial y} - z\dfrac{\partial \theta_y}{\partial y} + \phi_y^k(z)\dfrac{\partial \psi_y}{\partial y} \\ \left(\dfrac{\partial u_0}{\partial y} + \dfrac{\partial v_0}{\partial x}\right) - z\left(\dfrac{\partial \theta_x}{\partial y} + \dfrac{\partial \theta_y}{\partial x}\right) + \left(\phi_x^k(z)\dfrac{\partial \psi_x}{\partial y} + \phi_y^k(z)\dfrac{\partial \psi_y}{\partial x}\right) \end{bmatrix} \tag{2.4}$$

$$\boldsymbol{\varepsilon}_t^k = \begin{bmatrix} \gamma_{xz} \\ \gamma_{yz} \end{bmatrix}^k = \begin{bmatrix} \left(\partial w/\partial x - \theta_x\right) + \beta_x^k \psi_x \\ \left(\partial w/\partial y - \theta_y\right) + \beta_y^k \psi_y \end{bmatrix} = \begin{bmatrix} \gamma_{xz} + \beta_x^k \psi_x \\ \gamma_{yz} + \beta_y^k \psi_y \end{bmatrix} \tag{2.5}$$

being γ_{iz}^k and β_i^k $\left(i = x, y\right)$, the transverse shear strain and the slope of ϕ_i^k in the thickness direction ($\beta_i^k = \partial \phi_i^k / \partial z$) for the kth layer, respectively. γ_{iz} represent the average transverse shear strains of the FSDT ($\gamma_{iz} = \partial w/\partial i - \theta_i$).

The stress-strain constitutive relationship for the kth orthotropic layer is written as

$$\begin{bmatrix} \sigma_x \\ \sigma_y \\ \underline{\tau_{xy}} \\ \tau_{xz} \\ \tau_{yz} \end{bmatrix}^k = \begin{bmatrix} D_{p11} & D_{p12} & D_{p13} & 0 & 0 \\ D_{p21} & D_{p22} & D_{p23} & 0 & 0 \\ D_{p31} & D_{p32} & D_{p33} & 0 & 0 \\ 0 & 0 & 0 & D_{t11} & D_{t12} \\ 0 & 0 & 0 & D_{t21} & D_{t22} \end{bmatrix}^k \begin{bmatrix} \varepsilon_x \\ \varepsilon_y \\ \underline{\gamma_{xy}} \\ \gamma_{xz} \\ \gamma_{yz} \end{bmatrix}^k \qquad 2.6$$

or

$$\boldsymbol{\sigma}^k = \mathbf{D}^k \boldsymbol{\varepsilon}^k \qquad 2.7$$

where $\mathbf{D}^k$ is the constitutive matrix referred to the reference coordinate system (x,y,z). Matrix $\mathbf{D}^k$ is computed by Eq.(3.50) in Section 3.3.3.

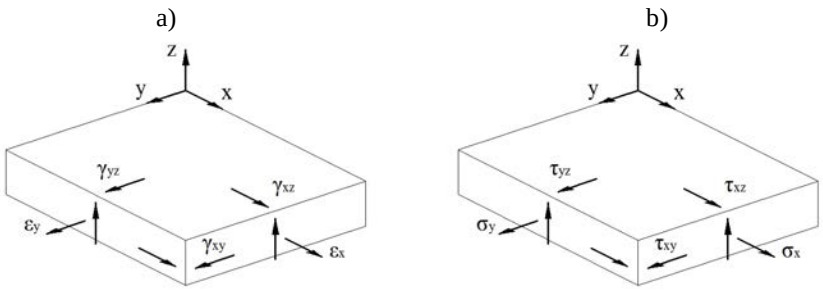

Figure 2.2 – Strain (a) and stress (b) field.

The zigzag functions ϕ_i^k are defined by piecewise linear continuous functions through the laminate thickness as

$$\phi_i^k = \frac{1}{2}(1-\xi)\bar{\phi}_i^{k-1} + \frac{1}{2}(1+\xi)\bar{\phi}_i^k = \frac{\bar{\phi}_i^k + \bar{\phi}_i^{k-1}}{2} + \frac{\bar{\phi}_i^k - \bar{\phi}_i^{k-1}}{2}\xi^k \qquad 2.8$$

where $\bar{\phi}_i^k$ and $\bar{\phi}_i^{k-1}$ are the zigzag function valued at k and $k-1$ interface, respectively, with $\bar{\phi}_i^0 = \bar{\phi}_i^N = 0$ and $\xi^k = 2\dfrac{\left(z - z^{k-1}\right)}{h^k} - 1$.

Figure 2.2 schematizes the zigzag function ϕ_x^k, the zigzag displacements $\bar{u}^k$, and the axial displacements u^k along x direction for a four-layered laminate. Similar distributions of these values are found for the y direction.

The computation of β_i^k is obtained by computing the derivative of ϕ_i^k (Eq.(2.8)) with respect to the z coordinate as

$$\beta_i^k = \frac{\partial \phi_i^k}{\partial z} = \frac{\left(\overline{\phi}_i^k - \overline{\phi}_i^{k-1}\right)}{h^k} \tag{2.9}$$

which result in piecewise constant functions.

The piecewise linear zigzag functions of Eq.(2.8) can be written as functions of β_i^k as

$$\phi_i^k = \overline{\phi}_i^{k-1} + \frac{h^k \beta_i^k}{2}\left(\zeta^k + 1\right) \tag{2.10}$$

Because the zigzag function vanishes on the top and bottom surfaces, the through-the-thickness integrals of the slope functions β_i^k is equal to zero, i.e.

$$\int_{-h/2}^{+h/2} \beta_i^k dz = \sum_{k=1}^{N} \int_{-h^k/2}^{+h^k/2} \left(\frac{\overline{\phi}_i^k - \overline{\phi}_i^{k-1}}{h^k} \right) dz = \sum_{k=1}^{N} \left(\overline{\phi}_i^k - \overline{\phi}_i^{k-1}\right) = \overline{\phi}_i^N - \overline{\phi}_i^{k-1} = 0 \tag{2.11}$$

Integrating the layer transverse shear strains of Eq.(2.5) across the laminate thickness and using Eq.(2.11) reveals that

$$\gamma_{iz} = \frac{1}{h}\int_{-h/2}^{+h/2} \gamma_{iz}^k dz = \partial w / \partial_i - \theta_i \tag{2.12}$$

which verifies that γ_{iz} represent the average transverse shear strains of the FSDT. Moreover, Eq.(2.12) shows that the zigzag amplitude variables ψ_i do not contribute to γ_{iz}.

For convenience, a new difference function η_i is defined as

$$\eta_i = \gamma_{iz} - \psi_i \tag{2.13}$$

which leads to the following expression of the transverse shear strains for the kth layer as

$$\gamma_{iz}^k = \eta_i + \left(1 + \beta_i^k\right)\psi_i \tag{2.14}$$

Using Eqs.(2.14) and (2.6), the transverse shear stresses are written in matrix form as

$$\begin{bmatrix} \tau_{xz} \\ \tau_{yz} \end{bmatrix}^k = \begin{bmatrix} D_{t11} & D_{t12} \\ D_{t21} & D_{t22} \end{bmatrix}^k \left(\begin{bmatrix} \eta_x \\ \eta_y \end{bmatrix} + \begin{bmatrix} \left(1+\beta_x^k\right) & 0 \\ 0 & \left(1+\beta_y^k\right) \end{bmatrix} \begin{bmatrix} \psi_x \\ \psi_y \end{bmatrix} \right) \tag{2.15}$$

or, alternatively, they can be expressed as

$$\begin{bmatrix}\tau_{xz}\\ \tau_{yz}\end{bmatrix}^k=\begin{bmatrix}D_{t11} & D_{t12}\\ D_{t21} & D_{t22}\end{bmatrix}^k\begin{bmatrix}\eta_x\\ \eta_y\end{bmatrix}+ \\ +\left\{D_{t11}\left(1+\beta_x^k\right)\right\}\begin{bmatrix}\psi_x\\ \dfrac{D_{t21}}{D_{t11}}\psi_x\end{bmatrix}+\left\{D_{t22}\left(1+\beta_y^k\right)\right\}\begin{bmatrix}\dfrac{D_{t12}}{D_{t22}}\psi_y\\ \psi_y\end{bmatrix} \qquad 2.16$$

In this equation, the first stress vector associated with η_i functions is independent of the zigzag functions. The second and third stress vectors contain the coefficients $\left\{D_{t11}\left(1+\beta_x^k\right)\right\}$ and $\left\{D_{t22}\left(1+\beta_y^k\right)\right\}$, which are dependent on the zigzag functions. In this theory, both coefficients are set to be constant quantities, denoted as G_{iz} $\left(i=x,y\right)$, whose constraint leads to constraint conditions on the distribution of the zigzag function. Thus, the continuity of the transverse shear stresses at each layer interface, i.e. $\tau_{iz}^k=\tau_{iz}^{k+1}$, is not enforced. In addition, Eq.(2.16) revels that τ_{iz}^k is piecewise constant across the thickness.

The constraints give

$$\begin{bmatrix}\beta_x\\ \beta_y\end{bmatrix}^k=\begin{bmatrix}\dfrac{G_{xz}}{D_{t11}^k}-1\\ \dfrac{G_{yz}}{D_{t22}^k}-1\end{bmatrix} \qquad 2.17$$

where the explicit form of G_{iz} is obtained by substituting Eq.(2.17) in the integral of Eq.(2.11), i.e.

$$\begin{bmatrix}G_{xz}\\ G_{yz}\end{bmatrix}=\begin{bmatrix}h\left[\displaystyle\sum_{k=1}^{N}\frac{h^k}{D_{t11}^k}\right]^{-1}\\ h\left[\displaystyle\sum_{k=1}^{N}\frac{h^k}{D_{t22}^k}\right]^{-1}\end{bmatrix} \qquad 2.18$$

The coefficients G_{iz} are considered as an average transverse shear stiffness properties of the laminate referred to the reference coordinates system (x,y,z).

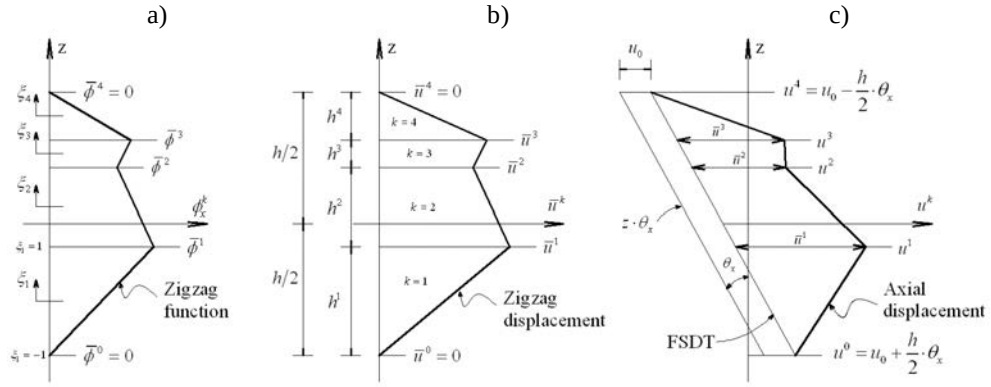

Figure 2.3 - Thickness distribution of the zigzag function ϕ_x^k a), zigzag displacement $\bar{u}^k$ b), and axial displacement u^k c) in the RZT theory.

2.1.4 Influence of the span-to-thickness ratio and the transverse heterogeneity on the zigzag pattern of the in-plane displacements

The obective of this section it is to analyze how the amplitud and shape of the zigzag in-plane displacement is afected by not only the through-thickness anisotropy of transverse shear stiffness but also the laminate span-to-thickness ratio.

In order to assess the objective, a clamped beam of thickness h = 1and span-to-thickness ratio λ = 5, 10, 20 and 50 is studied. The beam is submitted under a unitary vertical displacement Δw at the free end (Figure 2.3a). The laminated material is formed by three layers of thickness $h^k = h/3$ (k = 1,2,3) with symmetry distribution (Figure 2.3b). Four levels of transverse heterogeneity are performed defining different transverse shear modulus for the middle layer (G_M) (Table 2.1). Heterogeneity ranges from the "lowest" (H1) to the "highest" (H4) level for which the shear modulus of the middle layer is two to thousand times smaller than that of the top/bottom layers ($G_{T/B}$), respectively. All cases were solved via plane stress analysis.

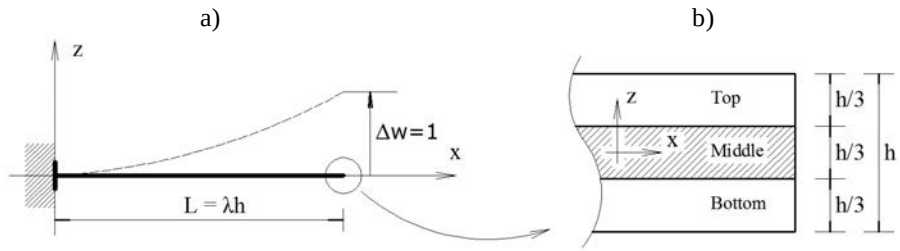

Figure 2.4 - Cantilever beam under vertical displacement a) and symmetric three-layered material b).

Transverse heterogeneities	
	$G_{T/B} / G_M$
H1	2
H2	10
H3	100
H4	1000

Table 2.1 – Relation between the shear moduli of the top/bottom layer and the middle layer. The less and most heterogeneous configurations are the heterogeneity H1 and H4, respectively.

Figure 2.4 show the normalized axial displacement for all span-to-thickness ratios.

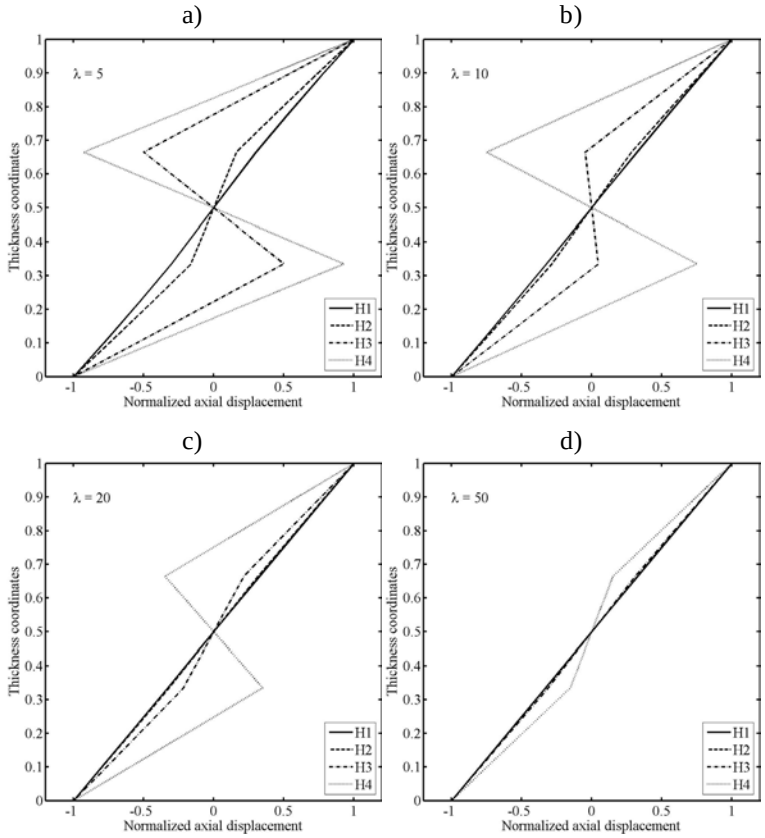

Figure 2.5 – Normalized axial displacement for span-to-thickness ratio $\lambda = 5$ a), $\lambda = 10$ b), $\lambda = 20$ c) and $\lambda = 50$ d).

Figure 2.4a shows that only a difference of ten times (H2) between the shear moduli is enough to obtain a zigzag distribution of the axial displacement for the less slender beam ($\lambda = 5$). On the contrary, a difference of thousand times (H4) gives

a slight zigzag distribution for the most slender beam (λ = 50) (Figure 2.4c). Another interesting observation is that a difference of two orders of magnitude (H3) between the shear moduli provokes an almost linear distribution for the most slender beam and a slight zigzag pattern for the beam of λ = 20. Furthermore, a difference of one order of magnitude (H2) gives a zigzag kinematics for the less slender beam only where the lowest heterogeneity (H1) provokes a linear distribution for all span-to-thickness ratios.

Therefore, the amplitude of the zigzag in-plane displacement is increased according the transverse anisotropy of the shear modulus is higher whereas it is reduced according the laminate is more slender.

2.2 Advanced composite materials and delamination phenomenon

Advanced composites laminates are a stacking of fiber reinforced plastic (FRP) layers. FRP plies are composed of continuous fibers embedded in a polymeric matrix. Although there is a large bandwidth of fiber materials, carbon are the most widely used for high-performance applications. In addition, there are a countless number of different carbon fibers, e.g. high strength, high stiffness, surface treated or non-surface-treated, etc., and polymeric matrixes, e.g. thermosetting, thermostable or thermoplastic. This wide variety of material leads to an almost infinite number of potential mixtures. Moreover, the chance to orient the fibers according an optimum distribution of strength and stiffness provides a very customizable design. Furthermore, the use of very light and strong raw materials leads to lightweight laminates with a considerable high specific strength and stiffness[5]. Other well valued characteristics of these materials are the fatigue and corrosion resistance and the high energy absorption capacity.

These features made the advanced composites a good alternative for applications where the weight saving implies substantial cost reductions. Moreover, they are also the material of choice for structures under high strengths. Aviation and astronautics are some examples of application. The use of advanced composites in aeronautics has been considerable increased in last decades [46]. For example, about 25 and 50 percent of the airplanes Airbus A380 and Boing 787 Dreamliner are made of composite materials. In addition, composite materials represent about 80 percent of the structure weight in the construction of satellites. Automotive, marine, civil engineering, sport and medical industries are also interested in advanced composite materials.

[5] The specific strength is the strength per unit weight. It is also known as the strength/weight ratio. The same holds for specific stiffness.

In order to define the load carrying capacity of the structure, the study of material fracture process is a very important topic. Advanced composite laminate may suffer from different failure mechanisms. These can be grouped into intra- and inter-laminar fracture modes, depending where the failure occurs: within or between the layers. The fiber fracture[6], the matrix cracking[7] and the fiber-matrix shear failure[8] (debonding) are distinguished as intra-laminar failure modes since they occur within the layer. Delamination, i.e. the relative displacement between neighboring layers, is a common inter-laminar failure mode that once it has been occurred the load carrying capacity of the composite member could be considerately reduced. Moreover, this phenomenon may take place suddenly without any notice. These characteristics made the delamination a really dangerous failure mechanism in advanced composite materials.

Although all these failure modes have to be accounted for accurately simulating the fracture behavior of advanced composites materials, this thesis is focused on the numerical simulation of delamination only. However, for the sake of completeness, the modeling of intra-laminar fracture modes is also treated below.

2.2.1 Modeling of intra-laminar fracture modes

In order to simulate intra-laminar fracture modes, intra-laminar damage models or also called failure models can be employed. These models consist of failure criteria, which evaluate if stress leads to the failure, and degradation models, which manage the material degradation.

A simple and well known failure criterion is the maximum stress/strain criterion, which is computed by comparing the uni-axial stresses/strains with their threshold value for each component. Despite its simplicity, no interaction of stresses is taken into account.

[6] Fiber fracture can be provoked by not only tensile but also compressive stresses. Failure due to tensile stress occurs when the fiber strength is achieved. Longitudinal compressive stress can induce micro-buckling of fiber if the matrix is unable to hold the fibers in their position.

[7] When matrix strength is exceeded a crack is produced which tends to propagate perpendicularly to the stress direction until the fiber. If fiber strength is enough strong the crack can be stopped, otherwise, the discontinuity will be continue causing fiber fracture. Furthermore, fracture can grow parallel to the fiber at the fiber-matrix interface, i.e. debonding.

[8] Debonding occurs when fibers are disjointed from the matrix due to the fiber-matrix interface is unable to support the shear stresses acting parallel to the fibers.

Failure criteria that consider interactions between stresses can be subdivided into two classes, namely the global criteria, which use only one equation for all failure modes, and the physically-based criteria, which employ different criteria for different failure modes.

One of first attempts to develop a global criterion was presented by Hill [47], who proposed a single formula that take into account different strengths in various principal directions. Another very interesting global criterion has been proposed by Tsai and Wu [48], where a strength-based second order polynomial is proposed for all intra-laminar failures modes.

Among hundreds of physically-based criteria, a well-known damage criterion and widely used by commercial finite element codes is the Hashin's failure criterion [49]. This damage model is able to model fiber fracture and matrix cracking under tensile and compressive stress state. An improvement of the Hashin's model was proposed by Goyal et al. [50] where fiber-matrix shear failure is also considered. Goyal's model is also known as the extended Hashin's model. Based on Hashin's ideas, Puck [51] proposed a failure criterion where three different types of matrix cracking are considered. Dávila et al. [52] have developed a damage model, denoted LaRC03, that consists of six phenomenological failure criteria which can predict matrix and fiber failures without curve-fitting parameters. An improvement of the LaRC03 failure criteria, denoted LaRC04, was proposed by Pinho et al. [53].

Intra-laminar material properties of FRP composite laminates, such as stiffness/strengths parallel and transverse to the fiber, can be characterized according the American [54, 55] and the European [56-58] standards. These experimental tests are carried out under tensile and compressive load states.

Oller et al. [59] and Martínez [60] proposed another way for modeling the non-linear mechanical behavior of FRP laminated structures. Their methods are based on the combination of the constitutive models of each phase, i.e. fibers and matrix, together with governing equations that control the mechanical behavior of the composite. In other words, the mechanical behavior of each component is treated separately whereas the global response of the composite is obtained by assembling all contributions of components. In order to separately model the phases in a uni-directional (UD) composite material, the Classical mixing theory [61, 62] or the Serial/Parallel mixing theory [63] can be employed.

2.2.2 Inter-laminar fracture mode - Delamination phenomenon

According to Bolotin [64], two kinds of delamination can be distinguished: internal and near-surface delamination. The first one is situated within the bulk of

material (Figure 2.5a) whereas the second one, as its name suggests, is placed near the surface of the laminate (Figure 2.5b).

After near-surface delamination, delaminated part does not necessarily have the same deformation as the rest of laminate. That leads to a complex fracture process where have to be accounted for not only the delamination growth but also local stability of the delaminated part.

Unlike near-surface delamination, the delaminated parts after internal delamination have similar deformation because of the interaction between them. Moreover, local instabilities are almost improbable to occur after internal delamination. However, this type of delamination may considerably modify the stiffness of the composite member provoking a substantial reduction of the load carrying capacity.

Furthermore, many delamination processes can take place within the laminate, which is known as multi-delamination (Figure 2.5c).

Local forces, thermal actions and low-energy impacts may serve as sources of delamination during transportation, storage, montage or service life of the structure. In addition, geometry discontinuities such as access holes, notches, free edges or bonded and bolted joints can also induce delamination due to high stress gradients.

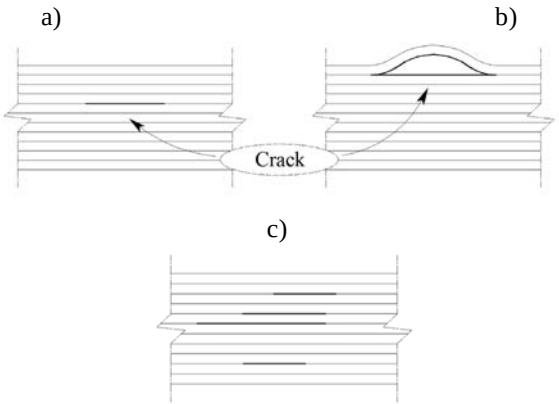

Figure 2.6 – Internal (a), near-surface (b) and multiple (c) delamination according to Bolotin.

At a microscopic scale, delamination is preceded by the formation of micro-cracks in a resin-rich zone between layers (Figure 2.6). Although micro-cracks could migrate through the plies [65], delamination is usually assumed to propagate parallel

to the ply planes within the interface, which is an acceptable idealization for its numerical modeling. Furthermore, according to fracture mechanics, delamination may occur as a single fracture mode I, mode II, mode III (Figure 2.7), or more likely as any combination of these (mixed mode). Mode I or opening mode corresponds to transverse normal tensile stress where mode II and III are provoked by the sliding and the scissoring shear stresses[9], respectively. These stresses are known as inter-laminar stresses also.

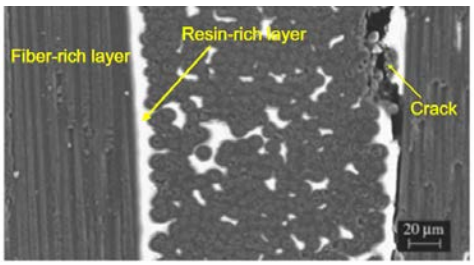

Figure 2.7 – Photomicrograph of an advanced composite where resin-rich zones and delamination are shown, from Barut et al. [44].

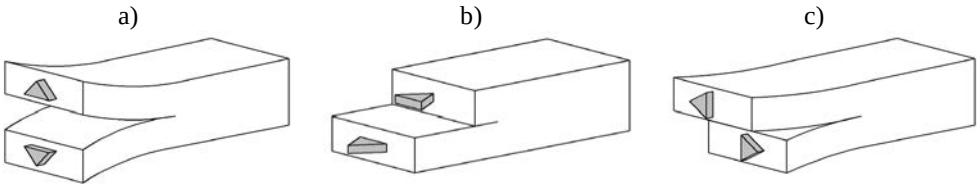

Figure 2.8 – Fracture mode I a), mode II b) and mode III c).

Delamination process, i.e. the onset and the growth, are governed by two inter-laminar properties, namely the strength and the fracture toughness (G_c). These properties depend on the delamination mode. The fracture toughness is also known as fracture energy, since it is defined as the amount of energy dissipated per unit area during the fracture process.

Both inter-laminar properties can be characterized via experimental tests. The mode II strength can be determined by the American standard ASTM D2344 [66]. It is not clear to the author if exist experimental tests to characterize strength for modes I and III. However, mode I strength is usually considered equal to the in-plane transverse tensile strength because the opening mode is matrix-dominated. Regarding to mode III strength, an assumption of safe design is to define it equal to mode II strength.

[9] Sliding and scissoring shear stresses correspond to the transverse shear stresses parallel and transversal to fiber direction, respectively.

Fracture toughness for pure modes I (G_{Ic}) and II (G_{IIc}) can be determined via the double cantilever beam (DCB) [67, 68] and the end notched flexure (ENF) [69] standardized tests, respectively. Mode III fracture energy (G_{IIIc}) can be characterized via the no standardized edge crack torsion (ECT) test proposed by Lee [70].

In order to compute the fracture toughness (G_c) for different mode mixing ratios ($\rho = G_{II}/G_T$)[10] from the pure mode I (DCB) to the pure mode II (ENF), the mixed mode bending (MMB) [71] standardized test can be employed. However, the experimental characterization of the fracture energy for all possible mixed mode results impossible to carry out. For this reason, the fracture toughness is usually determined by means of curves that approximately fit the data generated by experimental tests. For example, among many others [65, 72], the BK model [73], the power law model [74] and the polynomial curve [75] (Table 2.2) are some of the most common mixed mode criteria. The fracture energy characterization is schematized in Figure 2.8.

Mixed mode criteria	
BK	$G_c = G_{Ic} + \left(G_{IIc} - G_{Ic}\right)\rho^{\kappa}$
Power law	$\left(\frac{G_I}{G_{Ic}}\right)^{\kappa_1} + \left(\frac{G_{II}}{G_{IIc}}\right)^{\kappa_2} = 1$ For $\kappa_1 = \kappa_2 = \kappa$ $G_c = \left[\left(\frac{1-\rho}{G_{Ic}}\right)^{\kappa} + \left(\frac{\rho}{G_{IIc}}\right)^{\kappa}\right]^{-1/\kappa}$
Polynomial	$G_c = G_{Ic} + \kappa_1\rho + \kappa_2\rho^2$

Table 2.2 – Mixed mode criteria for computing the mixed mode fracture toughness. ρ is the mode mixing ratio defined as G_{II}/G_T, whereas κ_1, κ_2 and κ are curve fitting parameters.

[10] The mode mixing ratio ρ relates the mode II energy release rate (G_{II}) with the total energy release rate (G_T) in order to distinguish different mixed modes. This value ranges from 0 (pure mode I - DCB) to 1 (pure mode II – ENF).

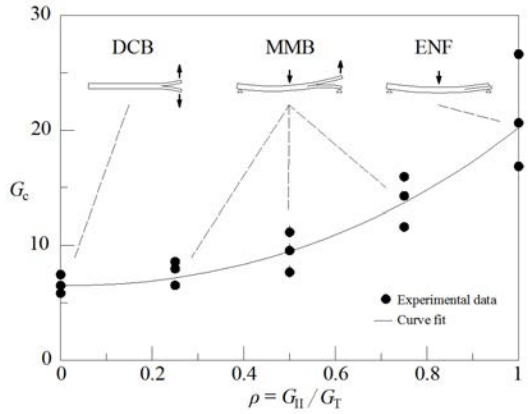

Figure 2.9 – Characterization of the fracture toughness for different mode mixing ratios.

2.2.2.1 Modeling of delamination

Methods based on the linear elastic fracture mechanics (LEFM), such as the Virtual Crack Closure Technique (VCCT) [7, 76], the J-integral method [77, 78] and the virtual crack extension method [79], have proved to be suitable for predicting delamination growth. These methods are used to compute the energy release rate by means of results obtained from finite elements analyses. Then, delamination propagation occurs when the energy release rate is higher than the fracture thoroughness.

Nowadays, the VCCT technique is widely used to study several delamination cases, such as delamination buckling [80-82] and skin-stiffener debond [83-85], where the structure can be discretized with 3D, plane stress and/or plate finite elements. An interesting overview of this technique is presented by Kruger [7], where expressions to compute the energy release rate with different kinds of finite elements are also derived.

LEFM-based methods can be also employed together with simpler models such as the LW theories. Recently, Saeedi et al. [86] formulated a delamination model based on a LW description where the energy release rate is computed via the VCCT technique. In addition, Saeedi's model is contrasted with a 3D analysis that employs the J-integral method. Also, Barbero et al. [87] proposed a model based on a LW description where the virtual crack extension method is employed.

Although the efficacy of these techniques to predict delamination growth is well known, an initial crack must be predefined since they are unable to predict delamination onset. This is a significant drawback for certain geometries and load cases where the predefined crack can be difficult to locate.

Nowadays, cohesive or interface finite elements are other effective numerical method to fully simulate the delamination process. These elements are based on the

cohesive zone approach (CZM) proposed by Dudgale [88] and Barenblatt [89] where it is assumed that molecular forces or cohesive forces act in the close vicinity of the crack tip. As a result, the crack is extended within a fracture process zone where a softening process takes place instead of a sudden decohesion.

The softening process is described by cohesive laws[11] which use different criteria[12] to control not only the onset but also the growth of delamination. Usually, onset criteria relate inter-laminar stress and strength whereas delamination growth is governed by the energy dissipated during the process[13].

Interface elements can be formulated based on solid-like [90, 91] or zero-thickness [92-97] approaches.

Solid-like interface elements are based on hexahedral solid elements with finite thickness. However, the transverse normal and shear stresses are accounted for only. All other stresses are set to zero. In addition, the initial thickness of the element has to be thin enough[14] in order to avoid membrane effects.

Unlike solid-like elements, zero-thickness elements are defined by two surfaces that are initially coincident, i.e. the thickness is equal to zero. These surfaces are held together by inter-laminar tractions as long as the interface is intact.

Cohesive laws are usually written in stress-strain and traction-displacement relationships for solid-like and zero-thickness elements, respectively. An interesting comparison between both types of interface element can be found in Balzani's PhD thesis [5].

Cohesive elements do not require initial crack to provide delamination onset, which is an important advantages respect to the LEFM-based methods, but they have to be placed between the plies where delamination is expected to occur. Thus, in cases where delamination paths are unknown it would be necessary to place interface elements between all layers. As a result, the computational resources needed for carrying out the simulation is considerably increased, especially in laminates of many plies. For this reason interface elements are peculiar suitable for studies where delamination path is known a priori, such as skin-stiffener delamination problems [5, 94, 95, 98].

Methods based on the continuum damage mechanics (CDM) are also able to simulate delamination. Martinez et al. [6] successfully analyzed delamination in a ply drop-off test using 3D finite elements to discretize the laminate and an isotropic damage model to manage the material mechanical behavior.

[11] Cohesive laws are frequently defined by means of bi-linear and exponential curves.
[12] These criteria are usually formulated taking into account mixed-mode delamination.
[13] When the area under cohesive law curve is equal to the fracture toughness complete decohesion occurs and delamination is propagated.
[14] A thickness of 1/100 of the thinnest layer thickness is usually adopted.

For this method, it is not necessary to know a priori where delamination is expected to occur because any layer can suffer from damage. However, 3D finite elements are required to describe the laminate. Because of this, the study of delamination in large laminated structures of many layers may be unaffordable with this method. In addition, the discretization of very thin layers can lead to highly distorted elements carrying numerical issues.

Reduced models, such as those treated in Section 2.1, can be also employed to simulate delamination.

ESL-based finite elements can be employed together with LEFM-based techniques [7] or interface elements [5, 91]. However, these elements cannot simulate delamination by themselves since their kinematics are unable to predict discontinuities in the displacement field.

LW models can be also used in conjunction with LEFM-based methods [86, 87, 99], as already mentioned. In addition, it is also possible to use interface elements in LW descriptions as proposed by Hosseini-Toudeshky et al. [100]. Furthermore, delamination can be simulated via LW models by incorporating constitutive laws to manage the non-linear behavior of the interface continuity condition [101]. However, the main disadvantage of LW-based models is that the number of variable depends on the number of analysis layers, which could result computationally too expensive to simulate large composite structures of many layers.

To the knowledge of the author, the use of ZZT theories to model delamination in advanced composite laminates has been quite limited so far.

Di Sciuva and Gherlone [102] developed a refined version of the cubic zigzag theory, where both, the displacement and the transverse shear stress are defined as variables on the surfaces of the laminate. This feature allows the model to be employed in sub-laminate approaches[15] [103]. Although these approaches are able to simulate discontinuities on the displacement field, they may require excessive computational resources since the number of variables depends on the number of analysis layer.

Icardi et al. [104-106] have proposed a model based on a refined 3D cubic zigzag theory to analyze damage induced by low velocity impacts on composites laminates. However, in order to overcome the C^2 continuity requirement, FSDT-based C^0 plate elements are employed to approximate the solution. Then, stresses and other quantities of the zigzag theory are computed by a post-processing procedure based on strain energy updating from the FSDT model to the zigzag one.

[15] Sub-laminate approaches are special cases of the LW description where the laminate thickness is conveniently divided in several sub-domains.

RZT theory is a good alternative to simulate laminate structures with highly transverse anisotropy. Among many reason, the efficiency and efficacy to capture the zigzag in-plane displacement are some of the most important, as already mentioned in Section 2.1.3. However, in order to predict the relative displacement between layers, the definition of the zigzag function is the key feature. This function depends on the transverse shear modulus of each layer, which provides to the RZT theory the ability of changing the shape of the in-plane displacement by simply modifying the shear properties of the plies. Thus, the relative displacement between neighboring layers can be modeled by simply locating a thin enough ply between them and then reduce the shear modulus of the added ply.

Based on this idea, the author and advisors of this thesis have recently proposed a numerical model for predicting delamination in advanced composite beams [40] and plates [41] using the LRZ [38] and QLRZ [39] finite elements, respectively. This delamination model is presented in Chapter 4.

3 Formulation of the beam LRZ and the plate QLRZ multilayered finite elements

Formulation of the two-noded beam LRZ [38] and four-noded plate QLRZ [39] finite elements are presented in this Chapter. These elements are based on the refined zigzag theory of Tessler et al. [4, 36] presented in Section 2.1.3.1.

Both finite elements are formulated under the following consideration:

- Small deformations and displacements.
- Quasi-static application of loads and displacements.

3.1 Weak form of equilibrium equations via the principle of virtual work

The strong form of the differential equations is defined by the local Lagrangian equation of motion given by

$$\operatorname{div}[\boldsymbol{\sigma}] + \mathbf{b} - \rho\ddot{\mathbf{a}} = \mathbf{0} \tag{3.1}$$

being $\boldsymbol{\sigma}$ the stresses tensor, $\mathbf{b}$ the body forces and $\rho\ddot{\mathbf{a}}$ the dynamics forces vectors. This equation must be satisfied at each point within the volume of the body, denoted by Ω.

Now, boundary conditions have to be defined in order to formulate a complete boundary value problem. Thus, the stress-like (Newmann) and the displacement (Dirichlet) boundary condition, which are prescribed at the surfaces of the body Γ_t and Γ_u, respectively, are defined by

$$\mathbf{t} = \boldsymbol{\sigma}\mathbf{n} = \bar{\mathbf{t}} \quad \text{on} \quad \Gamma_t \qquad \text{and} \qquad \mathbf{u} = \bar{\mathbf{u}} \quad \text{on} \quad \Gamma_u \tag{3.2}$$

where $\mathbf{n}$ is the unit normal vector. $\bar{\mathbf{t}}$ and $\bar{\mathbf{u}}$ are the external forces and displacement vector, respectively.

Eqs.(3.1) and (3.2) define a complete boundary value problem, where its weak form is obtained via the principle of virtual work (PVW) [107] as

$$\int_{\Omega} \delta\mathbf{a}^T \rho\ddot{\mathbf{a}}\, d\Omega + \int_{\Omega} \delta\boldsymbol{\varepsilon}^T \boldsymbol{\sigma}\, d\Omega - \int_{\Omega} \delta\mathbf{a}^T \mathbf{b}\, d\Omega - \int_{\Gamma_t} \delta\mathbf{a}^T \overline{\mathbf{t}}\, d\Gamma_t = 0 \qquad 3.3$$

Since dynamic effects forces are not considered in this work, Eq.(3.3) is rewritten as

$$\int_{\Omega} \delta\boldsymbol{\varepsilon}^T \boldsymbol{\sigma}\, d\Omega - \int_{\Gamma_t} \delta\mathbf{a}^T \overline{\mathbf{t}}\, d\Gamma_t = 0 \qquad 3.4$$

where $\int_{\Omega} \delta\boldsymbol{\varepsilon}^T \boldsymbol{\sigma}\, d\Omega = W^{int}$ is the internal work and $\int_{\Gamma_t} \delta\mathbf{a}^T \overline{\mathbf{t}}\, d\Gamma_t = W^{ext}$ is the work of the external forces.

Here, Eq.(3.4) is solved by the finite element method. Thus, the integrand of Eq.(3.4) is computed by the summation of the contribution of each finite element *e* as

$$\int_{\Omega} \delta\boldsymbol{\varepsilon}^T \boldsymbol{\sigma}\, d\Omega - \int_{\Gamma_t} \delta\mathbf{a}^T \overline{\mathbf{t}}\, d\Gamma_t = \sum_{e=1}^{n} \left(\int_{\Omega^{(e)}} \delta\boldsymbol{\varepsilon}^{(e)^T} \boldsymbol{\sigma}^{(e)}\, d\Omega - \int_{\Gamma_t^{(e)}} \delta\mathbf{a}^{(e)^T} \overline{\mathbf{t}}^{(e)}\, d\Gamma_t^{(e)} \right) = 0 \qquad 3.5$$

being $\Omega^{(e)}$ and $\Gamma_t^{(e)}$ the volume and the contour of the element. Therefore, it is possible firstly to compute the stiffness matrix and the forces vector element by element and then assemble them all.

3.2 LRZ beam finite element

An isoparametric two-noded C^0 beam element, named LRZ, with four kinematic variables per node based on the RZT theory is formulated in this Section. This element is able to simulate thick and thin beams of highly heterogeneous laminated materials. Since this element suffers of shear looking, as shown in Section 3.2.7.1, a selective numerical integration of the transverse stiffness matrices is employed to overcoming this effect. In order to evaluate the performance of the LRZ element for simulating laminated materials, convergence and comparison studies are carried out in Section 3.2.7.2 and 3.2.7.3, respectively.

3.2.1 Beam RZT kinematics

From Eq.(2.1), the RZT kinematics for a beam is obtained by considering the axial *u* displacement and the transverse deflection *w* only. Thus, the beam displacement field is defined as

$$\begin{aligned} u^k(x,z) &= u_0(x) - z\cdot\theta(x) + \bar{u}^k(x,z) \\ w\,(x) &= w_0(x) \end{aligned} \qquad 3.6$$

with

$$\bar{u}^k = \phi^k(z)\cdot\psi(x)$$

The four kinematics variables of the RZT beam theory are

$$\mathbf{a} = \begin{bmatrix} u_0 & w_0 & \theta & \psi \end{bmatrix}^T \qquad 3.7$$

3.2.2 Strain and generalized strain

For convenience, the strain $\boldsymbol{\varepsilon}^k$ of the kth layer is split into the in-plane (ε_p^k) and the transverse shear (ε_t^k) strains as

$$\boldsymbol{\varepsilon}^k = \begin{bmatrix} \varepsilon_p \\ \varepsilon_t \end{bmatrix}^k = \begin{bmatrix} \dfrac{\partial u^k}{\partial x} \\ \dfrac{\partial u^k}{\partial z} + \dfrac{\partial w}{\partial x} \end{bmatrix} = \begin{bmatrix} \dfrac{\partial u_0}{\partial x} \\ 0 \end{bmatrix} + \begin{bmatrix} -z\dfrac{\partial \theta_x}{\partial x} \\ \dfrac{\partial w_0}{\partial x} - \theta_x \end{bmatrix} + \begin{bmatrix} \phi_x^k(z)\dfrac{\partial \psi_x}{\partial x} \\ \dfrac{\partial \phi_x^k}{\partial z}\psi_x \end{bmatrix} =$$

$$= \begin{bmatrix} \varepsilon_m \\ 0 \end{bmatrix} + \begin{bmatrix} \varepsilon_b \\ \varepsilon_s \end{bmatrix} + \begin{bmatrix} \varepsilon_{mb\phi} \\ \varepsilon_{s\phi} \end{bmatrix}^k = \begin{bmatrix} \mathbf{S}_p & 0 \\ 0 & \mathbf{S}_t \end{bmatrix}^k \cdot \begin{bmatrix} \hat{\boldsymbol{\varepsilon}}_p \\ \hat{\boldsymbol{\varepsilon}}_t \end{bmatrix} \qquad 3.8$$

where ε_m, ε_b and ε_s are the strain value duo to membrane, bending and transverse shear effects of the RMT theory, respectively. The in-plane and transverse shear strains values emanating from the RZT theory are denoted by $\varepsilon_{mb\phi}$ and $\varepsilon_{s\phi}$. $\hat{\boldsymbol{\varepsilon}}_p$ and $\hat{\boldsymbol{\varepsilon}}_t$ are the generalized in-plane and transverse shear strains vectors, respectively, defined as

$$\hat{\boldsymbol{\varepsilon}}_p = \begin{bmatrix} \hat{\varepsilon}_m \\ \hat{\varepsilon}_b \\ \hat{\varepsilon}_{mb\phi} \end{bmatrix} = \begin{bmatrix} \dfrac{\partial u_0}{\partial x} \\ \dfrac{\partial \theta}{\partial x} \\ \dfrac{\partial \psi}{\partial x} \end{bmatrix} \quad ; \quad \hat{\boldsymbol{\varepsilon}}_t = \begin{bmatrix} \hat{\varepsilon}_s \\ \hat{\varepsilon}_{s\phi} \end{bmatrix} = \begin{bmatrix} \dfrac{\partial w_0}{\partial x} - \theta \\ \psi \end{bmatrix} \qquad 3.9$$

$$\mathbf{S}_p^k = \begin{bmatrix} S_m \\ S_b \\ S_{mb\phi}^k \end{bmatrix}^T = \begin{bmatrix} 1 \\ -z \\ \phi^k(z) \end{bmatrix}^T \quad ; \quad \mathbf{S}_t^k = \begin{bmatrix} S_s \\ S_{s\phi}^k \end{bmatrix}^T = \begin{bmatrix} 1 \\ \dfrac{\partial \phi^k}{\partial z} \end{bmatrix}^T$$

where $(\hat{\bullet})$ denotes the generalized strain values.

3.2.3 Stress-strain constitutive relationships

The relationship between the in-plane and the transverse shear stresses and the strains for the *k*th layer are expressed in matrix form as

$$\boldsymbol{\sigma}^k = \begin{bmatrix} \sigma_x \\ \tau_{xz} \end{bmatrix}^k = \begin{bmatrix} E & 0 \\ 0 & G \end{bmatrix}^k \cdot \begin{bmatrix} \varepsilon_p \\ \varepsilon_t \end{bmatrix}^k = \mathbf{D}^k \boldsymbol{\varepsilon}^k \qquad 3.10$$

being E^k and G^k the Young and the shear modulus for the *k*th layer, respectively.

3.2.4 Stress resultants

According to the subdivision of the strains (Eq.(3.8)), the stress resultant vector $\hat{\boldsymbol{\sigma}}$ is subdivided into in-plane $\hat{\boldsymbol{\sigma}}_p$ and transverse shear $\hat{\boldsymbol{\sigma}}_t$ stress resultants as

$$\hat{\boldsymbol{\sigma}} = \begin{bmatrix} \hat{\boldsymbol{\sigma}}_p \\ \hat{\boldsymbol{\sigma}}_t \end{bmatrix} = \begin{bmatrix} N \\ M \\ M_\phi \\ Q \\ Q_\phi \end{bmatrix} \qquad 3.11$$

where N, M and Q are the membrane force, the bending moment, and the transverse shear force of standard beam theory, respectively. M_ϕ and Q_ϕ are respectively an additional bending moment and an additional shear force, which are derived from the RZT theory (Figure 3.1).

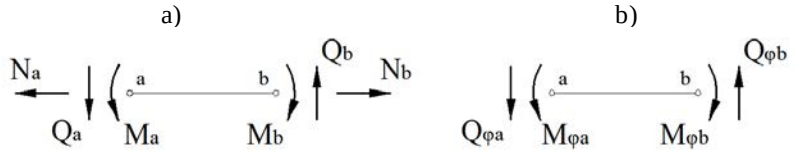

Figure 3.1 – Direction of stress resultants of standard beam theory (a) and those derived from the RZT beam theory (b).

The stress resultants for a beam are obtained by integrating stresses (Eq.(3.10)) over the transverse section A as

$$\begin{aligned}\hat{\boldsymbol{\sigma}}_p &= \int_{\mathrm{A}} \mathbf{S}_p^{k^T} \sigma_x^k \mathrm{dA} = \int_{\mathrm{A}} \mathbf{S}_p^{k^T} E^k \mathbf{S}_p^k \hat{\varepsilon}_p \mathrm{dA} = \left(\int_{\mathrm{A}} \mathbf{S}_p^{k^T} E^k \mathbf{S}_p^k \mathrm{dA} \right) \hat{\varepsilon}_p = \hat{\mathbf{D}}_p \hat{\varepsilon}_p \\ \hat{\boldsymbol{\sigma}}_t &= \int_{\mathrm{A}} \mathbf{S}_t^{k^T} \tau_{xz}^k \mathrm{dA} = \int_{\mathrm{A}} \mathbf{S}_t^{k^T} G^k \mathbf{S}_t^k \hat{\varepsilon}_t \mathrm{dA} = \left(\int_{\mathrm{A}} \mathbf{S}_t^{k^T} G^k \mathbf{S}_t^k \mathrm{dA} \right) \hat{\varepsilon}_t = \hat{\mathbf{D}}_t \hat{\varepsilon}_t \end{aligned} \qquad 3.12$$

being $\hat{\mathbf{D}}_p$ and $\hat{\mathbf{D}}_t$ the generalized constitutive matrices given as

$$\begin{aligned}\hat{\mathbf{D}}_p &= \int_{\mathrm{A}} \mathbf{S}_p^{k^T} E^k \mathbf{S}_p^k \mathrm{dA} = \int_{\mathrm{A}} E^k \begin{bmatrix} 1 & -z & \phi^k \\ -z & z^2 & -z\phi^k \\ \phi^k & -z\phi^k & \left(\phi^k\right)^2 \end{bmatrix} \mathrm{dA} \\ \hat{\mathbf{D}}_t &= \int_{\mathrm{A}} \mathbf{S}_t^{k^T} G^k \mathbf{S}_t^k \mathrm{dA} = \int_{\mathrm{A}} G^k \begin{bmatrix} 1 & \beta^k \\ \beta^k & \left(\beta^k\right)^2 \end{bmatrix} \mathrm{dA} \end{aligned} \qquad 3.13$$

The generalized constitutive matrices $\hat{\mathbf{D}}$ are exactly computed using analytical integration. The ϕ^k function and its derivate β^k within each layer *k* are computed by Eqs.(2.10) and (2.17), respectively. Note that functions for *x* direction are only considered. Moreover, in case of beams, the parameter D_{t11}^k in Eqs.(2.17) and (2.18) is the shear modulus G^k.

3.2.5 Principle of virtual work

Let us consider a beam of length L and transverse section $\mathrm{A} = bh$ which is subjected to distributed **q** loads applied on the contour Γ and point loads $\mathrm{p_i}$. For this case, the differential equations of equilibrium (Eq.3.4) is rewritten as

$$\int_{\mathrm{V}} \delta\boldsymbol{\varepsilon}^{k^T} \boldsymbol{\sigma}^k \, \mathrm{dV} = \int_{\Gamma} \delta\mathbf{a}^T \mathbf{q} \, \mathrm{d}\Gamma + \sum_{i=1}^{pl} \delta \mathrm{a}_i \, \mathrm{p}_i \qquad 3.14$$

where the l.h.s. is the internal virtual work performed by the stresses $\boldsymbol{\sigma}^k$ and the r.h.s. is the external virtual work.

Substituting Eq.(3.8) into the l.h.s. of Eq.(3.14) gives

$$\int_{\mathrm{V}} \delta\boldsymbol{\varepsilon}^{k^T} \boldsymbol{\sigma}^k \, \mathrm{dV} = \int_{\mathrm{V}} \delta\hat{\boldsymbol{\varepsilon}}_p^T \mathbf{S}_s^{k^T} \sigma_x \, \mathrm{dV} + \int_{\mathrm{V}} \delta\hat{\boldsymbol{\varepsilon}}_t^T \mathbf{S}_t^{k^T} \tau_{xz} \, \mathrm{dV}$$

Using Eqs.(3.8), (3.10), (3.12) yields

$$\int_{\mathrm{V}} \delta\boldsymbol{\varepsilon}^{k^T} \boldsymbol{\sigma}^k \, \mathrm{dV} = \int_{\mathrm{L}} \delta\hat{\boldsymbol{\varepsilon}}_p^T \hat{\boldsymbol{\sigma}}_p \, \mathrm{dL} + \int_{\mathrm{L}} \delta\hat{\boldsymbol{\varepsilon}}_t^T \hat{\boldsymbol{\sigma}}_t \, \mathrm{dL}$$

Finally, the equilibrium equations of Eq.(3.4) can be written as

$$\int_{\mathrm{L}} \left(\delta\hat{\boldsymbol{\varepsilon}}_p^T \hat{\boldsymbol{\sigma}}_p + \delta\hat{\boldsymbol{\varepsilon}}_t^T \hat{\boldsymbol{\sigma}}_t \right) \mathrm{dL} = \int_{\Gamma} \delta\mathbf{a}^T \mathbf{q}\, \mathrm{d}\Gamma + \sum_{i=1}^{pl} \delta \mathrm{a}_i \, \mathrm{p}_i \qquad 3.15$$

The integrands in Eq.(3.15) contain kinematic variables derivatives up to first order only, which allows to use C0[16] continuous finite elements.

3.2.6 LRZ formulation

3.2.6.1 Discretization of the displacement field

The middle axis of the beam is discretized by using 2-noded isoparametric finite elements, where the kinematic variables **a** of Eq.(3.7) are interpolated within each element as

$$\mathbf{a}^{(\mathrm{e})} = \begin{bmatrix} u_0 \\ w_0 \\ \theta \\ \psi \end{bmatrix} = \sum_{i=1}^{2} \mathbf{N}_i \mathbf{a}_i^{(\mathrm{e})} = \begin{bmatrix} \mathbf{N}_1 & \mathbf{N}_2 \end{bmatrix} \cdot \begin{bmatrix} \mathbf{a}_1 \\ \mathbf{a}_2 \end{bmatrix}^{(\mathrm{e})} = \mathbf{N_n} \mathbf{a_n}^{(\mathrm{e})} \qquad 3.16$$

where

$$\mathbf{N}_i = N_i \mathbf{I}_4 \quad ; \quad \mathbf{a}_i^{(\mathrm{e})} = \begin{bmatrix} u_0 & w_0 & \theta & \psi \end{bmatrix}_i^T$$

being $N_i = \frac{1}{2}\left(1 + \xi\xi_i\right)$ (Table 3.1 and Figure 3.2) the linear shape function[17] of node *i*th and I_4 is the 4x4 unit matrix.

Node	ξ_i
1	-1
2	1

Table 3.1 - Values of ξ_i for each node.

[16] In general, a finite element is Cm continuous if the displacement field and its m first derivatives are continuous between elements. Thus, a finite element is C0 continuous if the kinematic variables are inter-elements continuous only.

[17] In order to standardize the process of developing the elemental matrices, the shape functions N_i are established in the normalized natural coordinate system (ξ). In case of bilinear shape functions, N_i are normalized to the natural coordinate system (ξ,η).

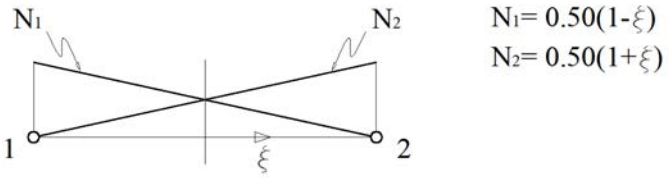

Figure 3.2 – Linear shape functions of two-noded element.

The element geometry is interpolated as

$$x = \sum_{i=1}^{2} \hat{N}_i x_i \qquad 3.17$$

where $\hat{N}_i = N_i$, which leads to an isoparametric formulation[18].

Considering the length of the finite element defined by $\mathrm{L}^{(e)} = x_2 - x_1$ and the form of N_i, the value $\mathrm{d}x/\mathrm{d}\xi$ is computed from Eq.(3.17) as

$$\frac{\mathrm{d}x}{\mathrm{d}\xi} = \frac{\mathrm{d}N_1}{\mathrm{d}\xi} x_1 + \frac{\mathrm{d}N_2}{\mathrm{d}\xi} x_2 = -\frac{1}{2} x_1 + \frac{1}{2} x_2 = \frac{\mathrm{L}^{(e)}}{2}$$

wherewith

$$\mathrm{d}x = \frac{\mathrm{L}^{(e)}}{2}\mathrm{d}\xi \qquad \text{and} \qquad \frac{\mathrm{d}\xi}{\mathrm{d}x} = \frac{2}{\mathrm{L}^{(e)}} \qquad 3.18$$

Thus, the derivatives of the shape functions with respect to the Cartesian coordinates are computed using the chain rule as

$$\frac{\mathrm{d}N_1}{\mathrm{d}x} = \frac{\mathrm{d}N_1}{\mathrm{d}\xi}\frac{\mathrm{d}\xi}{\mathrm{d}x} = -\frac{1}{2}\frac{2}{\mathrm{L}^{(e)}} = -\frac{1}{\mathrm{L}^{(e)}}$$
$$\frac{\mathrm{d}N_2}{\mathrm{d}x} = \frac{\mathrm{d}N_2}{\mathrm{d}\xi}\frac{\mathrm{d}\xi}{\mathrm{d}x} = \frac{1}{2}\frac{2}{\mathrm{L}^{(e)}} = \frac{1}{\mathrm{L}^{(e)}} \qquad 3.19$$

3.2.6.2 Generalized strain field

The interpolated generalized in-plane strains $\hat{\boldsymbol{\varepsilon}}_p^{(e)}$ within each finite element are obtained by substituting Eq.(3.16) into Eq.3.9 as

[18] The formulation is named *isoparametric* when kinematic variables as well as element geometry are approximated using the same shape function, e.g. $N_i = \hat{N}_i$. If the polynomial degree of $\hat{N}_i$ is higher than that of N_i, then a *super-parametric* formulation is obtained; otherwise, the formulation is called *sub-parametric*.

$$\hat{\boldsymbol{\varepsilon}}_p^{(\mathrm{e})} = \begin{bmatrix} \hat{\varepsilon}_m \\ \hat{\varepsilon}_b \\ \hat{\varepsilon}_{mb\phi} \end{bmatrix}^{(\mathrm{e})} = \begin{bmatrix} \dfrac{\partial u_0}{\partial x} \\ \dfrac{\partial \theta}{\partial x} \\ \dfrac{\partial \psi}{\partial x} \end{bmatrix}^{(\mathrm{e})} = \sum_{i=1}^{2} \begin{bmatrix} \dfrac{\partial N_i}{\partial x} u_0 \\ \dfrac{\partial N_i}{\partial x} \theta \\ \dfrac{\partial N_i}{\partial x} \psi \end{bmatrix}_i = \sum_{i=1}^{2} \mathbf{B}_{p_i} \mathbf{a}_i^{(\mathrm{e})} = \mathbf{B}_p \mathbf{a}_{\mathbf{n}}^{(\mathrm{e})} \qquad 3.20$$

where $\mathbf{B}_p$ and $\mathbf{B}_{p_i}$ are the in-plane generalized strain matrices for the element *e* and the *i*th node, respectively. The matrix $\mathbf{B}_{p_i}$ is split into membrane (m), bending (b) and zigzag $(mb\phi)$ contributions, which leads to

$$\mathbf{B}_{p_i} = \begin{bmatrix} \mathbf{B}_m \\ \mathbf{B}_b \\ \mathbf{B}_{mb\phi} \end{bmatrix}_i = \begin{bmatrix} \dfrac{\partial N_i}{\partial x} & 0 & 0 & 0 \\ 0 & 0 & \dfrac{\partial N_i}{\partial x} & 0 \\ 0 & 0 & 0 & \dfrac{\partial N_i}{\partial x} \end{bmatrix} \qquad 3.21$$

In the same manner, the generalized transverse strains $\hat{\boldsymbol{\varepsilon}}_t^{(\mathrm{e})}$ are obtained as

$$\hat{\boldsymbol{\varepsilon}}_t^{(\mathrm{e})} = \begin{bmatrix} \hat{\varepsilon}_s \\ \hat{\varepsilon}_{s\phi} \end{bmatrix}^{(\mathrm{e})} = \begin{bmatrix} \dfrac{\partial w_0}{\partial x} - \theta_x \\ \psi \end{bmatrix}^{(\mathrm{e})} = \sum_{i=1}^{2} \begin{bmatrix} \dfrac{\partial N_i}{\partial x} w_0 - N_i \theta \\ N_i \psi \end{bmatrix}_i = \sum_{i=1}^{2} \mathbf{B}_{t_i} \mathbf{a}_i^{(\mathrm{e})} = \mathbf{B}_t \mathbf{a}_{\mathbf{n}}^{(\mathrm{e})} \qquad 3.22$$

where $\mathbf{B}_t$ and $\mathbf{B}_{t_i}$ are the transverse generalized strain matrices for the element *e* and the *i*th node, respectively. Matrix $\mathbf{B}_{t_i}$ is split into shear (s) and zigzag $(s\phi)$ contributions as

$$\mathbf{B}_{t_i} = \begin{bmatrix} \mathbf{B}_s \\ \mathbf{B}_{s\phi} \end{bmatrix}_i = \begin{bmatrix} 0 & \dfrac{\partial N_i}{\partial x} & -N_i & 0 \\ 0 & 0 & 0 & N_i \end{bmatrix} \qquad 3.23$$

3.2.6.3 Element stiffness matrix and nodal forces vector

Considering Eqs.(3.5), (3.15), the beam element stiffness matrix and the nodal forces vector are obtained via the following equation

$$\int_{\mathrm{L}^{(\mathrm{e})}} \left(\delta \hat{\boldsymbol{\varepsilon}}_p^{(\mathrm{e})^T} \hat{\boldsymbol{\sigma}}_p + \delta \hat{\boldsymbol{\varepsilon}}_t^{(\mathrm{e})^T} \hat{\boldsymbol{\sigma}}_t \right) \mathrm{dL} = \int_{\mathrm{L}^{(\mathrm{e})}} \delta \mathbf{a}^{(\mathrm{e})^T} \mathbf{q} \, \mathrm{dL} + \delta \mathbf{a}_{\mathbf{n}}^{(\mathrm{e})^T} \mathbf{p} \qquad 3.24$$

being $\mathrm{L}^{(\mathrm{e})}$ the length of the finite element.

Considering that

$$\delta\hat{\boldsymbol{\varepsilon}}_p^{(e)^T} = \delta\mathbf{a}_\mathbf{n}^{(e)^T}\mathbf{B}_p^T \qquad ; \qquad \delta\hat{\boldsymbol{\varepsilon}}_t^{(e)^T} = \delta\mathbf{a}_\mathbf{n}^{(e)^T}\mathbf{B}_t^T \qquad ; \qquad \delta\mathbf{a}^{(e)^T} = \delta\mathbf{a}_\mathbf{n}^{(e)^T}\mathbf{N}_\mathbf{n}^T$$

and substituting Eq.(3.12) into Eq.(3.24) gives

$$\int_{L^{(e)}} \left(\delta\mathbf{a}_\mathbf{n}^{(e)^T}\mathbf{B}_p^T\hat{\mathbf{D}}_p\hat{\boldsymbol{\varepsilon}}_p + \delta\mathbf{a}_\mathbf{n}^{(e)^T}\mathbf{B}_t^T\hat{\mathbf{D}}_t\hat{\boldsymbol{\varepsilon}}_t \right) dL = \int_{L^{(e)}} \delta\mathbf{a}_\mathbf{n}^{(e)^T}\mathbf{N}_\mathbf{n}^T\mathbf{q}\ dL + \delta\mathbf{a}_\mathbf{n}^{(e)^T}\mathbf{p}$$

Then, substituting Eqs.(3.20), (3.22) into the previous equation yields

$$\int_{L^{(e)}} \left(\delta\mathbf{a}_\mathbf{n}^{(e)^T}\mathbf{B}_p^T\hat{\mathbf{D}}_p\mathbf{B}_p\mathbf{a}_\mathbf{n}^{(e)} + \delta\mathbf{a}_\mathbf{n}^{(e)^T}\mathbf{B}_t^T\hat{\mathbf{D}}_t\mathbf{B}_t\mathbf{a}_\mathbf{n}^{(e)} \right) dL = \int_{L^{(e)}} \delta\mathbf{a}_\mathbf{n}^{(e)^T}\mathbf{N}_\mathbf{n}^T\mathbf{q}\ dL + \delta\mathbf{a}_\mathbf{n}^{(e)^T}\mathbf{p}$$

Thus, the equation can be factored as

$$\delta\mathbf{a}_\mathbf{n}^{(e)^T}\left\{ \left[\int_{L^{(e)}} \left(\mathbf{B}_p^T\hat{\mathbf{D}}_p\mathbf{B}_p + \mathbf{B}_t^T\hat{\mathbf{D}}_t\mathbf{B}_t \right) dL \right] \mathbf{a}_\mathbf{n}^{(e)} \right\} = \left(\int_{L^{(e)}} \mathbf{N}_\mathbf{n}^T\mathbf{q}\ dL + \mathbf{p} \right) \delta\mathbf{a}_\mathbf{n}^{(e)^T}$$

$$\left[\int_{L^{(e)}} \left(\mathbf{B}_p^T\hat{\mathbf{D}}_p\mathbf{B}_p + \mathbf{B}_t^T\hat{\mathbf{D}}_t\mathbf{B}_t \right) dL \right] \mathbf{a}_\mathbf{n}^{(e)} = \int_{L^{(e)}} \mathbf{N}_\mathbf{n}^T\mathbf{q}\ dL + \mathbf{p}$$

Finally, Eq.(3.24) is reduced to

$$\mathbf{K}^{(e)}\ \mathbf{a}_\mathbf{n}^{(e)} = \int_{L^{(e)}} \mathbf{N}_\mathbf{n}^T\mathbf{q}\ dL + \mathbf{p} \tag{3.25}$$

with

$$\mathbf{K}^{(e)} = \int_{L^{(e)}} \left(\mathbf{B}_p^T\hat{\mathbf{D}}_p\mathbf{B}_p + \mathbf{B}_t^T\hat{\mathbf{D}}_t\mathbf{B}_t \right) dL \tag{3.26}$$

Matrix $\mathbf{K}^{(e)}$ is the elemental stiffness matrix, which for convenience is computed as

$$\mathbf{K}^{(e)} = \mathbf{K}_p^{(e)} + \mathbf{K}_t^{(e)}$$

being $\mathbf{K}_p^{(e)}$ and $\mathbf{K}_t^{(e)}$ the in-plane and the transverse elemental stiffness matrices, respectively, defined as

$$\begin{aligned} \mathbf{K}_p^{(e)} &= \int_{L^{(e)}} \mathbf{B}_p^T\hat{\mathbf{D}}_p\mathbf{B}_p dL \\ \mathbf{K}_t^{(e)} &= \int_{L^{(e)}} \mathbf{B}_t^T\hat{\mathbf{D}}_t\mathbf{B}_t dL \end{aligned} \tag{3.27}$$

To assess the influence of the reduced integration of matrix $\mathbf{K}_t^{(e)}$ for overcoming the shear locking of the solution, matrix $\mathbf{K}_t^{(e)}$ is split as follows

$$\mathbf{K}_t^{(e)} = \mathbf{K}_s^{(e)} + \mathbf{K}_{s\phi}^{(e)} + \mathbf{K}_{ss\phi}^{(e)} + \left[\mathbf{K}_{ss\phi}^{(e)} \right]^T \tag{3.28}$$

with

$$\begin{aligned}\mathbf{K}_{s}^{(\mathrm{e})} &= \int_{\mathrm{L}^{(\mathrm{e})}} \mathbf{B}_{s}^{T} \hat{\mathbf{D}}_{s(1,1)} \mathbf{B}_{s} \mathrm{dL} \\ \mathbf{K}_{s\phi}^{(\mathrm{e})} &= \int_{\mathrm{L}^{(\mathrm{e})}} \mathbf{B}_{s\phi}^{T} \hat{\mathbf{D}}_{s(2,2)} \mathbf{B}_{s\phi} \mathrm{dL} \\ \mathbf{K}_{ss\phi}^{(\mathrm{e})} &= \int_{\mathrm{L}^{(\mathrm{e})}} \mathbf{B}_{s}^{T} \hat{\mathbf{D}}_{s(1,2)} \mathbf{B}_{s\phi} \mathrm{dL}\end{aligned} \qquad 3.29$$

The external nodal forces vector $\mathbf{F}^{\mathrm{ext}}$ are defined by the r.h.s. of Eq.(3.25) as

$$\mathbf{F}^{\mathrm{ext}} = \int_{\mathrm{L}^{(\mathrm{e})}} \mathbf{N}_{\mathbf{n}}^{T} \mathbf{q} \ \mathrm{dL} + \mathbf{p} \qquad 3.30$$

Considering Eq.(3.18), the integrals of Eq.(3.27) defined in the Cartesian coordinate are transformed to the natural coordinate as

$$\begin{aligned}\mathbf{K}_{p}^{(\mathrm{e})} &= \int_{\mathrm{L}^{(\mathrm{e})}} \mathbf{B}_{p}^{T} \hat{\mathbf{D}}_{p} \mathbf{B}_{p} \mathrm{dL} = \int_{-1}^{+1} \mathbf{B}_{p}^{T} \hat{\mathbf{D}}_{p} \mathbf{B}_{p} \frac{\mathrm{L}^{(\mathrm{e})}}{2} \mathrm{d}\xi \\ \mathbf{K}_{t}^{(\mathrm{e})} &= \int_{\mathrm{L}^{(\mathrm{e})}} \mathbf{B}_{t}^{T} \hat{\mathbf{D}}_{t} \mathbf{B}_{t} \mathrm{dL} = \int_{-1}^{+1} \mathbf{B}_{p}^{T} \hat{\mathbf{D}}_{t} \mathbf{B}_{p} \frac{\mathrm{L}^{(\mathrm{e})}}{2} \mathrm{d}\xi\end{aligned} \qquad 3.31$$

The derivatives of the shape functions with respect to the Cartesian coordinates contained into the generalized strain matrices $\mathbf{B}$ are computed by Eq.(3.19).

The integrals of the in-plane element stiffness matrix $\mathbf{K}_{p}^{(\mathrm{e})}$ (Eq.(3.31)) is exactly computed by using the one-point Gauss quadrature as

$$\begin{aligned}\mathbf{K}_{p}^{(\mathrm{e})} &= \int_{-1}^{+1} \mathbf{B}_{p}^{T} \hat{\mathbf{D}}_{p} \mathbf{B}_{p} \frac{\mathrm{L}^{(\mathrm{e})}}{2} \mathrm{d}\xi = \frac{\mathrm{L}^{(\mathrm{e})}}{2} \left[\mathbf{B}_{p}^{T} \hat{\mathbf{D}}_{p} \mathbf{B}_{p} \right]_{(\xi_{GP})} W_{GP} \\ \mathbf{K}_{p}^{(\mathrm{e})} &= \mathrm{L}^{(\mathrm{e})} \left[\mathbf{B}_{p}^{T} \hat{\mathbf{D}}_{p} \mathbf{B}_{p} \right]_{(\xi_{GP}=0.0)}\end{aligned} \qquad 3.32$$

where $W_{GP} = 2$ and $\xi_{GP} = 0.0$ are respectively the weighting factor and the natural coordinate of the center integration point (or Gauss points (GP)). Matrices $\mathbf{B}$ are evaluated at $\xi_{GP} = 0.0$.

The exact integration of matrix $\mathbf{K}_{t}^{(\mathrm{e})}$ is obtained by using two Gauss points. However, the full numerical integration of $\mathbf{K}_{t}^{(\mathrm{e})}$ leads to shear locking effects for slender beams. For this reason, a selective integration scheme is used, where matrices $\mathbf{K}_{s}^{(\mathrm{e})}$ and $\mathbf{K}_{ss\phi}^{(\mathrm{e})}$ are solved by employing a reduced integration (one integration point only) as

$$\mathbf{K}_{s}^{(e)} = \int_{-1}^{+1} \mathbf{B}_{s}^{T} \hat{\mathbf{D}}_{s(1,1)} \mathbf{B}_{s} \frac{\mathrm{L}^{(e)}}{2} \mathrm{d}\xi = \mathrm{L}^{(e)} \left[\mathbf{B}_{s}^{T} \hat{\mathbf{D}}_{s(1,1)} \mathbf{B}_{s} \right]_{(\xi_{GP}=0.0)}$$
$$\mathbf{K}_{ss\phi}^{(e)} = \int_{-1}^{+1} \mathbf{B}_{s}^{T} \hat{\mathbf{D}}_{s(1,2)} \mathbf{B}_{s\phi} \frac{\mathrm{L}^{(e)}}{2} \mathrm{d}\xi = \mathrm{L}^{(e)} \left[\mathbf{B}_{s}^{T} \hat{\mathbf{D}}_{s(1,2)} \mathbf{B}_{s\phi} \right]_{(\xi_{GP}=0.0)} \quad 3.33$$

and matrix $\mathbf{K}_{s\phi}^{(e)}$ (Eq.(3.29)) is full integrated using two Gauss point as

$$\mathbf{K}_{s\phi}^{(e)} = \int_{-1}^{+1} \mathbf{B}_{s\phi}^{T} \hat{\mathbf{D}}_{s(2,2)} \mathbf{B}_{s\phi} \frac{\mathrm{L}^{(e)}}{2} \mathrm{d}\xi = \sum_{GP=1}^{2} \frac{\mathrm{L}^{(e)}}{2} \left[\mathbf{B}_{s\phi}^{T} \hat{\mathbf{D}}_{s(2,2)} \mathbf{B}_{s\phi} \right]_{(\xi_{GP})} W_{GP} \quad 3.34$$

Both natural coordinate ξ_{GP} and weighting factor W_{GP} for the two-point Gauss quadrature are listed in Table 3.2.

GP	ξ_{GP}	W_{GP}
1	$-\frac{1}{\sqrt{3}}$	1
2	$+\frac{1}{\sqrt{3}}$	1

Table 3.2 – Natural coordinates and weighting factors of integration points.

A study of the accuracy of the LRZ solution for modeling slender beams using this selective integration scheme is presented in Section 3.2.7.1.

3.2.6.4 Boundary conditions

The boundary conditions are:

- Clamped side:

$$w = u = \theta = \psi = 0$$

- Simply supported side:

$$w = 0$$

- Symmetry axis:

$$u_n = \theta_n = \psi_n = 0$$

where “n” is the orthogonal direction to the symmetry axis.

3.2.6.5 Improved computation of transverse shear stresses

Since the constitutive equation (Eq.(3.10)) yields a constant value of the transverse shear stress τ_{xz}^{k} into each layer, a discontinuous thickness distribution of τ_{xz} is obtained. A useful alternative to improve the computation of τ_{xz} is to use the equilibrium equations

$$\frac{\partial \sigma_x}{\partial x} + \frac{\partial \tau_{xz}}{\partial z} = 0 \qquad 3.35$$

from which, the transverse shear stress at a point "P" located within the finite element is computed across the thickness by

$$\tau_{xz}(z)\Big|_P = -\int_{-h/2}^{z} \left.\frac{\partial \sigma_x}{\partial x}\right|_P dz \qquad 3.36$$

The axial stress σ_x at point "P" is calculated by the following approximation

$$\sigma_x(z)\Big|_P = \sum_{i=1}^{2} N_i\Big|_P \cdot \sigma_x^i(z) \qquad 3.37$$

where N_i is the shape function previously defined and *i* denotes the *i*th node. The nodal axial stress $\sigma_x^i(z)$ is obtained by the averaging of Gauss stresses from neighboring elements at the *i*th node.

Finally, the thickness distribution of transverse shear stress is obtained by replacing Eq.(3.37) into Eq(3.36),

$$\tau_{xz}(z)\Big|_P = -\int_{-h/2}^{z} \left(\sum_{i=1}^{2} \left.\frac{\partial N_i}{\partial x}\right|_P \cdot \sigma_x^i(z) \right) \qquad 3.38$$

3.2.7 LRZ studies

3.2.7.1 Shear locking

The selective integration scheme, as solution of the shear locking effects, is studied by analyzing a cantilever beam of length L subjected to a unit point load F = 1 N (Figure 3.3). The beam is formed by a three-layered laminate, whose properties are listed on Table 3.3.

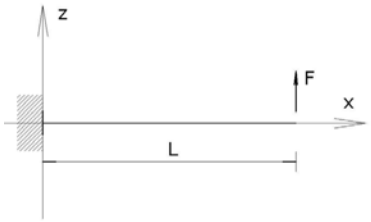

Figure 3.3 – Cantilever beam under point load.

Laminated Material			
	Layer 1 (bottom)	Layer 2 (core)	Layer 3 (top)
h [mm]	6.6667	6.6667	6.6667
E [MPa]	2.19×10^5	2.19×10^3	2.19×10^5
G [MPa]	0.876×10^5	8.80×10^2	0.876×10^5

Table 3.3 – Material properties of shear locking study.

The study is performed for four span-to-thickness ratios: λ = 5, 10, 50, 100 (λ = L/h) using a mesh of 100 LRZ beam elements. The reference solution was obtained by a plane stress analysis (PS) using a mesh of 27000 4-noded quadrilateral (Figure 3.4).

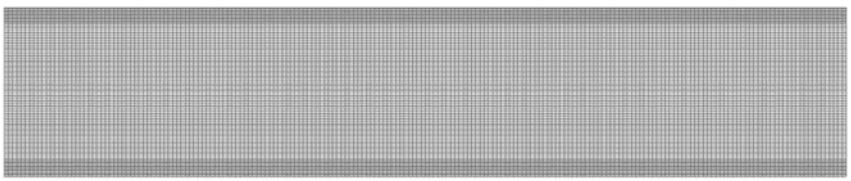

Figure 3.4 – Structured mesh of 27000 four-noded plane stress quadrilaterals elements.

The ratio $r = w_{LRZ} / w_{PS}$ between the vertical displacement at the free end computed with the LRZ element mesh (w_{LRZ}) and with the PS analysis (w_{PS}) for each span-to-thickness λ is shown in Figure 3.5. Results for the LRZ mesh have been obtained using exact two-point integration for all terms of matrix $\mathbf{K}_t^{(e)}$ (Eq.(3.28)) and a one-point reduced integration for the following three groups of matrices: $\mathbf{K}_s^{(e)}$; $\mathbf{K}_s^{(e)}$ and $\mathbf{K}_{s\phi}^{(e)}$; and all terms of $\mathbf{K}_t^{(e)}$. Labels “all”, “S”, “SPsi”, and “Psi” in Figures 3.5-3.8 refer to matrices $\mathbf{K}_t^{(e)}$, $\mathbf{K}_s^{(e)}$, $\mathbf{K}_{ss\phi}^{(e)}$, and $\mathbf{K}_{s\phi}^{(e)}$, respectively.

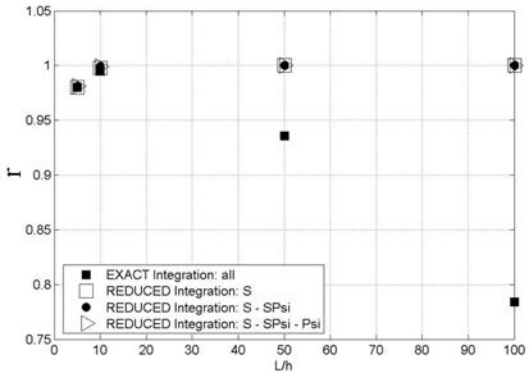

Figure 3.5 – r ratio versus λ for cantilever beam under point load.

Figure 3.5 clearly shows that the LRZ element suffers shear locking when matrix $\mathbf{K}_t^{(e)}$ is full integrated. It is also shown that the finite element is shear locking-free when the reduced integration is used.

The influence of the selective integration in the distribution of the transverse shear stress is also studied. Figures 3.6-3.8 show the thickness distribution of τ_{xz} in sections located at distances L/20, L/4, L/2 and 3L/4 from the clamped end for span-to-thickness ratios λ = 5, 10 and 100. For this analysis, the Timoshenko solution (TBT) is also analyzed using a mesh of 300 standard 2-noded elements. A shear correction factor of $5/6$ is used for all TBT results presented in this work.

Results show that for thick beams (small values of λ) similar solutions are obtained for both, the reduced and the exact integration of matrix $\mathbf{K}_t^{(e)}$. For slender beams, however, results obtained using reduced integration of the three matrix groups are different.

It is shown that slightly more accurate results are obtained when matrices $\mathbf{K}_s^{(e)}$ and $\mathbf{K}_{s\phi}^{(e)}$ are integrated using a one-point quadrature, whereas matrix $\mathbf{K}_{ss\phi}^{(e)}$ is computed by using two Gauss points. Hence, this selective integration scheme is adopted to overcoming shear locking effects.

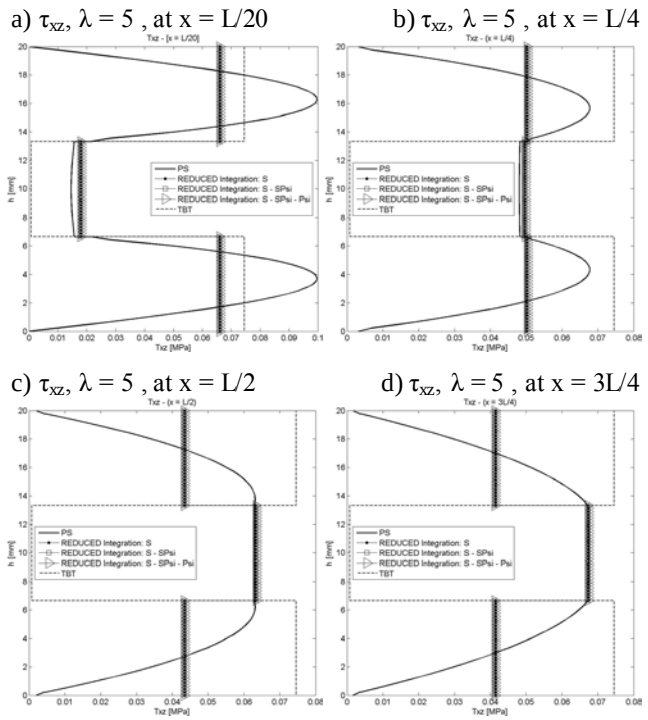

Figure 3.6 – Thickness distribution of the transverse shear stress for λ = 5 at different sections.

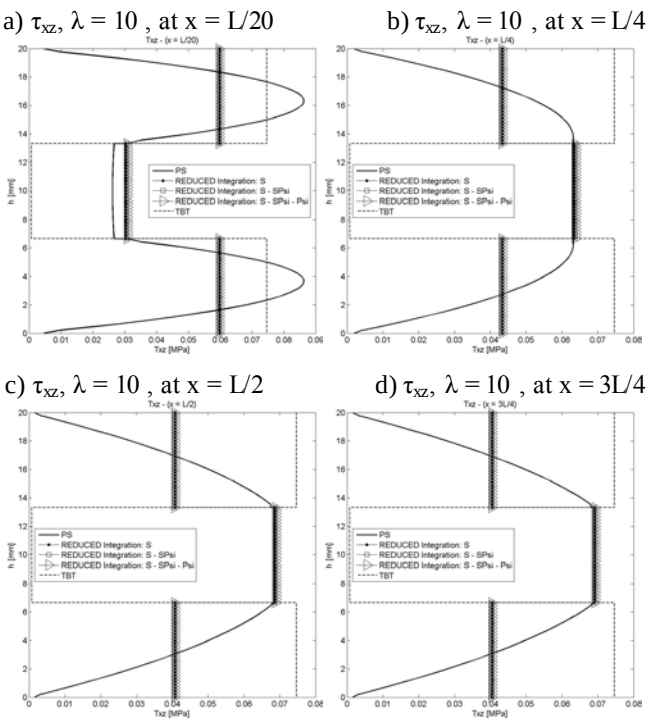

Figure 3.7 – Thickness distribution of the transverse shear stress for λ = 10 at different sections.

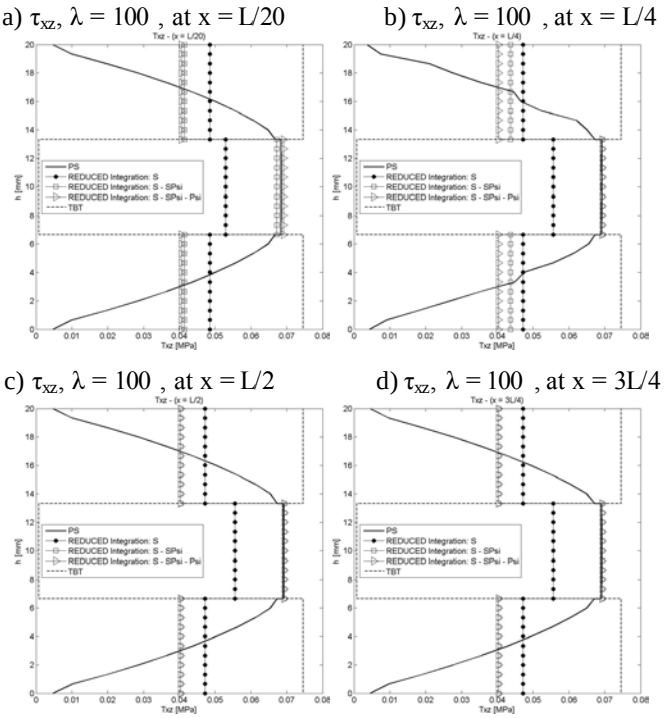

Figure 3.8 – Thickness distribution of the transverse shear stress for λ = 100 at different sections.

3.2.7.2 Convergence

The beam of Figure 3.3 is studied for three laminated materials of different degree of heterogeneity. Materials properties are listed in Table 3.4. Material A is the most homogeneous one, while material C is clearly the most heterogeneous.

Composite Materials				
		Layer 1 (bottom)	Layer 2 (core)	Layer 3 (top)
Composite A	h [mm]	6.66	6.66	6.66
	E [MPa]	$2.19x10^5$	$2.19x10^4$	$4.4E^5$
	G [MPa]	$8.76x10^4$	$8.80x10^3$	$2.00E^5$
Composite B	h [mm]	6.66	6.66	6.66
	E [MPa]	$2.19x10^5$	$2.19x10^3$	$2.19E^5$
	G [MPa]	$8.76x10^4$	$8.80x10^2$	$8.76E^4$
Composite C	h [mm]	2	16	2
	E [MPa]	$2.19x10^5$	$0.73x10^3$	$7.3x10^5$
	G [MPa]	$0.876x10^5$	$0.29x10^3$	$2.92x10^5$

Table 3.4 – Material properties of laminated materials used for convergence study.

In order to evaluate mesh convergence of the LRZ solution, six meshes ranging from 5 to 300 elements are used.

Convergence is measured by the relative error defined as

$$e_r = \frac{m_6 - m_i}{m_6} \qquad 3.39$$

where m_6 and m_i are the values of the magnitude of interest obtained using the finest grid (300 elements) and the *i*th mesh (i = 1, 2, … 5), respectively.

Table 3.5 and Figure 3.9 show the convergence for deflection w and function ψ at the free end, the maximum axial stress σ_x at the end section and the maximum shear stress τ_{xz} at the mid-section.

Results clearly show that convergence is always slower for the most heterogeneous material. For the mesh of 25 elements the errors for all the magnitudes considered are less than 1% for materials A and B. For material C the maximum error does not exceed 5%. For the 50 element mesh errors around 1% were obtained in all cases.

Results for the 10 element mesh are good for material A (errors less than 0.4%), relatively good for material B (errors less than around 5%) and unacceptable for material C (errors ranging from around 8% to 20%).

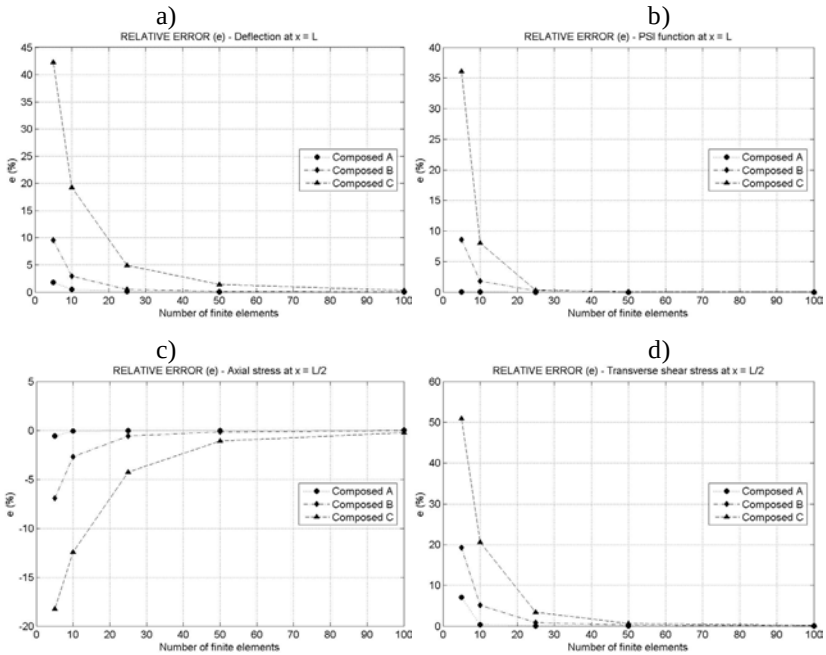

Figure 3.9 – Convergence relative error for: a) w at x = L, b) ψ at x = L, c) maximum axial stress at x = L, d) and maximum shear stress at x = L/2.

a)

$e_r(\%)$ - ***w* at x = L**

Number of elements	Composites		
	A	B	C
5	1.800	9.588	42.289
10	0.506	2.901	19.277
25	0.0860	0.499	4.913
50	0.0191	0.123	1.406
100	0.0048	0.031	0.339
300	0.0000	0.0000	0.0000

b)

$e_r(\%)$ - ψ **at x = L**

Number of elements	Composites		
	A	B	C
5	0.040	8.563	36.113
10	0.003	1.814	8.042
25	0.000	0.259	0.328
50	0.000	0.063	0.033
100	0.000	0.016	0.007
300	0.000	0.000	0.000

c)

$e_r(\%)$ - $\left(\sigma_x\right)_{\max}$ **at x = L**

Number of elements	Composites		
	A	B	C
5	-0.568	-6.923	-18.239
10	-0.076	-2.704	-12.437
25	-0.013	-0.568	-4.266
50	-0.003	-0.131	-1.095
100	0.001	-0.029	-0.250
300	0.000	0.000	0.000

d)

$e_r(\%)$ - $\left(\tau_{xz}\right)_{\max}$ **at x = L/2**

Number of elements	Composites		
	A	B	C
5	7.020	19.283	50.938
10	0.352	5.176	20.602
25	0.052	0.888	3.408
50	0.010	0.210	0.707
100	0.003	0.049	0.147
300	0.000	0.000	0.000

Table 3.5 – Convergence relative error for: a) w at x = L, b) ψ at x = L, c) maximum axial stress at x = L, d) and maximum shear stress at x = L/2.

3.2.7.3 Numerical examples

Cantilever beam under an end point load

The beam material is the highly heterogeneous laminate C defined in the previous analysis (Table 3.4). The span-to-thickness ratio is $\lambda = 5$.

The reference solution is a PS analysis using the structured mesh of 27000 four-noded quadrilaterals shown in Figure 3.4. TBT theory is also compared employing a mesh of 300 two-noded beam elements. Labels “LRZ-300”, “LRZ-50”, “LRZ-25”, and “LRZ-10” refer to the solution obtained by the LRZ meshes of 300, 50, 25 and 10 elements, respectively.

Deflection w along the beam length is shown in Figure 3.10. Very good agreement with the PS solution is obtained already for the LRZ-50 mesh. TBT results are considerable stiffer. Deflection value computed by TBT is about six times stiffer at the free edge.

Figure 3.11 shows the distribution of the axial displacements at the top and bottom surfaces of the top layer along the beam length. Excellent results are again obtained with the LRZ-50 mesh. The TBT results are far from the correct ones.

The thickness distribution for the axial displacement at sections located at distances $L/4$, $L/2$ and $3L/4$ from the clamped end are shown in Figure 3.12. Results for the LRZ element are in good agreement with the reference solution. The standard linear distribution of TBT theory is far from the correct zigzag results.

Figure 3.13 shows the distribution of the axial stress σ_x at the top and bottom surfaces of the beam cross section along the beam length. Very good results are obtained for the LRZ-50 and LRZ-300 meshes. Results for the LRZ-25 mesh compare reasonably well with the PS solution except in the vicinity of the clamped edge. However, this error is corrected for the LRZ-50 and LRZ-300 meshes. The TBT results yield a linear distribution of the axial stress along the beam, as expected. This introduces large errors in the axial stress values in the vicinity of the clamped support.

Thickness distribution for the transverse shear stress τ_{xz} at different sections are shown in Figure 3.14. LRZ results provide an accurate estimate of the average transverse shear stress value for each layer. The distribution of τ_{xz} across the thickness can be improved by using Eq.(3.38).

Figure 3.15 shows the thickness distribution of the axial stress σ_x at the clamped end and at the center of the beam. LRZ results are well approximated to the reference solution. TBT results have an erroneous stress distribution for the top and bottom layers at the clamped end. These differences are less important at the central section.

LRZ and TBT results for the distribution of the tangential shear stress τ_{xz} for each layer along the beam length are shown in Figure 3.16.

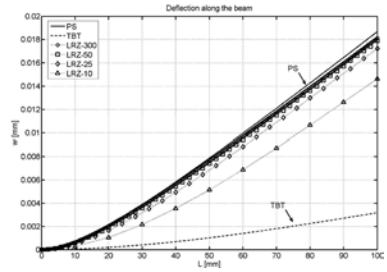

Figure 3.10 – Distribution of vertical displacement *w* along the beam length.

a) b)

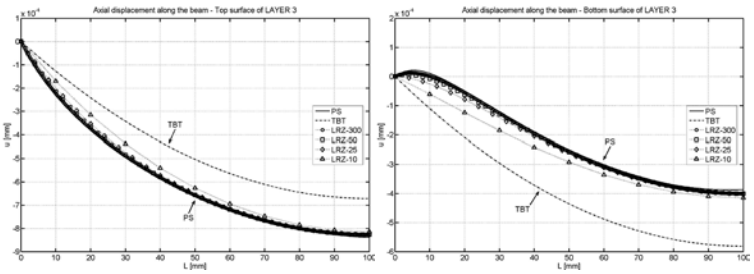

Figure 3.11 – Axial displacement *u* at the upper (a) and lower (b) surfaces of the top layer along the beam length.

a) b)

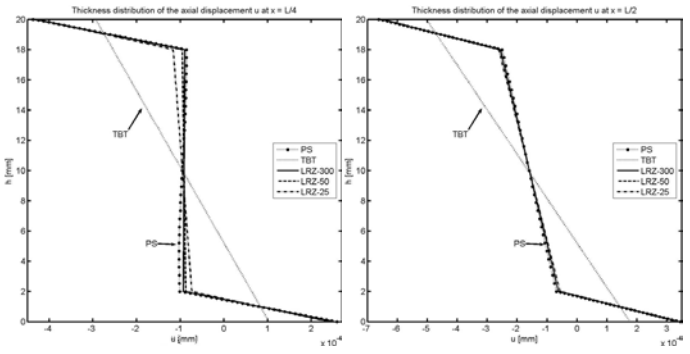

c)

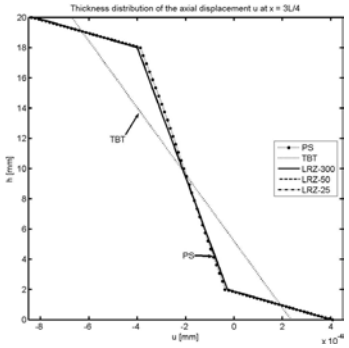

Figure 3.12 – Thickness distribution of the axial displacement *u* at x = L/4 (a), x = L/2 (b), and x = 3L/4 (c).

a) b)

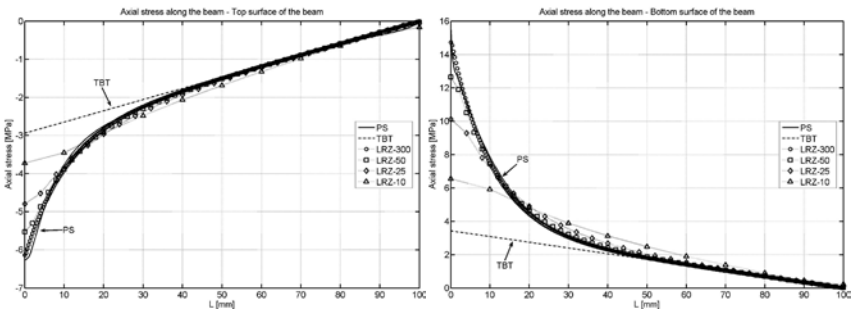

Figure 3.13 – Axial stress at the upper (a) and lower (b) surfaces of the cross section along the beam length.

a) b)

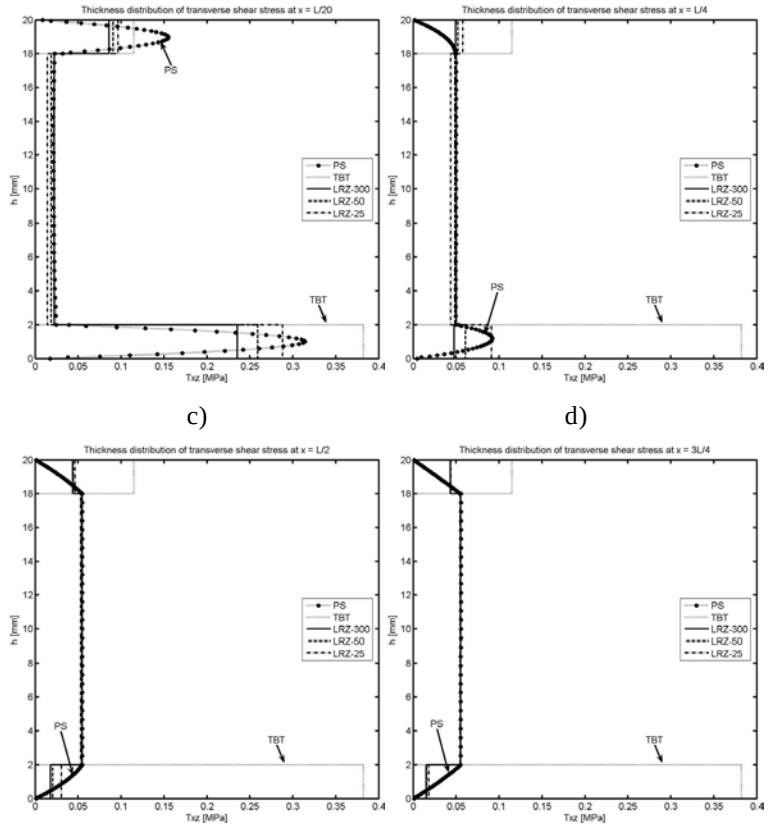

Figure 3.14 – Thickness distribution of the transverse shear stress at x = L/20 (a), x = L/4 (b), x = L/2 (c), and x = 3L/4 (d).

a) b)

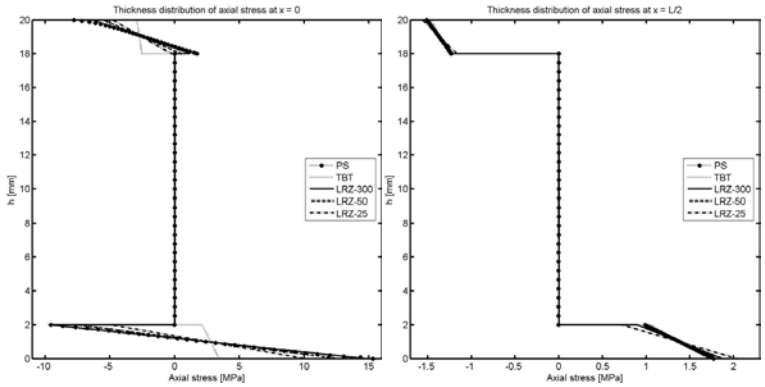

Figure 3.15 – Thickness distribution of the axial stress at x = 0 (a) and x = L/2 (b).

a) b)

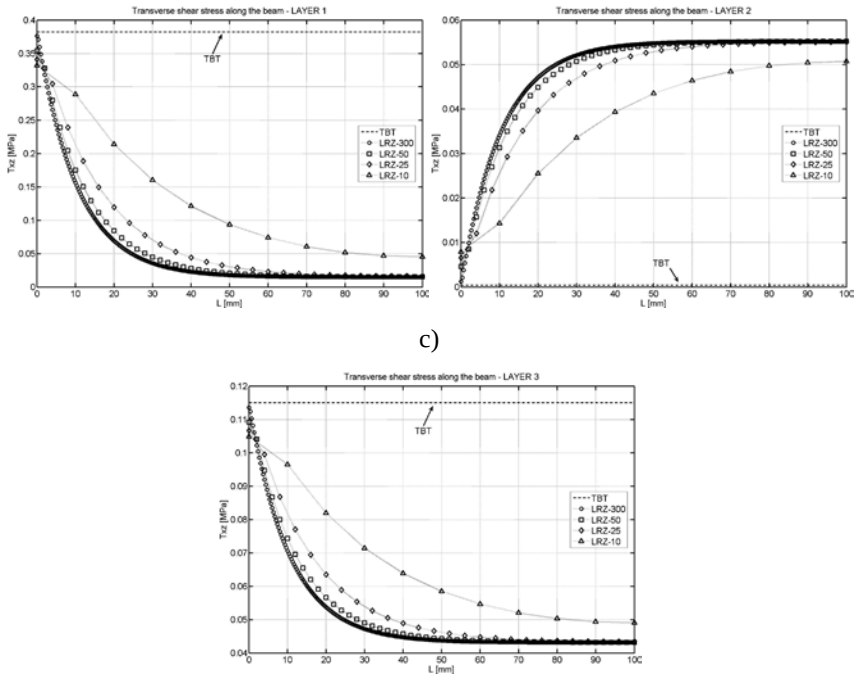

c)

Figure 3.16 – Transverse shear stress along the beam length for layer 1(a), layer 2 (b), and layer 3 (c).

Simple supported beam under uniformly distributed unit load

Laminated material properties are listed in Table 3.6. The span-to-thickness ratio is $\lambda = 5$.

Laminated Material			
	Layer 1 (bottom)	Layer 2 (core)	Layer 3 (top)
h [mm]	6.6667	6.6667	6.6667
E [MPa]	2.19×10^5	5.30×10^5	7.39×10^5
G [MPa]	0.876×10^5	2.90×10^2	2.92×10^5

Table 3.6 – Material properties.

LRZ results are once more compared with those obtained with the TBT mesh of 300 two-noded elements and with a structured mesh of 27000 4-noded plane stress quadrilateral elements. PS solution is obtained by fixing the vertical displacement of all nodes at the end sections and the horizontal displacement for the mid-line edge nodes only. No advantage of symmetry was taken into account.

The distribution of the vertical deflection along the beam length is shown in Figure 3.17. For the finest LRZ mesh the central deflection is around 12% stiffer than the PS solution. The discrepancy is due to the difference in the way the simple support condition is modelled in beam and PS theories, as well as to the limitations of beam theory to model accurately very thick beams. TBT results are inaccurate, as expected.

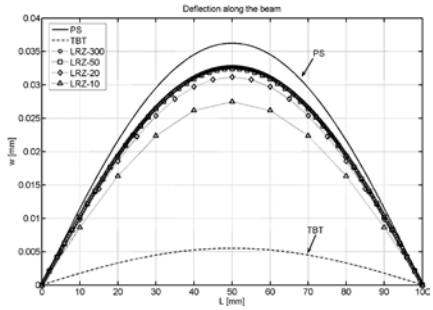

Figure 3.17 – Distribution of vertical displacement *w* along the beam length.

Figure 3.18 shows the distribution of the axial stress σ_x along the beam at the top surface for the second and third layer. Results show an acceptable accuracy of the LRZ solution with a maximum error of 10% for the finest mesh. On the contrary, the TBT model gives a too poor solution.

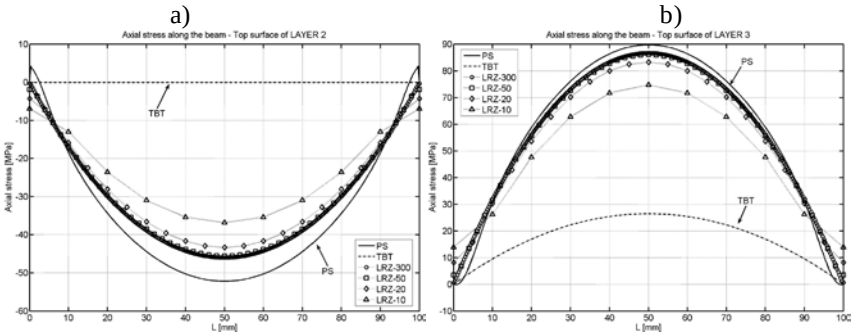

Figure 3.18 – Axial stress at the top surface for the second (a) and third (b) layer along the beam length.

Figure 3.19 shows the thickness distribution of the axial displacement at the left end section (x = 0) and at x = $L/4$. The LRZ element captures very well the zigzag shape of the axial displacement field even for a coarse mesh of 10 elements. The TBT element yields an unrealistic linear distribution.

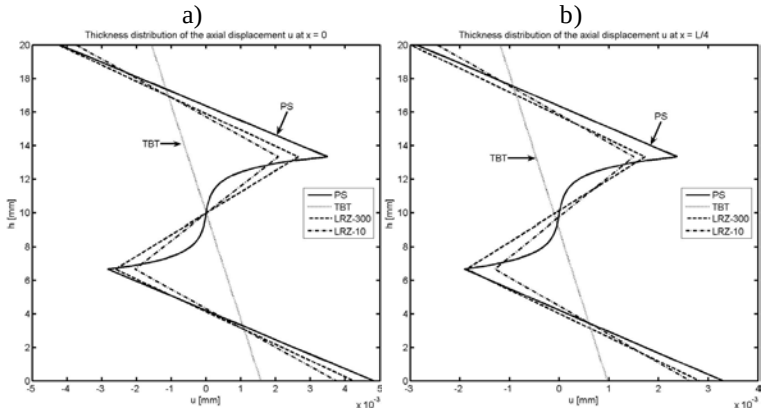

Figure 3.19 – Thickness distribution of the axial displacement *u* at x = 0 (a) and x = L/4 (b).

Thickness distribution of the axial stress (at x = L/4, L/2) and the transverse shear stress (at x = L/20, L/4) are shown in Figure 3.20 and Figure 3.21, respectively. The accuracy of the LRZ results is again noticeable (even for the coarse 10 element mesh). The TBT element fails to capture the zigzag distribution of the axial stress and gives a wrong value of almost zero shear stress at the core layer.

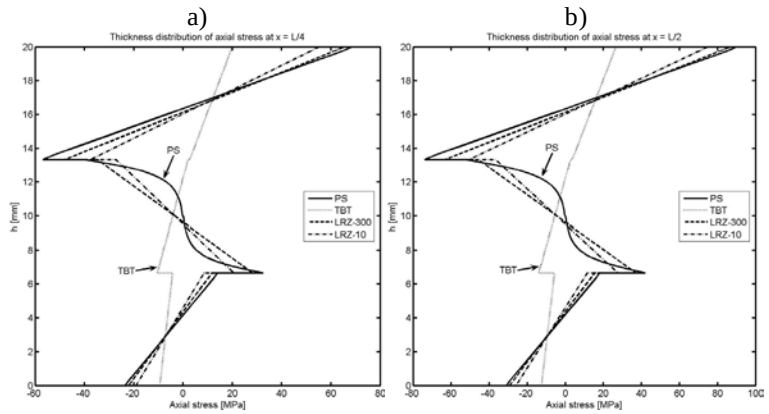

Figure 3.20 – Thickness distribution of the axial stress at x = L/4 (a) and x = L/2 (b).

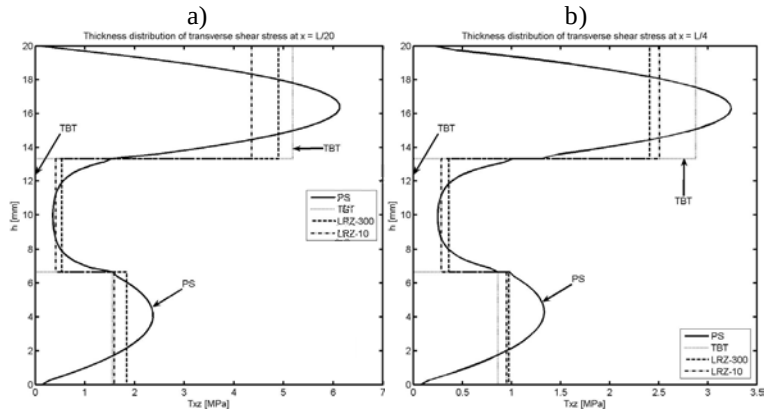

Figure 3.21 – Thickness distribution of the transverse shear stress at x = L/20 (a) and x = L/4 (b).

Figure 3.22 shows the distribution of the transverse shear stress along the beam for each ply obtained with the LRZ and TBT elements.

Figure 3.23 shows a similar set of results for a moderately thick SS beam (λ=10) and the same material properties. The distribution of the deflection and the axial stress along the beam length are shown in Figure 3.23a and Figure 3.23b, respectively. The accuracy of the LRZ element is again noticeable.

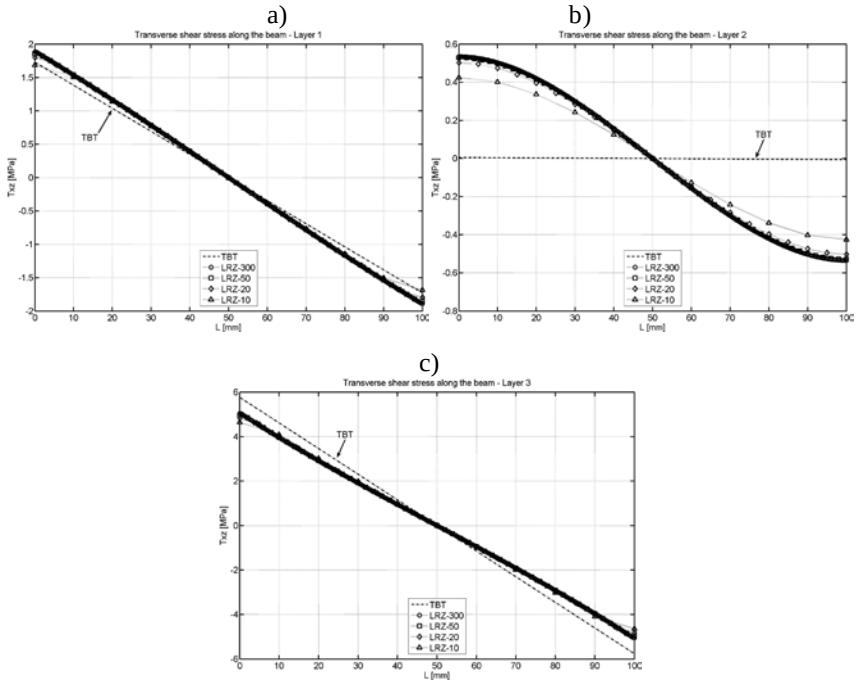

Figure 3.22 – Transverse shear stress along the beam length for layer 1(a), layer 2 (b), and layer 3 (c).

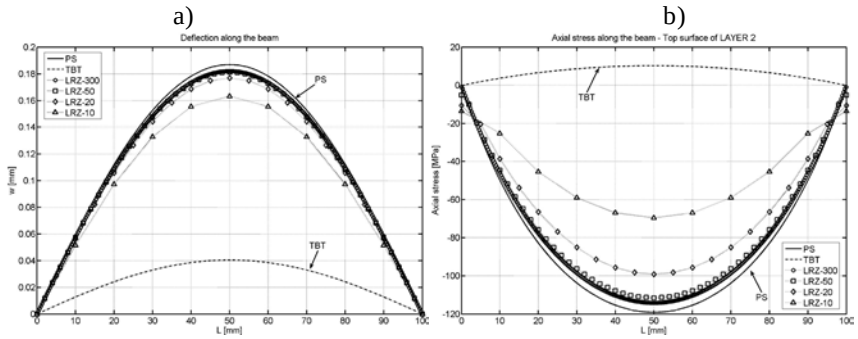

Figure 3.23 – Distribution of the vertical displacement *w* (a) and the axial stress at the top surface of second layer (b) along the beam length.

Non-symmetric ten-layered clamped beam under uniformly distributed unit load

In this example a ten-layered clamped slender beam (L = 100 mm, h = 5 mm, b = 1 mm, λ = 20) under uniformly distributed loading (q = 1KN/mm) is analyzed. Laminated material properties are listed in Table 3.7.

a)

Layer	h_i	Material
1	0.5	IV
2	0.6	I
3	0.5	V
4	0.4	III
5	0.7	IV
6	0.1	III
7	0.4	II
8	0.5	V
9	0.3	I
10	1	II

b)

Material	E [MPa]	G [MPa]
I	2.19×10^5	0.876×10^5
II	7.30×10^5	2.92×10^5
III	7.30×10^2	2.92×10^2
IV	5.30×10^5	2.12×10^5
V	0.82×10^5	0.328×10^5

Table 3.7 – Layer distribution (a) and material properties (b).

Figure 3.24 shows the deflection along the beam for LRZ meshes of 10 and 300 elements (LRZ-10 and LRZ-300). LRZ results are compared with PS and TBT results. A mesh of 27.000 4-noded PS quadrilaterals and a mesh of 300 TBT elements are used. Even for the coarse 10 element mesh the LRZ deflection is good approximated to the PS solution.

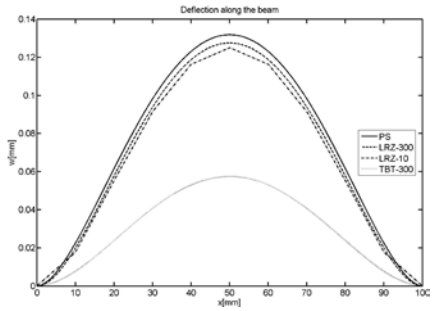

Figure 3.24 – Distribution of vertical displacement w along the beam length.

Figure 3.25 shows the thickness distribution of the axial displacement and the axial stress for the section at x = $L/4$. The accuracy of the LRZ results is once more remarkable.

Thickness distribution of the transverse shear stress at x = L4 is shown in Figure 3.26. Figure 3.26a shows the values obtained by the constitutive equation Eq.(3.10). These results are clearly better than those obtained with the TBT element but only coincide in an average sense with the plane stress FEM solution. The improved computation of the transverse shear stress using Eq.(3.38) is shown in Figure 3.26b,

where a very good approximation to the PS result is observed even for the coarse mesh of 10 LRZ elements.

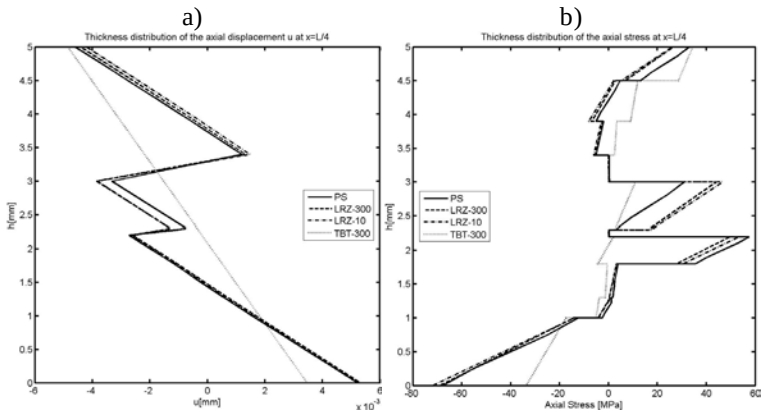

Figure 3.25 – Thickness distribution of the axial displacement *u* (a) and the axial stress (b) at x = L/4.

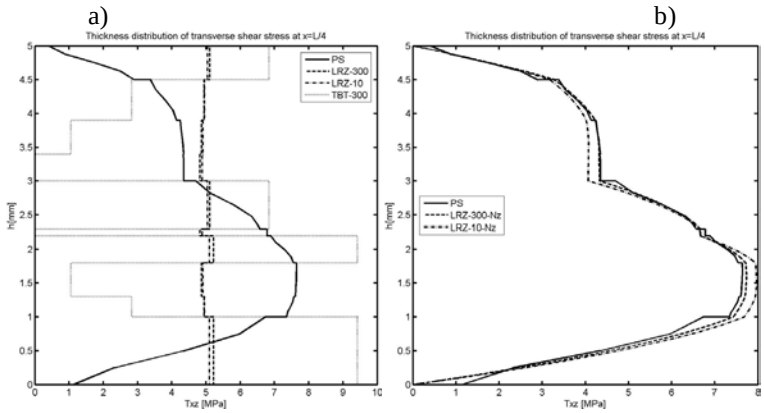

Figure 3.26 – Thickness distribution of the transverse shear stress at x = L/4 computed by the constitutive equation 3.10 (a) and by the improved equation 3.38 (b).

3.3 QLRZ plate finite element

The formulation of an isoparametric four-noded C^0 quadrilateral plate element, named QLRZ, with seven kinematic variables per node based on the RZT theory is presented in this Section. This element is designed for modeling thick and thin plate/shell structures of highly heterogeneous laminated materials. The original form of this element suffers of shear looking, as shown in Section 3.3.7.1, which is avoided by means of an *assumed linear shear strain field*. The performance of QLRZ is analyzed in three different studies: *verification*, *convergence* and *comparison*. The *verification* study (Section 3.3.7.2) aims at evaluating the performance of this element when the material is homogenous, i.e. when the zigzag

function vanishes. The influence of the material transverse heterogeneity on convergence and accuracy of the QLRZ element is analyzed in the *convergence* study (Section 3.3.7.3). Finally, the performance of the QLRZ element for modeling highly heterogeneous materials is evaluated in the *comparison* analysis (Section 3.3.7.4).

3.3.1 Plate RZT kinematics

The QLRZ kinematics is defined by Eq.(2.1) in Section 2.1.3.1 as

$$\begin{aligned} u^k(x,y,z) &= u_0(x,y) - z\cdot\theta_x(x,y) + \overline{u}^k(x,y,z) \\ v^k(x,y,z) &= v_0(x,y) - z\cdot\theta_y(x,y) + \overline{v}^k(x,y,z) \\ w\,(x,y) &= w_0(x,y) \end{aligned} \qquad 3.40$$

where the axial displacement zigzag function $\overline{u}^k$ and $\overline{v}^k$ are defined as

$$\begin{aligned} \overline{u}^k &= \phi_x^k(z)\cdot\psi_x(x,y) \\ \overline{v}^k &= \phi_y^k(z)\cdot\psi_y(x,y) \end{aligned} \qquad 3.41$$

The unknown variables for the plate RZT theory are

$$\mathbf{a} = \begin{bmatrix} u_0 & v_0 & w_0 & \theta_x & \theta_y & \psi_x & \psi_y \end{bmatrix}^T \qquad 3.42$$

where the uniform displacement u_0, v_0 and w_0, and the bending rotation θ_x and θ_y are derivate from the FSDT theory, where the ψ_i variables are associated with the added displacement zigzag functions $\overline{u}^k$ and $\overline{v}^k$.

3.3.2 Stain and generalized strain

For convenience, the strain $\boldsymbol{\varepsilon}^k$ of the kth layer is split into the in-plane ($\boldsymbol{\varepsilon}_p^k$) and the transverse shear ($\boldsymbol{\varepsilon}_t^k$) strains as

$$\boldsymbol{\varepsilon}^k = \begin{bmatrix} \boldsymbol{\varepsilon}_p \\ \boldsymbol{\varepsilon}_t \end{bmatrix}^k = \begin{bmatrix} \varepsilon_x \\ \varepsilon_y \\ \gamma_{xy} \\ \gamma_{xz} \\ \gamma_{yz} \end{bmatrix}^k = \begin{bmatrix} \dfrac{\partial u^k}{\partial x} \\ \dfrac{\partial v^k}{\partial y} \\ \dfrac{\partial u^k}{\partial y} + \dfrac{\partial v^k}{\partial x} \\ \dfrac{\partial u^k}{\partial z} + \dfrac{\partial w}{\partial x} \\ \dfrac{\partial v^k}{\partial z} + \dfrac{\partial w}{\partial y} \end{bmatrix} =$$

$$= \begin{bmatrix} \dfrac{\partial u_0}{\partial x} \\ \dfrac{\partial v_0}{\partial y} \\ \dfrac{\partial u_0}{\partial y} + \dfrac{\partial v_0}{\partial x} \\ 0 \\ 0 \end{bmatrix} + \begin{bmatrix} -z\dfrac{\partial \theta_x}{\partial x} \\ -z\dfrac{\partial \theta_y}{\partial y} \\ -z\left(\dfrac{\partial \theta_x}{\partial y} + \dfrac{\partial \theta_y}{\partial x}\right) \\ \dfrac{\partial w_0}{\partial x} - \theta_x \\ \dfrac{\partial w_0}{\partial y} - \theta_y \end{bmatrix} + \begin{bmatrix} \phi_x^k(z)\dfrac{\partial \psi_x}{\partial x} \\ \phi_y^k(z)\dfrac{\partial \psi_y}{\partial y} \\ \phi_x^k(z)\dfrac{\partial \psi_x}{\partial y} + \phi_y^k(z)\dfrac{\partial \psi_y}{\partial x} \\ \dfrac{\partial \phi_x^k}{\partial z}\psi_x \\ \dfrac{\partial \phi_y^k}{\partial z}\psi_y \end{bmatrix} =$$

$$= \begin{bmatrix} \boldsymbol{\varepsilon}_m \\ 0 \end{bmatrix} + \begin{bmatrix} \boldsymbol{\varepsilon}_b \\ \boldsymbol{\varepsilon}_s \end{bmatrix} + \begin{bmatrix} \boldsymbol{\varepsilon}_{mb\phi} \\ \boldsymbol{\varepsilon}_{s\phi} \end{bmatrix}^k = \begin{bmatrix} \mathbf{S}_p & 0 \\ 0 & \mathbf{S}_t \end{bmatrix}^k \cdot \begin{bmatrix} \hat{\boldsymbol{\varepsilon}}_p \\ \hat{\boldsymbol{\varepsilon}}_t \end{bmatrix} \qquad 3.43$$

where $\boldsymbol{\varepsilon}_m$, $\boldsymbol{\varepsilon}_b$ and $\boldsymbol{\varepsilon}_s$ are the strain vectors duo to membrane, bending and transverse shear effects of the RMT theory, respectively. The in-plane and transverse shear strains vectors emanating from the RZT theory are denoted by $\boldsymbol{\varepsilon}_{mb\phi}$ and $\boldsymbol{\varepsilon}_{s\phi}$. $\hat{\boldsymbol{\varepsilon}}_p$ and $\hat{\boldsymbol{\varepsilon}}_t$ are the generalized in-plane and transverse shear strains vectors, respectively, defined as

$$\hat{\boldsymbol{\varepsilon}}_p = \begin{bmatrix} \hat{\boldsymbol{\varepsilon}}_m \\ \hat{\boldsymbol{\varepsilon}}_b \\ \hat{\boldsymbol{\varepsilon}}_{mb\phi} \end{bmatrix} \quad ; \quad \hat{\boldsymbol{\varepsilon}}_t = \begin{bmatrix} \hat{\boldsymbol{\varepsilon}}_s \\ \hat{\boldsymbol{\varepsilon}}_{s\phi} \end{bmatrix} \qquad 3.44$$

$$\mathbf{S}_p^k = \begin{bmatrix} \mathbf{S}_m & \mathbf{S}_b & \mathbf{S}_{mb\phi}^k \end{bmatrix} \quad ; \quad \mathbf{S}_t^k = \begin{bmatrix} \mathbf{S}_s & \mathbf{S}_{s\phi}^k \end{bmatrix}$$

where $(\hat{\bullet})$ denotes the generalized strain vectors given by

$$\hat{\boldsymbol{\varepsilon}}_m = \begin{bmatrix} \dfrac{\partial u_0}{\partial x} & \dfrac{\partial v_0}{\partial y} & \dfrac{\partial u_0}{\partial y} + \dfrac{\partial v_0}{\partial x} \end{bmatrix}^T \quad ; \quad \hat{\boldsymbol{\varepsilon}}_s = \begin{bmatrix} \dfrac{\partial w_0}{\partial x} - \theta_x \\ \dfrac{\partial w_0}{\partial y} - \theta_y \end{bmatrix} = \begin{bmatrix} \gamma_{xz} \\ \gamma_{yz} \end{bmatrix}$$

$$\hat{\boldsymbol{\varepsilon}}_b = \begin{bmatrix} \dfrac{\partial \theta_x}{\partial x} & \dfrac{\partial \theta_y}{\partial y} & \dfrac{\partial \theta_x}{\partial y} + \dfrac{\partial \theta_y}{\partial x} \end{bmatrix}^T \quad ; \quad \hat{\boldsymbol{\varepsilon}}_{s\phi} = \begin{bmatrix} \psi_x \\ \psi_y \end{bmatrix} \qquad 3.45$$

$$\hat{\boldsymbol{\varepsilon}}_{mb\phi} = \begin{bmatrix} \dfrac{\partial \psi_x}{\partial x} & \dfrac{\partial \psi_y}{\partial y} & \dfrac{\partial \psi_x}{\partial y} & \dfrac{\partial \psi_y}{\partial x} \end{bmatrix}^T$$

and matrix operators $\mathbf{S}$ are defined as

$$\mathbf{S}_m = \begin{bmatrix} 1 & 0 & 0 \\ 0 & 1 & 0 \\ 0 & 0 & 1 \end{bmatrix} = \mathrm{I}_3 \quad ; \quad \mathbf{S}_b = -\mathrm{z}\,\mathbf{I}_3 \quad ; \quad \mathbf{S}_s = \begin{bmatrix} 1 & 0 \\ 0 & 1 \end{bmatrix} = \mathbf{I}_2$$

$$\mathbf{S}^k_{mb\phi} = \begin{bmatrix} \phi^k_x(z) & 0 & 0 & 0 \\ 0 & \phi^k_y(z) & 0 & 0 \\ 0 & 0 & \phi^k_x(z) & \phi^k_y(z) \end{bmatrix} \quad ; \quad \mathbf{S}^k_{s\phi} = \begin{bmatrix} \dfrac{\partial \phi^k_x}{\partial z} & 0 \\ 0 & \dfrac{\partial \phi^k_y}{\partial z} \end{bmatrix} \qquad 3.46$$

In Eq.(3.45) $\gamma_{iz}\ (i = x, y)$ is the average transverse shear strain of RMT. Note that ϕ^k_i is piecewise linear, hence, its derivative $\left(\dfrac{\partial \phi^k_i}{\partial z} = \beta^k_i\right)$ is constant within each layer.

3.3.3 Stress-strain constitutive relationships

The reduced elasticity matrix for the orthotropic *k*th layer is given by

$$\bar{\mathbf{D}}^k = \begin{bmatrix} \bar{\mathbf{D}}_p & \mathbf{0} \\ \mathbf{0} & \bar{\mathbf{D}}_t \end{bmatrix}^k \qquad 3.47$$

with

$$\bar{\mathbf{D}}^k_p = \frac{1}{1-\upsilon_{12}\upsilon_{21}} \begin{bmatrix} E_1 & \upsilon_{12}E_2 & 0 \\ \upsilon_{12}E_2 & E_2 & 0 \\ 0 & 0 & (1-\upsilon_{12}\upsilon_{21})G_{12} \end{bmatrix}$$

$$\bar{\mathbf{D}}^k_t = \begin{bmatrix} G_{13} & 0 \\ 0 & G_{23} \end{bmatrix} \qquad 3.48$$

being E and G the Young and the shear moduli, respectively, and υ the Poisson's ratio. It is important to note that the strains $\boldsymbol{\varepsilon}^k$ are referred to the local coordinate system (x,y,z) whereas the $\bar{\mathbf{D}}^k_{ij}$ magnitudes are referred to the material orientation (e1,e2,e3) (Figure 3.27). Direction e1 is parallel to the main in-plane direction[19], e2 is the in-plane direction transverse to the e1, and e3 is the through-

[19] The main in-plane orientation e1 is coincident to that on which the higher in-plane Young's modulus is oriented. For advanced composite materials, direction e1 is parallel to the fibre orientation.

thickness direction that is coincident with the local vertical direction z. The relations between the basis vectors are defined by

$$\begin{bmatrix} e1 \\ e2 \\ e3 \end{bmatrix} = \mathbf{T} \cdot \begin{bmatrix} x \\ y \\ z \end{bmatrix} \qquad \text{with} \qquad \mathbf{T} = \begin{bmatrix} c & s & 0 \\ -s & c & 0 \\ 0 & 0 & 1 \end{bmatrix} \tag{3.49}$$

where $c = \cos(\alpha)$ and $s = \sin(\alpha)$.

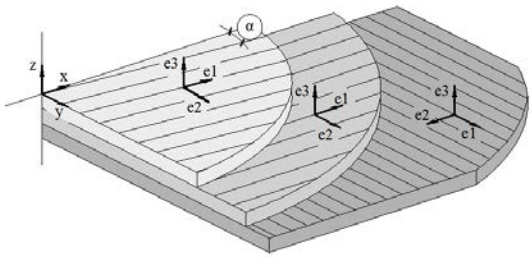

Figure 3.27 – Local coordinate system (x,y,z) and material orientation (e1,e2,e3). The angle between vector x and e1 is defined by α.

When material orientation is not correlated with local coordinate, e.g. the angle α between vectors x and e1 is different to cero, a transformation of the constitutive matrix $\bar{\mathbf{D}}^k$ to the local orientation has to be done by

$$\mathbf{D}^k = \mathbf{\Pi}^T \cdot \bar{\mathbf{D}}^k \cdot \mathbf{\Pi} = \begin{bmatrix} \mathbf{D}_p & \mathbf{0} \\ \mathbf{0} & \mathbf{D}_t \end{bmatrix}^k \tag{3.50}$$

with

$$\mathbf{\Pi} = \begin{bmatrix} c^2 & s^2 & sc & 0 & 0 \\ s^2 & c^2 & -sc & 0 & 0 \\ -2sc & 2sc & c^2 - s^2 & 0 & 0 \\ 0 & 0 & 0 & c & s \\ 0 & 0 & 0 & -s & c \end{bmatrix}$$

Note, if $\alpha = 0$, that implies: $\mathbf{\Pi} = \mathbf{I}_5$ and $\mathbf{D}^k = \bar{\mathbf{D}}^k$.

Then, the stress-strain constitutive relationship of the *k*th layer referred to the local coordinate system (x,y,z) is defined as

$$\boldsymbol{\sigma}^k = \begin{bmatrix} \boldsymbol{\sigma}_p \\ \boldsymbol{\sigma}_t \end{bmatrix}^k = \begin{bmatrix} \sigma_x \\ \sigma_y \\ \tau_{xy} \\ \hline \tau_{xz} \\ \tau_{yz} \end{bmatrix}^k = \begin{bmatrix} \mathbf{D}_p & \mathbf{0} \\ \mathbf{0} & \mathbf{D}_t \end{bmatrix}^k \cdot \begin{bmatrix} \boldsymbol{\varepsilon}_p \\ \boldsymbol{\varepsilon}_t \end{bmatrix}^k = \mathbf{D}^k \boldsymbol{\varepsilon}^k \qquad 3.51$$

where $\boldsymbol{\sigma}_p^k$ and $\boldsymbol{\sigma}_t^k$ are the in-plane and the transverse shear stresses vectors, respectively.

Finally, the stresses $\overline{\boldsymbol{\sigma}}^k$ and strains $\overline{\boldsymbol{\varepsilon}}^k$ vector referred to the material coordinate system (e1,e2,e3) for the *k*th layer are computed by

$$\begin{aligned} \overline{\boldsymbol{\sigma}}^k &= \left(\boldsymbol{\Pi}^{k^T}\right)^{-1} \cdot \boldsymbol{\sigma}^k = \overline{\mathbf{D}}^k \cdot \overline{\boldsymbol{\varepsilon}}^k \\ \overline{\boldsymbol{\varepsilon}}^k &= \boldsymbol{\Pi}^k \cdot \boldsymbol{\varepsilon}^k \end{aligned} \qquad 3.52$$

Although layers are treated as isotropic or orthotropic material in this work, the mechanical behavior of each component within FRP laminates (e.g. fibers and matrix) can be separately modeled using the well-known Mixing theory [61, 62] or a more advanced mixing theory called Serial/Parallel [63].

3.3.4 Stress resultants

Due to the subdivision of the strains (Eq.(3.43)) also the stress resultant vector $\hat{\boldsymbol{\sigma}}$ is subdivided into membrane forces $\hat{\boldsymbol{\sigma}}_m$, bending moments $\hat{\boldsymbol{\sigma}}_b$, transverse shear forces $\hat{\boldsymbol{\sigma}}_s$, pseudo-bending moments $\hat{\boldsymbol{\sigma}}_{mb\phi}$ and pseudo-shear forces $\hat{\boldsymbol{\sigma}}_{s\phi}$ (Figure 3.28). $\hat{\boldsymbol{\sigma}}_m$, $\hat{\boldsymbol{\sigma}}_b$, and $\hat{\boldsymbol{\sigma}}_s$ derives from the standard plate theory, whereas $\hat{\boldsymbol{\sigma}}_{mb\phi}$ and $\hat{\boldsymbol{\sigma}}_{s\phi}$ are pseudo stress resultants from the RZT plate theory.

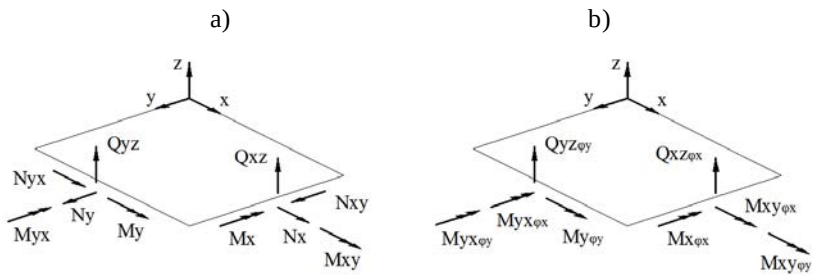

Figure 3.28 – Direction of stress resultants of standard plate theory (a) and those derived from the RZT plate theory (b).

The stress resultants for a plate are obtained by integrating stresses (Eq.(3.51)) over the thickness as

Membrane forces $\hat{\boldsymbol{\sigma}}_m$

$$\hat{\boldsymbol{\sigma}}_m = \begin{bmatrix} N_x \\ N_y \\ N_{xy} \end{bmatrix} = \int_z \mathbf{S}_m^T \boldsymbol{\sigma}_p^k \mathrm{d}z \tag{3.53}$$

$$\hat{\boldsymbol{\sigma}}_m = \left(\int_z \mathbf{S}_m^T \mathbf{D}_p^k \mathbf{S}_m \mathrm{d}z\right)\hat{\boldsymbol{\varepsilon}}_m + \left(\int_z \mathbf{S}_m^T \mathbf{D}_p^k \mathbf{S}_b \mathrm{d}z\right)\hat{\boldsymbol{\varepsilon}}_{\boldsymbol{b}} + \left(\int_z \mathbf{S}_m^T \mathbf{D}_p^k \mathbf{S}_{mb\phi}^k \mathrm{d}z\right)\hat{\boldsymbol{\varepsilon}}_{\boldsymbol{mb\phi}}$$

$$\hat{\boldsymbol{\sigma}}_m = \hat{\mathbf{D}}_m \hat{\boldsymbol{\varepsilon}}_m + \hat{\mathbf{D}}_{mb} \hat{\boldsymbol{\varepsilon}}_{\boldsymbol{b}} + \hat{\mathbf{D}}_{mmb\phi} \hat{\boldsymbol{\varepsilon}}_{\boldsymbol{mb\phi}}$$

$$\hat{\mathbf{D}}_m = \int_z \mathbf{S}_m^T \mathbf{D}_p^k \mathbf{S}_m \mathrm{d}z$$
$$\hat{\mathbf{D}}_{mb} = \int_z \mathbf{S}_m^T \mathbf{D}_p^k \mathbf{S}_b \mathrm{d}z$$
$$\hat{\mathbf{D}}_{mmb\phi} = \int_z \mathbf{S}_m^T \mathbf{D}_p^k \mathbf{S}_{mb\phi}^k \mathrm{d}z$$

Bending moments $\hat{\boldsymbol{\sigma}}_b$

$$\hat{\boldsymbol{\sigma}}_b = \begin{bmatrix} M_x \\ M_y \\ M_{xy} \end{bmatrix} = \int_z \mathbf{S}_b^T \boldsymbol{\sigma}_p^k \mathrm{d}z \tag{3.54}$$

$$\hat{\boldsymbol{\sigma}}_b = \left(\int_z \mathbf{S}_b^T \mathbf{D}_p^k \mathbf{S}_m \mathrm{d}z\right)\hat{\boldsymbol{\varepsilon}}_m + \left(\int_z \mathbf{S}_b^T \mathbf{D}_p^k \mathbf{S}_b \mathrm{d}z\right)\hat{\boldsymbol{\varepsilon}}_{\boldsymbol{b}} + \left(\int_z \mathbf{S}_b^T \mathbf{D}_p^k \mathbf{S}_{mb\phi}^k \mathrm{d}z\right)\hat{\boldsymbol{\varepsilon}}_{\boldsymbol{mb\phi}}$$

$$\hat{\boldsymbol{\sigma}}_b = \hat{\mathbf{D}}_{bm} \hat{\boldsymbol{\varepsilon}}_m + \hat{\mathbf{D}}_b \hat{\boldsymbol{\varepsilon}}_{\boldsymbol{b}} + \hat{\mathbf{D}}_{bmb\phi} \hat{\boldsymbol{\varepsilon}}_{\boldsymbol{mb\phi}}$$

$$\hat{\mathbf{D}}_{bm} = \int_z \mathbf{S}_b^T \mathbf{D}_p^k \mathbf{S}_m \mathrm{d}z$$
$$\hat{\mathbf{D}}_b = \int_z \mathbf{S}_b^T \mathbf{D}_p^k \mathbf{S}_b \mathrm{d}z$$
$$\hat{\mathbf{D}}_{bmb\phi} = \int_z \mathbf{S}_b^T \mathbf{D}_p^k \mathbf{S}_{mb\phi}^k \mathrm{d}z$$

Transverse shear forces $\hat{\boldsymbol{\sigma}}_s$

$$\hat{\boldsymbol{\sigma}}_s = \begin{bmatrix} Q_{xz} \\ Q_{yz} \end{bmatrix} = \int_z \mathbf{S}_s^T \boldsymbol{\sigma}_t^k \mathrm{d}z \tag{3.55}$$

$$\hat{\boldsymbol{\sigma}}_s = \left(\int_z \mathbf{S}_s^T \mathbf{D}_t^k \mathbf{S}_s \mathrm{dz}\right)\hat{\boldsymbol{\varepsilon}}_s + \left(\int_z \mathbf{S}_s^T \mathbf{D}_t^k \mathbf{S}_{s\phi}^k \mathrm{dz}\right)\hat{\boldsymbol{\varepsilon}}_{s\phi}$$

$$\hat{\boldsymbol{\sigma}}_s = \hat{\mathbf{D}}_s \hat{\boldsymbol{\varepsilon}}_s + \hat{\mathbf{D}}_{ss\phi}\hat{\boldsymbol{\varepsilon}}_{s\phi}$$

$$\hat{\mathbf{D}}_s = \int_z \mathbf{S}_s^T \mathbf{D}_t^k \mathbf{S}_s \mathrm{dz}$$
$$\hat{\mathbf{D}}_{ss\phi} = \int_z \mathbf{S}_s^T \mathbf{D}_t^k \mathbf{S}_{s\phi}^k \mathrm{dz}$$

Pseudo-bending moments $\hat{\boldsymbol{\sigma}}_{mb\phi}$

$$\hat{\boldsymbol{\sigma}}_{mb\phi} = \begin{bmatrix} M_{x\phi_x} \\ M_{y\phi_y} \\ M_{xy\phi_x} \\ M_{xy\phi_y} \end{bmatrix} = \int_z \mathbf{S}_{mb\phi}^{k^T} \boldsymbol{\sigma}_p^k dz \qquad 3.56$$

$$\hat{\boldsymbol{\sigma}}_{mb\phi} = \left(\int_z \mathbf{S}_{mb\phi}^{k^T} \mathbf{D}_p^k \mathbf{S}_m \mathrm{dz}\right)\hat{\boldsymbol{\varepsilon}}_m + \left(\int_z \mathbf{S}_{mb\phi}^{k^T} \mathbf{D}_p^k \mathbf{S}_b \mathrm{dz}\right)\hat{\boldsymbol{\varepsilon}}_{\boldsymbol{b}} + \left(\int_z \mathbf{S}_{mb\phi}^{k^T} \mathbf{D}_p^k \mathbf{S}_{mb\phi}^k \mathrm{dz}\right)\hat{\boldsymbol{\varepsilon}}_{\boldsymbol{mb\phi}}$$

$$\hat{\boldsymbol{\sigma}}_{mb\phi} = \hat{\mathbf{D}}_{mb\phi m}\hat{\boldsymbol{\varepsilon}}_m + \hat{\mathbf{D}}_{mb\phi b}\hat{\boldsymbol{\varepsilon}}_{\boldsymbol{b}} + \hat{\mathbf{D}}_{mb\phi}\hat{\boldsymbol{\varepsilon}}_{\boldsymbol{mb\phi}}$$

$$\hat{\mathbf{D}}_{mb\phi m} = \int_z \mathbf{S}_{mb\phi}^{k^T} \mathbf{D}_p^k \mathbf{S}_m \mathrm{dz}$$
$$\hat{\mathbf{D}}_{mb\phi b} = \int_z \mathbf{S}_{mb\phi}^{k^T} \mathbf{D}_p^k \mathbf{S}_b \mathrm{dz}$$
$$\hat{\mathbf{D}}_{mb\phi} = \int_z \mathbf{S}_{mb\phi}^{k^T} \mathbf{D}_p^k \mathbf{S}_{mb\phi}^k \mathrm{dz}$$

and finally *pseudo-shear forces* $\hat{\boldsymbol{\sigma}}_{s\phi}$

$$\hat{\boldsymbol{\sigma}}_{s\phi} = \begin{bmatrix} Q_{xz\phi_x} \\ Q_{xz\phi_y} \end{bmatrix} = \int_z \mathbf{S}_{s\phi}^{k^T} \boldsymbol{\sigma}_t^k \mathrm{dz} \qquad 3.57$$

$$\hat{\boldsymbol{\sigma}}_{s\phi} = \left(\int_z \mathbf{S}_{s\phi}^{k^T} \mathbf{D}_t^k \mathbf{S}_s \mathrm{dz}\right)\hat{\boldsymbol{\varepsilon}}_s + \left(\int_z \mathbf{S}_{s\phi}^{k^T} \mathbf{D}_t^k \mathbf{S}_{s\phi}^k \mathrm{dz}\right)\hat{\boldsymbol{\varepsilon}}_{s\phi}$$

$$\hat{\boldsymbol{\sigma}}_{s\phi} = \hat{\mathbf{D}}_{s\phi s}\hat{\boldsymbol{\varepsilon}}_s + \hat{\mathbf{D}}_{s\phi}\hat{\boldsymbol{\varepsilon}}_{s\phi}$$

$$\hat{\mathbf{D}}_{s\phi s} = \int_z \mathbf{S}_{s\phi}^{k^T} \mathbf{D}_t^k \mathbf{S}_s \mathrm{dz}$$
$$\hat{\mathbf{D}}_{s\phi} = \int_z \mathbf{S}_{s\phi}^{k^T} \mathbf{D}_t^k \mathbf{S}_{s\phi}^k \mathrm{dz}$$

The matrix expression for the stress resultants $\hat{\boldsymbol{\sigma}}$ can be written as

$$\hat{\boldsymbol{\sigma}} = \begin{bmatrix} \hat{\boldsymbol{\sigma}}_p \\ \hat{\boldsymbol{\sigma}}_t \end{bmatrix} = \begin{bmatrix} \tilde{\mathbf{D}}_p & \mathbf{0} \\ \mathbf{0} & \tilde{\mathbf{D}}_t \end{bmatrix} \cdot \begin{bmatrix} \hat{\boldsymbol{\varepsilon}}_p \\ \hat{\boldsymbol{\varepsilon}}_t \end{bmatrix} \qquad 3.58$$

where $\hat{\boldsymbol{\sigma}}_p$ and $\hat{\boldsymbol{\sigma}}_t$ contain the in-plane and transverse shear stress resultants, respectively,

$$\hat{\boldsymbol{\sigma}}_p = \begin{bmatrix} \hat{\boldsymbol{\sigma}}_m \\ \hat{\boldsymbol{\sigma}}_b \\ \hat{\boldsymbol{\sigma}}_{mb\phi} \end{bmatrix} \quad ; \quad \hat{\boldsymbol{\sigma}}_t = \begin{bmatrix} \hat{\boldsymbol{\sigma}}_s \\ \hat{\boldsymbol{\sigma}}_{s\phi} \end{bmatrix} \qquad 3.59$$

and the in-plane and transverse shear generalized constitutive matrices, $\tilde{\mathbf{D}}_p$ and $\tilde{\mathbf{D}}_t$ respectively, are given by

$$\tilde{\mathbf{D}}_p = \begin{bmatrix} \hat{\mathbf{D}}_m & \hat{\mathbf{D}}_{mb} & \hat{\mathbf{D}}_{mmb\phi} \\ \hat{\mathbf{D}}_{bm} & \hat{\mathbf{D}}_b & \hat{\mathbf{D}}_{bmb\phi} \\ \hat{\mathbf{D}}_{mb\phi m} & \hat{\mathbf{D}}_{mb\phi b} & \hat{\mathbf{D}}_{mb\phi} \end{bmatrix} \quad ; \quad \tilde{\mathbf{D}}_t = \begin{bmatrix} \hat{\mathbf{D}}_s & \hat{\mathbf{D}}_{ss\phi} \\ \hat{\mathbf{D}}_{s\phi s} & \hat{\mathbf{D}}_{s\phi} \end{bmatrix} \qquad 3.60$$

Analytical integration is used to compute the generalized constitutive matrices $\hat{\mathbf{D}}$.

3.3.5 Principle of virtual work

Let us consider a plate of volume V, which is subjected to the distributed surface **q** and line **f** loads applied on the surface Γ_A and the contour Γ_L, respectively. Point loads p_i are also acting on the plate. For this case, the differential equations of equilibrium (Eq.(3.4)) is rewritten as

$$\int_V \delta\boldsymbol{\varepsilon}^{k^T} \boldsymbol{\sigma}^k \, dV = \int_{\Gamma_A} \delta\mathbf{a}^T \mathbf{q} \, d\Gamma_A + \int_{\Gamma_L} \delta\mathbf{a}^T \mathbf{f} \, d\Gamma_L + \sum_{i=1}^{pl} \delta a_i \, p_i \qquad 3.61$$

where the l.h.s. is the internal virtual work performed by the stresses $\boldsymbol{\sigma}^k$ and the r.h.s. is the external virtual work.

Substituting Eq.(3.43) into the l.h.s. of Eq.(3.61) gives

$$\begin{aligned}\int_{\mathrm{V}} \delta\boldsymbol{\varepsilon}^{k^T}\boldsymbol{\sigma}^k \,\mathrm{dV} &= \int_{\mathrm{V}} \left(\delta\hat{\boldsymbol{\varepsilon}}_m^T\mathbf{S}_m^T + \delta\hat{\boldsymbol{\varepsilon}}_b^T\mathbf{S}_b^T + \delta\hat{\boldsymbol{\varepsilon}}_{mb\phi}^T\mathbf{S}_{mb\phi}^{k^T}\right)\boldsymbol{\sigma}_p^k \,\mathrm{dV} + \\ &\quad + \int_{\mathrm{V}} \left(\delta\hat{\boldsymbol{\varepsilon}}_s^T\mathbf{S}_s^T + \delta\hat{\boldsymbol{\varepsilon}}_{s\phi}^T\mathbf{S}_{s\phi}^{k^T}\right)\boldsymbol{\sigma}_t^k \,\mathrm{dV} \\ &= \int_{\mathrm{V}} \left(\delta\hat{\boldsymbol{\varepsilon}}_m^T\mathbf{S}_m^T\boldsymbol{\sigma}_p^k + \delta\hat{\boldsymbol{\varepsilon}}_b^T\mathbf{S}_b^T\boldsymbol{\sigma}_p^k + \delta\hat{\boldsymbol{\varepsilon}}_{mb\phi}^T\mathbf{S}_{mb\phi}^{k^T}\boldsymbol{\sigma}_p^k\right)\mathrm{dV} + \\ &\quad + \int_{\mathrm{V}} \left(\delta\hat{\boldsymbol{\varepsilon}}_s^T\mathbf{S}_s^T\boldsymbol{\sigma}_t^k + \delta\hat{\boldsymbol{\varepsilon}}_{s\phi}^T\mathbf{S}_{s\phi}^{k^T}\boldsymbol{\sigma}_t^k\right)\mathrm{dV}\end{aligned}$$

Using Eq.(3.43), (3.51), (3.58) yields

$$\int_{\mathrm{V}} \delta\boldsymbol{\varepsilon}^{k^T}\boldsymbol{\sigma}^k \,\mathrm{dV} = \int_{\mathrm{A}} \left(\delta\hat{\boldsymbol{\varepsilon}}_m^T\hat{\boldsymbol{\sigma}}_m + \delta\hat{\boldsymbol{\varepsilon}}_b^T\hat{\boldsymbol{\sigma}}_b + \delta\hat{\boldsymbol{\varepsilon}}_{mb\phi}^T\hat{\boldsymbol{\sigma}}_{mb\phi}\right)\mathrm{dA} + \int_{\mathrm{A}} \left(\delta\hat{\boldsymbol{\varepsilon}}_s^T\hat{\boldsymbol{\sigma}}_s + \delta\hat{\boldsymbol{\varepsilon}}_{s\phi}^T\hat{\boldsymbol{\sigma}}_{s\phi}\right)\mathrm{dA}$$

being A the in-plate area of the plate.

Finally, the equilibrium equations of Eq.(3.4) can be written as

$$\int_{\mathrm{A}} \left(\delta\hat{\boldsymbol{\varepsilon}}_p^T\hat{\boldsymbol{\sigma}}_p + \delta\hat{\boldsymbol{\varepsilon}}_t^T\hat{\boldsymbol{\sigma}}_t\right)\mathrm{dA} = \int_{\Gamma_{\mathrm{A}}} \delta\mathbf{a}^T\mathbf{q} \,\mathrm{d}\Gamma_{\mathrm{A}} + \int_{\Gamma_{\mathrm{L}}} \delta\mathbf{a}^T\mathbf{f} \,\mathrm{d}\Gamma_{\mathrm{L}} + \sum_{i=1}^{pl} \delta\mathrm{a}_i\,\mathrm{p}_i \qquad 3.62$$

Theses integrands contain kinematics variables derivatives up to first order only, which allows to use C0 continuous finite elements.

3.3.6 QLRZ formulation

3.3.6.1 Discretization of the displacement field

The middle surface of the plate is discretized into 4-node planar isoparametric finite elements of quadrilateral shape.

The kinematic variables **a** of Eq.(2.3) are interpolated within each element as

$$\mathbf{a}^{(\mathrm{e})} = \begin{bmatrix} u_0 \\ v_0 \\ w_0 \\ \theta_x \\ \theta_y \\ \psi_x \\ \psi_y \end{bmatrix} = \sum_{i=1}^{4} \mathbf{N}_i\mathbf{a}_i^{(\mathrm{e})} = \begin{bmatrix}\mathbf{N}_1 & \mathbf{N}_2 & \mathbf{N}_3 & \mathbf{N}_4\end{bmatrix} \cdot \begin{bmatrix} \mathbf{a}_1 \\ \mathbf{a}_2 \\ \mathbf{a}_3 \\ \mathbf{a}_4 \end{bmatrix}^{(\mathrm{e})} = \mathbf{N}_{\mathbf{n}}\mathbf{a}_{\mathbf{n}}^{(\mathrm{e})} \qquad 3.63$$

Where

$$\mathbf{N}_i = N_i\mathbf{I}_7 \quad ; \quad \mathbf{a}_i^{(\mathrm{e})} = \begin{bmatrix} u_0 & v_0 & w_0 & \theta_x & \theta_y & \psi_x & \psi_y \end{bmatrix}_i^T$$

being $N_i = \frac{1}{4}(1+\xi\xi_i)(1+\eta\eta_i)$ (Table 3.8 and Figure 3.29) the bi-linear shape function of node *i*th and I_7 is the 7x7 unit matrix.

Node	ξ_i	η_i
1	-1	-1
2	1	-1
3	1	1
4	-1	1

Table 3.8 - Values of ξ_i and η_i for each node.

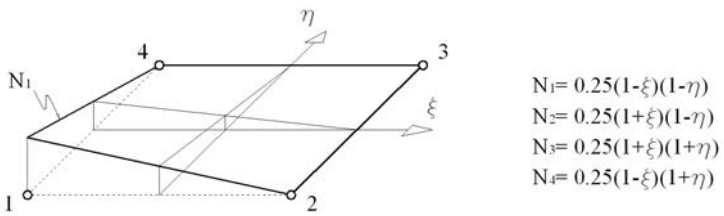

Figure 3.29 – Bi-linear shape functions of quadrilateral four-noded element.

The element geometry is interpolated as

$$x = \sum_{i=1}^{4} \hat{N}_i x_i \qquad ; \qquad y = \sum_{i=1}^{4} \hat{N}_i y_i \tag{3.64}$$

where $\hat{N}_i = N_i$, which leads to an isoparametric formulation.

The Jacobian matrix $\mathbf{J}^{(e)}$ of the transformation from the natural coordinates to the Cartesian coordinates is obtained using the chain rule as

$$\frac{\partial N_i}{\partial \xi} = \frac{\partial N_i}{\partial x}\frac{\partial x}{\partial \xi} + \frac{\partial N_i}{\partial y}\frac{\partial y}{\partial \xi}$$
$$\frac{\partial N_i}{\partial \eta} = \frac{\partial N_i}{\partial x}\frac{\partial x}{\partial \eta} + \frac{\partial N_i}{\partial y}\frac{\partial y}{\partial \eta}$$

or in a matrix form

$$\begin{bmatrix} \frac{\partial N_i}{\partial \xi} \\ \frac{\partial N_i}{\partial \eta} \end{bmatrix} = \begin{bmatrix} \frac{\partial x}{\partial \xi} & \frac{\partial y}{\partial \xi} \\ \frac{\partial x}{\partial \eta} & \frac{\partial y}{\partial \eta} \end{bmatrix} \cdot \begin{bmatrix} \frac{\partial N_i}{\partial x} \\ \frac{\partial N_i}{\partial y} \end{bmatrix} = \mathbf{J}^{(e)} \begin{bmatrix} \frac{\partial N_i}{\partial x} \\ \frac{\partial N_i}{\partial y} \end{bmatrix} \tag{3.65}$$

where $\mathbf{J}^{(e)}$ is the Jacobian matrix.

$$\begin{bmatrix} \dfrac{\partial N_i}{\partial x} \\ \dfrac{\partial N_i}{\partial y} \end{bmatrix} = \left[\mathbf{J}^{(e)}\right]^{-1} \begin{bmatrix} \dfrac{\partial N_i}{\partial \xi} \\ \dfrac{\partial N_i}{\partial \eta} \end{bmatrix}$$

with

$$\left[\mathbf{J}^{(e)}\right]^{-1} = \frac{1}{\left|\mathbf{J}^{(e)}\right|} \begin{bmatrix} \dfrac{\partial y}{\partial \eta} & -\dfrac{\partial y}{\partial \xi} \\ -\dfrac{\partial x}{\partial \eta} & \dfrac{\partial x}{\partial \xi} \end{bmatrix}$$

being $\left|\mathbf{J}^{(e)}\right|$ the Jacobian determinant. Thus,

$$\begin{aligned} \frac{\partial N_i}{\partial x} &= \frac{1}{\left|\mathbf{J}^{(e)}\right|}\left(\frac{\partial y}{\partial \eta}\frac{\partial N_i}{\partial \xi} - \frac{\partial y}{\partial \xi}\frac{\partial N_i}{\partial \eta}\right) \\ \frac{\partial N_i}{\partial y} &= \frac{1}{\left|\mathbf{J}^{(e)}\right|}\left(\frac{\partial x}{\partial \xi}\frac{\partial N_i}{\partial \eta} - \frac{\partial x}{\partial \eta}\frac{\partial N_i}{\partial \xi}\right) \end{aligned} \qquad 3.66$$

The Jacobian determinant is also used to determinate the differential area in natural coordinates as

$$dx\,dy = \left|\mathbf{J}^{(e)}\right| d\xi\, d\eta \qquad 3.67$$

The term of $\mathbf{J}^{(e)}$ are computed using the isoparametric transformation of Eq.(3.64) as

$$\begin{aligned} \frac{\partial x}{\partial \xi} &= \sum_{i=1}^{4} \frac{\partial N_i}{\partial \xi} x_i \quad ; \quad \frac{\partial x}{\partial \eta} = \sum_{i=1}^{4} \frac{\partial N_i}{\partial \eta} x_i \\ \frac{\partial y}{\partial \xi} &= \sum_{i=1}^{4} \frac{\partial N_i}{\partial \xi} y_i \quad ; \quad \frac{\partial y}{\partial \eta} = \sum_{i=1}^{4} \frac{\partial N_i}{\partial \eta} y_i \end{aligned}$$

Thus, the Jacobian matrix is defined by

$$\mathbf{J}^{(e)} = \begin{bmatrix} \dfrac{\partial x}{\partial \xi} & \dfrac{\partial y}{\partial \xi} \\ \dfrac{\partial x}{\partial \eta} & \dfrac{\partial y}{\partial \eta} \end{bmatrix} = \sum_{i=1}^{4} \begin{bmatrix} \dfrac{\partial N_i}{\partial \xi} x_i & \dfrac{\partial N_i}{\partial \xi} y_i \\ \dfrac{\partial N_i}{\partial \eta} x_i & \dfrac{\partial N_i}{\partial \eta} y_i \end{bmatrix} \qquad 3.68$$

3.3.6.2 Generalized strain field

The interpolated generalized in-plane strains $\hat{\boldsymbol{\varepsilon}}_p^{(e)}$ within each finite element are obtained by substituting Eq.(3.63) into Eq.(3.43) as

$$\hat{\boldsymbol{\varepsilon}}_p^{(e)} = \begin{bmatrix} \hat{\boldsymbol{\varepsilon}}_m \\ \hat{\boldsymbol{\varepsilon}}_b \\ \hat{\boldsymbol{\varepsilon}}_{mb\phi} \end{bmatrix}^{(e)} = \begin{bmatrix} \dfrac{\partial u_0}{\partial x} \\ \dfrac{\partial v_0}{\partial y} \\ \dfrac{\partial u_0}{\partial y} + \dfrac{\partial v_0}{\partial x} \\ \dfrac{\partial \theta_x}{\partial x} \\ \dfrac{\partial \theta_y}{\partial y} \\ \dfrac{\partial \theta_x}{\partial y} + \dfrac{\partial \theta_y}{\partial x} \\ \dfrac{\partial \psi_x}{\partial x} \\ \dfrac{\partial \psi_y}{\partial y} \\ \dfrac{\partial \psi_x}{\partial y} \\ \dfrac{\partial \psi_y}{\partial x} \end{bmatrix}^{(e)} = \sum_{i=1}^{4} \begin{bmatrix} \dfrac{\partial N_i}{\partial x} u_0 \\ \dfrac{\partial N_i}{\partial y} v_0 \\ \dfrac{\partial N_i}{\partial y} u_0 + \dfrac{\partial N_i}{\partial x} v_0 \\ \dfrac{\partial N_i}{\partial x} \theta_x \\ \dfrac{\partial N_i}{\partial y} \theta_y \\ \dfrac{\partial N_i}{\partial y} \theta_x + \dfrac{\partial N_i}{\partial x} \theta_y \\ \dfrac{\partial N_i}{\partial x} \psi_x \\ \dfrac{\partial N_i}{\partial y} \psi_y \\ \dfrac{\partial N_i}{\partial y} \psi_x \\ \dfrac{\partial N_i}{\partial x} \psi_y \end{bmatrix}_i = \sum_{i=1}^{4} \mathbf{B}_{p_i} \mathbf{a}_i^{(e)} = \mathbf{B}_p \mathbf{a}_{\mathbf{n}}^{(e)} \qquad 3.69$$

where $\mathbf{B}_p$ and $\mathbf{B}_{p_i}$ are the in-plane generalized strain matrices for the element and the *i*th node, respectively. The matrix $\mathbf{B}_{p_i}$ is split into membrane (m), bending (b) and zigzag $(mb\phi)$ contributions, which leads to

$$\mathbf{B}_{p_i} = \begin{bmatrix} \mathbf{B}_m \\ \mathbf{B}_b \\ \mathbf{B}_{mb\phi} \end{bmatrix}_i \qquad 3.70$$

with

$$\mathbf{B}_{m_i}=\begin{bmatrix}\dfrac{\partial N_i}{\partial x} & 0 & 0 & 0 & 0 & 0 & 0\\ 0 & \dfrac{\partial N_i}{\partial y} & 0 & 0 & 0 & 0 & 0\\ \dfrac{\partial N_i}{\partial y} & \dfrac{\partial N_i}{\partial x} & 0 & 0 & 0 & 0 & 0\end{bmatrix} \qquad \mathbf{B}_{b_i}=\begin{bmatrix}0 & 0 & 0 & \dfrac{\partial N_i}{\partial x} & 0 & 0 & 0\\ 0 & 0 & 0 & 0 & \dfrac{\partial N_i}{\partial y} & 0 & 0\\ 0 & 0 & 0 & \dfrac{\partial N_i}{\partial y} & \dfrac{\partial N_i}{\partial x} & 0 & 0\end{bmatrix}$$

$$\mathbf{B}_{mb\phi_i}=\begin{bmatrix}0 & 0 & 0 & 0 & 0 & \dfrac{\partial N_i}{\partial x} & 0\\ 0 & 0 & 0 & 0 & 0 & 0 & \dfrac{\partial N_i}{\partial y}\\ 0 & 0 & 0 & 0 & 0 & \dfrac{\partial N_i}{\partial y} & 0\\ 0 & 0 & 0 & 0 & 0 & 0 & \dfrac{\partial N_i}{\partial x}\end{bmatrix} \qquad 3.71$$

Generalized transverse strains $\hat{\boldsymbol{\varepsilon}}_t^{(\mathrm{e})}$ are also obtained by the same manner as

$$\hat{\boldsymbol{\varepsilon}}_t^{(\mathrm{e})}=\begin{bmatrix}\hat{\boldsymbol{\varepsilon}}_s\\ \hat{\boldsymbol{\varepsilon}}_{s\phi}\end{bmatrix}^{(\mathrm{e})}=\begin{bmatrix}\dfrac{\partial w_0}{\partial x}-\theta_x\\ \dfrac{\partial w_0}{\partial y}-\theta_y\\ \hline \psi_x\\ \psi_y\end{bmatrix}^{(\mathrm{e})}=\sum_{i=1}^{4}\begin{bmatrix}\dfrac{\partial N_i}{\partial x}w_0-N_i\theta_x\\ \dfrac{\partial N_i}{\partial y}w_0-N_i\theta_y\\ \hline N_i\psi_x\\ N_i\psi_y\end{bmatrix}_i=\sum_{i=1}^{4}\mathbf{B}_{t_i}\mathbf{a}_i^{(\mathrm{e})}=\mathbf{B}_t\mathbf{a}_{\mathbf{n}}^{(\mathrm{e})} \qquad 3.72$$

where $\mathbf{B}_t$ and $\mathbf{B}_{t_i}$ are the transverse generalized strain matrices for the element and the *i*th node, respectively. Matrix $\mathbf{B}_{t_i}$ is split into shear (s) and zigzag $(s\phi)$ contributions as

$$\mathbf{B}_{t_i}=\begin{bmatrix}\mathbf{B}_s\\ \mathbf{B}_{s\phi}\end{bmatrix}_i \qquad 3.73$$

where

$$\mathbf{B}_{s_i} = \begin{bmatrix} 0 & 0 & \dfrac{\partial N_i}{\partial x} & -N_i & 0 & 0 & 0 \\ 0 & 0 & \dfrac{\partial N_i}{\partial y} & 0 & -N_i & 0 & 0 \end{bmatrix} \qquad 3.74$$

$$\mathbf{B}_{s\phi_i} = \begin{bmatrix} 0 & 0 & 0 & 0 & 0 & N_i & 0 \\ 0 & 0 & 0 & 0 & 0 & 0 & N_i \end{bmatrix}$$

3.3.6.3 Element stiffness matrix and nodal forces vector

Considering Eqs.(3.5), (3.62), the element stiffness matrix and nodal forces vector are obtained via the following equation

$$\int_{A^{(e)}} \left(\delta\hat{\boldsymbol{\varepsilon}}_p^{(e)^T} \hat{\boldsymbol{\sigma}}_p + \delta\hat{\boldsymbol{\varepsilon}}_t^{(e)^T} \hat{\boldsymbol{\sigma}}_t \right) dA = \int_{A^{(e)}} \delta\mathbf{a}^{(e)^T} \mathbf{q}\ dA + \int_{S^{(e)}} \delta\mathbf{a}^{(e)^T} \mathbf{f}\ dS + \delta\mathbf{a}_{\mathbf{n}}^{(e)^T} \mathbf{p} \qquad 3.75$$

being $A^{(e)}$ the element area and $S^{(e)}$ the element side where $\mathbf{f}$ is applied.

Considering that

$$\delta\hat{\boldsymbol{\varepsilon}}_p^{(e)^T} = \delta\mathbf{a}_{\mathbf{n}}^{(e)^T} \mathbf{B}_p^T \qquad ; \qquad \delta\hat{\boldsymbol{\varepsilon}}_t^{(e)^T} = \delta\mathbf{a}_{\mathbf{n}}^{(e)^T} \mathbf{B}_t^T \qquad ; \qquad \delta\mathbf{a}^{(e)^T} = \delta\mathbf{a}_{\mathbf{n}}^{(e)^T} \mathbf{N}_{\mathbf{n}}^T$$

and substituting Eq.(3.58) into Eq.(3.75) gives

$$\int_{A^{(e)}} \left(\delta\mathbf{a}_{\mathbf{n}}^{(e)^T} \mathbf{B}_p^T \tilde{\mathbf{D}}_p \hat{\boldsymbol{\varepsilon}}_p + \delta\mathbf{a}_{\mathbf{n}}^{(e)^T} \mathbf{B}_t^T \tilde{\mathbf{D}}_t \hat{\boldsymbol{\varepsilon}}_t \right) dA = \int_{A^{(e)}} \delta\mathbf{a}_{\mathbf{n}}^{(e)^T} \mathbf{N}_{\mathbf{n}}^T \mathbf{q}\ dA + \\ + \int_{S^{(e)}} \delta\mathbf{a}_{\mathbf{n}}^{(e)^T} \mathbf{N}_{\mathbf{n}}^T \mathbf{f}\ dS + \delta\mathbf{a}_{\mathbf{n}}^{(e)^T} \mathbf{p}$$

Substituting Eqs.(3.69), (3.72) into previous equation yields

$$\int_{A^{(e)}} \left(\delta\mathbf{a}_{\mathbf{n}}^{(e)^T} \mathbf{B}_p^T \tilde{\mathbf{D}}_p \mathbf{B}_p \mathbf{a}_{\mathbf{n}}^{(e)} + \delta\mathbf{a}_{\mathbf{n}}^{(e)^T} \mathbf{B}_t^T \tilde{\mathbf{D}}_t \mathbf{B}_t \mathbf{a}_{\mathbf{n}}^{(e)} \right) dA = \int_{A^{(e)}} \delta\mathbf{a}_{\mathbf{n}}^{(e)^T} \mathbf{N}_{\mathbf{n}}^T \mathbf{q}\ dA + \\ + \int_{S^{(e)}} \delta\mathbf{a}_{\mathbf{n}}^{(e)^T} \mathbf{N}_{\mathbf{n}}^T \mathbf{f}\ dS + \delta\mathbf{a}_{\mathbf{n}}^{(e)^T} \mathbf{p}$$

Thus, the equation is factorized as

$$\delta\mathbf{a}_{\mathbf{n}}^{(e)^T} \left\{ \left[\int_{A^{(e)}} \left(\mathbf{B}_p^T \tilde{\mathbf{D}}_p \mathbf{B}_p + \mathbf{B}_t^T \tilde{\mathbf{D}}_t \mathbf{B}_t \right) dA \right] \mathbf{a}_{\mathbf{n}}^{(e)} \right\} = \left(\int_{A^{(e)}} \mathbf{N}_{\mathbf{n}}^T \mathbf{q}\ dA + \int_{S^{(e)}} \mathbf{N}_{\mathbf{n}}^T \mathbf{f}\ dS + \mathbf{p} \right) \delta\mathbf{a}_{\mathbf{n}}^{(e)^T}$$

$$\left[\int_{A^{(e)}} \left(\mathbf{B}_p^T \tilde{\mathbf{D}}_p \mathbf{B}_p + \mathbf{B}_t^T \tilde{\mathbf{D}}_t \mathbf{B}_t \right) dA \right] \mathbf{a}_{\mathbf{n}}^{(e)} = \int_{A^{(e)}} \mathbf{N}_{\mathbf{n}}^T \mathbf{q}\ dA + \int_{S^{(e)}} \mathbf{N}_{\mathbf{n}}^T \mathbf{f}\ dS + \mathbf{p}$$

Finally, Eq.(3.75) is reduced to

$$\mathbf{K}^{(e)}\ \mathbf{a}_{\mathbf{n}}^{(e)} = \int_{A^{(e)}} \mathbf{N}_{\mathbf{n}}^T \mathbf{q}\ dA + \int_{S^{(e)}} \mathbf{N}_{\mathbf{n}}^T \mathbf{f}\ dS + \mathbf{p} \qquad 3.76$$

with

$$\mathbf{K}^{(e)} = \int_{A^{(e)}} \left(\mathbf{B}_p^T \tilde{\mathbf{D}}_p \mathbf{B}_p + \mathbf{B}_t^T \tilde{\mathbf{D}}_t \mathbf{B}_t \right) dA \qquad 3.77$$

Matrix $\mathbf{K}^{(e)}$ is the elemental stiffness matrix, which for convenience is split as

$$\mathbf{K}^{(e)} = \mathbf{K}_p^{(e)} + \mathbf{K}_t^{(e)}$$

being $\mathbf{K}_p^{(e)}$ and $\mathbf{K}_t^{(e)}$ the in-plane and the transverse elemental stiffness matrices, respectively, defined as

$$\begin{aligned} \mathbf{K}_p^{(e)} &= \int_{A^{(e)}} \mathbf{B}_p^T \tilde{\mathbf{D}}_p \mathbf{B}_p \, dA \\ \mathbf{K}_t^{(e)} &= \int_{A^{(e)}} \mathbf{B}_t^T \tilde{\mathbf{D}}_t \mathbf{B}_t \, dA \end{aligned} \qquad 3.78$$

To facilitate subsequent shear locking studies, matrix $\mathbf{K}_t^{(e)}$ is split as follows

$$\mathbf{K}_t^{(e)} = \mathbf{K}_s^{(e)} + \mathbf{K}_{s\phi}^{(e)} + \mathbf{K}_{ss\phi}^{(e)} + \left[\mathbf{K}_{ss\phi}^{(e)}\right]^T \qquad 3.79$$

with

$$\begin{aligned} \mathbf{K}_s^{(e)} &= \int_{A^{(e)}} \mathbf{B}_s^T \hat{\mathbf{D}}_s \mathbf{B}_s \, dA \\ \mathbf{K}_{s\phi}^{(e)} &= \int_{A^{(e)}} \mathbf{B}_{s\phi}^T \hat{\mathbf{D}}_{s\phi} \mathbf{B}_{s\phi} \, dA \\ \mathbf{K}_{ss\phi}^{(e)} &= \int_{A^{(e)}} \mathbf{B}_s^T \hat{\mathbf{D}}_{ss\phi} \mathbf{B}_{s\phi} \, dA \end{aligned} \qquad 3.80$$

The external nodal forces vector $\mathbf{F}^{ext}$ are defined by the r.h.s. of Eq.(3.76) as

$$\mathbf{F}^{ext} = \int_{A^{(e)}} \mathbf{N}_\mathbf{n}^T \mathbf{q} \; dA + \int_{S^{(e)}} \mathbf{N}_\mathbf{n}^T \mathbf{f} \; dS + \mathbf{p} \qquad 3.81$$

Considering Eq.(3.67) and $dA = dx\,dy$, the integrals of Eq.(3.78) defined in the Cartesian coordinate are transformed to the natural coordinate as

$$\begin{aligned} \mathbf{K}_p^{(e)} &= \int_{A^{(e)}} \mathbf{B}_p^T \tilde{\mathbf{D}}_p \mathbf{B}_p \, dA = \int_{-1}^{+1}\int_{-1}^{+1} \mathbf{B}_p^T \tilde{\mathbf{D}}_p \mathbf{B}_p \left|\mathbf{J}^{(e)}\right| d\xi \, d\eta \\ \mathbf{K}_t^{(e)} &= \int_{A^{(e)}} \mathbf{B}_t^T \tilde{\mathbf{D}}_t \mathbf{B}_t \, dA = \int_{-1}^{+1}\int_{-1}^{+1} \mathbf{B}_t^T \tilde{\mathbf{D}}_t \mathbf{B}_t \left|\mathbf{J}^{(e)}\right| d\xi \, d\eta \end{aligned} \qquad 3.82$$

Note that, the derivatives of the shape functions with respect to the Cartesian coordinates contained into the generalized strain matrices $\mathbf{B}$ are computed by Eq.(3.66). The integrals of Eqs.(3.82) are solved via numerical integration using the Gauss quadrature as

$$\begin{aligned} \mathbf{K}_p^{(e)} &= \int_{-1}^{+1}\int_{-1}^{+1} \mathbf{B}_p^T \tilde{\mathbf{D}}_p \mathbf{B}_p \left|\mathbf{J}^{(e)}\right| d\xi \, d\eta = \sum_{GP=1}^{4} \left[\mathbf{B}_p^T \tilde{\mathbf{D}}_p \mathbf{B}_p \left|\mathbf{J}^{(e)}\right|\right]_{(\xi_{GP},\eta_{GP})} W_{GP} \\ \mathbf{K}_t^{(e)} &= \int_{-1}^{+1}\int_{-1}^{+1} \mathbf{B}_t^T \tilde{\mathbf{D}}_t \mathbf{B}_t \left|\mathbf{J}^{(e)}\right| d\xi \, d\eta = \sum_{GP=1}^{4} \left[\mathbf{B}_t^T \tilde{\mathbf{D}}_t \mathbf{B}_t \left|\mathbf{J}^{(e)}\right|\right]_{(\xi_{GP},\eta_{GP})} W_{GP} \end{aligned} \qquad 3.83$$

where a 2x2 integration scheme is used for providing an exact integration of both, the $\mathbf{K}_p^{(e)}$ and the $\mathbf{K}_t^{(e)}$ matrices. The subscript *GP* indicates the actual integration point (the Gauss points) under consideration, which weighting factor is W_{GP}. Matrices $\mathbf{B}$ and the Jacobian determinant are evaluated at point GP.

The natural coordinates and the weighting factor of each Gauss point (ξ_{GP}, η_{GP}) are listed in Table 3.9.

GP	(ξ_{GP}, η_{GP})		W_{GP}
	ξ_{GP}	η_{GP}	
1	$-\frac{1}{\sqrt{3}}$	$-\frac{1}{\sqrt{3}}$	1
2	$+\frac{1}{\sqrt{3}}$	$-\frac{1}{\sqrt{3}}$	1
3	$+\frac{1}{\sqrt{3}}$	$+\frac{1}{\sqrt{3}}$	1
4	$-\frac{1}{\sqrt{3}}$	$+\frac{1}{\sqrt{3}}$	1

Table 3.9 – Natural coordinates and weighting factors of each Gauss point.

However, when full Gauss integration is used, the QLRZ element suffers from shear locking for slender plates, which leads to too stiff solutions. Note that for homogeneous plate the QLRZ becomes to the 4-noded quadrilateral Reissner-Mindlin finite element (QLLL), which is based on the FSDT theory. Taking into account that the QLLL element also suffers from shear locking it is reasonable to think that the causes of shear locking in the QLRZ element are the same as in the QLLL element. For the QLLL element, it is demonstrated [108] that according the plate is more slender the contribution of $\mathbf{K}_s^{(e)}$ (Eq.(3.79)) in the stiffness matrix $\mathbf{K}^{(e)}$ is progressively increasing until infinity in the limit case for h = 0. Thus, it is considered that the source of shear locking in the QLRZ element is also related to the shear stiffness contribution of $\mathbf{K}_s^{(e)}$, as showed below in this chapter.

In order to avoid this numerical problem, a reduced integration of the shear contribution using a selective integration technique, where the $\mathbf{K}_s^{(e)}$ matrix is

integrated by using one Gauss point only, can be used. However, it may further lead to undesired hour-glassing, which can propagate through the finite element mesh. For this reason, it is has to be carefully used.

Another robust technique is the *assumed transverse shear strains* approach developed by Dvorkin and Bathe [109, 110], which is adopted for overcoming the shear locking effects in the QLRZ element. This approach is based on the imposition of a special transverse shear strain $\hat{\boldsymbol{\varepsilon}}_s$ field, which satisfies the Kirchhoff condition for thin plate, e.g. $\hat{\boldsymbol{\varepsilon}}_s = 0$. Note, $\hat{\boldsymbol{\varepsilon}}_s$ is the shear strain of the Reissner-Mindlin theory.

The assumed elemental shear strain $\hat{\boldsymbol{\varepsilon}}_s^{(e)}$ related to the Cartesian coordinate is defined as

$$\hat{\boldsymbol{\varepsilon}}_s^{(e)} = \overline{\mathbf{B}}_s \mathbf{a}_{\mathbf{n}}^{(e)} \tag{3.84}$$

where $\overline{\mathbf{B}}_s$ is the sought *substitute transverse shear strain matrix*. Thus, this technique leads to matrix $\mathbf{B}_s$ (Eq.(3.73)) being replaced by the substitutive matrix $\overline{\mathbf{B}}_s$ of Eq.(3.96) . Therefore, the stiffness matrices $\mathbf{K}_s^{(e)}$ and $\mathbf{K}_{s\phi}^{(e)}$ (Eq.(3.80)) of $\mathbf{K}_t^{(e)}$ are now computed by

$$\begin{aligned} \mathbf{K}_s^{(e)} &= \int_{A^{(e)}} \overline{\mathbf{B}}_s^T \hat{\mathbf{D}}_s \overline{\mathbf{B}}_s \mathrm{dA} \\ \mathbf{K}_{ss\phi}^{(e)} &= \int_{A^{(e)}} \overline{\mathbf{B}}_s^T \hat{\mathbf{D}}_{ss\phi} \mathbf{B}_{s\phi} \mathrm{dA} \end{aligned} \tag{3.85}$$

The computation of $\overline{\mathbf{B}}_s$ is briefly explained at following. A detailed description of this technique can be found in [108].

Computation of the substitutive shear strain generalized matrix $\overline{\mathbf{B}}_s$

The assumed natural transverse shear strain field is given by

$$\hat{\boldsymbol{\varepsilon}}_s^{'} = \begin{bmatrix} \gamma_\xi \\ \gamma_\eta \end{bmatrix} = \begin{bmatrix} \alpha_1 + \alpha_2 \eta \\ \alpha_3 + \alpha_4 \xi \end{bmatrix} = \begin{bmatrix} 1 & \eta & 0 & 0 \\ 0 & 0 & 1 & \xi \end{bmatrix} . \begin{bmatrix} \alpha_1 \\ \alpha_2 \\ \alpha_3 \\ \alpha_4 \end{bmatrix} = \mathbf{A}\boldsymbol{\alpha} \tag{3.86}$$

where coefficients α_i are obtained by sampling the natural shear strains at the four points I, II, III and IV. Points I and III are denoted by symbol + whereas points II and IV by x. Figure 3.30 shows the assumed strain field.

The transverse shear strains in the Cartesian coordinate system are expressed as

$$\hat{\boldsymbol{\varepsilon}}_s = \begin{bmatrix} \gamma_{xz} \\ \gamma_{yz} \end{bmatrix} = \mathbf{J}^{-1}\hat{\boldsymbol{\varepsilon}}_s' \qquad 3.87$$

where $\mathbf{J}$ is the 2D Jacobian matrix defined by Eq.(3.68).

For convenience, a transverse shear stress along the predefined orientations $\overline{\xi}_i$ (Figure 3.31) is defined as

$$\gamma_{\overline{\xi}_i} = \left(\alpha_1 + \alpha_2\eta\right)\cdot\cos\delta_i + \left(\alpha_3 + \alpha_4\xi\right)\cdot\sin\delta_i \quad ; \quad i = 1, 4 \qquad 3.88$$

where δ_i is the angle between direction $\overline{\xi}_i$ and the natural axis ξ. The matrix form of Eq.(3.88) is written as

$$\boldsymbol{\gamma}_{\overline{\xi}} = \begin{bmatrix} \gamma_{\overline{\xi}_1} \\ \gamma_{\overline{\xi}_2} \\ \gamma_{\overline{\xi}_3} \\ \gamma_{\overline{\xi}_4} \end{bmatrix} = \begin{bmatrix} 1 & -1 & 0 & 0 \\ 0 & 0 & 1 & 1 \\ 1 & 1 & 0 & 0 \\ 0 & 0 & 1 & -1 \end{bmatrix} \cdot \begin{bmatrix} \alpha_1 \\ \alpha_2 \\ \alpha_3 \\ \alpha_4 \end{bmatrix} = \mathbf{P}\boldsymbol{\alpha} \qquad 3.89$$

where $\boldsymbol{\gamma}_{\overline{\xi}}$ contains the values of the assumed transverse shear strain at each sampling points (+ and x).

From Eq.(3.89)

$$\boldsymbol{\alpha} = \mathbf{P}^{-1}\boldsymbol{\gamma}_{\overline{\xi}} \qquad 3.90$$

where the strains $\gamma_{\overline{\xi}_i}$ are related to γ_{ξ_j} and γ_{η_j} $(j = I, IV)$ by

$$\boldsymbol{\gamma}_{\overline{\xi}} = \begin{bmatrix} \gamma_{\overline{\xi}_1} \\ \gamma_{\overline{\xi}_2} \\ \gamma_{\overline{\xi}_3} \\ \gamma_{\overline{\xi}_4} \end{bmatrix} = \begin{bmatrix} 1 & 0 & 0 & 0 & 0 & 0 & 0 & 0 \\ 0 & 0 & 0 & 1 & 0 & 0 & 0 & 0 \\ 0 & 0 & 0 & 0 & 1 & 0 & 0 & 0 \\ 0 & 0 & 0 & 0 & 0 & 0 & 0 & 1 \end{bmatrix} \cdot \begin{bmatrix} \gamma_{\xi_I} \\ \gamma_{\eta_I} \\ \gamma_{\xi_{II}} \\ \gamma_{\eta_{II}} \\ \gamma_{\xi_{III}} \\ \gamma_{\eta_{III}} \\ \gamma_{\xi_{IV}} \\ \gamma_{\eta_{IV}} \end{bmatrix} = \mathbf{T}\hat{\boldsymbol{\gamma}}' \qquad 3.91$$

Combining Eqs.(3.86), (3.90), (3.91) gives

$$\hat{\boldsymbol{\varepsilon}}_s^{'} = \mathbf{A}\mathbf{P}^{-1}\mathbf{T}\hat{\boldsymbol{\gamma}}^{'} \tag{3.92}$$

The Cartesian transverse shear strains $\hat{\boldsymbol{\gamma}}$ at the sampling points are related to the natural transverse shear strains $\hat{\boldsymbol{\gamma}}^{'}$ by

$$\hat{\boldsymbol{\gamma}}^{'} = \begin{bmatrix} \mathbf{J}_{\mathrm{I}} & \mathbf{0} & \mathbf{0} & \mathbf{0} \\ \mathbf{0} & \mathbf{J}_{\mathrm{II}} & \mathbf{0} & \mathbf{0} \\ \mathbf{0} & \mathbf{0} & \mathbf{J}_{\mathrm{III}} & \mathbf{0} \\ \mathbf{0} & \mathbf{0} & \mathbf{0} & \mathbf{J}_{\mathrm{IV}} \end{bmatrix} \cdot \begin{bmatrix} \hat{\boldsymbol{\gamma}}_{\mathrm{I}} \\ \hat{\boldsymbol{\gamma}}_{\mathrm{II}} \\ \hat{\boldsymbol{\gamma}}_{\mathrm{III}} \\ \hat{\boldsymbol{\gamma}}_{\mathrm{IV}} \end{bmatrix} = \mathbf{C}\hat{\boldsymbol{\gamma}} \quad ; \quad \hat{\boldsymbol{\gamma}}_j = \begin{bmatrix} \gamma_{xz} \\ \gamma_{yz} \end{bmatrix}_j \tag{3.93}$$

The Cartesian shear strains and the nodal displacements $\mathbf{a}$ are related as

$$\hat{\boldsymbol{\gamma}} = \mathbf{B}_s\mathbf{a} \tag{3.94}$$

where $\mathbf{B}_s$ is the original transverse generalized strain matrix (Eq.(3.74)) evaluated at the *j*th sampling point. Note that matrix $\mathbf{C}$ is also evaluated at each *j*th point.

Substituting Eqs.(3.92), (3.93), (3.94) into (3.87) yields

$$\hat{\boldsymbol{\varepsilon}}_s = \mathbf{J}^{-1}\mathbf{A}\mathbf{P}^{-1}\mathbf{T}\mathbf{C}\mathbf{B}_s\mathbf{a} = \overline{\mathbf{B}}_s\mathbf{a} \tag{3.95}$$

where $\overline{\mathbf{B}}_s$ is the sought substitute transverse shear strain matrix given by

$$\overline{\mathbf{B}}_s = \mathbf{J}^{-1}\mathbf{A}\mathbf{P}^{-1}\mathbf{T}\mathbf{C}\mathbf{B}_s \tag{3.96}$$

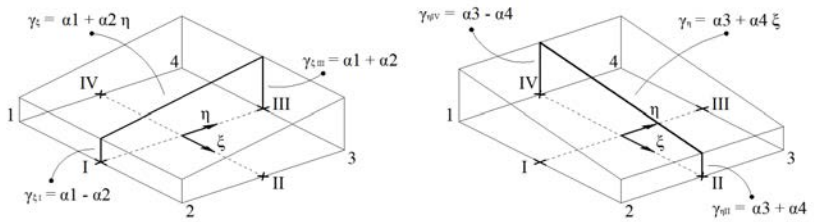

Figure 3.30 – Assumed transverse shear strain field.

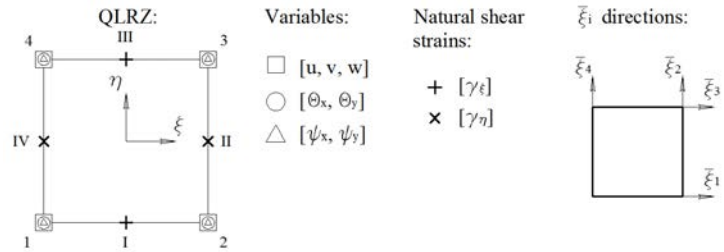

Figure 3.31 - QLRZ element. Evaluation points of the kinematics variables and the assumed shear strains.

3.3.6.4 Boundary conditions

The boundary conditions are:

- Clamped side:

$$w = 0$$
$$u = \theta_x = \psi_x = 0$$
$$v = \theta_y = \psi_y = 0$$

- Simply supported side:
  Hard Support

$$w = u_s = \theta_s = \psi_s = 0$$

  Soft Support

$$w = 0$$

  where "s" is the direction of the side.

- Symmetry axis:

$$u_n = \theta_n = \psi_n = 0$$

  where "n" is the orthogonal direction to the symmetry axis.

3.3.6.5 Improved computation of transverse shear stresses

Whereas in-plane stresses $\left(\sigma_x, \sigma_y \text{ and } \tau_{xy}\right)$ are well predicted by Eq.(3.51), the transverse shear stresses $\left(\tau_{xz} \text{ and } \tau_{yz}\right)$ are not. The reason is that the constitutive yields a constant value into each layer, leading to a discontinuous thickness distribution of τ_{xz} and τ_{yz}. A useful alternative is to compute τ_{xz} and τ_{yz} from the in-plane stresses using the equilibrium equations

$$\frac{\partial \sigma_x}{\partial x} + \frac{\partial \tau_{xy}}{\partial y} + \frac{\partial \tau_{xz}}{\partial z} = 0$$
$$\frac{\partial \tau_{xy}}{\partial x} + \frac{\partial \sigma_y}{\partial y} + \frac{\partial \tau_{yz}}{\partial z} = 0 \qquad 3.97$$

from which, the transverse shear stresses at a point "P" within the finite element across the thickness coordinates *z* are computed by

$$\tau_{xz}(z)\big|_P = -\int_{-h/2}^{z} \left.\frac{\partial \sigma_x}{\partial x}\right|_P dz - \int_{-h/2}^{z} \left.\frac{\partial \tau_{xy}}{\partial y}\right|_P dz$$
$$\tau_{yz}(z)\big|_P = -\int_{-h/2}^{z} \left.\frac{\partial \sigma_y}{\partial y}\right|_P dz - \int_{-h/2}^{z} \left.\frac{\partial \tau_{xy}}{\partial x}\right|_P dz \qquad 3.98$$

The in-plane stresses at point "P" are approximated by

$$\sigma_x(z)\big|_P = \sum_{i=1}^{4} N_i\big|_P \cdot \sigma_x^i(z)$$
$$\sigma_y(z)\big|_P = \sum_{i=1}^{4} N_i\big|_P \cdot \sigma_y^i(z) \qquad 3.99$$
$$\tau_{xy}(z)\big|_P = \sum_{i=1}^{4} N_i\big|_P \cdot \tau_{xy}^i(z)$$

where N_i is the shape function and *i* denotes the *i*th node. The nodal stresses $\sigma_x^i(z)$, $\sigma_y^i(z)$ and $\tau_{xy}^i(z)$ are obtained by the averaging of Gauss stresses from neighboring elements at the *i*th node. Finally, the transverse shear stresses are obtained by replacing Eq.(3.99) into Eq.(3.98),

$$\tau_{xz}(z)\big|_P = -\int_{-h/2}^{z} \left(\sum_{i=1}^{4} \left.\frac{\partial N_i}{\partial x}\right|_P \cdot \sigma_x^i(z) \right) - \int_{-h/2}^{z} \left(\sum_{i=1}^{4} \left.\frac{\partial N_i}{\partial y}\right|_P \cdot \tau_{xy}^i(z) \right)$$
$$\tau_{yz}(z)\big|_P = -\int_{-h/2}^{z} \left(\sum_{i=1}^{4} \left.\frac{\partial N_i}{\partial y}\right|_P \cdot \sigma_y^i(z) \right) - \int_{-h/2}^{z} \left(\sum_{i=1}^{4} \left.\frac{\partial N_i}{\partial x}\right|_P \cdot \tau_{xy}^i(z) \right) \qquad 3.100$$

3.3.7 QLRZ studies

3.3.7.1 Shear locking

In order to show the efficiency of the *assumed transverse shear strain* technique for overcoming shear looking effects, a simply supported (SS) square plate of length side $L = 2$ under a uniformly distributed load of unit value ($q = 1$) is analyzed (Figure 3.32).

Moreover, the selective integration technique of $\mathbf{K}_t^{(e)}$ matrix is analyzed. Considering that

$$\mathbf{K}_t^{(e)} = \mathbf{K}_s^{(e)} + \mathbf{K}_{s\phi}^{(e)} + \mathbf{K}_{ss\phi}^{(e)} + \left[\mathbf{K}_{ss\phi}^{(e)}\right]^T$$

it is possible to define the following three different combinations of selective integration

Integration combinations		
Combinations	Exact	Reduced
C1	$\mathbf{K}_{s\phi}^{(e)}$; $\mathbf{K}_{ss\phi}^{(e)}$	$\mathbf{K}_{s}^{(e)}$
C2	$\mathbf{K}_{s\phi}^{(e)}$	$\mathbf{K}_{s}^{(e)}$; $\mathbf{K}_{ss\phi}^{(e)}$
C3	-	$\mathbf{K}_{t}^{(e)}$

Table 3.10 – Integration combinations used to assess the selective integration of K_t.

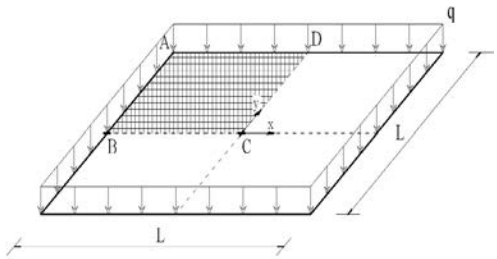

Figure 3.32 – Simply supported square plate under uniformly distributed load.

The analysis is performed for four span-to-thickness ratios: $\lambda = L/h = 5,10,50,100$. A 3-layer composite material is used, whose properties are listed in Table 3.11.

Laminated Material			
	Layer 1 (bottom)	Layer 2 (core)	Layer 3 (top)
h_i [mm]	$L/4\lambda$	$L/2\lambda$	$L/4\lambda$
E [MPa]	$2.19\text{x}10^5$	$2.19\text{x}10^4$	$4.40\text{x}10^5$
G [MPa]	$0.876\text{x}10^5$	$8.80\text{x}10^4$	$1.76\text{x}10^5$

Table 3.11 – Material properties of shear locking study.

Only one quarter of the plate is studied due to symmetry (Figure 3.32) using a mesh of 16x16 QLRZ elements (Figure 3.33a) with 289 nodes and 1445 DOFs. The reference solution is obtained by a 3D finite element analysis using a mesh of 10x10x9 (3 elements per ply) of 20-noded hexahedral elements (HEXA20) involving 4499 nodes and 13497 DOFs (Figure 3.33b).

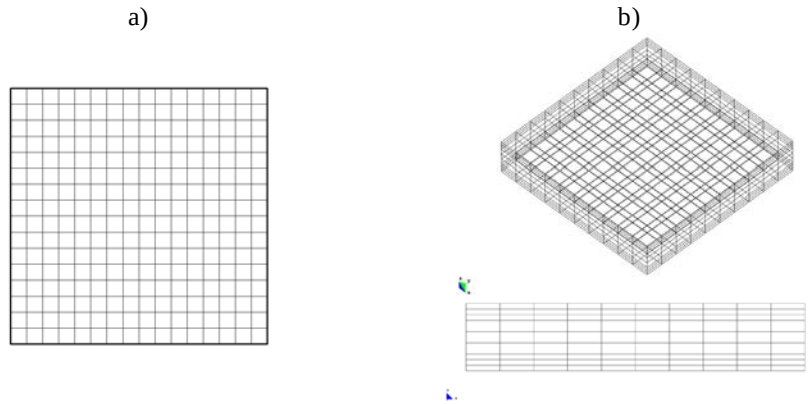

Figure 3.33 – Meshes used for the analysis of one quarter of the SS plate. 16x16 QLRZ elements (a) and 10x10x9 HEXA20 elements (b).

Figure 3.34 shows the *r* ratio defined as

$$r = \frac{w_{QLRZ}}{w_{3D}} \qquad 3.101$$

where w_{QLRZ} and w_{3D} are the middle (z = 0) deflection at the plate center obtained with the QLRZ element and the 3D finite element analysis, respectively. The QLRZ element results have been obtained with *exact* integration of matrix $\mathbf{K}_t^{(e)}$ (exact), employing the three selective integration listed in Table 3.10 (C1, C2, and C3), and finally using the *assumed transverse shear strain field* technique (QLRZ).

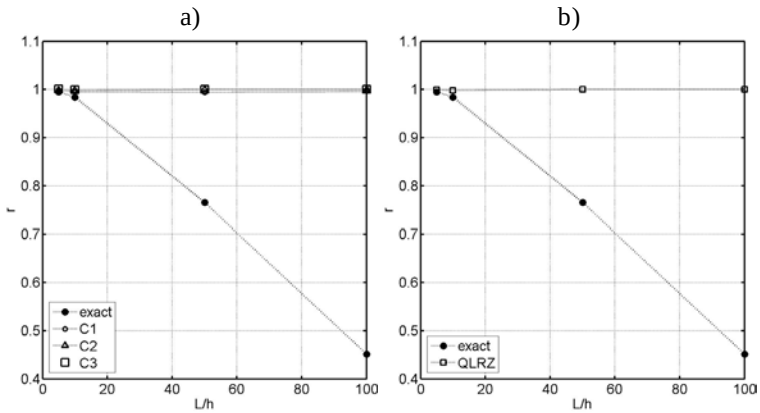

Figure 3.34 – *r* ratio vs. span-to-thickness ratio $\lambda = L/h$. Simply supported square plate under uniformly distributed load. Figure a): exact integration (exact) and the three integration combinations (C1, C2, and C3) of Table 3.10. Figure b): exact integration and assumed transverse shear strain fields (QLRZ).

Figure 3.34 clearly shows shear locking defects when exact integration of $\mathbf{K}_t^{(e)}$ is used. However, it is shown that this defect disappears for both techniques.

Figure 3.35 shows the distribution of the vertical deflection *w* along the plate central line BC (Figure 3.32). Figure 3.35a reveals the existence of mechanisms when reduced integration is used. These mechanisms do not appear if the *assumed transverse shear strain* technique is used (Figure 3.35b).

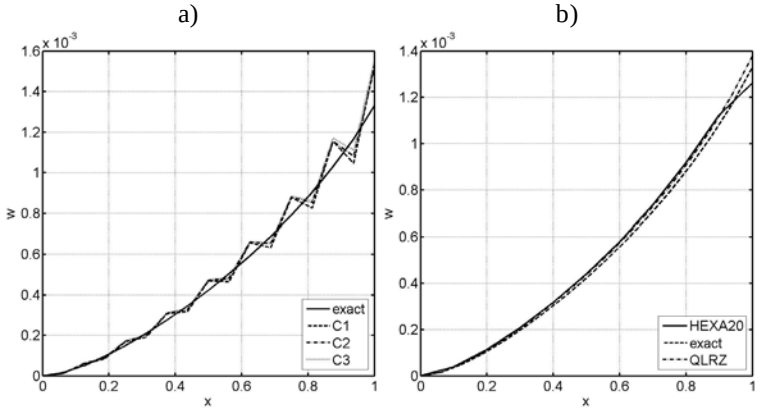

Figure 3.35 - Vertical deflection w along BC. Clamped square plate ($\lambda = 10$) under a center point load. Figure a): exact integration (exact) and the three integration combinations (C1, C2, and C3) of table AI-1. Figure b): exact integration, assumed transverse shear strain fields (QLRZ), and 3D analysis (HEXA20).

3.3.7.2 Verification

The accuracy of the *QLRZ element* for isotropic homogeneous material is studied in this section. The aim is to evaluate the behavior of the QLRZ element when ϕ_i ($i = x, y$) vanishes which leads to $\psi_i = 0$ and the RZT kinematics becomes the RMT displacement field.

This study consists in analyzing a SS and a clamped square plate of side length L = 2 and thickness h = 0.05 (λ = L/h = 40) under a uniformly distributed load q = 1 and a point load P = 4 acting at the center (Figure 3.36). Isotropic homogeneous material properties are assumed with: E = 0.219, μ = 0.25, and G = E/2(1+ μ).

Assuming symmetry along both axes, only one quarter of the plate is analyzed. Five different meshes of QLRZ elements whose properties are listed in Table 3.12 are employed (Figure 3.37).

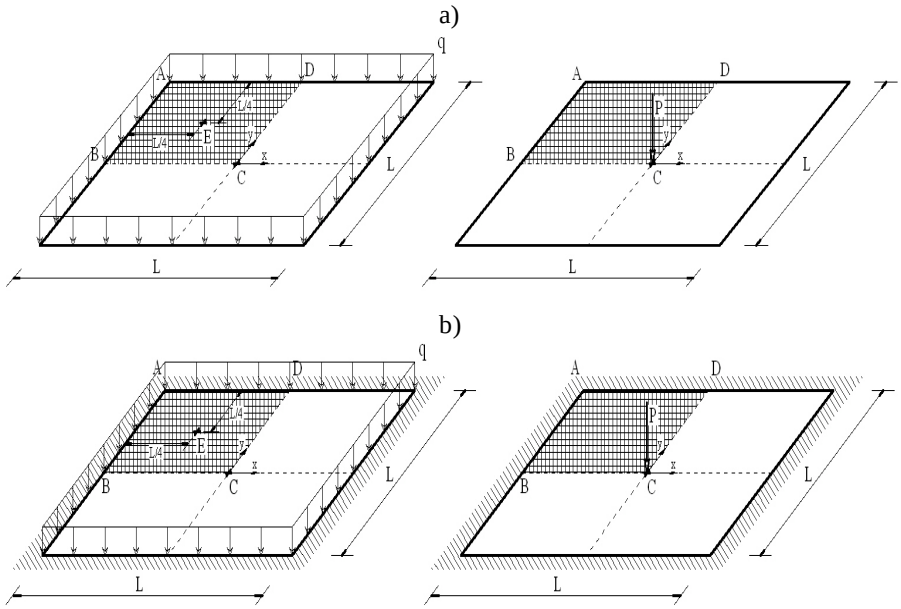

Figure 3.36 – Square plate ($\lambda = 40$) for verification and convergence analysis. SS plate (a) and clamped plate (b) under uniformly distributed load and central point load.

QLRZ meshes properties				
Mesh	N	Elements	Nodes	DOFs
1	2	4	9	45
2	4	16	25	150
3	8	64	81	405
4	16	256	289	1445
5	32	1024	1089	5445

Table 3.12 – QLRZ meshes properties.

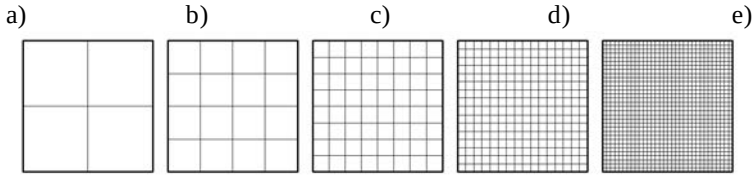

Figure 3.37 – Meshes of nxn QLRZ elements employed for verification and convergence analysis. (a) n = 2; (b) n = 4; (c) n = 8; (d) n = 16; (e) n = 32.

The reference solution was obtained by a finite element analysis using a mesh of 32x32 4-noded quadrilateral Reissner-Mindlin (FSDT) element with substitute shear strain fields [111].

In order to assess the element accuracy, the following relative error is defined

$$e_r = \frac{w_i - w_{RMT}}{w_{RMT}} \qquad 3.102$$

where w_i is the vertical deflection at the center point computed with the *i*th QLRZ mesh $(i = 1, 2, ..., 5)$ and w_{RMT} is the reference solution. The w_{RMT} values for all cases are listed in Table 3.13.

Reissner-Mindlin solutions		
Boundary	Load	w_{RMT}
SS	Distributed	0.02680
	Point	0.07730
Clamped	Distributed	0.00841
	Point	0.03790

Table 3.13 – Reissner-Mindlin solutions using a mesh of 32x32 four-noded quadrilateral elements.

The QLRZ solution of the problem and the relative error are listed in Table 3.14.

Relative error (e_r%) of w at center point					
Load	Mesh	SS		Clamped	
		w	er (%)	w	er (%)
Distributed	2x2	0.026150	-2.43	0.0080239	-4.59
	4x4	0.026638	-0.60	0.0082998	-1.31
	8x8	0.026744	-0.21	0.0083747	-0.42
	16x16	0.026770	-0.11	0.0083939	-0.19
	32x32	0.026776	-0.09	0.0083988	-0.13
Point	2x2	0.076049	-1.62	0.0322470	-14.92
	4x4	0.076392	-1.17	0.0360900	-4.78
	8x8	0.076767	-0.69	0.0371910	-1.87
	16x16	0.076966	-0.43	0.0375650	-0.88
	32x32	0.077097	-0.26	0.0377400	-0.42

Table 3.14 – Relative error e_r of *w* at center point.

Figure 3.38 shows the behavior of the error. Labels "SS-P", "SS-q", "C-P", and "C-q" refer to simply-supported-point-load, simply-supported-distributed-load, clamped-point-load, and clamped-distributed-load, respectively.

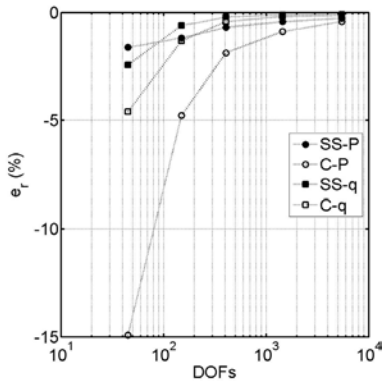

Figure 3.38 – Relative error e_r of central deflection.

Figure 3.38 clearly shows the convergence of the QLRZ solution to the Reissner-Mindlin solution for all cases. Good accuracy is obtained already for the 4x4 mesh (e_r less than 2.5%) except for the C-p case (e_r approximately equal to 5%). Results for the SS case (error < 2.5%) are better than for the clamped one. The worst result is obtained for the clamped plate under central point load for the 2x2 mesh (e_r=-14.92%).

3.3.7.3 Convergence

In order to study the influence of the heterogeneity of the laminated material on the convergence and accuracy of the QLRZ element, a SS and a clamped square plates of length side L = 2m and thickness h = 0.1m (λ = 20) under uniformly distributed load q = 1N/m^2 (Figure 3.36a and Figure 3.36c) are analyzed. Three different laminated materials, whose properties are listed in Table 3.15, are considered for each example. The material heterogeneity increases from composite C1 to C3.

Taking advantage of symmetry only one quarter of plate is analyzed using the QLRZ meshes shown in Figure 3.37. The reference solution was obtained by a 3D finite element analysis using a mesh of 10x10x9 (3 elements per ply) 20-noded hexahedral elements involving 4499 nodes and 13497 DOFs (Figure 3.39).

Composite Materials				
		Layer 1 (bottom)	Layer 2 (core)	Layer 3 (top)
Composite C1	h_i	h/3	h/3	h/3
	E [MPa]	$2.19\text{x}10^{-1}$	$2.19\text{x}10^{-2}$	$4.40\text{x}10^{-1}$
	υ	0.25	0.25	0.25
Composite C2	h_i	h/3	h/3	h/3
	E [MPa]	$2.19\text{x}10^{-1}$	$2.19\text{x}10^{-3}$	$2.19\text{x}10^{-1}$
	υ	0.25	0.25	0.25
Composite C3	h_i	h/10	4h/5	h/10
	E [MPa]	$2.19\text{x}10^{-1}$	$7.25\text{x}10^{-4}$	$7.30\text{x}10^{-2}$
	υ	0.25	0.25	0.25

Table 3.15 – Composite material properties.

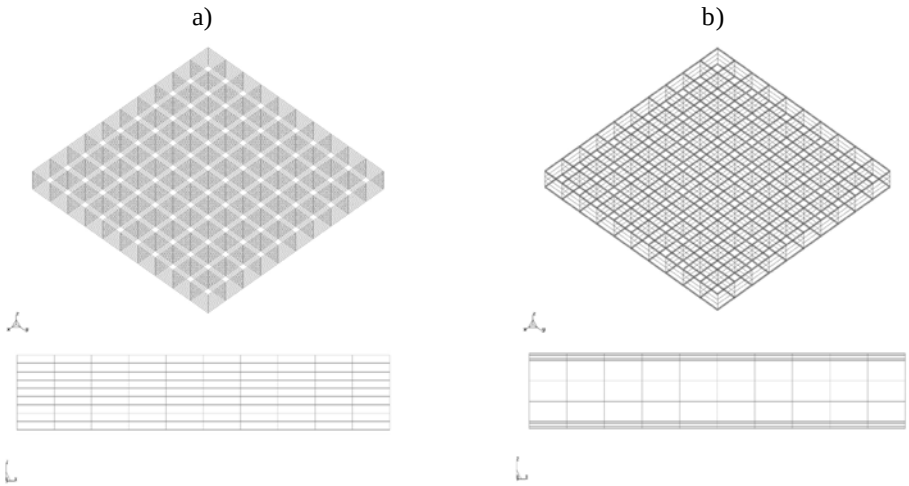

Figure 3.39 – 10x10x9 HEXA20 meshes employed to compute the reference solution for composite C1 and C2 (a), and composite C3 (b).

Convergence is quantified by the relative error defined as

$$e_r = \frac{m_i - m_{3D}}{m_{3D}} \qquad 3.103$$

where m_i and m_{3D} are the magnitudes of interest obtained with the *i*th QLRZ mesh (i = 1,2,…,5) and the 3D reference solution, respectively. The magnitudes studied m are: the middle (z = 0) vertical deflection w at the center point C (Figure 3.36), the axial stress σ_x on the top surface of ply 1 at point E, and ψ_x at point E.

Since ψ_x does not appear in 3D finite element analyses, m_i and m_{3D} are the values of this magnitude obtained with the ith QLRZ mesh (i = 1,…,4) and the finest mesh (32x32), respectively. The results obtained are listed in Table 3.16 and Table 3.17, and Figure 3.40 and Figure 3.41.

It is clearly seen that convergence is always slower for the most heterogeneous material and for the clamped plate.

For the clamped plate and the three materials (Table 3.16) errors are less than 10% for the 16x16 mesh for all variables. For the SS plate (Table 3.17) errors are less than 2.3% for the 8x8 mesh in all cases.

For composite C1 (the most homogeneous) errors are less than 2.9% for the 8x8 mesh in all cases and less than 6.3% for the 4x4 mesh in all cases except for σ_x in the clamped plate.

For the most heterogeneous material (composite C3), the difference in the results between the SS and the clamped plate is larger. For the SS plate (Table 3.17) errors are less than 2.3% for the 8x8 mesh in all variables. For the clamped plate (Table 3.16) errors are less than 23% for the 8x8 mesh and less than 10% for the 16x16 mesh in all cases. The quality of results obtained for the composite C2 is between that of composites C1 and C3.

Relative error e_r (%) in clamped plate

Mesh	**w** at point C			$\boldsymbol{\sigma_x}$ at point E			$\boldsymbol{\psi_x}$ at point E		
	C1	C2	C3	C1	C2	C3	C1	C2	C3
2x2	11.71	50.28	60.99	99.99	100	100	26.13	80.09	86.48
4x4	4.65	30.16	43.47	20.86	44.14	45.53	6.28	43.34	54.80
8x8	1.60	12.32	22.44	2.90	14.35	17.24	1.47	13.68	18.58
16x16	0.29	3.67	9.25	-1.21	-0.40	-1.15	0.30	2.58	2.22
32x32	-0.14	0.69	2.85	-2.22	-4.70	-4.62	0.00	0.00	0.00

Table 3.16 – Clamped square plate ($\lambda = 20$) under uniformly distributed load. Relative error e_r (%) for w, σ_x, and ψ_x.

Relative error e_r (%) in SS plate

Mesh	**w** at point C			σ_x at point E			ψ_x at point E		
	C1	C2	C3	C1	C2	C3	C1	C2	C3
2x2	2.69	19.36	25.83	26.98	32.89	33.24	9.11	41.06	51.92
4x4	0.68	6.50	10.14	4.86	7.70	9.05	3.99	8.95	13.67
8x8	0.25	1.54	2.22	-0.30	-0.79	0.44	0.71	0.40	1.84
16x16	0.15	0.38	0.35	-1.55	-3.04	-1.92	0.07	0.45	1.44
32x32	0.12	0.12	-0.02	-1.86	-3.49	-2.07	0.00	0.00	0.00

Table 3.17 – SS square plate ($\lambda = 20$) under uniformly distributed load. Relative error e_r (%) for *w*, σ_x, and ψ_x.

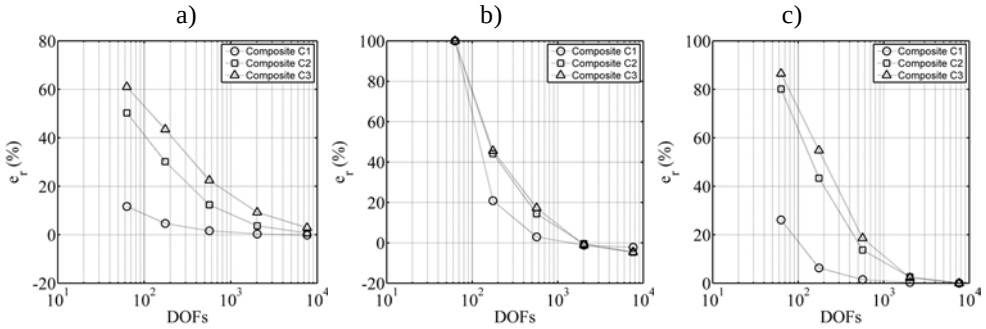

Figure 3.40 – Clamped square plate ($\lambda = 20$) under uniformly distributed load. Relative error e_r (%) for *w* (a), σ_x (b), and ψ_x (c).

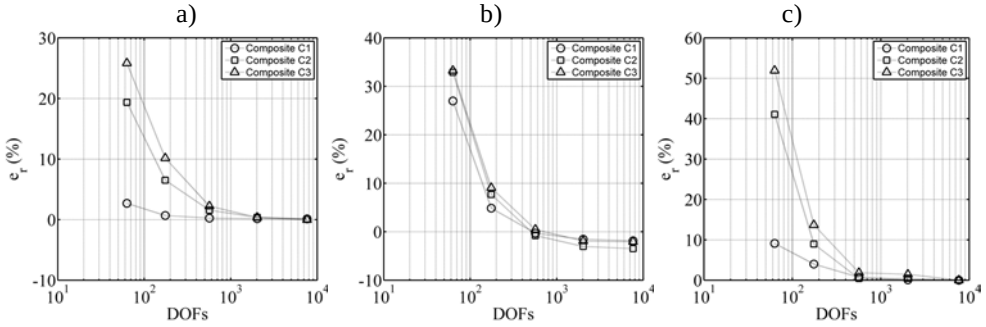

Figure 3.41 – SS square plate ($\lambda = 20$) under uniformly distributed load. Relative error e_r (%) for *w* (a), σ_x (b), and ψ_x (c).

3.3.7.4 Numerical examples

Comparison for SS square and circular composite laminated plates

In order to show the performance of the QLRZ element for highly heterogeneous composite material, a square SS plate of length L = 2m and thickness h = 0.1m, and a circular SS plate of diameter D = 2m and thickness h = 0.1m are studied. The structures are loaded under a uniformly distributed load, q=10000N/m^2 (Figure 3.42).

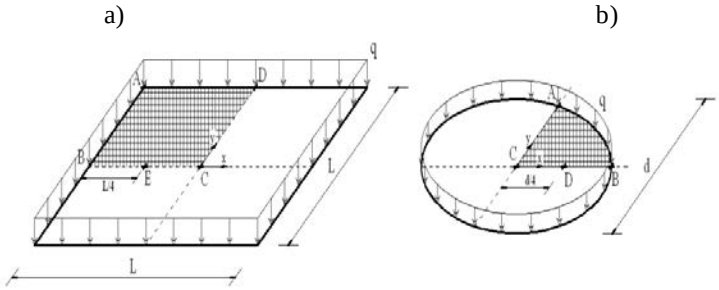

Figure 3.42 – Square SS plate (a) and circular SS plate (b) under uniformly distributed load.

Each plate is studied for different composite laminated materials with properties listed in Table 3.18 and Table 3.19. The square plate is analyzed for composites C4-7 and the circular plate for composites C6-7.

Do to symmetry only one quarter of plate is analyzed with the QLRZ meshes shown in Figure 3.43 whose properties are listed in Table 3.20. The reference solution is a 3D finite element analysis using HEXA20 elements. The different 3D meshes for each case are shown in Figure 3.44. Details of each mesh are listed in Table 3.21.

Layer material properties				
	A	B	C	D
E_1	157.9×10^2	19.15		
E_2	9.58×10^2	19.15	0.104×10^2	104.1×10^2
E_3	9.58×10^2	191.5		
μ_{12}	0.32	6.58×10^{-4}		
μ_{13}	0.32	6.43×10^{-8}	0.30	0.31
μ_{23}	0.49	6.43×10^{-8}		
G_{12}	5.93×10^2	42.3×10^{-7}	0.04×10^2	39.73×10^2
G_{13}	5.93×10^2	36.51		
G_{23}	3.23×10^2	124.8		

Table 3.18 – Layer material properties. E and G are given in MPa.

Composite laminated materials		
Composite	Layer distribution	h_i / h
C4	(A/C/A)	(0.1/0.8/0.1)
C5	(A/B)	(0.5/0.5)
C6	(A/B/C/D)	(0.1/0.3/0.5/0.1)
C7	(A/C/A/C/B/C/A/C/A)	(0.1/0.1/0.1/0.1/0.2/0.1/0.1/0.1/0.1)

Table 3.19 – Layer distribution of composite materials.

QLRZ meshes properties				
Mesh	nxn	Number of elements	Nodes	DOFs
a	8x8	64	81	567
b	16x16	256	289	2023
c	--	40	53	371
d	--	168	193	1351

Table 3.20 – QLRZ meshes properties.

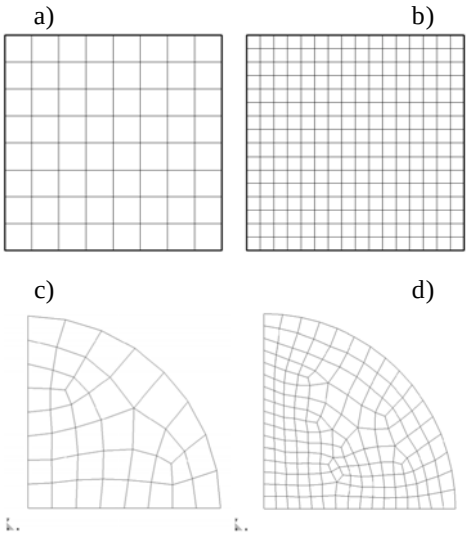

Figure 3.43 – QLRZ meshes. Square plate: 8x8 (a) and 16x16 element (b). Circular plate: 40 (c) and 168 (d) elements.

HEXA20 mesh properties				
Mesh	Composite	Number of elements	Nodes	DOFs
a	C4	640	3285	9855
b	C5	512	2673	8019
c	C6	768	3897	11691
d	C7	1728	8487	25461
e	C6	602	3094	9282
f	C7	1161	5824	17472

Table 3.21 – HEXA20 meshes properties.

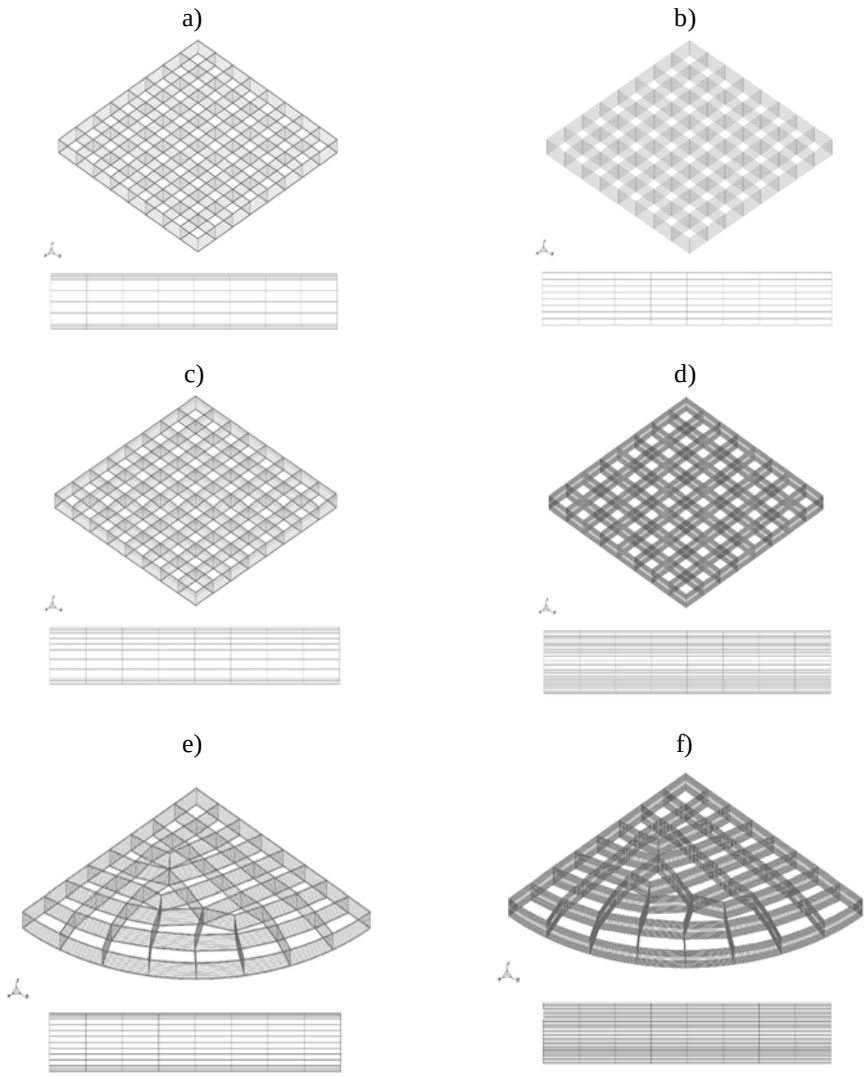

Figure 3.44 – HEXA20 reference meshes. Square meshes for composites C4 (a), C5 (b), C6 (c), C7 (d), and circular meshes for composites C6 (e) and C7 (f).

The RMT results for the square plate of composite C4 are also shown in Figure 3.45. The RMT solution was obtained by using a mesh of 16x16 four-noded QLLL plate element [108, 112].

Figures 3.45-3.50 show the computed vertical deflection w (a), the thickness distribution of the axial displacement u (b), the axial stress σ_x (c), the transverse shear stress τ_{xz} (d) for each plate under study.

The vertical deflection is accurately captured. At the center of plate, the maximum error (14%) is given by the circular plate of composite C6 for the 40-element mesh (Figure 3.46a). The errors are less than 10% for the finest mesh (168 elements).

The thickness distribution of the axial displacement is accurately predicted in all cases. The ability to capture the complex kinematics of laminated composite materials is a key feature of the QLRZ plate element. The successful axial displacement prediction leads to accurate axial stress values as shown in Figures c). Figures d) displays the good results for the thickness distribution of the transverse shear stresses computed by means of Eq.(3.100).

Figure 3.45 shows the inaccurate results when modeling a composite laminated plate using QLLL elements based on RMT. The deflection at the plate center is three times stiffer than the reference solution (Figure 3.45a). The RMT solution also yields an erroneous linear thickness distribution of the axial displacement (Figure 3.45b), which leads to a distorted distribution of the axial stress (Figure 3.45c). Finally, the RMT is unable to capture the correct transverse shear stress distribution (Figure 3.45d).

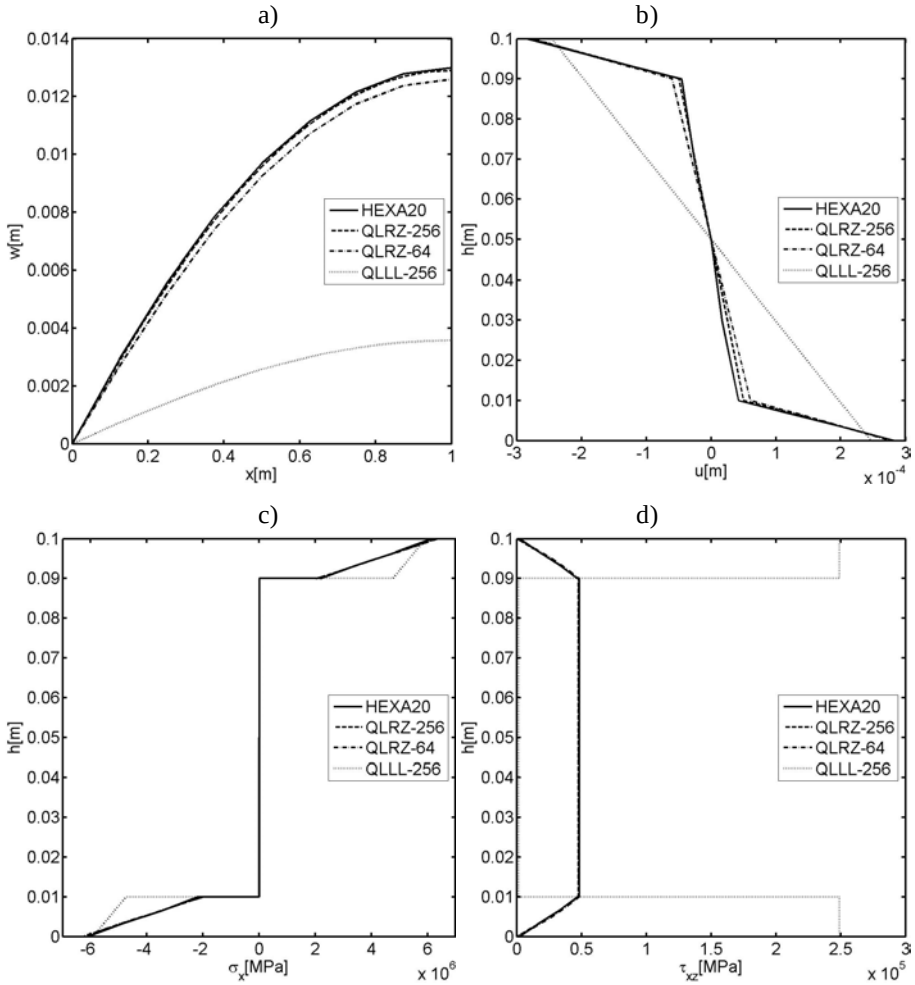

Figure 3.45 – SS square plate under uniformly distributed load. Composite C4. (a) Vertical deflection along central line BC. Thickness distribution of: (b) axial displacement *u* at point B, (c) axial stress σ_x at the center point C, and (d) transverse shear stress τ_{xz} at point E.

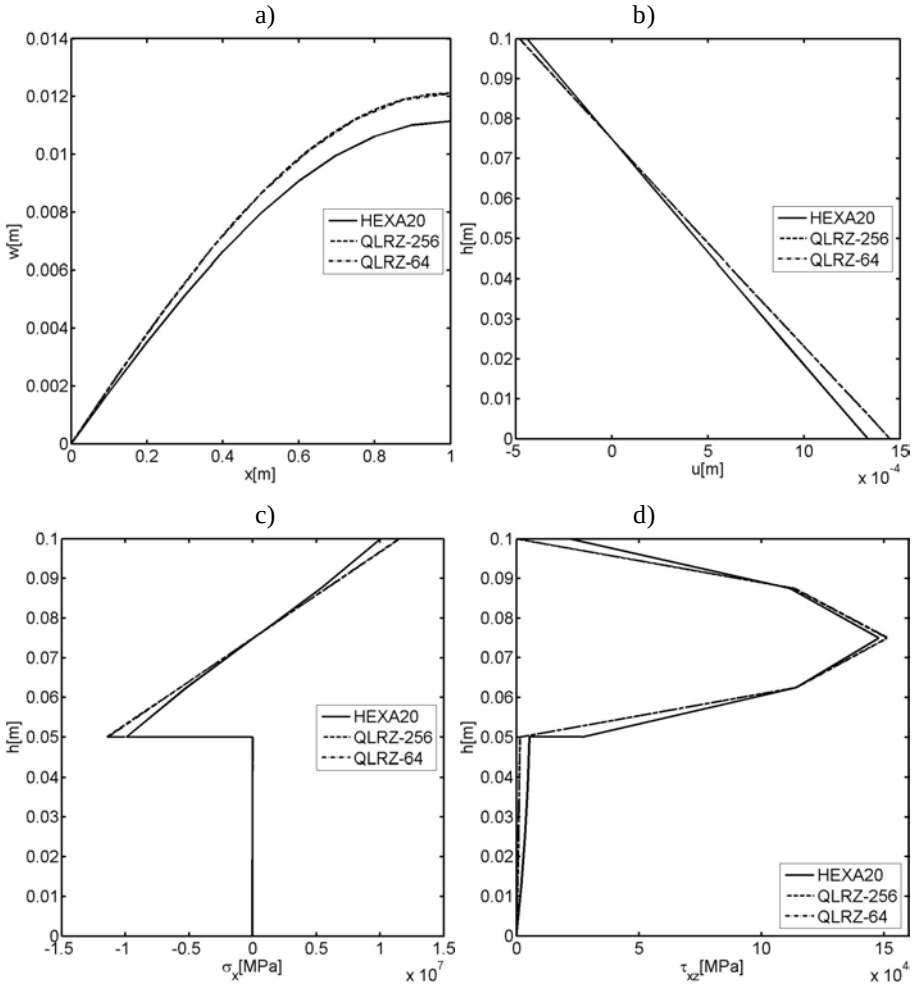

Figure 3.46 – SS square plate under uniformly distributed load. Composite C5. (a) Vertical deflection along central line BC. Thickness distribution of: (b) axial displacement *u* at point B, (c) axial stress σ_x at the center point C, and (d) transverse shear stress τ_{xz} at point E.

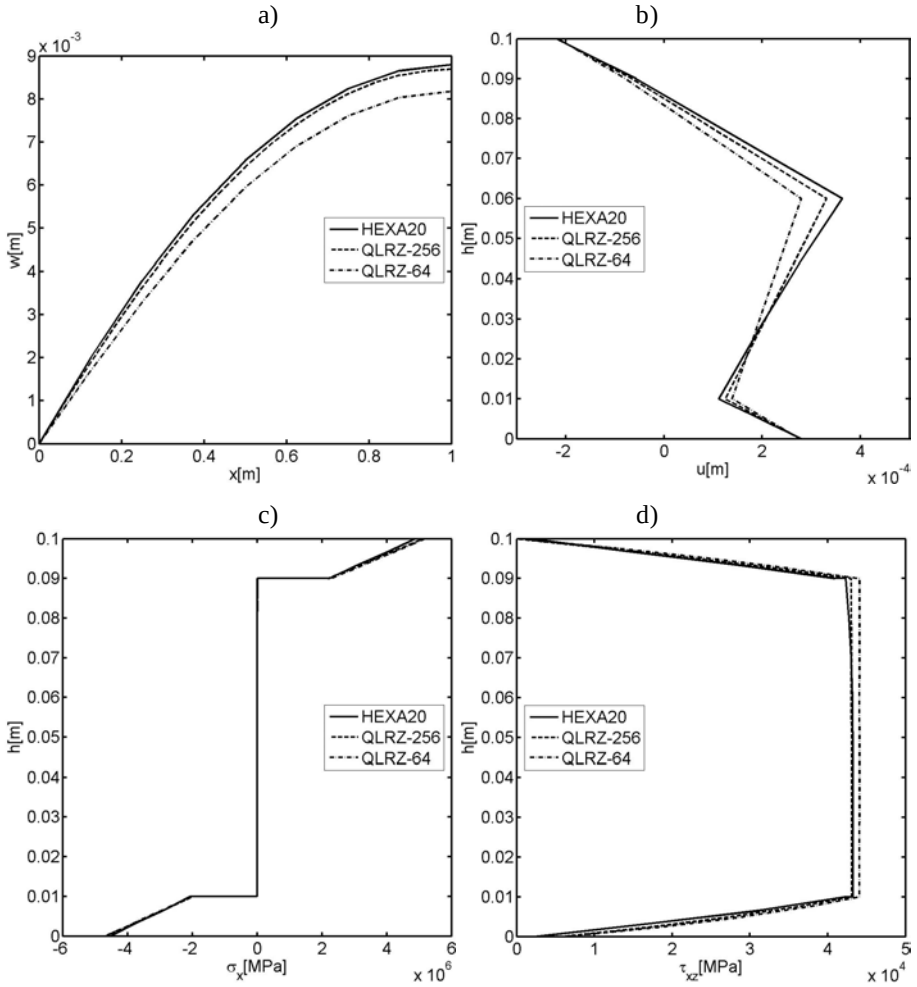

Figure 3.47 – SS square plate under uniformly distributed load. Composite C6. (a) Vertical deflection along central line BC. Thickness distribution of: (b) axial displacement *u* at point B, (c) axial stress σ_x at the center point C, and (d) transverse shear stress τ_{xz} at point E.

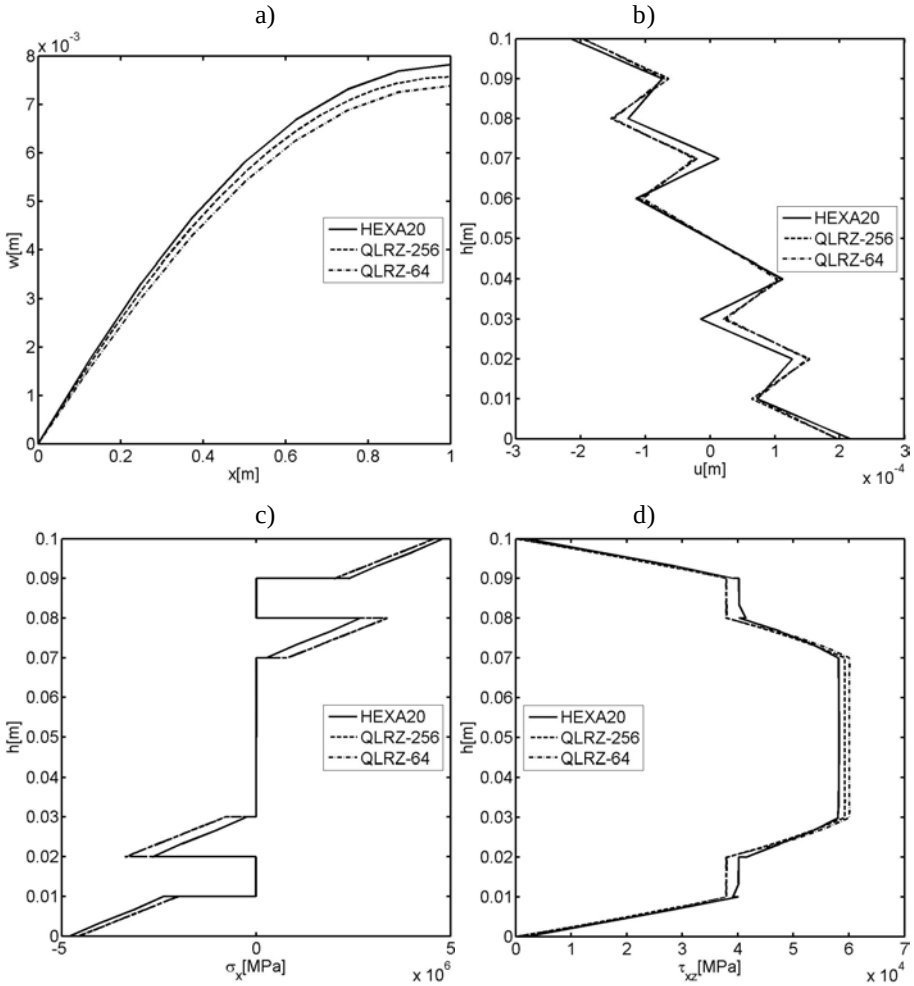

Figure 3.48 – SS square plate under uniformly distributed load. Composite C7. (a) Vertical deflection along central line BC. Thickness distribution of: (b) axial displacement *u* at point B, (c) axial stress σ_x at the center point C, and (d) transverse shear stress τ_{xz} at point E.

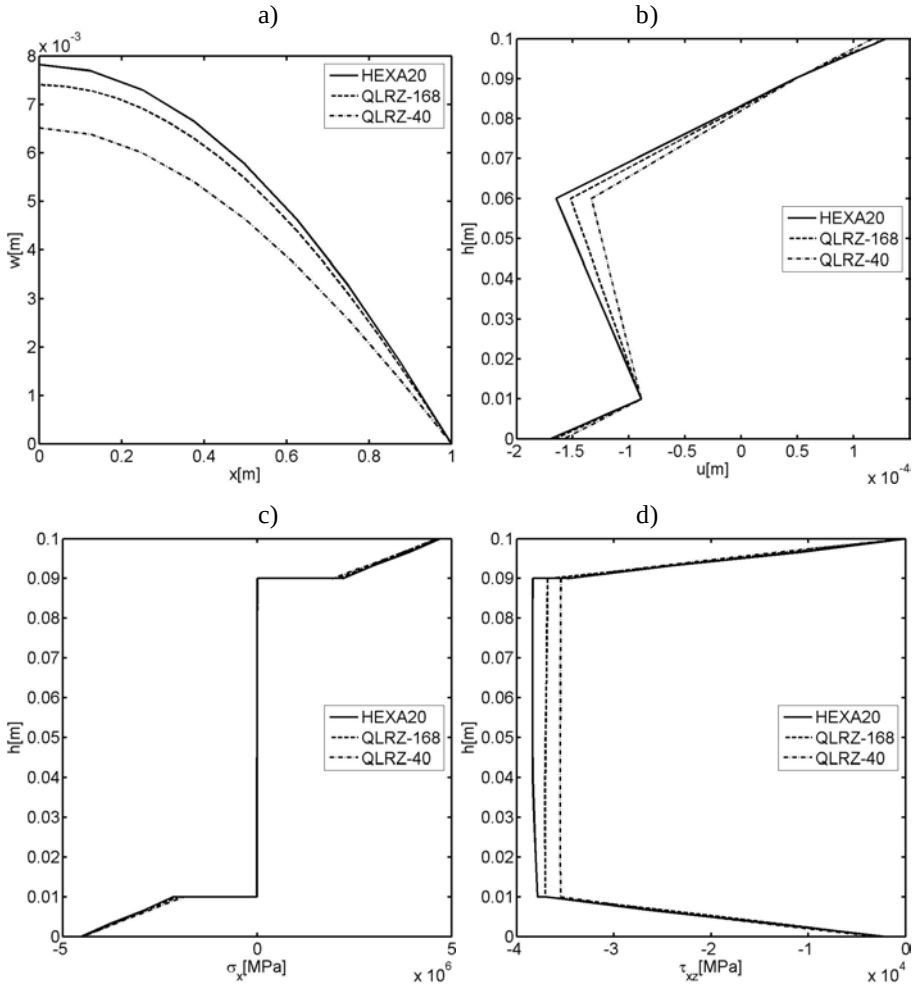

Figure 3.49 – SS circular plate under uniformly distributed load. Composite C6. (a) Vertical deflection along line BC. Thickness distribution of: (b) axial displacement *u* at point D, (c) axial stress σ_x at the center point C, and (d) transverse shear stress τ_{xz} at point D.

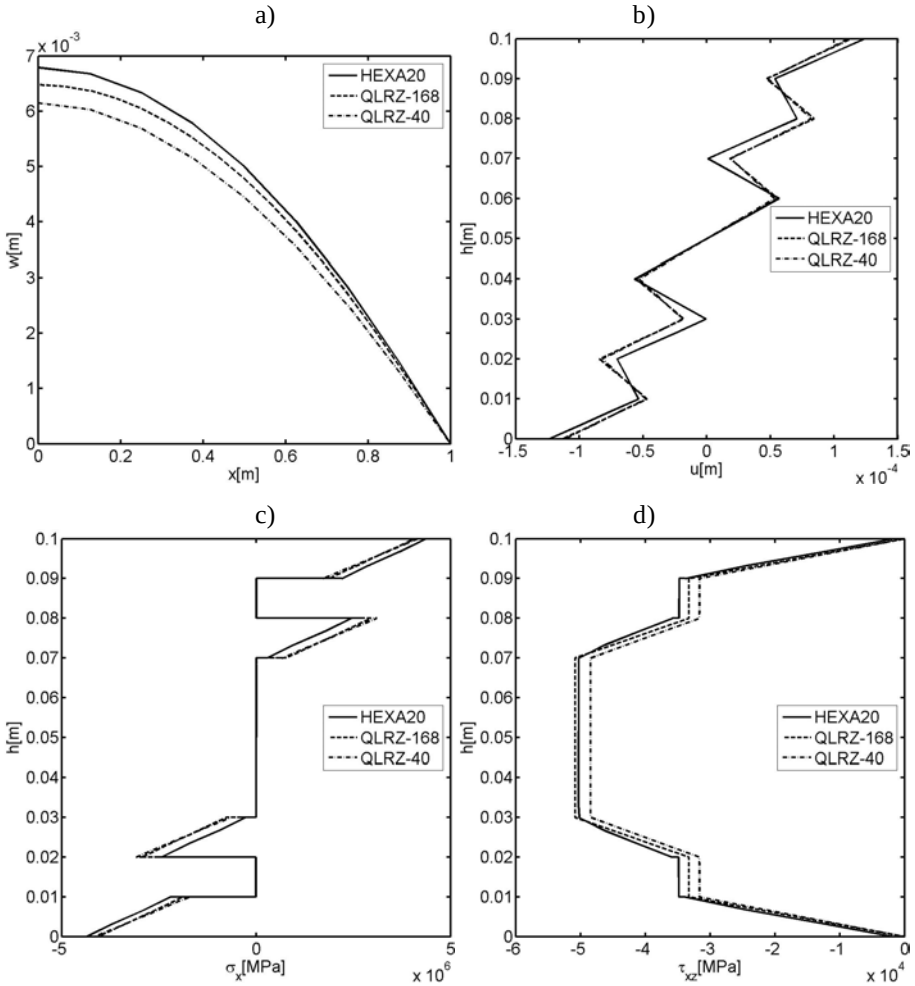

Figure 3.50 – SS circular plate under uniformly distributed load. Composite C7. (a) Vertical deflection along line BC. Thickness distribution of: (b) axial displacement *u* at point D, (c) axial stress σ_x at the center point C, and (d) transverse shear stress τ_{xz} at point D.

4 Numerical model of delamination using the beam LRZ and the plate QLRZ finite elements

A numerical model to simulate mode II/III delamination in advanced composite beams and plates based on the RZT theory is presented in this Chapter.

The method uses the LRZ and QLRZ finite elements for describing the whole laminated material including the resin-rich zone at the interface between plies where delamination occurs. In other words, no additional technique for modeling the delamination paths is required.

Some limitations of the model are discussed below in Section 4.1.

The key attribute of the RZT theory that makes it able to capture relative displacement between layers is that the zigzag function depends on the transverse shear modulus of each layer. This feature allows changing the shape of the zigzag in-plane displacement by modifying the shear properties of plies. With this in mind, the relative displacement between neighboring layers can be modeled by simply discretizing the resin-rich interface zone between them (Figure 2.6) with an additional thin enough ply and then considerately reduce its shear modulus in comparison with those of neighboring layers. It is important to note that no additional kinematics variables are introduced in the model by incorporating these interface plies.

The additional layers, which describe the delamination path, are also named as cohesive layers (cl) henceforth. Moreover, layers that make up the laminate are named as material layers (ml).

The resin-rich zone at the interface is considered as an isotropic material. Therefore, the mechanical behavior of “cl” layers is controlled by an isotropic damage model which is developed below in Section 4.2. Note that delamination process is described by the intra-laminar damage of the “cl” ply.

Intra-laminar failure mechanisms within “ml” layers are not considered. The mechanical behavior of these layers is considered as linear elastic. As a result, delamination cannot migrate through layers but it can propagate parallel to the ply planes within the “cl” layers. Although failure mechanisms of material layers are despised in the present form of the LRZ/QLRZ delamination model, they can be accounted for in the future.

The non-linear problem induced by the degradation process is solved by the modified Newton-Raphson method presented in Section 4.3.

4.1 Kinematics limitations of the LRZ and QLRZ elements for simulation delamination

The most relevant limitations of the LRZ/QLRZ delamination model proceed from the definition of the displacement field and the zigzag function.

Definition of the through-thickness displacement: The model is unable to simulate opening fracture mode (mode I) because the vertical displacement is defined constant along the laminate thickness. Thus, sliding (mode II) and scissoring (mode III) fracture modes can be simulated only. Of course, fracture mode III is not accounted for in beams since the transversal in-plane displacement is not considered (Eq.(3.6)).

Definition of the zigzag function: After delamination, the laminate is divided into sub-laminates with their own kinematics. According to Section 2.1.4, for a given structural slenderness ratio, if the transverse anisotropy of the resultant sub-laminates is enough high, the in-plane displacement may describe a zigzag form, as shown in Figure 4.1b.

Zigzag patterns of in-plane displacement within sub-laminates after delamination cannot be captured by the present model because of the zigzag function definition. The reasons are deducted immediately below. For simplicity, no distinction between orthogonal directions (x,y) is considered.

The zigzag function is computed by Eq.(2.10) as

$$\phi^k = \bar{\phi}^{k-1} + \frac{h^k \beta^k}{2}\left(\zeta^k + 1\right)$$

where the slope of ϕ^k function for the kth layer is computed by Eq.(2.17) as

$$\beta^k = \frac{G}{D_t^k} - 1$$

being D_t^k and G the transverse shear stiffness of the *k*th layer and the average transverse shear stiffness properties of the laminate, respectively. G is defined by Eq.(2.18) as

$$G = h\left[\sum_{k=1}^{N} \frac{h^k}{D_t^k}\right]^{-1}$$

In order to capture relative in-plane displacement between plies with the LRZ/QLRZ delamination model, the zigzag function must be updated by reducing the shear modulus of the damaged cohesive layer, as demonstrated below in Section 4.4. Thus, when the transverse shear properties of a damaged layer *d* are reduced almost to zero, i.e. $D^d \rightarrow 0$, G tends to zero. As a result, the slope of the zigzag function for all undamaged layers is approximately equal to the negative unit value, i.e. $\beta^k \simeq -1$, whereas the slope for the damaged layer is defined positive by $\beta^d \simeq h / h^d - 1$. Therefore, the zigzag function is defined by a piecewise linear function, where its slope changes at the damaged ply only, as schematized in Figure 4.2a. Thus, the in-plane displacement of the sub-laminates can be represented by a linear distribution only (Figure 4.2b) because similar slopes are computed for all undamaged layers.

According to Section 2.1.4 and what has been previously stated, delamination in multilayered structures having low span-to-thickness ratio and high transverse anisotropy cannot be correctly simulated with the present model.

However, that is not the case of advanced composite materials where the shear modulus does not differ generally in more than one order of magnitude between layers [113]. Moreover, laminated structures of composite materials are generally characterized by high slenderness ratios.

Furthermore, delamination in three-layered laminates can be modeled with independence of the level of transverse anisotropy and the slenderness of the structures[20] because the in-plane displacement within each sub-laminate presents a linear distribution. For these materials, sub-laminates consist of at most two layers where the linear kinematics is governed by the stiffer ply only.

Because of this, skin-core delamination in sandwich materials can be also modeled with the LRZ/QLRZ delamination model, as shown in Section 4.6.1.

[20] In order to avoid tall beams/plates, the span-to-thickness ratio has to be at least 5.

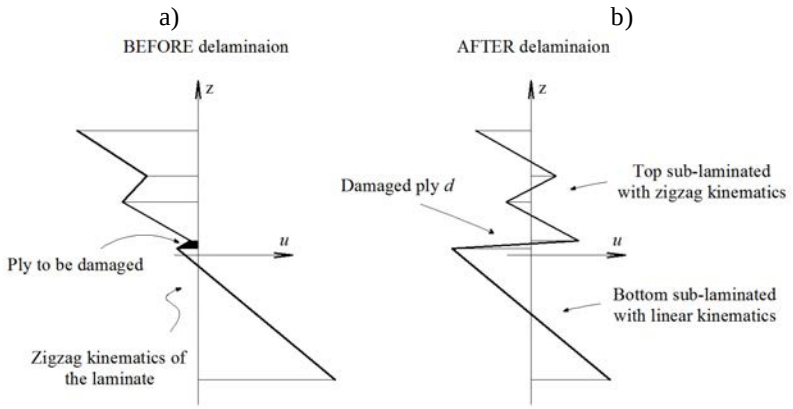

Figure 4.1 – In-plane displacement before a) and after b) delamination.

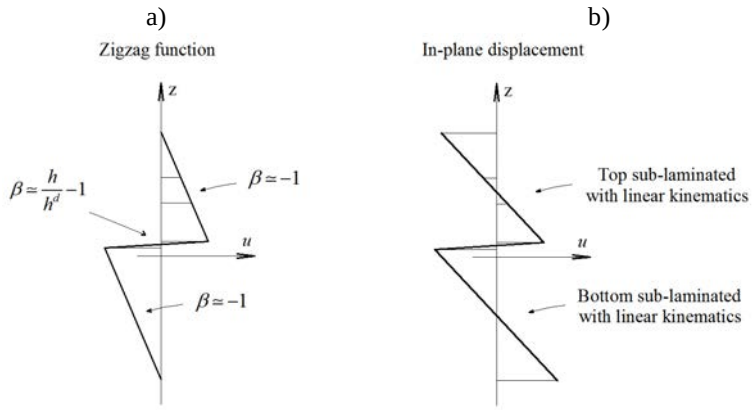

Figure 4.2 – Zigzag function a) and RZT in-plane displacement b) after delamination.

4.2 Isotropic damage model

The mechanical behavior of the cohesive layer is described by the isotropic damage model detailed below.

Among different continuum damage models such as those found in Ref. [114-117], the simple and robust isotropic damage model proposed by Oliver et al. [118] is used to manage the non-linear behavior of the “cl” layers.

The level of damage or degradation is monitored through a single internal scalar variable *d*, which takes values ranged between 0 (no damage) and 1 (full damage). This variable represents the loss of the material stiffness as shown in Figure 4.3a. Physically, the degradation process is characterized by the presence and the growth of micro-cracks and -cavities within the solid which leads to a reduction of the

effective area of load transfer. Thus, the real stresses vector $\boldsymbol{\sigma}$ of any isotropic layer is transformed to an effective one $\boldsymbol{\sigma}_0$ as

$$\boldsymbol{\sigma}_0 = \frac{\boldsymbol{\sigma}}{\left(1-d\right)} \tag{4.1}$$

where d measures the degradation level of the isotropic layer in all direction.

From Eq.(4.1), the real stresses vector is defines as

$$\boldsymbol{\sigma} = \left(1-d\right)\boldsymbol{\sigma}_0 = \left(1-d\right)\mathbf{D}_0\boldsymbol{\varepsilon} \tag{4.2}$$

where $\boldsymbol{\varepsilon}$ is the strain vector and $\mathbf{D}_0$ is the undamaged isotropic constitutive matrix which can be easily obtained from Eq.(3.10) and Eq.(3.48) for beams and plates, respectively.

In order to distinguish between a damage state and an undamaged one, it is necessary to define a damage criterion which is formulated here in the undamaged stress space as

$$F\left(\boldsymbol{\sigma}_0, d\right) = f\left(\boldsymbol{\sigma}_0\right) - c\left(d\right) \leq 0 \tag{4.3}$$

where f is a norm used to compare different states of deformation and c is the damage threshold. Note that f depends on the effective stresses whereas c is a function of the damage variable. Damage occurs when the value of f is larger than c. Damage starts for $f > c_0$, being c_0 the initial damage threshold value, which depends on the material properties, defined as

$$c_0 = \frac{f_t}{\sqrt{E_0}} \tag{4.4}$$

where f_t is the tensile strength and E_0 the Young modulus of the undamaged isotropic material.

The norm f adopted in this work is defined as

$$f = \sqrt{\boldsymbol{\varepsilon} : \boldsymbol{\sigma}_0} \tag{4.5}$$

For convenience, a fully equivalent expression for Eq.(4.3) is defined as

$$\overline{F} = \Theta\left(f\right) - \Theta\left(c\right) \leq 0 \tag{4.6}$$

where $\Theta\left(\cdot\right)$ is a suitable monotonic scalar function.

The evolution laws for the damage variable d and the damage threshold c are expressed as

$$\begin{aligned} \dot{c} &= \dot{\mu} \\ \dot{d} &= \dot{\mu}\frac{\partial \bar{F}}{\partial f} = \frac{\partial \Theta(f)}{\partial f} \end{aligned} \qquad 4.7$$

where μ is a damage consistency parameter which is used to define loading and unloading/reloading (Figure 4.3a) conditions according to the Kuhn-Tucker conditions

$$\dot{\mu} \geq 0 \quad ; \quad \bar{F} \leq 0 \quad ; \quad \dot{\mu}\bar{F} = 0 \qquad 4.8$$

From Eq.(4.7), the evolution of variables d and c is obtained via integrating [119] as

$$\begin{aligned} d &= \Theta(f) \\ c &= \max\{c_0 \,;\, \max\{f\}\} \end{aligned} \qquad 4.9$$

In this work an exponential evolution law is adopted for $\Theta(f)$ (Figure 4.3b) as

$$\Theta(f) = 1 - \frac{c_0}{f} e^{B\left(1-\frac{f}{c_0}\right)} \qquad 4.10$$

Considering the norm of Eq.(4.5), the exponential softening of Eq.(4.10), and the initial damage threshold value c_0 (Eq.(4.4)), the parameter B is computed as

$$B = \left(\frac{G_f \cdot E_0}{l^* \cdot (f_t)^2} - \frac{1}{2} \right)^{-1} \geq 0 \qquad 4.11$$

being G_f the fracture energy per unit area and l^* a characteristic length, which is here defined as the influence length of each Gauss point for LRZ element and is equal to the square root of the influence area of each Gauss point for QLRZ element.

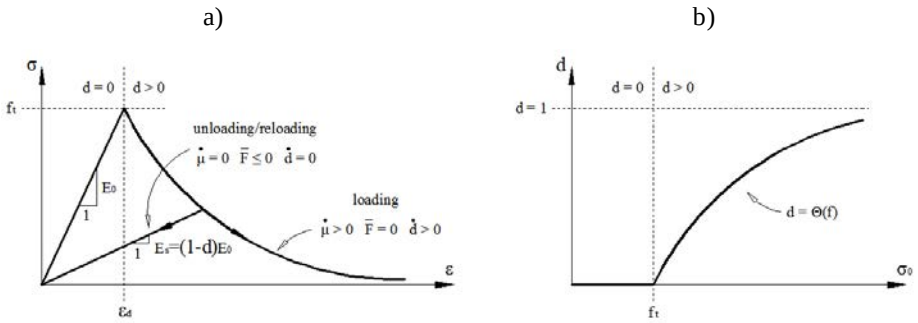

Figure 4.3 – Uniaxial stress-strain curve with softening (a) and exponential damage variable evolution (b).

4.3 Non-lineal problem solution: modified Newton-Raphson method

During a material degradation process, the structure stiffness suffers changes that induce a non-linear response of the structure. The resulting non-linear set of equilibrium equations can be written as

$$\mathbf{F}^{\text{ext}} - \mathbf{F}^{\text{int}}\left(\mathbf{q}\right) = \mathbf{R}\left(\mathbf{q}\right) = 0 \qquad 4.12$$

where $\mathbf{q}$, $\mathbf{F}^{\text{ext}}$ and $\mathbf{F}^{\text{int}}\left(\mathbf{q}\right)$ are the discretization parameters, the external and the internal forces vectors, respectively. $\mathbf{R}\left(\mathbf{q}\right)$ is the residual forces vector. Note, dynamic forces are not considered.

The solution of Eq.(4.12) is achieved by using an incremental-iterative method employing sufficiently small increment from a known solution. Thus, the non-lineal problems is formulated as the solution of

$${}_{n}\mathbf{F}^{\text{ext}} - \mathbf{F}^{\text{int}}\left({}_{n}\mathbf{q}\right) = \mathbf{R}\left({}_{n}\mathbf{q}\right) = 0 \qquad 4.13$$

for the *n*th increment and from the last known solution

$$\mathbf{q} = {}_{n-1}\mathbf{q} \quad ; \quad \mathbf{F}^{\text{ext}} = {}_{n-1}\mathbf{F}^{\text{ext}} \quad ; \quad {}_{n-1}\mathbf{R} = 0 \qquad 4.14$$

The well-known iterative Newton-Raphson method proposes a linear approximation of Eq.(4.13) via the truncated Taylor series as

$${}^{i}_{n}\mathbf{R} \approx {}^{i-1}_{n}\mathbf{R} + {}^{i-1}_{n}\left(\frac{\partial \mathbf{R}}{\partial \mathbf{q}}\right) {}^{i}d\mathbf{q} = 0 \qquad 4.15$$

where $d\mathbf{q}$ is the increment of the nodal DOF at *i*th iteration.

From Eq.(4.13)

$${}^{i-1}_{n}\left(\frac{\partial \mathbf{R}}{\partial \mathbf{q}}\right) = -{}^{i-1}_{n}\left(\frac{\partial \mathbf{F}^{\text{int}}}{\partial \mathbf{q}}\right) = -{}^{i-1}\mathbf{K}_{\text{T}} \qquad 4.16$$

where $\mathbf{K}_{\text{T}}$ is the tangent stiffness matrix at *i*-1th iteration.

Substituting Eq.(4.16) into Eq.(4.15) gives

$${}^{i-1}_{n}\mathbf{R} = {}^{i-1}\mathbf{K}_{\text{T}}\, {}^{i}d\mathbf{q} \qquad 4.17$$

or

$${}^{i}d\mathbf{q} = \left({}^{i-1}\mathbf{K}_{\text{T}}\right)^{-1} {}^{i-1}_{n}\mathbf{R} \qquad 4.18$$

Finally, the solution is found by updating the nodal DOF $\mathbf{q}$ as

$$ {}^{i}_{n}\mathbf{q} = {}^{i-1}_{n}\mathbf{q} + {}^{i}d\mathbf{q} \tag{4.19} $$

or

$$ {}^{i}_{n}\mathbf{q} = {}_{n-1}\mathbf{q} + {}^{i}\Delta\mathbf{q} \tag{4.20} $$

with

$$ {}^{i}\Delta\mathbf{q} = \sum_{m=1}^{i} {}^{m}d\mathbf{q} \tag{4.21} $$

The process is repeated until the convergence criterion $\left\|\mathbf{R}\right\| \leq \varsigma \left\|\mathbf{F}^{\text{ext}}\right\|$ is satisfied being ς a predefined error tolerance [120].

In this work a modification of the Newton-Raphson method is used, where the tangent stiffness matrix $\mathbf{K}_{\text{T}}$ is approximated by

$$ {}^{i-1}\mathbf{K}_{\text{T}} \approx {}^{i-1}\mathbf{K}_{\text{d}} \tag{4.22} $$

where $\mathbf{K}_{\text{d}}$ is the damaged stiffness matrix defined as

$$ {}^{i-1}\mathbf{K}_{\text{d}} = \int_{\omega} \mathbf{B}^{T}\, {}^{i-1}\overset{\cdots}{\mathbf{D}}_{\text{d}}\mathbf{B}\ \text{d}\omega \tag{4.23} $$

with

$$ {}^{i-1}\overset{\cdots}{\mathbf{D}}_{\text{d}} = \int_{\zeta} \left[{}^{i-1}\mathbf{S}^{k}_{\text{d}} \right]^{T}\, {}^{i-1}\mathbf{D}^{k}_{\text{d}}\ {}^{i-1}\mathbf{S}^{k}_{\text{d}} \text{d}\zeta \tag{4.24} $$

being ${}^{i-1}\mathbf{D}^{k}_{\text{d}}$ and $\ddot{\mathbf{D}}_{\text{d}}$ the damaged constitutive matrix for the *k*th layer computed by Eqs.(3.10, 3.48) and the damaged generalized constitutive matrix of the whole laminate defined by Eqs.(3.13, 3.60), respectively. The integration domains ω and ζ depend on the finite element employed.

Note, the subscript d indicates damaged quantities which are computed by reducing the mechanical properties of those layers where damage occurs. In order to capture delamination, the zigzag function has to be updated. Thus, the matrix ${}^{i-1}\mathbf{S}^{k}_{\text{d}}$ is set as a damaged quantity since it contains the zigzag function.

Furthermore, the solution at the first iteration of a new *n*th step has to be calculated by means of the damaged stiffness matrix $\mathbf{K}_{\text{d}}$ computed at the last iteration of the previous *n*-1th step.

Figure 4.4 schematizes the original and the modified Newton-Raphson method.

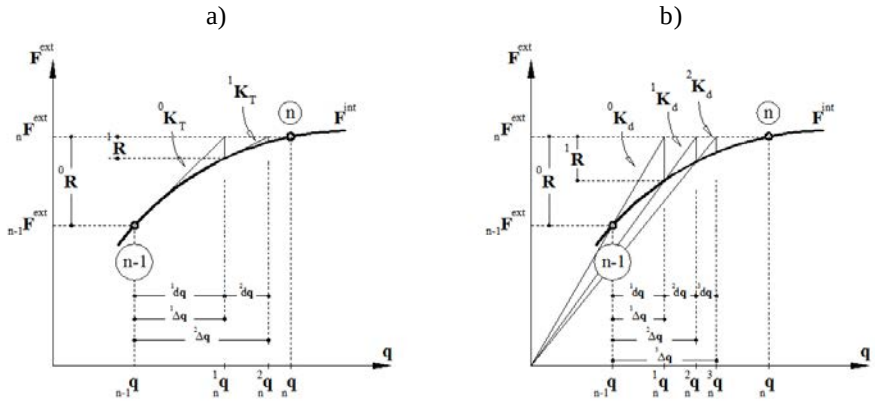

Figure 4.4 – Original (a) and modified (b) Newton-Raphson method.

4.4 Update of the zigzag function to simulate delamination

In order to capture relative displacements between layers, a technique based on updating the zigzag function during the degradation process of the "cl" plies is employed by the LRZ/QLRZ delamination model. The basics of this strategy are explained below.

In 3D finite element analyses, the nodal internal forces are obtained by integrating stresses over the finite elements volume. When a finite element suffers from softening because the damage threshold is reached, stresses within that damaged element are reduced. As a result, a lack of equilibrium between the internal forces of the damaged element and the neighboring elements happens, which induces nodal residual forces. These forces generate the relative displacement between layers that typically occurs during a delamination process. Then, equilibrium is achieved with an iterative process such as that of Section 4.3. This process is schematized in Figure 4.5a.

The kinematic variables (Eq.(2.3)) and stress resultants (Eqs.(3.11),(3.58)) of the LRZ/QLRZ finite elements are computed at the in-plane middle surface of the element ($z = 0$). Because of this, there are no forces within the laminate able to induce relative displacements between plies. Consequently, the LRZ/QLRZ elements are unable to provoke any change on the zigzag shape of the in-plane displacement by reducing stresses only.

In case stresses are reduced only, a variation of the amplitude of the previous displacement field is obtained, instead of capturing a delaminated kinematics. That is because the LRZ/QLRZ kinematics variables are not able to modify by

themselves the shape of the zigzag displacement, but they can vary the amplitude only. This is outlined in Figure 4.5b – Without ϕ update.

The kinematics of the RZT theory is defined by a superposition of a linear piecewise zigzag function over the linear FSDT displacement fields (Figure 2.2). As a result, the zigzag shape of the in-plane displacement is governed by the zigzag function ϕ only. Comprehensibly, in order to modify the zigzag form of the RZT in-plane displacement, the zigzag function must be updated according with the delamination process. Taking into account that the zigzag function depends on the transverse shear stiffness of each layer, the update of this function by reducing the shear properties of the damaged layer is a natural manner for provoking changes in the zigzag pattern of the in-plane displacement.

Taking into account that only "cl" plies are able to suffer damage in the LRZ/QLRZ delamination model and the degradation level is measured by the damage variable *d*, the update of the zigzag function is proposed by reducing the initial elastic shear moduli G_0^{cl} of the damaged cohesive layers "cl" as

$$G_d^{cl} = \left(1 - d^{cl}\right) G_0^{cl} \tag{4.25}$$

which leads to the definition of the average transverse shear stiffness G_{iz} as

$$\begin{bmatrix} G_{xz} \\ G_{yz} \end{bmatrix} = \begin{bmatrix} h\left[\sum_{ml=1}^{Nml} \frac{h^{ml}}{D_{t11}^{ml}} + \sum_{cl=1}^{Ncl} \frac{h^{cl}}{G_d^{cl}}\right]^{-1} \\ h\left[\sum_{ml=1}^{Nml} \frac{h^{ml}}{D_{t22}^{ml}} + \sum_{cl=1}^{Ncl} \frac{h^{cl}}{G_d^{cl}}\right]^{-1} \end{bmatrix} \tag{4.26}$$

where *Nml* and *Ncl* denote the number of material and cohesive layers, respectively. The slope of zigzag function for the material layer "ml" and the cohesive layer "cl" are computed by

$$\begin{bmatrix} \beta_x \\ \beta_y \end{bmatrix}^{ml} = \begin{bmatrix} \frac{G_{xz}}{D_{t11}^{ml}} - 1 \\ \frac{G_{yz}}{D_{t22}^{ml}} - 1 \end{bmatrix} \quad ; \quad \begin{bmatrix} \beta_x \\ \beta_y \end{bmatrix}^{cl} = \begin{bmatrix} \frac{G_{xz}}{G_d^{cl}} - 1 \\ \frac{G_{yz}}{G_d^{cl}} - 1 \end{bmatrix} \tag{4.27}$$

This simple update procedure of the zigzag function allows the method to capture the relative displacement between layers.

Figure 4.5 schematizes all mentioned above. The implicit algorithm proposed to compute delamination with the LRZ/QLRZ model is shown in Figure 4.6.

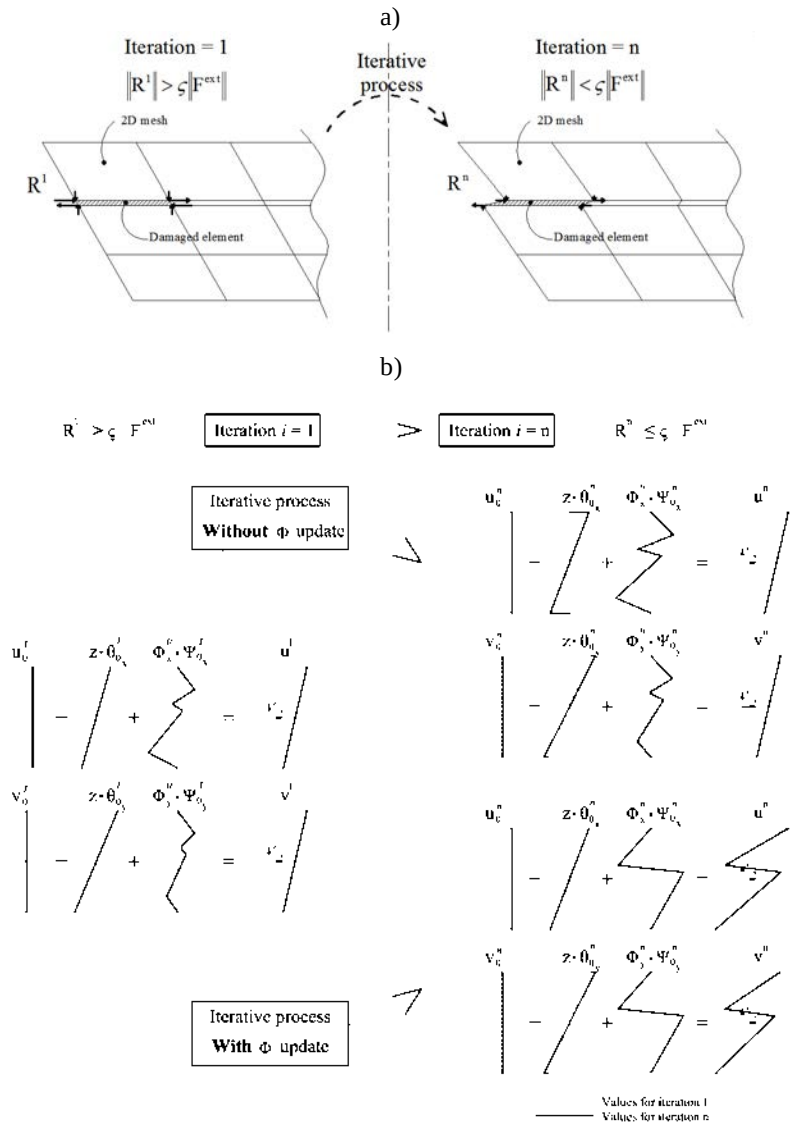

Figure 4.5 - The delaminated displacement field is achieved by the residual forces (R) in a plane stress analysis (PS) (a). Delaminación can be captured with the LRZ/QLRZ finite element when the zigzag function ϕ is updated by reducing the shear modulus of the damaged layer (b).

Loop over load increments

Update external forces $\mathbf{F}^{\text{ext}}$

Iterative process

If *i*th iteration = 1

$$^{1}\mathbf{a} = \mathbf{K}_{\text{d}}^{-1} \cdot \mathbf{F}^{\text{ext}}$$

$$^{1}\boldsymbol{\varepsilon}^{k} = \mathbf{S}_{d}^{k}\ \mathbf{B}\ ^{1}\mathbf{a}$$

Note that for the first iteration $\mathbf{K}_{\text{d}}^{-1}$ and $\mathbf{S}_{d}^{k}$ are computed at the last iteration of the previous load increment.

Else

$$^{i}d\mathbf{a} = {}^{i-1}\mathbf{K}_{\text{d}} \cdot {}^{i-1}\mathbf{R}$$

$$^{i}\mathbf{a} = {}^{i-1}\mathbf{a} + {}^{i}d\mathbf{a}$$

$$^{i}\boldsymbol{\varepsilon}^{k} = {}^{i-1}\mathbf{S}_{d}^{k}\ \mathbf{B}\ ^{i}\mathbf{a}$$

Remember that $^{i-1}\mathbf{S}_{d}^{k}$ contains the updated ϕ function of the *i-1*th iteration. As a consequence, the strain field $^{i}\boldsymbol{\varepsilon}^{k}$ corresponds to the delaminated kinematics.

End if

Evaluate undamaged stresses:

$$^{i}\boldsymbol{\sigma}^{k} = \mathbf{D}_{0}^{k} \cdot {}^{i}\boldsymbol{\varepsilon}^{k}$$

Damage evaluation in cohesive layers:

Compute damage variable:

$$^{i}d^{cl} = 1 - \frac{c_0}{{}^{i}f} e^{B\left(1-\frac{{}^{i}f}{c_0}\right)} \qquad \text{with} \qquad {}^{i}f = \sqrt{{}^{i}\boldsymbol{\varepsilon}^{cl} : {}^{i}\boldsymbol{\sigma}_{0}^{cl}}$$

Correct stresses and shear moduli:

$$^{i}\boldsymbol{\sigma}^{cl} = \left(1 - {}^{i}d^{cl}\right) {}^{i}\boldsymbol{\sigma}_{0}^{cl} \quad ; \quad {}^{i}G_{d}^{cl} = \left(1 - {}^{i}d^{cl}\right) {}^{i}G_{0}^{cl}$$

Update zigzag function:

Compute average transverse shear stiffness:

$$^{i}\begin{bmatrix} G_{xz} \\ G_{yz} \end{bmatrix} = \begin{bmatrix} h\left[\sum_{ml=1}^{Nml} \frac{h^{ml}}{D_{t11}^{ml}} + \sum_{cl=1}^{Ncl} \frac{h^{cl}}{{}^{i}G_{d}^{cl}}\right]^{-1} \\ h\left[\sum_{ml=1}^{Nml} \frac{h^{ml}}{D_{t22}^{ml}} + \sum_{cl=1}^{Ncl} \frac{h^{cl}}{{}^{i}G_{d}^{cl}}\right]^{-1} \end{bmatrix}$$

Figure 4.6 - Algorithm for solving the non-linear problem by means of the modified Newton-Raphson. Note that the zigzag function is updated at each iteration. Figure continued on the page.

Compute zigzag slope:

$$ {}^{i}\begin{bmatrix}\beta_x\\ \beta_y\end{bmatrix}^{ml} = \begin{bmatrix}\dfrac{{}^{i}G_{xz}}{D_{t11}^{ml}} - 1\\ \dfrac{{}^{i}G_{yz}}{D_{t22}^{ml}} - 1\end{bmatrix} \quad \text{for materials layers "}ml\text{"} $$

$$ {}^{i}\begin{bmatrix}\beta_x\\ \beta_y\end{bmatrix}^{cl} = \begin{bmatrix}\dfrac{{}^{i}G_{xz}}{{}^{i}G_{d}^{cl}} - 1\\ \dfrac{{}^{i}G_{yz}}{{}^{i}G_{d}^{cl}} - 1\end{bmatrix} \quad \text{for cohesive layers "}cl\text{"} $$

Compute zigzag function:

$$ {}^{i}\phi_x^k = \overline{\phi}_x^{k-1} + \frac{h^k\,{}^{i}\beta_x^k}{2}\left(\zeta^k + 1\right) \quad ; \quad {}^{i}\phi_y^k = \overline{\phi}_y^{k-1} + \frac{h^k\,{}^{i}\beta_y^k}{2}\left(\zeta^k + 1\right) $$

Computation of the damaged stiffness matrix and internal forces:

$$ {}^{i}\mathbf{K}_{\mathrm{d}} = \int_A \mathbf{B}^T\,{}^{i}\hat{\mathbf{D}}_{\mathrm{d}}\,\mathbf{B}\,dA $$

$$ {}^{i}\mathbf{F}^{\mathrm{int}} = \int_V \mathbf{B}^T\,{}^{i}\mathbf{S}^T\,{}^{i}\boldsymbol{\sigma}^k\,dV $$

Verification of convergence criteria

$$ \mathbf{F}^{\mathrm{ext}} - {}^{i}\mathbf{F}^{\mathrm{int}} = {}^{i}\mathbf{R} $$

$$ \left\| {}^{i}\mathbf{R} \right\| \le \varsigma \left\| \mathbf{F}^{\mathrm{ext}} \right\| $$

 # END iterative process

 # END loops over load increments

Figure 4.6 - Continuation.

4.5 Multi-delamination modeling with the LRZ/QLRZ delamination model

The simulation of multi-delamination with the LRZ/QLRZ delamination model is investigated in this section.

In the LRZ/QLRZ model, relative displacements are provoked by modifying the shape of the zigzag function using Eqs. (4.25)-(4.27). The alteration of this function is motived by reducing the shear modulus of damaged cohesive layers during degradation process. Note that these equations are written to simulate multi-delamination, i.e. several “cl” plies can be damaged. However, in order to capture

more than one relative displacement with the LRZ/QLRZ delamination model, some cares have to be accounted for when updating the zigzag function.

In order to analyze the potential of the QLRZ/LRZ model for simulating multi-delamination, a sandwich clamped beam with two possible delamination paths is studied.

The beam is subjected to a vertical displacement Δw = 1mm at the free end (Figure 4.7a). The length and thickness of the beam are L = 100mm and h = 20.02mm, respectively. The laminated material consists of two skins (the top and the bottom layers) and a less stiff core between them (the middle ply). The top and bottom delamination paths between skins and core are described by the cohesive layers "cl-1" and "cl-2", respectively (Figure 4.7b). Thickness and mechanical properties of each layer are listed in Table 4.1.

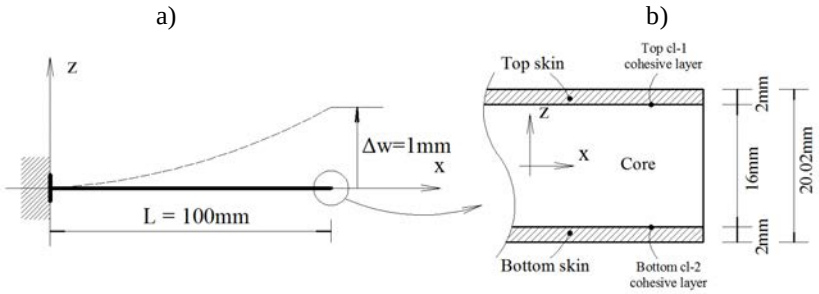

Figure 4.7 - Cantilever beam under vertical displacement a) and sandwich three-layered material b).

Thicknesses and material properties				
	Top Skin	Core	Bottom Skin	Cohesive layers
h [mm]	2	16	2	0.01
E [MPa]	$2.19\text{x}10^5$	$7.30\text{x}10^2$	$7.3\text{x}10^5$	$7.30\text{x}10^2$
G [MPa]	$0.876\text{x}10^5$	$2.90\text{x}10^2$	$2.92\text{x}10^5$	$2.90\text{x}10^2$

Table 4.1 – Layer properties for multi-delamination study.

In this case, the damage of each interface layer is induced by reducing the shear modulus from $G = 2.9\text{x}10^2$ MPa to $G = 2.9\text{x}10^{-8}$ MPa. Note that the reduction of the "cl" shear modulus is applied over the whole beam length.

The reference solution is computed by a plane stress analysis (PS) using a mesh of 3200 4-noded quadrilateral finite elements (Figure 4.8). The beam length is discretized with 100 elements whereas the thicknesses of the skins and core are

described with 3 and 24 finite elements, respectively. Only 1 finite element is required to define the cohesive layers.

Figure 4.8 - Four-noded quadrilateral finite element mesh for the PS analysis.

Figure 4.9 shows the thickness distribution of the axial displacement *u* at the free end for the undamaged beam (a), after first delamination at the top cohesive layer "cl-1" (b) (single-delamination) and after second delamination at the bottom layer "cl-2" (c) (multi-delamination).

Despite the low span-to-thickness ratio and high transverse anisotropy of the beam, results clearly show a great agreement between the LRZ/QLRZ model and the PS analysis. It is appreciated that both, the single- (Figure 4.9b) and the multi-delamination (Figure 4.9c) are well captured.

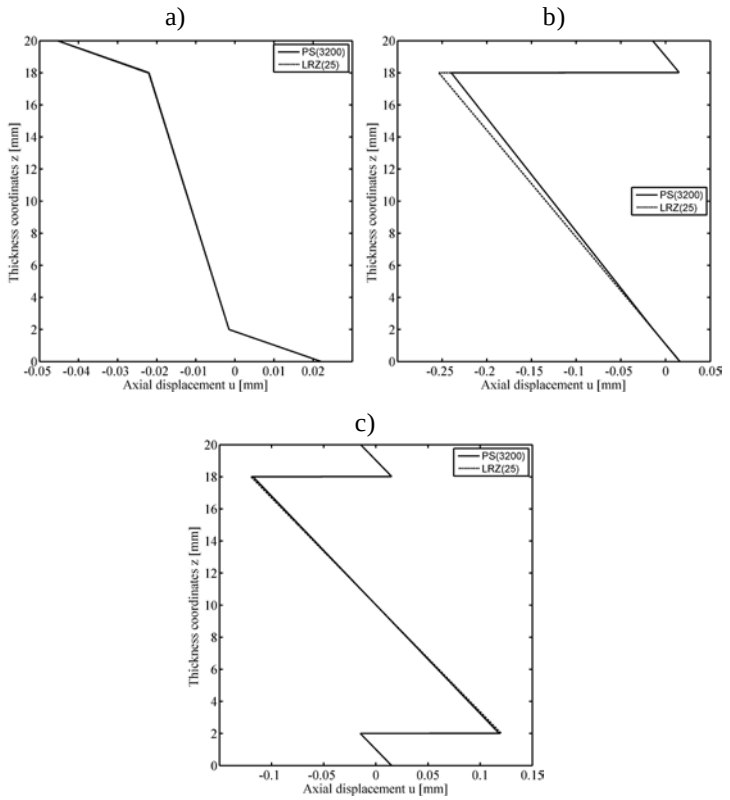

Figure 4.9 - Axial displacement u at the free end for the undamaged beam (a), for single-delamination at the cohesive layer "cl-1" (b) and for multi-delamination (c).

Before to continue analyzing results, it is important to remark that after delamination the slope of the zigzag function (Eq.(4.27)) is controlled by the average transverse shear stiffness of laminate (Eq.(4.26)) which in turn is governed by the smallest damaged shear modulus.

With this in mind, once the top delamination has been occurred, the shape of the zigzag function is controlled by the "cl-1" ply only. After second delamination, however, the zigzag function could be governed by the "cl-1" (if $G^{cl-1} < G^{cl-2}$), the "cl-2" (if $G^{cl-1} > G^{cl-2}$) or both cohesive layers (if $G^{cl-1} \approx G^{cl-2}$).

In consequence, the model was able to capture the second relative displacement at the bottom interface because the shear modulus of the "cl-2" ply have been reduced to the same value as the "cl-1" layer ($G^{cl-2} = G^{cl-1} = 2.9x10^{-8}$ MPa). Otherwise, the model could predict wrong displacement field, as detailed below.

With the aim to clarify the mentioned above, imagine a delamination process where the "cl-1" ply was full damage at the *n*th step by reducing its shear modulus to $G^{cl-1} = 2.9x10^{-8}$ MPa. As a result, the undamaged zigzag function (Figure 4.10a) has to be updated provoking a jump at the top cohesive layer (Figure 4.10b). This update of the zigzag function induces the top single-delamination of Figure 4.9b.

Then, some steps later, the shear modulus of the bottom cohesive layer is also reduced to $2.9x10^{-8}$ MPa ($G^{cl-2} = G^{cl-1}$). Consequently, the zigzag function is updated again leading to two jumps at top and bottom cohesive layers (Figure 4.10c). This new configuration of the zigzag function provokes the multi-delamination showed in Figure 4.9c.

Now, imagine that the shear modulus of the "cl-2" layer is decreased to $2.9x10^{-10}$ MPa instead of be reduced to $2.9x10^{-8}$ MPa, i.e. two orders of magnitude smaller than the shear modulus of the "cl-1" ply previously damaged.

Therefore, the updated zigzag function has only one jump at the bottom interface (Figure 4.11a), instead of having two jumps like in Figure 4.10c. In consequence, a single-delamination path at the cohesive ply "cl-2" is computed neglecting the previous delamination at layer "cl-1", as shown in Figure 4.11b. The reason is that the average transverse shear stiffness of laminate is now governed by the shear modulus of the "cl-2" because of $G^{cl-1} > G^{cl-2}$.

This situation is completely unreal since not only the double-delamination could not be captured, but also the in-plane displacement is modified to a new configuration which does not take into account the relative displacement at ply "cl-1" previously computed.

Thus, in order to maintain previous delamination state, the reduced shear modulus of new damaged cohesive layers must not be smaller than that of the first degraded cohesive layer.

It is important to note that the difference of two orders of magnitude between the damaged shear moduli (arbitrarily chosen for this example) implies a difference of the damage variable *d* between both layers approximately equal to $9.9x10^{-9}$ % only.

In addition, in order to capture new delamination paths, the sensibility of the zigzag function to be modified once first delamination has been occurred has to be studied.

Thus, imagine that the "cl-2" shear modulus is decreased to $2.9x10^{-6}$ MPa instead of $2.9x10^{-8}$ MPa, i.e. two orders of magnitude larger than that of the "cl-1" layer previously damaged. As a result, the update of the zigzag function does not provoke significant changes on its previous delaminated shape (Figure 4.10b), as shown in Figure 4.12a. Therefore, the second delamination path at the "cl-2" ply cannot be captured (Figure 4.12b). The reason is that the average transverse shear stiffness of laminate is still governed by the shear modulus of the "cl-1" because G^{cl-2} is quite larger than G^{cl-1}.

Consequently, although delamination process has begun at bottom interface layer ($G^{cl-2} = 2.9x10^{-6}$), it was not possible to capture the relative displacement at "cl-2" ply.

Note that, for this case, the difference of two orders of magnitude between the shear moduli implies a difference of the damage variable *d* equal to $9.9x10^{-7}$ % only.

Summarizing, in order to predict multi-delamination with the LRZ/QLRZ delamination model, the reduced shear properties of new degraded interfaces must be almost the same as that of the first damaged cohesive layer. This precaution allows the model to capture new relative displacement while maintaining previous delamination states.

In consequence, it is necessary to development an strategy for controlling the degradation process of each cohesive layer at Gauss point level. This topic is proposed as future work. Thus, the model is actually able to simulate single-delamination only.

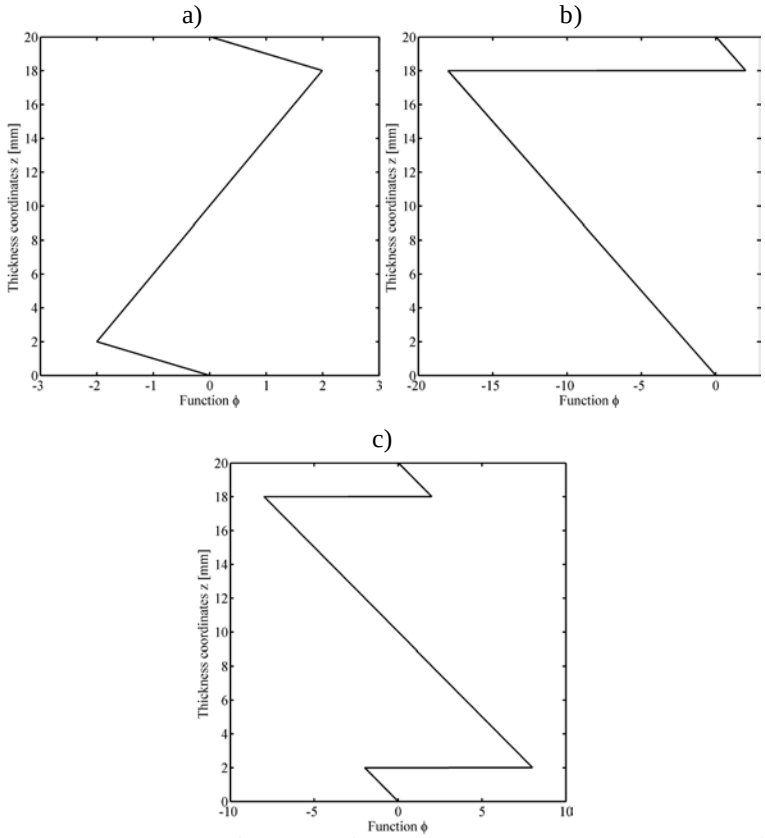

Figure 4.10 – Zigzag function for the undamaged beam (a), for single-delamination at the cohesive layer "cl-1" (b) and for multi-delamination (c).

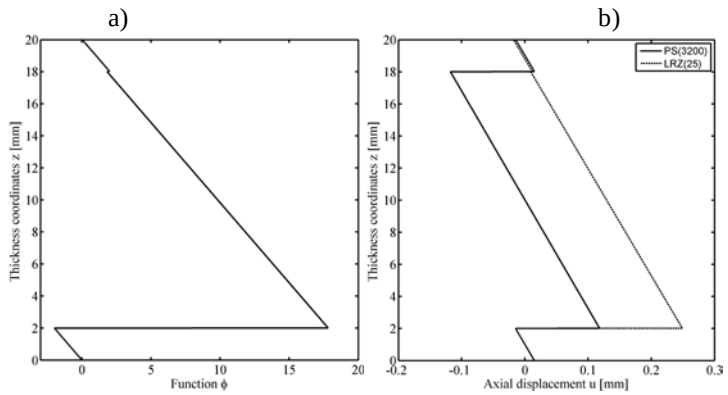

Figure 4.11 - Zigzag function (a) and axial displacement (b) for the case where the damage shear modulus of the bottom cohesive layer is smaller than that of the top damaged cohesive layer.

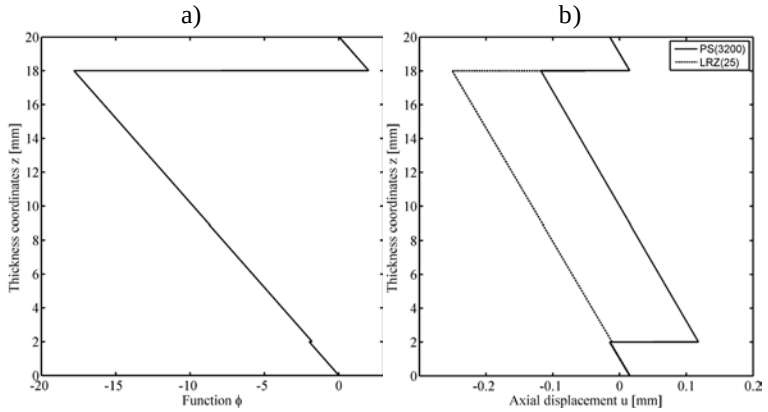

Figure 4.12 - Zigzag function (a) and axial displacement (b) for the case where the damage shear modulus of the bottom cohesive layer is higer than that of the top damaged cohesive layer.

4.6 Numerical examples

The performance of the LRZ/QLRZ delamination model is analyzed in this section. Only single-delamination cases are studied.

Simulations are carried out under the following considerations: quasi-static application of vertical displacement, geometrically linear problem and small deformation.

4.6.1 Delamination in beams

Sandwich clamped beam under vertical displacement

Skin-core delamination at the top interface (cl-1 ply) of the sandwich clamped beam of Section 4.5 is analyzed. The structure is subjected to a vertical displacement Δw = 10mm. Dimension, boundary conditions and layer stacking of the beam are schematized in Figure 4.7. Layer mechanical properties are listed in Table 4.1. Tensile strength and fracture energy of the "cl-1" layer are equal to f_t = 2MPa and G_f=5x10^{4}kN/m, respectively. The LRZ mesh contains 25 elements.

The reference solution is computed by a plane stress analysis (PS) using the mesh of Figure 4.8. The step increment is dw = 0.003mm for both solutions. The tolerance value is $\zeta = 1\text{x}10^{-3}$ for the LRZ analysis and $\zeta = 1\text{x}10^{-2}$ for the PS solution due to difficulties for getting convergence.

Figure 4.13 shows the load-displacement curve. Load P corresponds to the total vertical reaction computed at the clamped support whereas displacement w is the imposed vertical displacement Δw.

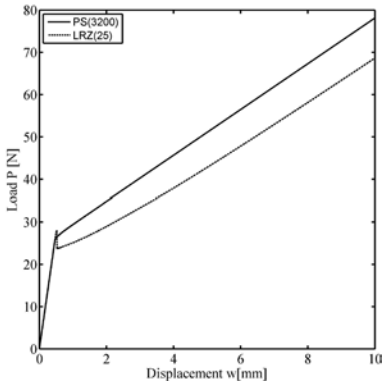

Figure 4.13 - Load vs. displacement curves for single-delamination in sandwich laminated materials.

Although the error at the end of simulation is approximately 12.0%, both, the onset and the growth of delamination are correctly predicted by the LRZ delamination model. Damage starts for Δw = 0.468mm and Δw=0.414mm for the PS and LRZ models, respectively.

After onset delamination, the LRZ solution exhibits a load drop at Δw=0.519mm, which is related to the update of the zigzag function.

At this increment, degradation of the "cl-1" layer is increased from d^{cl} = 0.98 (Δw=0.513mm) to d^{cl} = 0.998, approximately. This relatively small variation (2% approx.) of damage variable induces a significant change of the zigzag function, as shown in Figure 4.14, which provokes the load drop of Figure 4.13.

Figure 4.14a shows the zigzag function obtained with different degradation levels of the top cohesive layer. In other words, the sensibility of zigzag function to the damage variable is shown. It is observed that no major changes on the zigzag function are produced until damage variable d reaches values close to 0.998.

In order to reduce the load drop of Figure 4.13, smaller step increments can be used, as shown in Figure 4.14b. In this figure two LRZ solutions computed using dw=0.003mm (LRZ) and dw=0.00003mm (LRZ_{SI}) are compared.

Results show that immediately after onset delamination, i.e. at Δw = 0.417mm, a very small load drop is computed by the LRZ_{SI} solution when damage variable changes from 0.437 to 0.976 in a few number of finite elements. Although a degradation level of 0.976 does not induce relevant alterations in the zigzag function, it is enough to provoke a small fall.

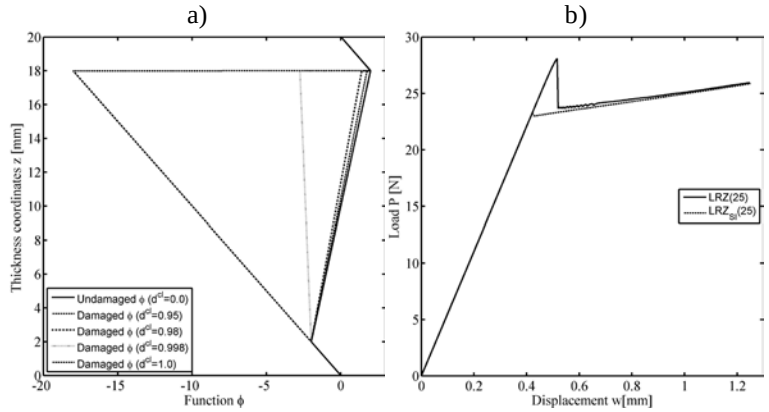

Figure 4.14 - Undamaged and damaged zigzag function (a) and load vs. displacement curves obtained by the LRZ model for two different step increments (b).

Figure 4.15 shows the evolution of the cl-1 damage variable for the LRZ and LRZ_{SI} solutions. The jump of d from 0.437 to 0.976 at Δw =0.417mm and from 0.98 to 0.998 at Δw =0.519mm for the LRZ_{SI} and the LRZ solutions, respectively, can be observed.

This figure also reveals that damage variable evolves faster for LRZ_{SI} than LRZ solution. The reason is that the strains $\boldsymbol{\varepsilon}$ used to calculate the predictor stresses ($\boldsymbol{\sigma} = \mathbf{D}\ \boldsymbol{\varepsilon}$) are computed from the previous delaminated kinematics. Consequently, the greater is the relative displacement at the *n-1*th step the higher is the predictor stresses at the *n*th step.

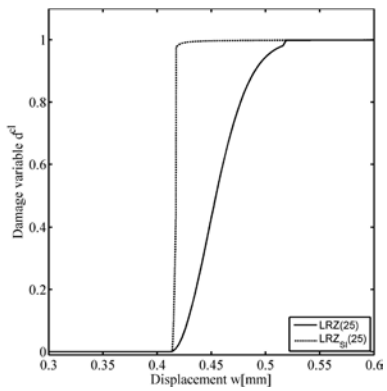

Figure 4.15 – Damage variable d of the "cl-1" ply at the Gauss point of the first finite element from the free end obtained by the LRZ model for two different step increments.

Figure 4.16 shows the thickness distribution of the axial displacement u at the free end for three different steps: before (a) (Δw =0.393mm) and after delamination onset (b) (Δw =2.013mm) and at the end of simulation (c) (Δw=9.993mm).

a) b)

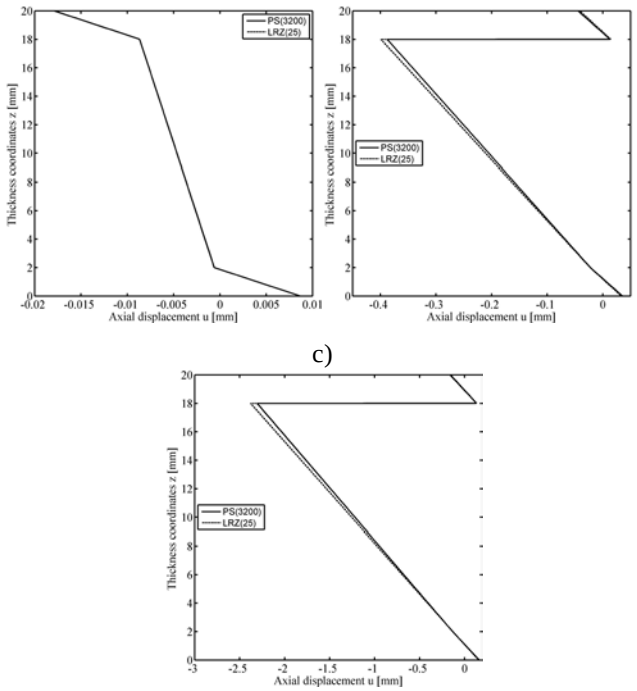

Figure 4.16 - Thickness distribution of the axial displacement *u* at the free end before (a) and after delamination (b) and at the end of simulation (c).

Multilayered clamped beams under vertical displacement

In this example single-delamination in multilayered beams is studied by modeling a beam of length L = 0.5m supported as shown in Figure 4.17. A vertical displacement Δw at the clamped support is imposed. The beam is analyzed for two laminates (L1 and L2) with properties listed in Tables 4.2- 4.4. Location of the cohesive layer for both laminates is shown in Figure 4.18.

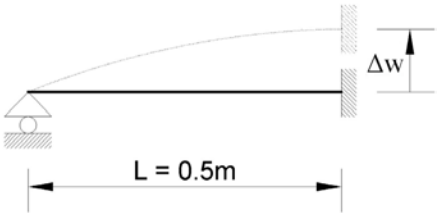

Figure 4.17 - Boundary conditions of the analyzed beam.

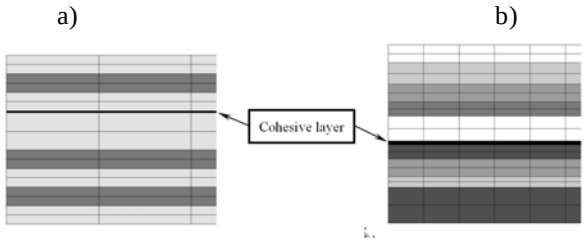

Figure 4.18 - Cohesive layer in laminate L1 a), and laminate L2 b).

Mechanical properties of *linear-elastic* plies [MPa]

Material	Young's Modulus (E_0)	Shear Modulus (G_0)
A	157.9×10^5	5.93×10^5
B	104.0×10^2	40.0×10^2
C	5.3×10^2	2.12×10^2
D	2.19×10^2	0.876×10^2
E	0.82×10^2	0.328×10^2
F	0.73	0.29
G	7.3×10^2	2.92×10^2

Table 4.2 - Mechanical properties of linear-elastic layers.

Mechanical properties of *cohesive* plies (cl)

Material	E_0 [MPa]	G_0 [MPa]	Tensile Strength (f_t) [MPa]	Fracture Energy (G_f) [kN/m]	
				Ductile ($G_f^{\,D}$)	Fragile ($G_f^{\,F}$)
H^{cl}	104.0×10^2	40.0×10^2	6.5	5.0×10^5	1.0×10^{-1}
I^{cl}	0.73	0.29	0.02	5.0×10^5	1.0×10^{-2}

Table 4.3 - Mechanical properties of cohesive layers (cl).

Laminated materials

Laminate	Layer distribution	h_i / h	h [mm]
L1	(A/B/A/H^{cl}/A/B/A/B/A)	(0.11/0.11/0.11/0.01/0.22/0.11/0.11/0.11/0.11)	9.1
L2	(C/D/E/F/C/I^{cl}/G/E/D/G)	(1.0/0.12/0.1/0.08/0.14/0.02/0.08/0.1/0.06/0.2)	25.0

Table 4.4 - Layer distribution of laminated materials.

In order to show the influence of the fracture energy G_f^{cl} in the delamination process, two values of this parameter (a larger one and a smaller one) are adopted for the cohesive layer in each laminate. For clarity, in the followings the largest value (G_f^D) is associated to a "ductile" property whereas the smallest (G_f^F) to a "fragile" one.

LRZ meshes of 2, 16, 128 finite elements are used in the analysis. The reference solution is obtained by means of a plane stress analysis (PS) using 4-noded quadrilateral finite elements and the isotropic damage model presented in Section 4.2 for managing the degradation of the cohesive layer. The beam length, the thickness of the elastic layers and the thickness of the cohesive ply are discretized with 100, 2 and 1 finite elements, respectively. The discretization chosen leads to meshes of 1700 (Figure 4.19a) and 1900 (Figure 4.19b) 4-noded quadrilateral PS elements for the laminates L1 and L2, respectively.

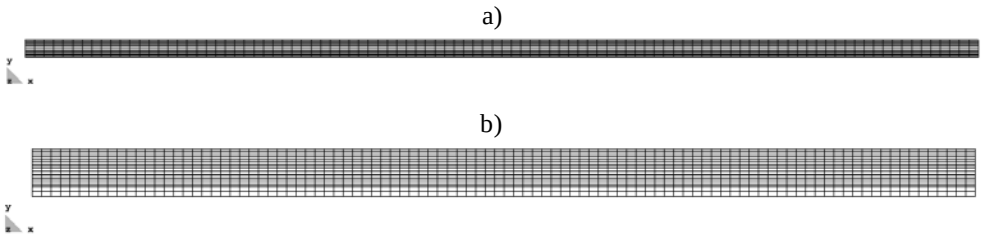

Figure 4.19 – Four-noded quadrilateral finite element meshes for laminate L1 a), and laminate L2 b).

Figure 4.20 and Figure 4.21 show the load-displacement curves for the laminates L1 and L2, respectively. The load corresponds to the vertical reaction at the clamped support. The displacement corresponds to the incremental displacement Δw applied at the clamped end (Figure 4.17). The curves shown in Figures a) are obtained when the "ductile" (G_f^D) fracture energy is considered. The response of the beam when the "fragile" (G_f^F) fracture energy is used is shown in Figures b). The fracture energy values are listed in Table 4.3.

Results reveal an admissible agreement between both solutions. The errors for the finest LRZ meshes at the end of simulation for the cases L1- G_f^D (Figure 4.20a), L1- G_f^F (Figure 4.20b), L2- G_f^D (Figure 4.20a) and L2- G_f^F (Figure 4.21b) are less than 11.0%, 2.5%, 7.5% and 2.9%, respectively. LRZ solution exhibits small drops of load for the case L1- G_f^D (Figure 4.20a), which are not present in the PS solution. The cause of these drops was mentioned in the previous skin-core delamination analysis.

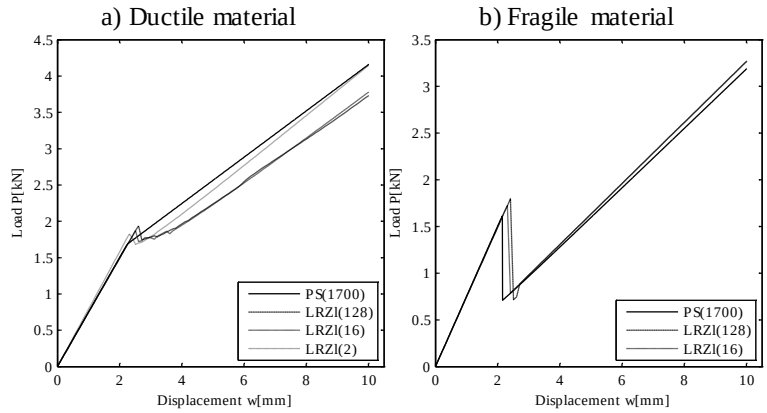

Figure 4.20 - Load vs. displacement curves for laminate L1 with ductile (a) and fragile (b) fracture energy.

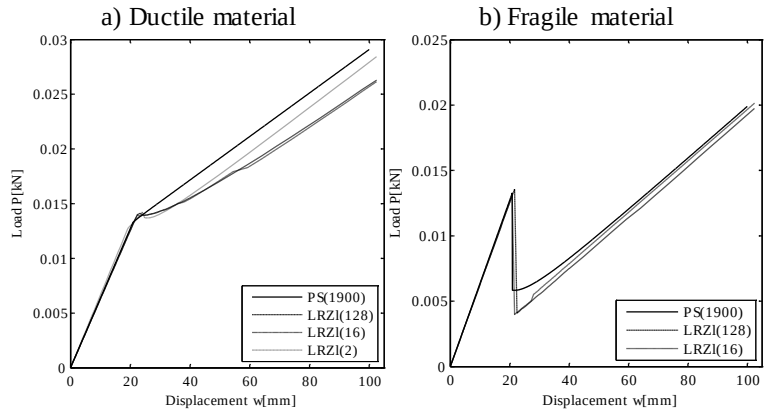

Figure 4.21 - Load vs. displacement curves for laminate L2 with ductile (a) and fragile (b) fracture energy.

When the "fragile" value of the fracture energy (G_f^F) is used, the cohesive layer completely loses its energy at the delamination onset, which provokes the sharp drop in the sample resistance, as shown in Figures b). The loss of resistance computed by the PS solution is around 56% for both laminates, whereas LRZ solution gives 60% and 70% for L1 and L2, respectively.

The initial stiffness and the stiffness once delamination process has been started are very close to the stiffness obtained by 2D analysis in all cases. Also, is shown that delamination starts for similar values of displacement and load.

The thickness distribution of the axial displacement u at the simply supported end, before and after delamination onset, is shown in Figure 4.22 and Figure 4.23 for laminates L1 and L2, respectively.

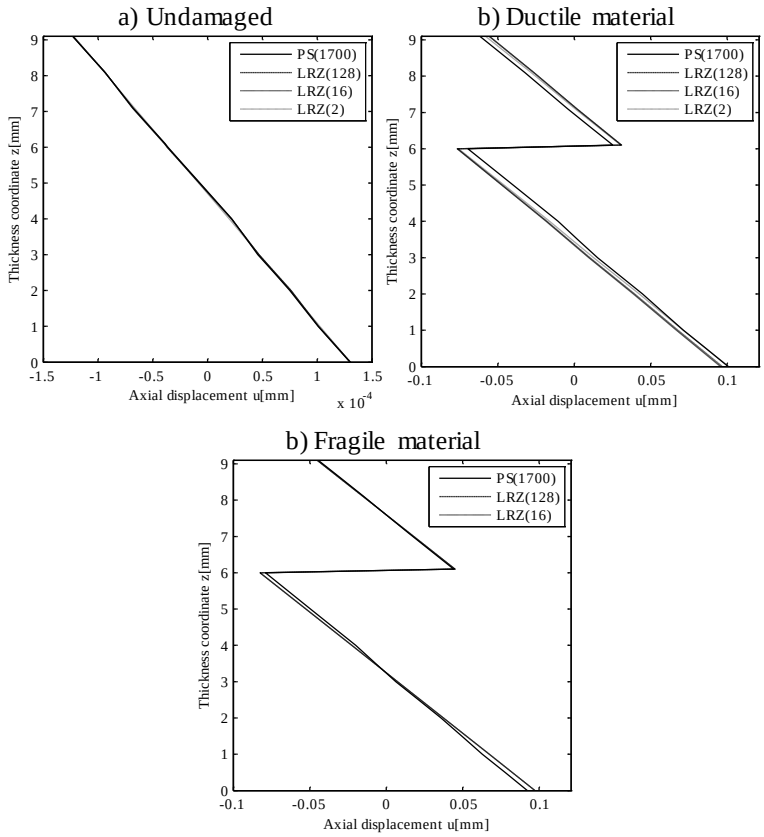

Figure 4.22 - Thickness distribution of the axial displacement *u* at the simply supported end for laminate L1. This figure shows the undamaged kinematics a) and the damaged kinematics when the "ductile" b) and the "fragile" c) fracture energy is used.

The undamaged kinematics is shown in Figures a), which make evident the very good match between PS and LRZ kinematics. Figures b) and c) show the delaminated kinematics at the end of simulation when the "ductile" and the "fragile" fracture energy values are used, respectively. In the "ductile" case, the LRZ elements are capable to capture the relative displacement with errors around 11% and 16% for laminates L1 and L2, respectively. In the "fragile" case, the errors are less than 3.3% for both laminates.

Almost identical results are obtained with the quadratic LRZ beam element.

Figure 4.24 shows the thickness distribution of the zigzag function ϕ for laminate L1 (a) and laminate L2 (b). The solid line represents the initial zigzag function (undamaged), whereas the dashed and the dash-dot line correspond to the damaged zigzag function when the damage variable of cohesive layer is equal to 0.9 and 1, respectively. As mentioned in Section 4.4, the ability of the LRZ element to

capture the relative displacement between plies during a delamination process lies in the zigzag function update according the layers are being damaged.

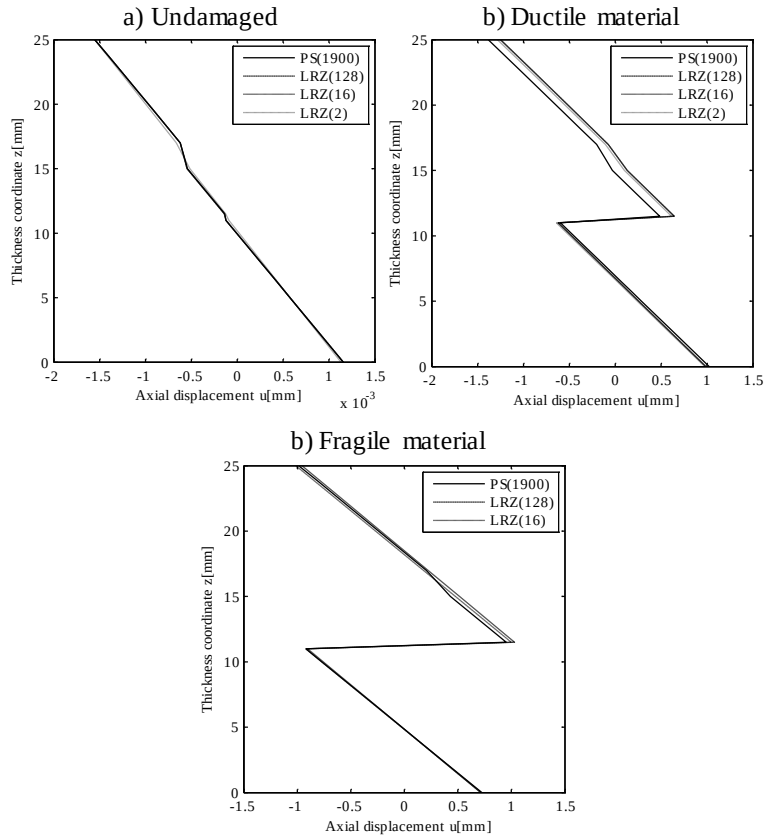

Figure 4.23 - Thickness distribution of the axial displacement *u* at the simply supported end for laminate L2. This figure shows the undamaged kinematics a) and the damaged kinematics when the "ductile" b) and the "fragile" c) fracture energy is used.

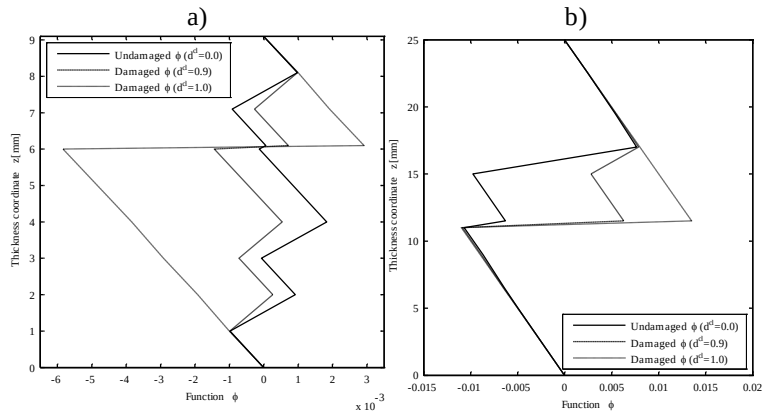

Figure 4.24 - Undamaged and damaged zigzag function for laminate L1 a) and laminate L2 b).

In order to compare the performance of the PS and the LRZ analyses, the total increment numbers and the incremental displacement values as well as the tolerance value ($\zeta = 1x10^{-4}$) are the same for both methods. The total increment numbers are equal to 1000 and 7000 for laminates L1 and L2, respectively. The incremental displacement value applied in each increment is $1x10^{-3}$mm and $4x10^{-3}$mm for L1 and L2, respectively. Table 4.5 and Table 4.6 show the total number of iterations, the maximum number of iteration needed for achieving convergence in any increment and the total CPU time used in the simulation for L1 and L2, respectively.

As expected, the computation time needed for the PS analysis is several times greater than that required for LRZ solutions. Comparing with the finest 128-LRZ mesh, PS uses at best around 67 times the time used by LRZ solution for laminate L2 and $G_f^F = 1.0x10^{-3}$ (Table 4.6). At worst, the time used by PS is 156 times greater than that required by the LRZ solution for laminate L1 and $G_f^D = 5.0x10^4$ (Table 4.5). If the comparison is made versus the 16-LRZ mesh, the time used by the PS solution is 530 and 1954 times of that needed by the LRZ solution at best and at worst scenarios, respectively.

Computational cost of the iterative process for laminate L1

Finite element		$G_f = 5.0x10^4$ (Ductile)			$G_f = 1.0x10^{-2}$ (Fragile)		
		Total Iter.	Max. Iter.	Time [seg]	Total Iter.	Max. Iter.	Time [seg]
2D	1700	9308	485	3069.0	3465	254	1127.0
LRZ	2	1543	166	1.52	-	-	-
	16	1286	81	1.57	1009	9	1.27
	128	2291	225	19.61	1036	23	9.45

Table 4.5 - Computational cost of the iterative process for laminate L1.

Computational cost of the iterative process for laminate L2

Finite element		$G_f = 5.0x10^4$ (Ductile)			$G_f = 1.0x10^{-3}$ (Fragile)		
		Total Iter.	Max. Iter.	Time [seg]	Total Iter.	Max. Iter.	Time [seg]
2D	1900	18374	88	6967.0	10141	144	4223.0
LRZ	2	7298	76	8.10	-	-	-
	16	7131	53	8.11	7016	11	7.96
	128	7072	71	64.51	7372	101	65.46

Table 4.6 - Computational cost of the iterative process for laminate L2.

4.6.2 Delamination in plates

The capability of the QLRZ element for simulating the relative in-plane displacements (Mode II and III) between plies is studied by modeling a simply supported rectangular plate of length L=1.0m, depth D=0.5m and thickness h=0.025m with a center hole of radius R=0.0125m (Figure 4.25a). Taking advantage of symmetry, only one quarter of plate is studied (Figure 4.25b). The structure is subjected to bending by imposing a uniform vertical displacement Δw along the segment $\overline{CF}$ (Figure 4.25b). The plate is analyzed for two laminates (L1 and L2) with properties listed in Tables 4.7- 4.9. The cohesive layers are denoted as I^{cl} and J^{cl} for the L1 and the L2 laminate, respectively.

The reference solution was obtained via a 3D finite element analysis using a mesh of 16416 8-noded hexahedral elements (HEXA8) involving 18620 nodes and 55860 DOFs (Figure 4.26). One and two finite elements are used to discretize the thickness of the cohesive layer and the thickness of the elastic layers, respectively. This mesh was used for both laminates as they share the same geometry.

Mesh convergence is studied using five QLRZ meshes of 44, 102, 216, 384 and 964 finite elements with 60, 126, 250, 429, 931 nodes and 420, 882, 1750, 3003, 6517 DOF, respectively, as shown in Figure 4.27.

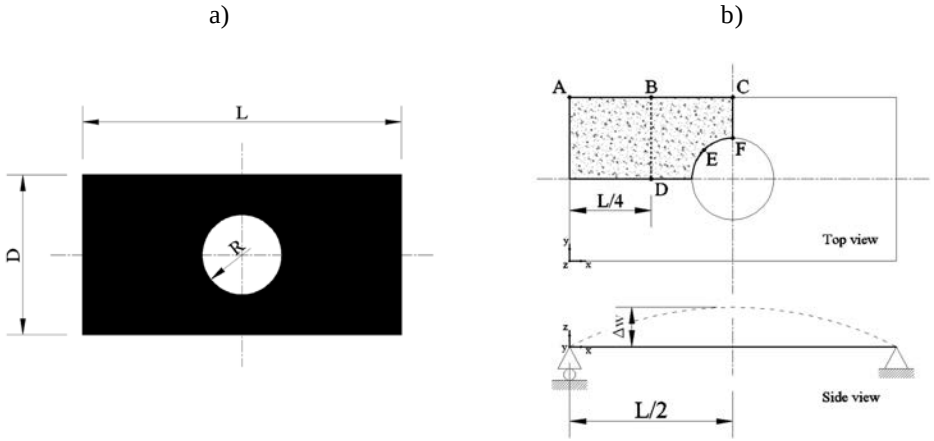

Figure 4.25 - Simply supported rectangular plate with a center hole. Whole structure dimensions a), quarter of plate under study with boundary conditions b).

Mechanical properties of *linear-elastic* plies [MPa]

Mat.	Young's Modulus			Shear Modulus			Poisson
	E_x	E_{xy}	E_z	G_{xy}	G_{xz}	G_{yz}	μ
A	$157.9x10^5$	$9.584x10^5$	$9.584x10^5$	$5.93x10^5$	$5.93x10^5$	$3.227x10^5$	0.32
B	$19.15x10^3$	$19.15x10^3$	$19.15x10^4$	$42.3x10^{-4}$	$36.51x10^3$	$124.8x10^3$	$6.58\ x10^{-4}$
C		$104.0x10^2$			$40.0x10^2$		0.30
D		$5.30x10^2$			$2.12x10^2$		0.25
E		$2.19x10^2$			$0.876x10^2$		0.25
F		$0.82\ x10^2$			$0.328\ x10^2$		0.25
G		0.73			0.29		0.25
H		$7.3\ x10^2$			$2.92\ x10^2$		0.25

Table 4.7 - Mechanical properties of linear-elastic layers.

Mechanical properties of *cohesive* plies (cl)

Materials	E_0 [MPa]	G_0 [MPa]	Tensile Strength (f_t) [MPa]	Fracture Energy (G_f) [kN/m]
I^{cl}	$104.0x10^2$	$40.0x10^2$	20.0	$5.0x10^5$
J^{cl}	0.73	0.29	$3.0\ x10^{-3}$	$5.0x10^5$

Table 4.8 - Mechanical properties of cohesive layers (cl).

Laminated materials

Laminate	Layer distribution	h_i / h	h [mm]
L1	(A/C/A/C/B/I^{cl}/C/A/C/A)	(1.0/0.12/0.1/0.08/0.14/0.02/0.08/0.1/0.06/0.2)	25.0
L2	(D/E/F/G/D/J^{cl}/H/F/E/H)	(1.0/0.12/0.1/0.08/0.14/0.02/0.08/0.1/0.06/0.2)	25.0

Table 4.9 - Layer distribution of laminated materials.

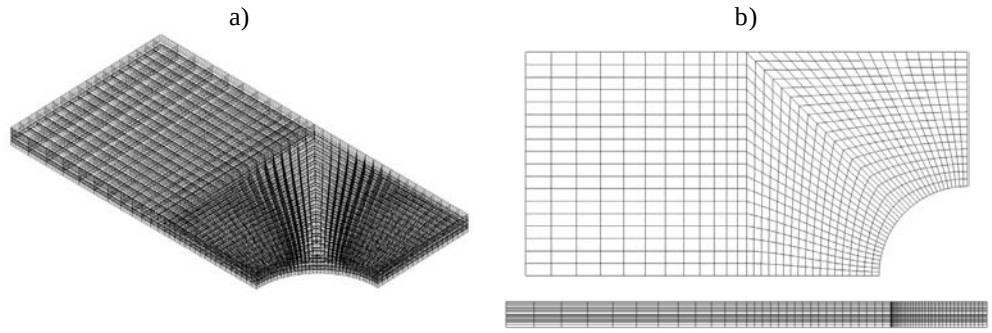

Figure 4.26 – HEXA8 mesh for both laminates. Isometric view a), top and side view b).

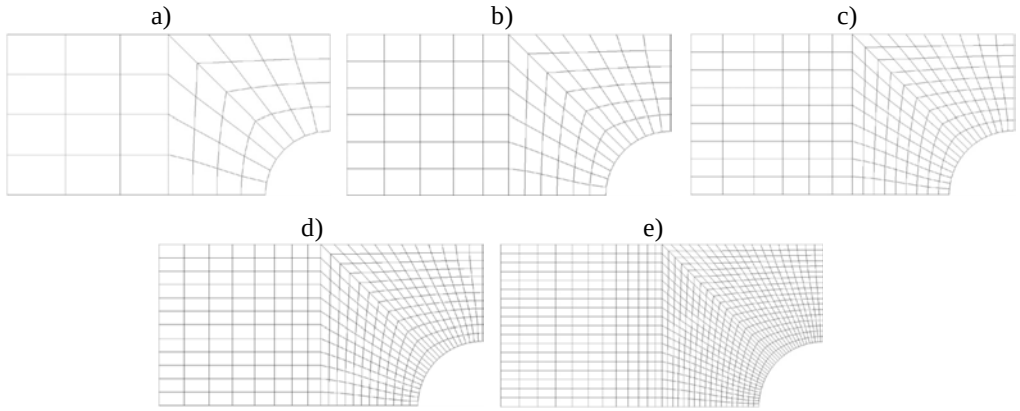

Figure 4.27 – QLRZ meshes of 44 a), 102 b), 216 c), 384 d) and 964 e) finite elements.

The load-displacement curves for both laminates are shown in Figure 4.28. The curves are obtained with the HEXA8 element (solid line) and the finest QLRZ mesh (dashed lines). The load corresponds to the total vertical reaction computed at the simply supported end whereas the displacement is the imposed vertical displacement Δw (Figure 4.25b). Results show a good agreement between both solutions. In all cases, the lineal-elastic QLRZ stiffness is very close to that computed by means of 3D analysis. Also, it is shown that delamination starts approximately at the same values of displacement and load.

Figure 4.29 shows the convergence of the normalized load value at the end of the simulation as the number of DOF is increased. The error for the coarser QLRZ mesh reaches almost 35% and 65% for the L1 and the L2 laminates, respectively. However, the error is around 1% (L1) and 10% (L2) for the finest QLRZ mesh.

The evolution of the transverse shear stress τ_{xz} for the cohesive layer for laminates L1 and L2 is shown in Figure 4.30 and Figure 4.31, respectively. For the

linear-elastic state, the HEXA8 solution gives about 12% (L1) and 30% (L2) higher maximum value of τ_{xz} as appreciated for Δw =0.01mm. Because of this, damage starts a little later for the QLRZ solution. This mismatch between both solutions is more evident for the L2 laminate where the τ_{xz} distribution obtained with the HEXA8 mesh at Δw =0.41mm is similar to that computed with the QLRZ mesh at Δw =0.51mm. For the L1 laminate, no great differences are observed between both solutions. In all cases, approximately the same values of τ_{xz} are predicted at the end of the simulation (Δw =2.51mm).

Figure 4.32 and Figure 4.33 show the evolution of the transverse shear distribution along the segments AC and BD (Figure 4.25b) for the L1 and the L2 laminate, respectively. Results along segment AC are influenced by the mesh topology especially for laminate L2 as shown in Figure 4.33 for Δw =0.01mm. However, this mesh dependence disappears once delamination has started.

Taking into account that the degradation of the cohesive layer is governed by the transverse shear stress in these examples, the norm f of Eq.(4.5) can be approximated by

$$f \simeq \sqrt{\tau^2 / G_0}$$

Thus, equating the initial threshold c_0 of Eq.(4.4) and the preceding equation, the transverse shear stress for which delamination starts is approx. computed by

$$\tau \simeq \sqrt{G_0 / E_0}\ f_t$$

which reveals that delamination onset occurs for a transverse shear stress smaller than the tensile strength f_t, as appreciated in Figure 4.32 and Figure 4.33.

The gray-scale images shown in Figure 4.34 and Figure 4.35 illustrate the damage growth of the cohesive ply for laminates L1 and L2, respectively. The black color denotes a full damage state (d = 1). These images confirm that damage starts earlier when the HEXA8 finite elements are used, especially for the L2 laminate. However, the global response of the structure (Figure 4.28) is similar for both finite elements. Although the cohesive layer seems to be full damaged at the last step (Δw=2.51mm), the damage variable just reaches at most a value of 0.997. For this reason, the transverse shear stress τ_{xz} did not decrease as expected in a softening process. Surely, if the test continues until the ply is full damaged, the stresses will be reduced to zero.

The thickness distribution of the axial displacement u at points A, B and E (Figure 4.25b), before (Δw =0.01mm) and after (Δw =2.51mm) delamination, is

plotted in Figure 4.36 (L1) and Figure 4.37 (L2), respectively. The QLRZ element captures the relative displacement with errors less than 6% and 2% for laminates L1 and L2, respectively. For all cases, a very good match between 3D and QLRZ kinematics was found.

To emphasize the importance of the zigzag function update to capture relative displacement between layers during a delamination process, Figure 4.38 shows the change of the zigzag thickness distribution from an undamaged to a full damaged state for laminates L1 (Figure 4.38a) and L2 (Figure 4.38b).

In order to compare the performance of the 3D solution and the QLRZ analysis, both, the total increment numbers and the incremental displacement values as well as the error tolerance value are the same for both methods. As expected, the computation time needed for the QLRZ solution is several times less than that required for the 3D analysis. The time used by the finest QLRZ mesh is approximately 20 and 12 times less than that required by the HEXA8 mesh for laminates L1 and L2, respectively. In addition, the computation storage space during the simulation is much greater for the 3D analysis as expected.

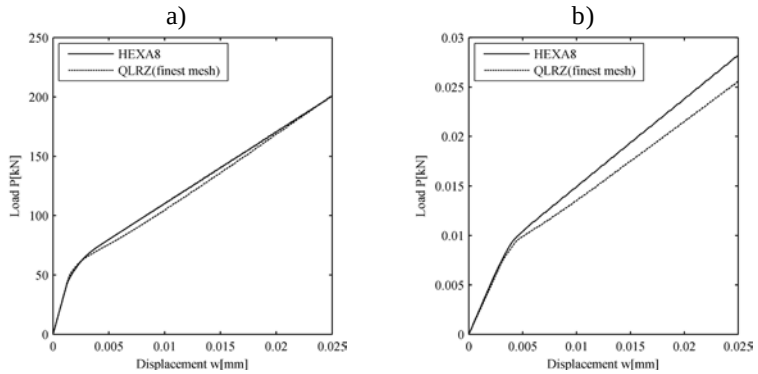

Figure 4.28 – Load vs vertical displacement for laminate L1 a) and L2 b).

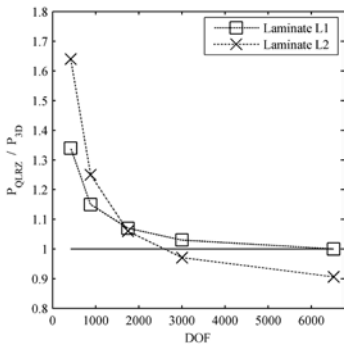

Figure 4.29 – Mesh convergence. Normalized load value for both laminates and all meshes.

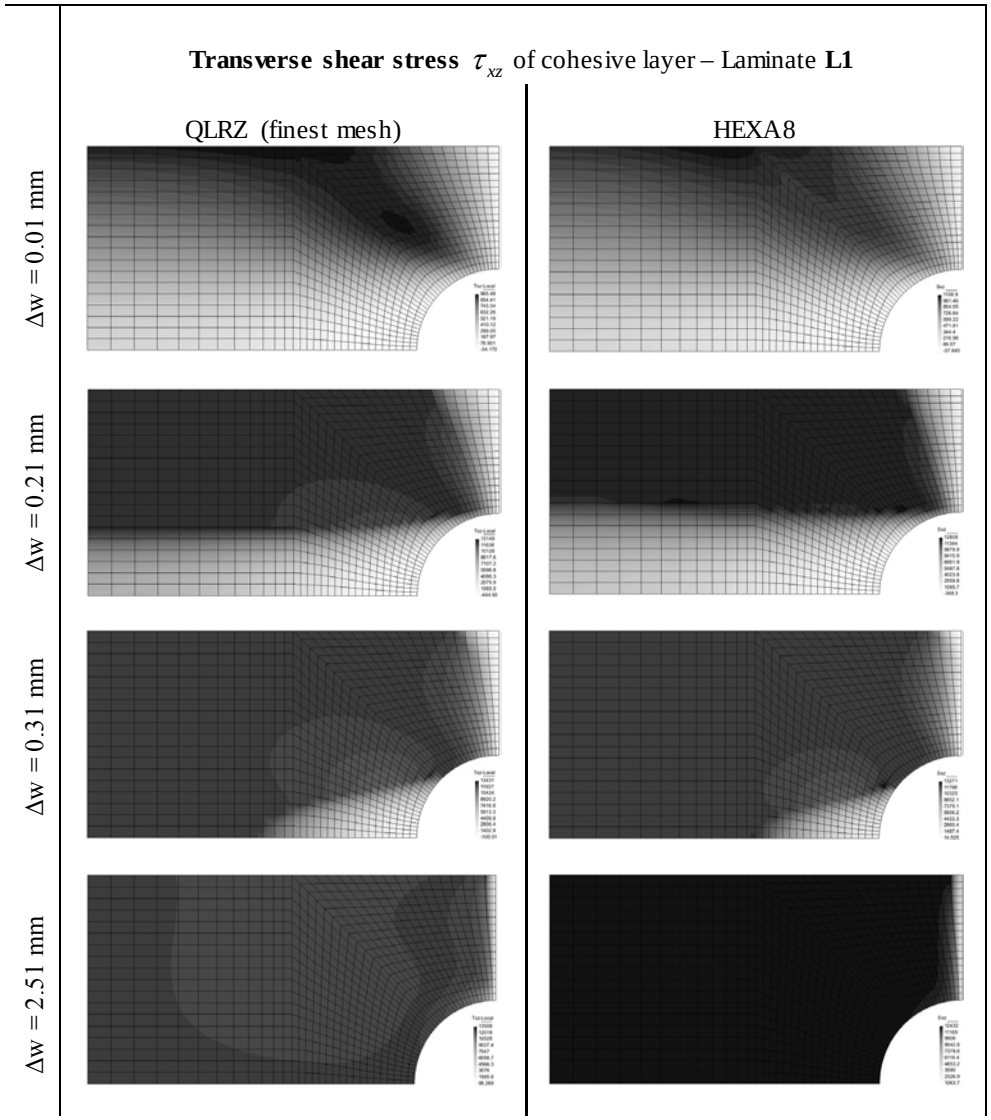

Figure 4.30 – Transverse shear distribution τ_{xz} of cohesive layer for laminate L1 computed with the finest QLRZ mesh (left) and the HEXA8 mesh (right) observed at four different Δw increments.

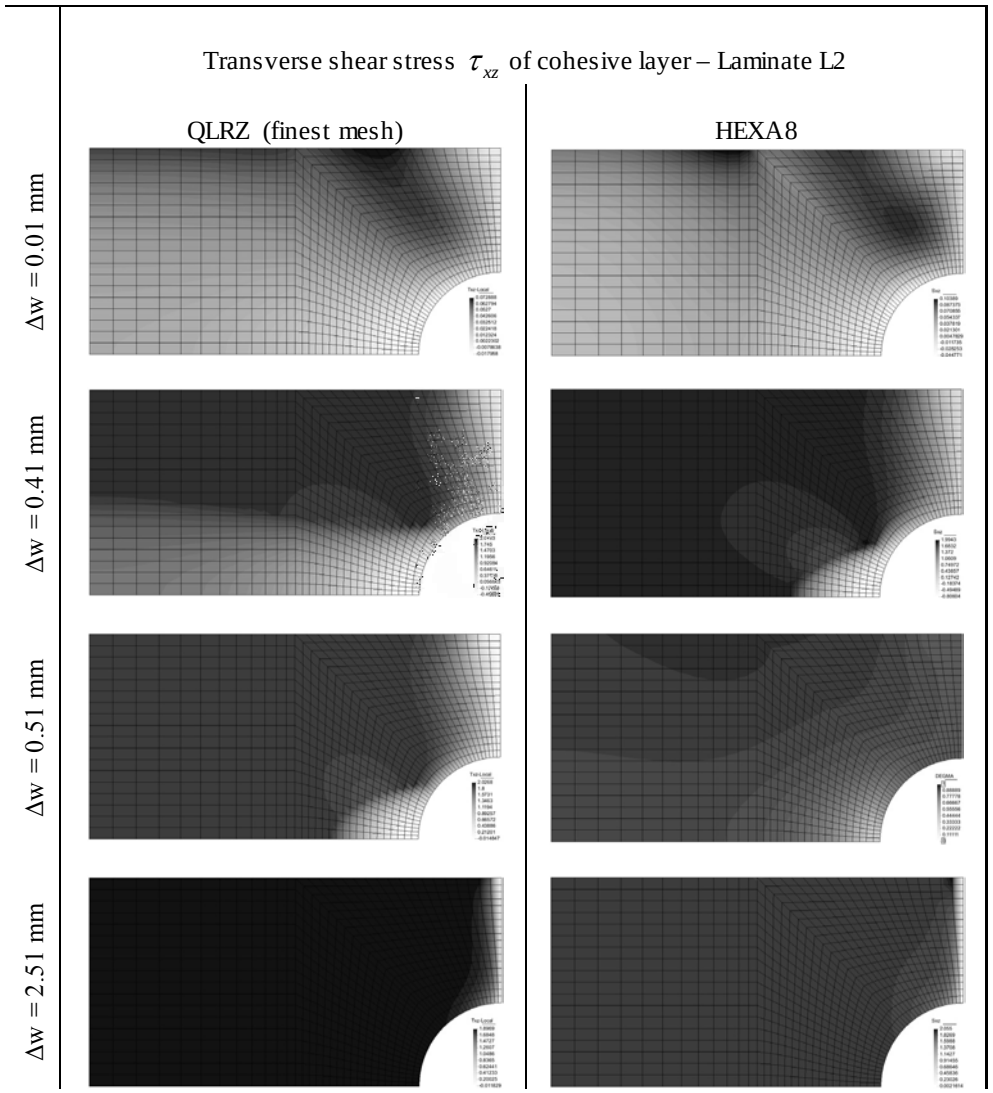

Figure 4.31 – Transverse shear distribution τ_{xz} of cohesive layer for laminate L2 computed with the finest QLRZ mesh (left) and the HEXA8 mesh (right) observed at four different Δw increments.

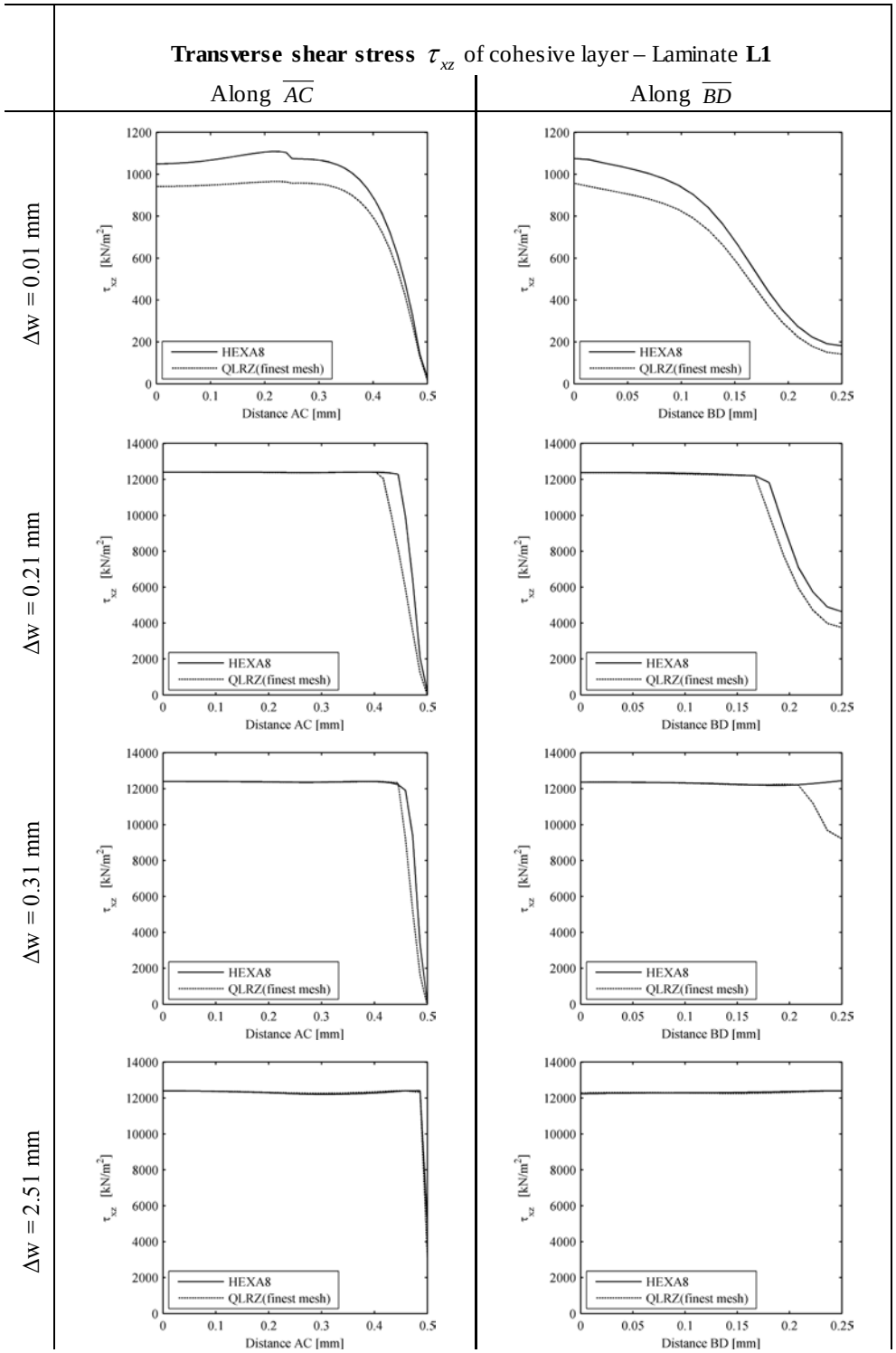

Figure 4.32 – Transverse shear distribution τ_{xz} of cohesive layer for laminate L1 along the segments $\overline{AC}$ (left) and $\overline{BD}$ (right), which were observed at four different Δw increments.

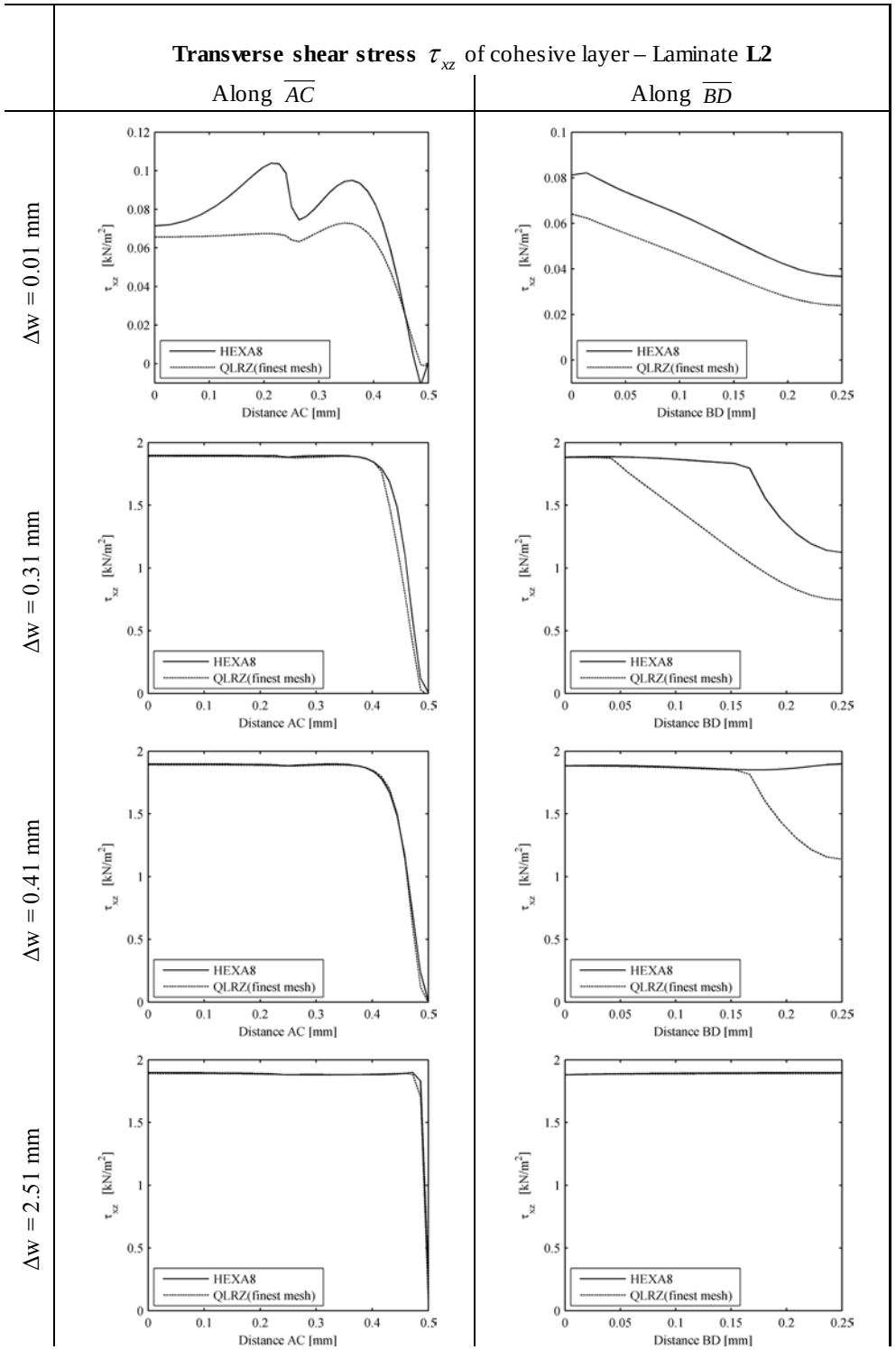

Figure 4.33 – Transverse shear distribution τ_{xz} of cohesive layer for laminate L2 along the segments $\overline{AC}$ (left) and $\overline{BD}$ (right), which were observed at four different Δw increments.

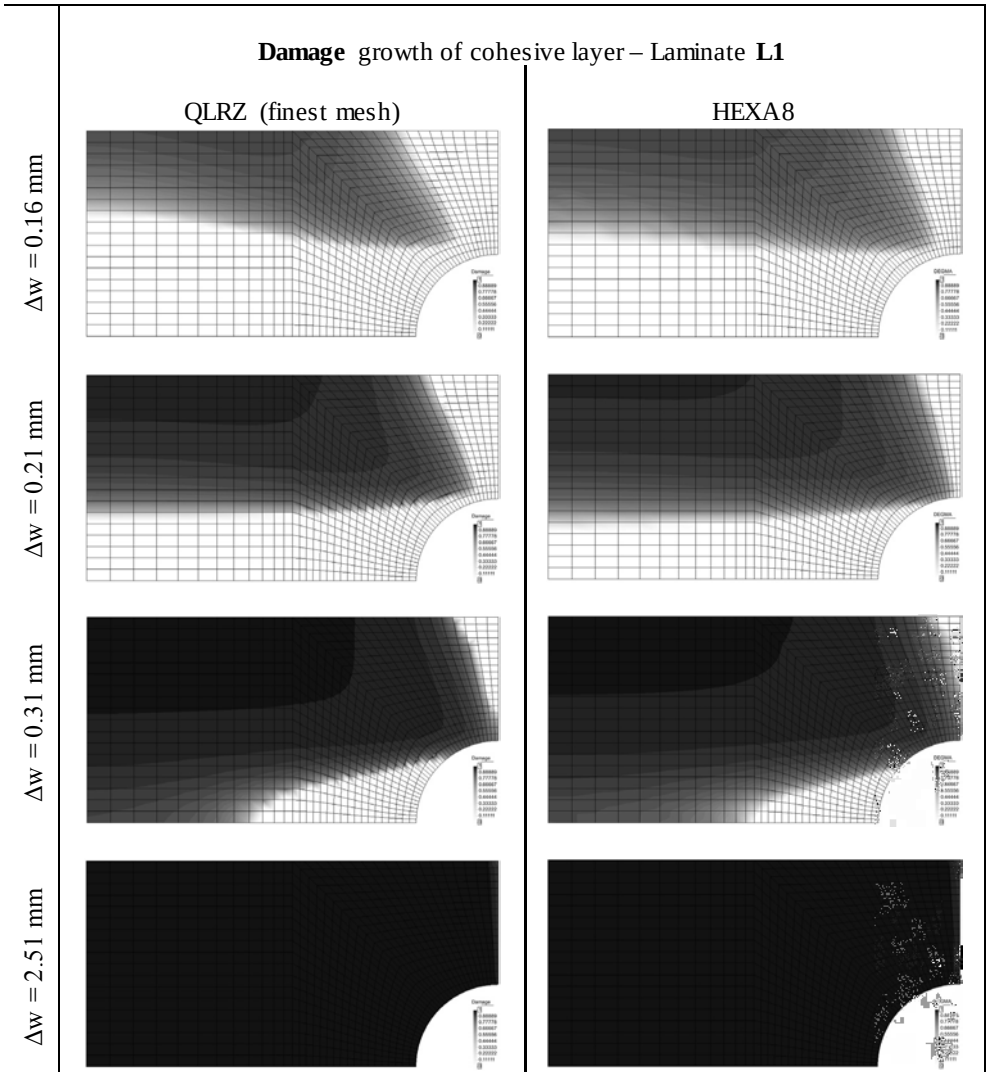

Figure 4.34 – Damage level of cohesive layer for laminate L1 computed with the finest QLRZ mesh (left) and the HEXA8 mesh (right) observed at four different Δw increments. White color is a sing of non-damage and black color indicates full damage.

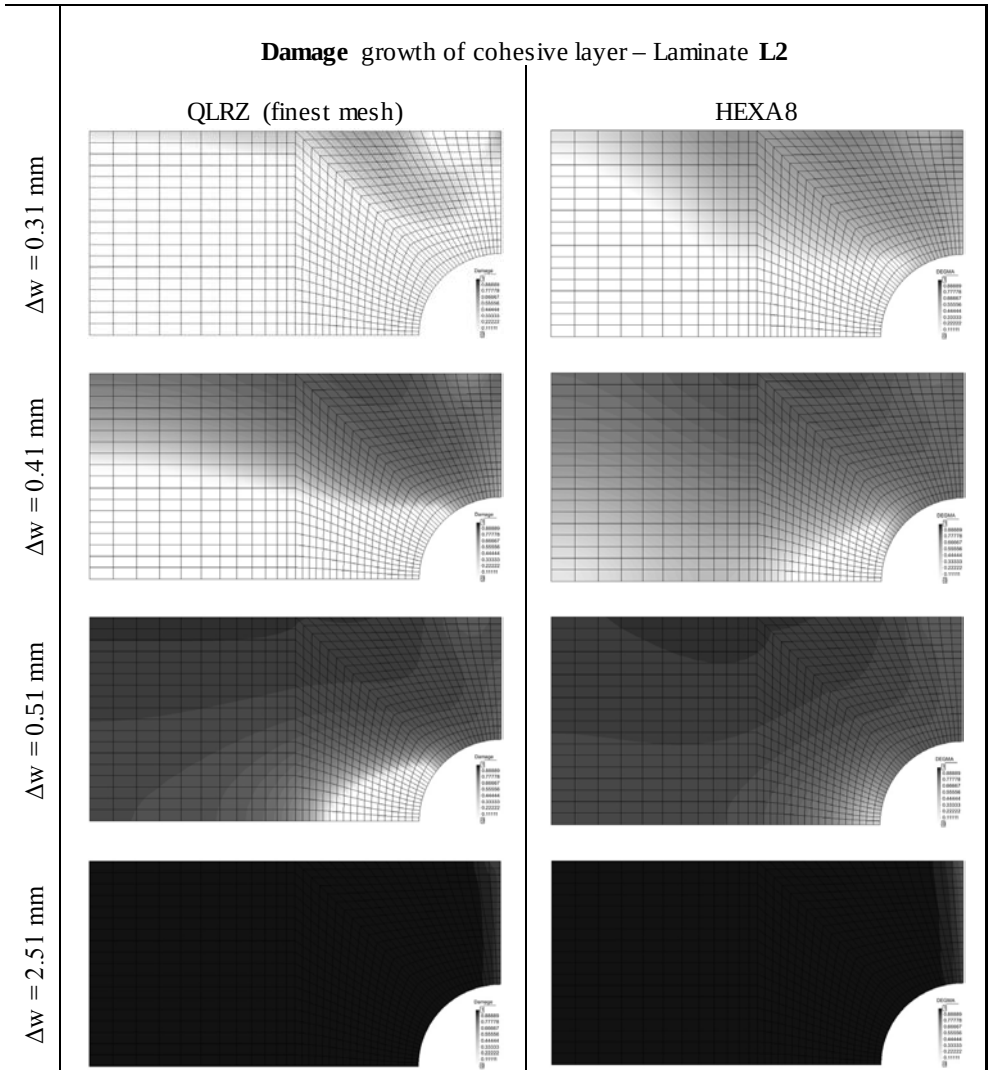

Figure 4.35 – Damage level of cohesive layer for laminate L2 computed with the finest QLRZ mesh (left) and the HEXA8 mesh (right) observed at four different Δw increments. White color is a sing of non-damage and black color indicates full damage.

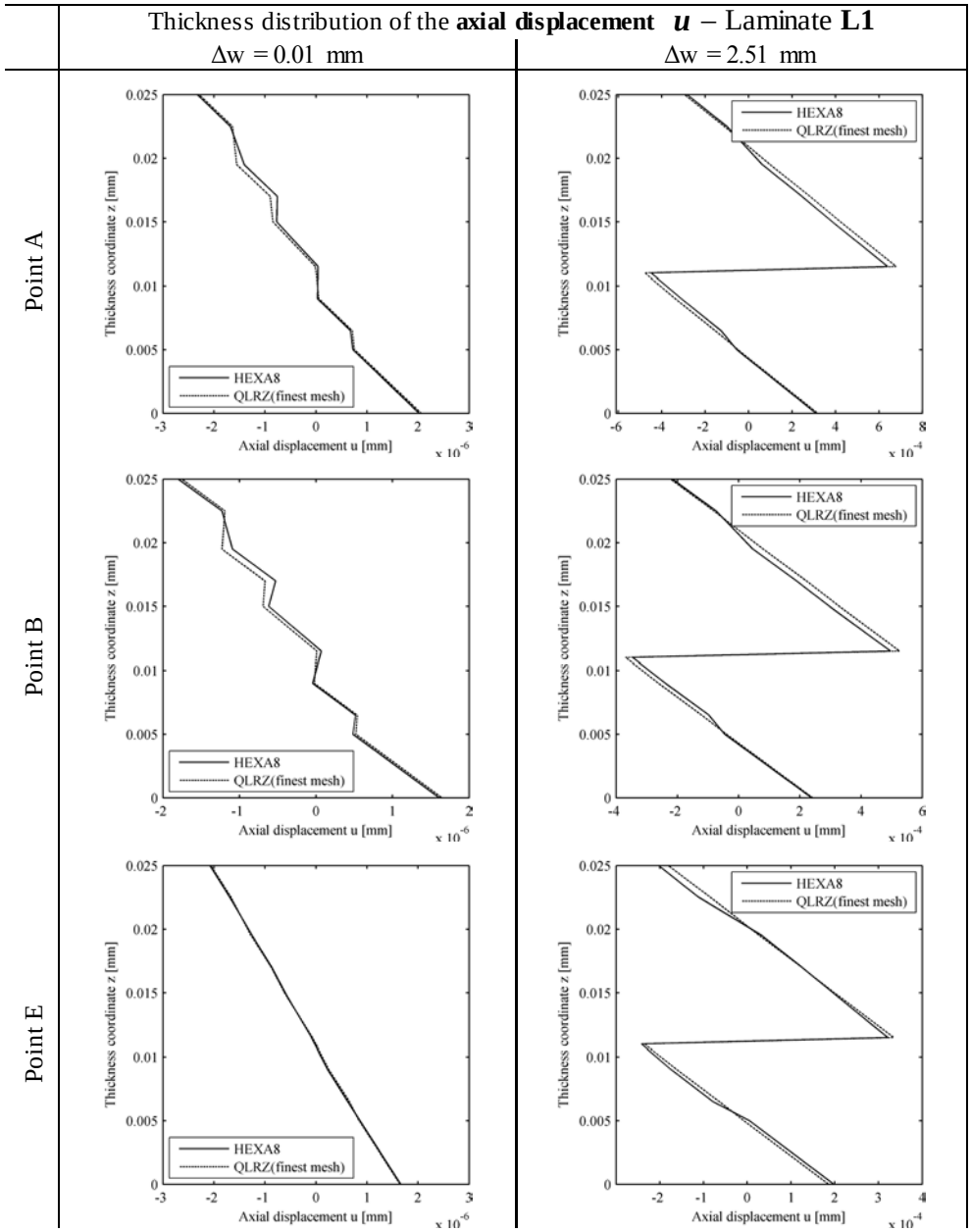

Figure 4.36 – Thickness distribution of the axial displacement *u* at three different points for laminate L1. Figures show the undamaged kinematics (left - Δw = 0.01 mm) and the delaminated kinematics at the end of simulation (right - Δw = 2.51 mm).

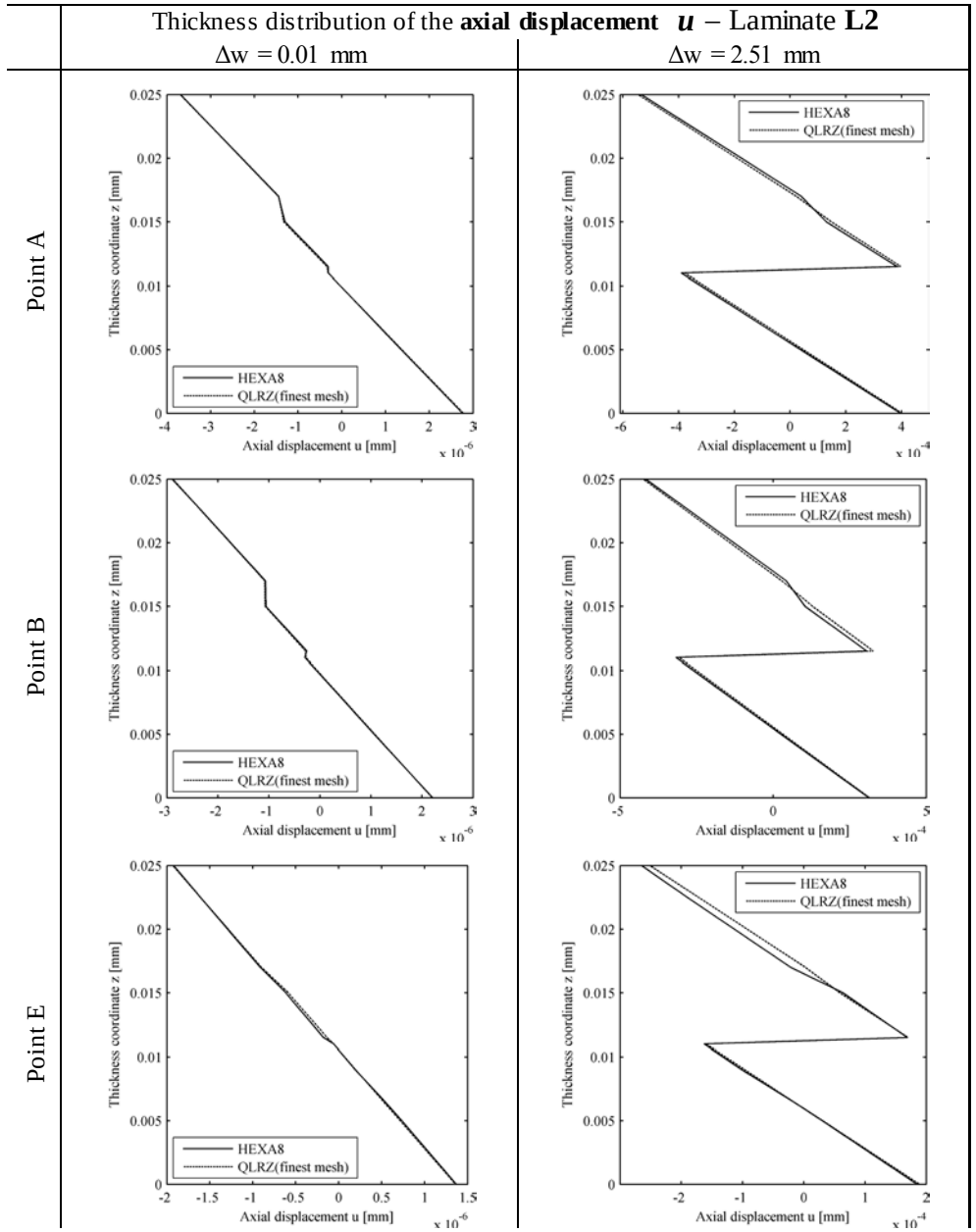

Figure 4.37 – Thickness distribution of the axial displacement u at three different points for laminate L2. Figures show the undamaged kinematics (left - Δw = 0.01 mm) and the delaminated kinematics at the end of simulation (right - Δw = 2.51 mm).

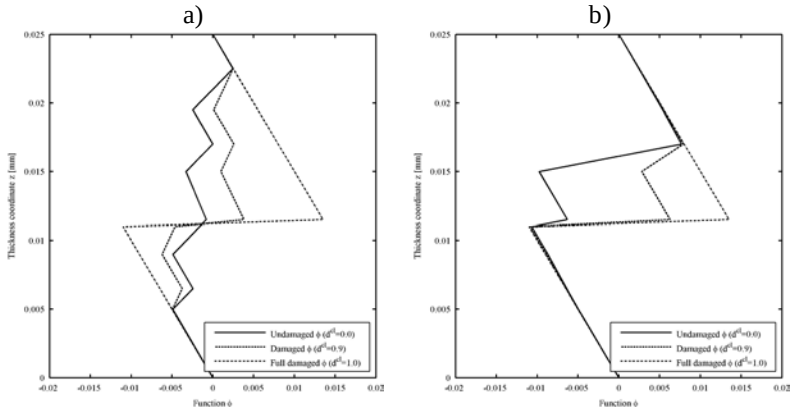

Figure 4.38 – Undamaged and damaged zigzag function ϕ_x for laminate L1 a) and L2 b).

5 Conclusions and future work

This thesis dealt with the modeling of laminated materials. The formulation of the beam (LRZ) and plate (QLRZ) finite elements based on the RZT theory for simulating highly heterogeneous multilayered laminates and the development of a numerical method based on these elements for modeling mode II/III delamination in advanced composite materials were the main goals.

The contents and main achievements of the present work are summarized in the following.

In Chapter 2, a review of more common beam/plate theories for modeling laminated materials was presented. In particular, the Refined Zigzag Theory (RZT) was described in detail since the finite elements here developed are based on this zigzag theory. Then, the influence on the zigzag in-plane displacement of both, the material transverse anisotropy and the laminate span-to-thickness ratio was also studied. Results showed that the amplitude of the zigzag kinematics is increased according the transverse anisotropy is higher whereas it is reduced according the laminate is more slender. Furthermore, advanced composite materials and their failure mechanisms were treated, with special attention on delamination. Common numerical methods to predict intra- and inter-laminar failure modes were discussed.

Chapter 3 dealt with development of two simple, robust, shear locking free and accurate isoparametric finite elements based on the RZT theory for simulating laminated beam and plate structures, which constitute the first achievement. The LRZ beam element is a two-node element with four variables per node, whereas the QLRZ plate element is a four-node quadrilateral element with seven variables per nodes. Both elements were formulated on small deformation and displacement.

A key attribute of these elements is that the number of node variables is constant and independent of the analysis layers used to define the laminate. In order to overcome the shear locking defect, a selective numerical integration of the transverse stiffness matrix is adopted in the LRZ element, and a linear shear strain field is assumed in the QLRZ element.

The performance of these elements was investigated through several studies. Results showed that the elements are able to accurately model highly heterogeneous laminated materials under different loads and boundary conditions. The influence of the transverse anisotropy on the convergence and accuracy of the LRZ/QLRZ solutions was also studied. It was found that as the transverse anisotropy is greater the LRZ/QLRZ solution gives worse results.

A very important feature of these elements is their ability to accurately capture the through-thickness distribution of both, the zigzag in-plane displacement and the axial stress. On the contrary, however, the transverse shear stresses distribution is defined by the constitutive equations as a constant pricewise function, which is far from the real distribution. There, the post-processing computation of the transverse shear stresses by means of the equilibrium equations has demonstrated to be a suitable alternative.

An acceptable agreement between the LRZ/QLRZ solutions and the reference solutions was observed in all cases studied.

The development of a numerical model for modeling delamination in advanced composite materials was addressed in Chapter 4. The model uses the LRZ/QLRZ finite elements for describing the whole laminated material including the resin-rich zone at the interface between plies where delamination takes place. In other words, no additional technique for modeling the delamination paths is required. The interfaces are defined by means of additional layers (cohesive layer), which need to be enough thin to avoid membrane effect. It is important to mention that no additional kinematics variables are introduced in the model by incorporating interface layers. Their mechanical behavior is managed by an isotropic damage model. Thus, the relative displacement between two neighbor layers occurs when the transverse shear modulus of the cohesive layers between them is considerably reduced in comparison with those of the neighbor plies.

Only the shear fracture modes (mode II and III) can be captured with the LRZ/QLRZ delamination model because the vertical displacement in the RZT theory is defined constant through the thickness.

In addition, as a result of the definition of the zigzag function, the model cannot predict the zigzag pattern of the in-plane displacement of sub-laminates after delamination. This limitation causes that delamination in multilayered structures

having low span-to-thickness ratio or high transverse anisotropy of shear properties cannot be properly simulated with the LRZ/QLRL delamination model. However, that is not the case of advanced composite laminates where the shear modulus does not differ generally in more than one order of magnitude between layers [113]. Moreover, laminated structures of composite materials are generally characterized by high slenderness ratios. Furthermore, delamination in three-layered laminates can be modeled with independence of the level of transverse anisotropy and the slenderness of the structures, because the sub-laminates, for this kind of material, present a linear displacement distribution after delamination. Because of this, skin-core delamination in sandwich materials can be also modeled with the model, as showed the results.

It was demonstrated that, in order to simulate delamination with this model it is necessary to update the zigzag function. This update was performed by taking into account the level of degradation of the interface layer.

It was also observed that, in order to predict multi-delamination with the LRZ/QLRZ delamination model the reduced shear properties of new degraded interfaces must be almost the same as that of the first damaged cohesive layer. Otherwise, the model may predict wrong displacements obviating previous delamination states or ignoring new delamination paths.

The performance of the LRZ delamination model was analyzed through some single-delamination cases. The analyses include the skin delamination from the core in a clamped sandwich beam and the internal delamination within two different multilayered materials in a simple supported beam. Moreover, the influence on the structural response of the fracture energy of the cohesive layer was also analyzed.

A comparison of the computational cost between the LRZ delamination model and the reference solution, i.e. the finite element plane stress (PS) analysis, was performed. As expected, the results showed that the computation time and the memory space needed by the LRZ model is several times less than that required by a PS analysis.

The performance of the QLRZ delamination model has been studied by simulating internal delamination in a simply supported rectangular plate with a center hole subjected to bending. Two different multilayered materials were used and the results were compared with a reference solution obtained with a 3D finite element analysis.

It was observed that the LRZ/QLRZ delamination model predicts with an acceptable precision the onset and growth of delamination. In addition, the in-plane displacement after delamination is also well predicted.

Summarizing, the main achievement of this work is the development of a preliminary numerical model based on the LRZ/QLRZ finite elements for predicting delamination in advanced composite materials as well as in sandwich laminates. In addition, the LRZ beam and the QLRZ plate finite elements based on the RZT theory are also contributions of this thesis.

It should be noted that some aspects of the developments should be still improved in order to obtain more generality. The following are some of the most relevant aspects which deserve future attention.

- The LRZ and QLRZ elements could be improved in order to obtain more generality. Membrane locking should be investigated. Finite displacements and rotations may be accounted for to simulate geometrically non-linear problems.

- A better definition of the zigzag function is needed to capture zigzag patterns in sub-laminates after delamination with independence of the span-to-thickness ratio and the transverse anisotropy.

- A strategy for controlling the degradation process should be developed in order to simulate multi-delamination with the LRZ/QLRZ delamination model. This strategy has to be applied at each integration points.

- Although the adopted isotropic damage model demonstrated to be able to predict the onset and growth of delamination, it would be interesting to evaluate other damage laws which can simulate the delamination process as a combination of the fracture mode II and III, i.e. mixed mode delamination.

- In order to simulate the complex fracture behavior of advanced composites materials, intra-laminar failure mechanisms should be also accounted for.

All numerical tools developed in this thesis were implemented by the author in his own finite element code. The reference solutions were computed by using the PLCD [121] software developed by the International Center for Numerical Methods in Engineering (CIMNE). Pre- and post-process tasks were carried out employing the GID [122] software developed by CIMNE.

References

[1] Carrera, E. Theories and Finite Elements for Multilayered, Anisotropic, Composite Plates and Shells. *Arch. Comput. Meth. Engng.*, 9: 87-140, 2002.

[2] Reddy, J. N. Mechanics of Laminated Composite Plates and Shells: Theory and Analysis. 2nd Ed. United States of America, CRC Press, 2003.

[3] Tessler, A., Sciuva, M. D., and Gherlone, M., "Refinement of Timoshenko Beam Theory for Composite and Sandwich Beams Using Zigzag Kinematics," NASA, Technical Publication TP-215086, 2007.

[4] Tessler, A., Sciuva, M. D., and Gherlone, M. A consistent refinement of first-order shear deformation theory for laminated composite and sandwich plates using improved zigzag kinematics. *Mechanics of Materials and Structures*, 5: 341-365, 2010.

[5] Balzani, C., "Finite element modeling of intra- and interlaminar damage growth in composite laminates," Fakultät für Bauingenieur-, Geo- und Umweltwissenschaften der Universität Fridericiana zu Karlsruhe, Karlsruhe, Germany, 2009.

[6] Martinez, X., Rastellini, F., Oller, S., Flores, F., and Oñate, E. Computationally optimized formulation for the simulation of composite materials and delamination failures. *Composites: Part B*, 47: 134-144, 2011.

[7] Krueger, R. The Virtual Crack Closure Technique: History, Approach and Applications. *Applied Mechanics Reviews,* 57: 109-143, 2002.

[8] Aymerich, F., Dore, F., and Priolo, P. Prediction of impact-induced delamination in cross-ply composite laminates using cohesive

interface elements. *Composites Science and Technology,* 68: 2383-2390, 2008.

[9] Sánchez-Palencia, E. S. Homogenization techniques for composite media. *Springer-Verlag, Berlin, Germany. Chapter: "Boundary layers and edge effects in composites",* 121-192, 1987.

[10] Oller, S., Miquel, J., and Zalamea, F. Composite material behavior using a homogenization double scale method. *Journal of Engineering Mechanics,* 131: 65-79, 2005.

[11] Carrera, E. C^{0z} Requirements-models for the two dimensional analysis of multilayered structures. *Composite Structures,* 37: 373-383, 1997.

[12] Kirchhoff, G. Über das Gleichgewicht und die Bewegung einer elastishen Scheibe. *J Angew Math,* 40: 51-88, 1850.

[13] Wanji, C. and Zhen, W. A Selective Review on Recent Development of Displacement-Based Laminated Plate Theories. *Recent Patents on Mechanical Engineering,* 1: 29-44, 2008.

[14] Timoshenko, S. P. and Woinowsky-Krieger, S. Theory of plates ans shells. 3rd Ed. New York, McGraw-Hill, 1959.

[15] Timoshenko, S. P. On the correction for shear of differential equations for transverse vibrations of prismatic bars. *Philosophical Magazine Series,* 41: 744-746, 1921.

[16] Reissner, E. The effect of transverse shear deformation on the bending of elastic plates. *Appl. Mech.,* 12: 69-79, 1945.

[17] Mindlin, R. D. Influence of rotatory inertia and shear in flexural motions of isotropic elastic plates. *Appl. Mech.,* 18: 31-38, 1951.

[18] Reddy, J. N. A simple higher-order theory for laminated composite plates. *Appl. Mech.,* 51: 745-752, 1984.

[19] Kant, T. and Swaminathan, K. Analytical solution for the static analysis of laminated composite and sandwich plates based on a higher order refined theory. *Composite Structures,* 56: 329-344, 2002.

[20] Matsunaga, H. Assessment of a global higher-order deformation theory for laminated composite and sandwich plates. *Composite Structures,* 56: 279-291, 2002.

[21] Auricchio, F. and Sacco, E. Partial-mixed formulation and refined models for the analysis of composite laminates within an FSDT. *Composite Structures,* 46: 103-113, 1999.

[22] Carrera, E. A priori vs. a posteriori evaluation of transverse stresses in multilayered orthotropic plates. *Composite Structures,* 48: 245-260, 2000.

[23] Reddy, J. N. and D. H. Robbins, J. Theories and computational models for composite laminates. *Applied Mechanics Reviews,* 47: 147-165, 1994.

[24] Robbins, D. H. and Reddy, J. N. Modelling of thick composites using a layerwise laminate theory. *Int. Journal for Numerical Methods in Engineering,* 36: 655-677, 1993.

[25] Carrera, E. Mixed layer-wise models for multilayered plates analysis. *Composite Structures,* 43: 57–70, 1998.

[26] Carrera, E. Evaluation of Layerwise Mixed theories for laminated Plates Analysis. *AIAA,* 36: 830-839, 1998.

[27] Murakami, H. Laminated composite plate theory with improved in-plane responses. *Journal of Applied Mechanics,* 53: 661-666, 1986.

[28] Murakami, H. A higher-order laminated plate theory with improved in-plane response. *Int. J. Solids Struct.,* 23: 111-131, 1987.

[29] Carrera, E. C0 Reissner-Mindlin multilayered plate elements including zigzag and interlaminar stress continuity. *Int. J. Numer. Meth. Engng,* 39: 1797-1820, 1996.

[30] Demasi, L. Refined multilayered plate elements based on Murakami zig–zag functions. *Composite Structures,* 70: 308-316, 2005.

[31] DiSciuva, M. A refinement of transverse shear deformation theory for multilayered orthotropic plates. *Atti Accademia delle Scienze di Torino,* 118: 279-295, 1984.

[32] DiSciuva, M. A third-order triangular multilayered plate finite element with continuous interlaminar stresses. *Int. J. Numer. Meth. Engng,* 38: 1-26, 1995.

[33] Cho, M. and Parmerter, R. An efficient higher-order plate theory for laminated composites. *Composite Structures,* 20: 113-123, 1992.

[34] Averill, R. C. Static and dynamic response of moderately thick laminated beams with damage. *Composites Engineering,* 4: 381-395, 1994.

[35] Averill, R. C. and Yip, Y. C. Development of simple, robust finite elements based on refined theories for thick laminated beams. *Computers & Structures,* 59: 529-546, 1996.

[36] Tessler, A., Sciuva, M. D., and Gherlone, M. A refined zigzag beam theory for composite and sandwich beams. *Journal of Composite Materials,* 43: 1051-1081, 2009.

[37] Tessler, A., Sciuva, M. D., and Gherlone, M. Refined zigzag theory for homogeneous, laminated composite, and sandwich plates: a homogeneous limit methodology for zigzag function selection. *Numerical Methods for Partial Differential Equations,* 27: 208-229, 2011.

[38] Oñate, E., Eijo, A., and Oller, S. Simple and accurate two-noded beam element for composite laminated beams using a refined zigzag theory. *Computer Methods in Applied Mechanics and Engineering,* 213–216: 362-382, 2012, DOI: http://dx.doi.org/10.1016/j.cma.2011.11.023.

[39] Eijo, A., Oñate, E., and Oller, S. A four-noded quadrilateral element for composite laminated plates/shells using the refined zigzag theory. *Int. J. Numer. Meth. Engng*, 95: 631-660, 2013, DOI: http://dx.doi.org/10.1002/nme.4503.

[40] Eijo, A., Oñate, E., and Oller, S. A numerical model of delamination in composite laminated beams using the LRZ beam element based on the refined zigzag theory. *Composite Structures*, 104: 270-280, 2013, DOI: http://dx.doi.org/10.1016/j.compstruct.2013.04.035.

[41] Eijo, A., Oñate, E., and Oller, S. Delamination in laminated plates using the 4-noded quadrilateral QLRZ plate element based on the refined zigzag theory. *Composite Structures*, 108: 456–471, 2014, DOI: http://dx.doi.org/10.1016/j.compstruct.2013.09.052.

[42] Gherlone, M., Tessler, A., and Di Sciuva, M. C^0 beam element based on the refined zigzag theory for multilayered composite and sandwich laminates. *Composite Structures*, 93: 2882-2894, 2011.

[43] Versino, D., Gherlone, M., Mattone, M., Sciuva, M. D., and Tessler, A. C0 triangular elements based on the Refined Zigzag Theory for multilayer composite and sandwich plates. *Composites Part B: Engineering (online)*, -: -, 2012.

[44] Barut, A., Madenci, E., and Tessler, A., "A refined zigzag theory for laminated composite and sandwich plates incorporating thickness stretch deformation," in *53rdAIAA/ASME/ASCE/AHS/ASC structures, structural dynamics, and materials conference*, Honolulu, Hawaii., 2012.

[45] Barut, A., Madenci, E., and Tessler, A. C0-continuous triangular plate element for laminated composite and sandwich plates using the {2,2} – Refined Zigzag Theory. *Composite Structures*, 106: 835-853, 2013.

[46] Harris, C. E., "Opportunities for Next Generation Aircraft Enabled by Revolutionary Materials," in *AIAA SDM Conference*, Denver, EEUU, 2011.

[47] Hill, R. A theory of the yielding and plastic flow of anisotropic metals. *Proceedings of the Royal Society of London, Serie A: Mathematical and Physical Sciences 193*, 1033: 281-297, 1948.

[48] Tsai, S. and Wu, E. M. A general theory of strength for anisotropic materials. *Journal of Composite Materials*, 5: 58-80, 1971.

[49] Hashin, Z. Failure criteria for unidirectional fiber composites. *Journal of Applied Mechanics*, 47: 329-334, 1980.

[50] Goyal, V. K., Jaunky, N. R., Johnson, E. R., and Ambur, D. R. Intralaminar and interlaminar progressive failure analyses of composite panels with circular cutouts. *Composite Structures*, 64: 91-105, 2004.

[51] Puck, A. and Schürmann, H. Failure analysis of FRP laminates by means of physically based phenomenological models. *Composites Science and Technology,* 58: 1045-1067, 1998.

[52] Dávila, C. G., Camanho, P. P., and Rose, C. A. Failure Criteria for FRP Laminates. *Journal of Composite Materials,* 39: 323-345, 2005.

[53] Pinho, S. T., Dávila, C. G., Camanho, P. P., Ianucci, L., and Robinson, P., "Failure models and criteria for FRP under in-plane or three-dimensional stress states including shear non-linearity," NASA, Technical Memorandum TM-2005-213530, 2005.

[54] ASTM Standard D3039 / D3039M - 00. *Standard Test Method for Tensile Properties of Polymer Matrix Composite Materials*. American Society for Testing and Materials, West Conshohokken, PA, USA, 2000.

[55] ASTM Standard D3410 / D3410M - 03. *Standard Test Method for Compressive Properties of Polymer Matrix Composite Materials with Unsupported Gage Section by Shear Loading*. American Society for Testing and Materials, West Conshohokken, PA, USA, 2003.

[56] DIN Standard DIN EN 2561. *Aerospace series - Carbon fibre reinforced plastics - Unidirectional Laminates - Tensile test parallel to the fibre direction*. Deutsches Institut für Normung, Berlin, Germany, responsible committee NA 131-02-01 AA, 1995.

[57] DIN Standard DIN EN 2597. *Aerospace series - Carbon fibre reinforced plastics - Unidirectional Laminates - Tensile test perpendicular to the fibre direction - German version EN 2597:1998*. Deutsches Institut für Normung, Berlin, Germany, responsible committee NA 131-02-01 AA, 1998.

[58] DIN Standard DIN EN 2850. *Aerospace series - Carbon fibre thermosetting resin unidirectional laminates - Compression test parallel to fibre direction*. Deutsches Institut für Normung, Berlin, Germany, responsible committee NA 131-02-01 AA, 1998.

[59] Oller, S., Martínez, X., Barbat, A., and Rastellini, F. Advanced composite material simulation. *Ciência e Tecnologia dos Materiais,* 20: 2008.

[60] Martinez, X., "Micro mechanical simulation of composite materials using the Serial/Parallel Mixing Theory," Dto. Resistencia de Materiales, Universidad Politécnica de Cataluña, Barcelona, Spain, 2008.

[61] Truesdell, C. and Toupin, R. The classical field theories, handbuch der physik iii/i ed. Berlin, Germany,, Springer-Verlag, 1960.

[62] Car, E., Oller, S., and Oñate, E. An anisotropic elastoplastic constitutive model for large strain analysis of fiber reinforced composite materials. *Computer Methods in Applied Mechanics and Engineering,* 185: 245–277, 2000.

[63] Rastellini, F., Oller, S., Salomon, O., and Oñate, E. Composite materials non-linear modelling for long fibre reinforced laminates: continuum basis, computational aspects and validations. *Computers & Structures,* 86: 879-896, 2008.

[64] Bolotin, V. V. Delaminations in composite structures: its origin, buckling, growth and stability. *Composites: Part B,* 27B: 129-145, 1996.

[65] Villaverde, B. N., "Variable mixed-mode delamination in composite laminates under fatigue conditions: Testing and analysis.," Departament of Physics of University of Girona, Girona, Spain, 2004.

[66] ASTM Standard D2344 / D2244M - 00 (2006). *Standard Test Method for Short-Beam Strength of Polymer Matrix Composite Materials and Their Laminates*. American Society for Testing and Materials, West Conshohokken, PA, USA, 2006.

[67] DIN Standard DIN EN 6033. *Aerospace series - Carbon fibre reinforced plastics - Test metod - Determination of interlaminar fracture toughness energy - Mode I - GIc*. Deutsches Institut für Normung, Berlin, Germany, responsible committee NA 131-02-01 AA, 1996.

[68] ASTM Standard D5528-01 (2007) E1. *Standard Test Method for Mode I Interlaminar Fracture Toughness of Inidirectional Fiber-Reinforced Polymer Matrix Composites*. American Society for Testing and Materials, West Conshohokken, PA, USA, 2007.

[69] DIN Standard DIN EN 6033. *Aerospace series - Carbon fibre reinforced plastics - Test metod - Determination of interlaminar fracture toughness energy - Mode II - GIIc*. Deutsches Institut für Normung, Berlin, Germany, responsible committee NA 131-02-01 AA, 1996.

[70] Lee, S. M. An edge crack torsion method for mode III delamination fracture testing. *Journal of Composites Technology and Research 15,* 3: 193-201, 1993.

[71] ASTM Standard D6671 / D6671M - 06. *Standard Test Method for Mixed Mode I - Mode II Interlaminar Fracture Toughness of Inidirectional Fiber-Reinforced Polymer Matrix Composites*. American Society for Testing and Materials, West Conshohokken, PA, USA, 2006.

[72] Reeder, J. 3d mixed mode delamination fracture criteria-an experimentalist perspective. NASA Langley research center,M/S 188E, Hampton VA 23681-2199,USA.

[73] Benzeggagh, M. and Kenane, M. Measurement of Mixed-Mode Delamination Fracture Toughness of Unidirectional Glass/Epoxy Composites with Mixed-Mode Bending Apparatus. *Composite Science and Technology,* 56: 439, 1996.

[74] Wu, E. M. and Reuter-Jr., R. C. Crack Extension in Fiberglass Reinforced Plastics. *T and M Report, University of Illinois,* 275: . 1965.

[75] Greenhalgh, E., Asp, L., and Singh, S., "Delamination resistance, failure criteria and fracture morphology of 0º/0º, 0º/5º and 0º/90º ply interface in cfrp," in *5th International Conference on Deformation and Fracture of Composite*, London, United Kingdom, 1999.

[76] Rybicki, E. F. and Kanninen, M. F. A finite element calculation of stress intensity factors by a modified crack closure integral. *Engineering Fracture Mechanics,* 9: 931-938, 1977.

[77] Cherepanov, G. P. The propagation of cracks in a continuous medium. *Journal of Applied Mathematics and Mechanics,* 31: 503-512, 1967.

[78] Rice, J. R. A Path Independent Integral and the Approximate Analysis of Strain Concentration by Notches and Cracks. *Journal of Applied Mechanics,* 35: 379-386, 1968.

[79] Hellen, T. K. On the Method of Virtual Crack Extension. *Int. J. Numer. Meth. Engng,* 9: 187-207, 1975.

[80] Klug, J., Wu, X. X., and Sun, C. T. Efficient modeling of postbuckling delamination growth in composite laminates using plate elements. *AIAA,* 34: 178-184, 1996.

[81] Gaudenzi, P., Perugini, P., and Riccio, A. Post-buckling behavior of composite panels in the presence of unstable delaminations. *Composite Structures,* 51: 301-309, 2001.

[82] Liu, P. F., Hou, S. J., Chu, J. K., Hu, X. Y., Zhou, C. L., Liu, Y. L., Zheng, J. Y., Zhao, A., and Yan, L. Finite element analysis of postbuckling and delamination of composite laminates using virtual crack closure technique. *Composite Structures,* 93: 1549–1560, 2011.

[83] Wang, J. T. and Raju, I. S. Strain energy release rate farmulae for skin-stiffener debond modeled with plate elements. *Engineering Fracture Mechanics,* 54: 211-228, 1996.

[84] Krueger, R., Paris, I. L., O'Brien, T. K., and Minguet, P. J., "Fatigue Lifo Methodology for Bonded Composite Skin Stringer Configurations," NASA, Technical Memorandum TM-2001-210842 ARL-TR-2432, 2002.

[85] Krueger, R., Paris, I. L., O'Brien, T. K., and Minguet, P. J. Comparison of 2D finite element modeling assumptions with results from 3D analysis for composite skin-stiffener debonding. *Composite Structures,* 57: 161-168, 2002.

[86] Saeedi, N., Sab, K., and Caron, J. F. Cylindrical bending of multilayered plates with multi-delamination via a layerwise stress approach. *Composite Structures,* 95: 728-739, 2013.

[87] Barbero, E. J. and Reddy, J. N. Modeling of delamination in laminates using a layer-wise plate theory. *International Journal of Solids and Structures,* 28: 373-388, 1991.

[88] Dudgale, D. S. Yielding of steel sheets containing slits. *Journal of Mechanics and Physics of Solids,* 8: 100-104, 1960.

[89] Barenblatt, G. I. The mathematical theory of equilibrium cracks in brittle failure. *Advances in Applied Mechanics,* 7: 1962.

[90] Wagner, W., Gruttmann, F., and Sprenger, W. A finite element formulation for the simulation of propagating delaminations in layered composite structures. *Int. J. Numer. Meth. Engng,* 51: 1337-1359, 2001.

[91] Balzani, C. and Wagner, W. An interface element for the simulation of delamination in unidirectional fiber-reinforced composite laminates. *Engineering Fracture Mechanics,* 75: 2597-2615, 2008.

[92] Camanho, P. P. and Dávila, C. G., "Mixed-mode decohesion finite elements for the simulation of delamination in composite materials," NASA, Technical Memorandum TM-211737, 2002.

[93] Zou, Z., Reid, S. R., and Li, S. A continuum damage model for delaminations in laminated composites. *Journal of the Mechanics and Physics of Solids,* 51: 333-356, 2003.

[94] Turon, A., Camanho, P. P., Costa, J., and Da´vila, C. G. A damage model for the simulation of delamination in advanced composites under variable-mode loading. *Mechanics of Materials,* 38: 1072–1089, 2006.

[95] Balzani, C. and Wagner, W. Numerical treatment of damage propagation in axially compressed composite airframe panels. *Int. J. Struct. Stab. Dyn.,* 10: 683-703, 2010.

[96] Turon, A., "Simulation of delamination in composite under quasi-static and fatigue loading using cohesive zone models," University of Girona, Girona, Spain, 2007.

[97] Turon, A., Camanho, P. P., Costa, J., and Renart, J. Accurate simulation of delamination growth under mixed-mode loading using cohesive elements: Definition of interlaminar strengths and elastic stiffness. *Composite Structures,* 92: 1857–1864, 2010.

[98] Wagner, W. and Balzani, C. Simulation of delamination in stringer stiffened fiber-reinforced composite shells. *Computers and Structures,* 86: 930-939, 2008.

[99] Na, W. J. and Reddy, J. N. Delamination in cross-ply laminated beams using the layerwise theory. *Asian Journal of Civil Engineering,* 10: 451-480, 2009.

[100] Hosseini-Toudeshky, H., Hosseini, S., and Mohammadi, B. Delamination buckling growth in laminated composites using

layerwise-interface element. *Composite Structures,* 92: 1846-1856, 2010.

[101] Williams, T. O. and Addessio, F. L. A general theory for laminated plates with delaminations. *International Journal of Solids and Structures,* 34: 2003-2024, 1997.

[102] Sciuva, M. D. and Gherlone, M. A global/local third-order Hermitian displacement field with damaged interfaces and transverse extensibility: FEM formulation. *Composite Structures,* 59: 433-444, 2003.

[103] Sciuva, M. D. and Gherlone, M. Quasi-3D static and dynamic analysis of undamaged and damaged sandwich beams. *Journal of Sandwich Structures and Materials,* 7: 31-52, 2005.

[104] Icardi, U. and Zardo, G. C0 Plate element for delamination damage analysis, based on a zig-zag model and strain energy updating. *International Journal of Impact Engineering,* 31: 579-606, 2005.

[105] Icardi, U. C0 plate element based on strain energy updating and spline interpolation, for analysis of impact damage in laminated composites. *International Journal of Impact Engineering,* 34: 1835-1868, 2007.

[106] Icardi, U. and Ferrero, L. Impact analysis of sandwich composites based on a refined plate element with strain energy updating. *Composite Structures,* 89: 35-51, 2009.

[107] Zienkiewicz, O. C. and Taylor, R. L. Finite element method. Vol. 1, 5 Ed. Oxford, UK, Butterworth-Heinemann, 2000.

[108] Oñate, E. Structural analysis by the finite element method. Vol. 2: Beams, plates and shells Barcelona, Springer-CIMNE, 2013.

[109] Dvorkin, E. N. and Bathe, K. J. A continuum mechanics based four node shell element for general non-linear analysis. *Engineering computations,* 1: 77-88, 1984.

[110] Bathe, K. J. and Dvorkin, E. N. A four node plate bending element based on Mindlin-Reissner plate theory and mixed interpolation. *Int. Journal for Numerical Methods in Engineering,* 21: 367-383, 1985.

[111] Hinton, E. and Huang, H. C. A family of quadrilateral Mindlin plate elements with substitute shear strain fields. *Computers & Structures,* 23: 409 - 431, 1986.

[112] Oñate, E., Zienkiewicz, O., Suárez, B., and Taylor, R. L. A general methodology for deriving shear constrained Reissner-Mindlin plate elements. *Int. Journal for Numerical Methods in Engineering,* 33: 345-367, 1992.

[113] Soden, S. P., Hinton, M. J., and Kaddour, A. S. Lamina properties, lay-up configurations and loading conditions for a range of fibre-reinforced composite laminates. *Compos Sci Technol,* 58: 1011-1022, 1998.

[114] Simo, J. C. and Ju, J. W. Strain - and stress - based continuum damage models - I. Formulation. *International Journal Solids Structures*, 23: 821-840, 1987.

[115] Simo, J. C. and Ju, J. W. Strain - and stress - based continuum damage models - II. Computational aspects. *International Journal Solids Structures*, 23: 841-869, 1987.

[116] Chaboche, J. L. Continuum damage mechanics: Part I - General concepts. *Journal of Applied Mechanics*, 55: 59-64, 1988.

[117] Chaboche, J. L. Continuum damage mechanics: Part II - Damage growth, crack initiation, and crack growth. *Journal of Applied Mechanics*, 55: 65-72, 1988.

[118] Oliver, J., Cervera, M., Oller, S., and Lubliner, J., "Isotropic damage models and smeared crack analysis of concret," in *Second international conference on computer aided analysis and design of concrete structures*. Zell am See, Austria, 1990.

[119] Oller, S. Fractura mecánica. Un enfoque global., 1ra Ed. Barcelona, España, CIMNE, 2001.

[120] Zienkiewicz, O. C. and Taylor, R. L. El método de los elementos finitos. Vol. 2, 5 Ed. Barcelona, CIMNE, 2004.

[121] International Center for Numerical Methods in Engineering, 2011. Implicit finite element code for the simulation of composite materials. https://web.cimne.upc.edu/users/plcd/.

[122] International Center for Numerical Methods in Engineering, 2010. Pre- and post-processor software. http://gid.cimne.upc.es/.

Appendix

Copies of following four papers are shown below:

- Oñate, E., Eijo, A., and Oller, S. Simple and accurate two-noded beam element for composite laminated beams using a refined zigzag theory. *Computer Methods in Applied Mechanics and Engineering* (IF: 2.617), 213–216: 362-382, 2012.
  DOI: http://dx.doi.org/10.1016/j.cma.2011.11.023.

- Eijo, A., Oñate, E., and Oller, S. A four-noded quadrilateral element for composite laminated plates/shells using the refined zigzag theory. *Int. J. Numer. Meth. Engng* (IF: 2.068), 95: 631-660, 2013.
  DOI: http://dx.doi.org/10.1002/nme.4503.

- Eijo, A., Oñate, E., and Oller, S. A numerical model of delamination in composite laminated beams using the LRZ beam element based on the refined zigzag theory. *Composite Structures* (IF: 2.231), 104: 270-280 2013.
  DOI: http://dx.doi.org/10.1016/j.compstruct.2013.04.035.

- Eijo, A., Oñate, E., and Oller, S. Delamination in laminated plates using the 4-noded quadrilateral QLRZ plate element based on the refined zigzag theory. *Composite Structures* (IF: 2.231), 108: 456–471, 2014.
  DOI: http://dx.doi.org/10.1016/j.compstruct.2013.09.052.

Comput. Methods Appl. Mech. Engrg. 213–216 (2012) 362–382

Contents lists available at SciVerse ScienceDirect

Comput. Methods Appl. Mech. Engrg.

journal homepage: www.elsevier.com/locate/cma

Simple and accurate two-noded beam element for composite laminated beams using a refined zigzag theory

E. Oñate [a,b,*], A. Eijo [a], S. Oller [a,b]

[a] International Center for Numerical Methods in Engineering (CIMNE), Campus Norte UPC, 08034 Barcelona, Spain
[b] Universitat Politècnica de Catalunya (UPC), Campus Norte UPC, 08034 Barcelona, Spain

ARTICLE INFO

Article history:
Received 7 October 2010
Received in revised form 2 November 2011
Accepted 24 November 2011
Available online 3 December 2011

Keywords:
Two-noded beam element
Zigzag kinematics
Timoshenko theory
Composite
Sandwich beams

ABSTRACT

In this work we present a new simple linear two-noded beam element adequate for the analysis of composite laminated and sandwich beams based on the combination of classical Timoshenko beam theory and the refined zigzag kinematics proposed by Tessler et al. [22]. The element has just four kinematic variables per node. Shear locking is eliminated by reduced integration. The accuracy of the new beam element is tested in a number of applications to the analysis of composite laminated beams with simple supported and clamped ends under point loads and uniformly distributed loads. An example showing the capability of the new element for accurately reproducing delamination effects is also presented.

1. Introduction

It is well known that both the classical Euler–Bernouilli beam theory [1] and the more advanced Timoshenko theory [2] produce inadequate predictions when applied to relatively thick composite laminated beams with material layers that have highly dissimilar stiffness characteristics. Even with a judiciously chosen shear correction factor, Timoshenko theory tends to underestimate the axial stress at the top and bottom outer fibers of a beam. Also, along the layer interfaces of a laminated beam the transverse shear stresses predicted exhibit erroneous discontinuities. These difficulties are due to the higher complexity of the "true" variation of the axial displacement field across a highly heterogeneous beam cross-section.

Indeed to achieve accurate computational results, 3D finite element analyses are often preferred over beam models. For composite laminates with hundred of layers, however, 3D modelling becomes prohibitively expensive, specially for non linear and progressive failure analyses.

Improvements to the classical beam theories have been obtained by the so called equivalent single layer (ESL) theories that assume a priori the behavior of the displacement and/or the stress through the laminate thickness [3,4]. Despite being computationally efficient, ESL theories often produce inaccurate distributions for the stresses and strains (in particular the transverse shear stress) across the thickness.

The need for composite laminated beam theories with better predictive capabilities has led to the development of the so-called *higher order* theories. In these theories higher-order kinematic terms with respect to the beam depth are added to the expression for the axial displacement and, in some cases, to the expressions for the deflection. A review of these theories can be found in [3,4].

Accurate predictions of the correct shear and axial stresses for thick and highly heterogenous composite laminated and sandwich beams can be obtained by using *layer-wise* theory. In this theory the thickness coordinate is split into a number of *analysis layers* that may or not coincide with the number of laminate plies. The kinematics are independently described within each layer and certain physical continuity requirements are enforced [3,4].

A drawback of layer-wise theory is that the number of kinematic variables depends on the number of analysis layers. The layer displacements can be condensed at each section in terms of the axial displacement for the top layer during the equation solution process [5,6]. The displacement condensation processes can be however expensive for problems involving many analysis layers.

* Corresponding author at: Universitat Politècnica de Catalunya (UPC), Campus Norte UPC, 08034 Barcelona, Spain.
E-mail address: onate@cimne.upc.edu (E. Oñate).
URL: http://www.cimne.com/eo (E. Oñate).

0045-7825/$ - see front matter © 2011 Elsevier B.V. All rights reserved.
doi:10.1016/j.cma.2011.11.023

Discrete layer theories in which the number of unknowns in the model does not depend on the number of layers in the laminate are described in [7–9]. In this class of discrete layerwise theories (called zigzag theories) a piecewise linear in-plane displacement function (the zigzag function) is superimposed over a linear displacement field [7,8], a quadratic displacement field [10,11] or a cubic displacement field [12–15] through the thickness of the laminate.

Many zigzag theories require C^1 continuity for the deflection field, which is a drawback versus simpler C^0 continuous FEM approximations. Also many zigzag theories run into theoretical difficulties to satisfy equilibrium of forces at a clamped support.

Averill et al. [9,10,16,17] developed linear, quadratic and cubic zigzag beam theories that overcame the need for C^1 continuity. The shear strain angle is introduced as a kinematic variable together with the deflection, the rotation and the zigzag function. A C^0 interpolation can be used for all these variables. The relationship between the shear angle, the deflection and the rotation of each layer is introduced as a constraint via a penalty method. This also ensures the continuity of the transverse shear stress across the laminate depth and the satisfaction of the shear traction boundary conditions. However, Averill theories have difficulties to model correctly clamped boundary conditions. For this reason, analytical and numerical (FEM) studies based on Averill theory have mainly focused on simple supported beams [16,17].

A 2-noded beam element based on Euler–Bernouilli beam theory and an extension of Averill's zigzag theory including a cubic in-plane displacement field within each layer has been recently proposed by Alam and Upadhyay [18]. Good results are reported for cantilever and clamped composite and sandwich beams.

An assessment of different zigzag theories for beam is reported in [19,20]. A review of zigzag theory for plate analysis can be found in [21].

Tessler et al. [22,23] have developed a refined zigzag (RZ) theory starting from the standard Timoshenko kinematic assumptions. This allows one using C^0 continuous interpolation for all the kinematic variables. Timoshenko beam theory also introduces naturally shear deformation effect for the homogeneous material case, which is advantageous for many problems. The zigzag functions chosen have the property of vanishing on the top and bottom surfaces of a laminate. A particular feature of this zigzag theory is that the transverse shear stresses are not required to be continuous at the layer interfaces. This results in simple piecewise-constant functions that approximate the true shear stress distribution. An accurate continuous thickness distribution of the transverse shear stress can be obtained "a posteriori" in terms of the axial stress by integrating the equilibrium equations. This theory also provides good results for clamped supports.

Gherlone et al. [24] have developed two and three-noded C^0 beam elements based on the RZ theory for analysis of multilayered composite and sandwich beams. Locking-free elements are obtained by using *anisoparametric* interpolations that are adapted to approximate the four independent kinematic variables that model the beam deformation. A family of beam elements is achieved by imposing different constraints on the original displacement approximation. The constraint conditions requiring a constant variation of the transverse shear force provide an accurate 2-noded beam element [24].

Quite simultaneously to the above work, Oñate et al. [25] proposed a simple 2-noded beam element for composite laminated beams based on the RZ theory. A standard linear displacement field is used to model the four variables of the so called LRZ element. Shear locking is avoided by using reduced integration on selected terms of the shear stiffness matrix.

In this paper we present in detail the formulation of the LRZ beam element originally reported in [25] and explore the capabilities of the new element for multilayered beams and delamination analysis. A study of the locking-free behavior of the LRZ element for slender beams is presented. The good performance of the element is demonstrated for simply supported and clamped composite laminated beams with different layers under point load and uniformly distributed loads.

Finally, an example showing the capability of the LRZ element to model delamination effects is presented.

2. General concepts of zigzag beam theory

The kinematic field in zigzag beam theory is generally written as

$$\begin{aligned} u^k(x,z) &= u_0(x) - z\theta(x) + \bar{u}^k(x,z), \\ w(x,z) &= w_0(x), \end{aligned} \tag{1a}$$

where

$$\bar{u}^k = \phi^k(z)\Psi(x), \quad k = 1, N \tag{1b}$$

is the *zigzag displacement function* (Fig. 1).

In Eqs. (1) N is the number of layers, superscript k indicates quantities within the kth layer with $z_k \leqslant z \leqslant z_{k+1}$ and z_k is the vertical coordinate of the kth interface. In Eq. (1a) the uniform axial displacement $u_0(x)$, the rotation $\theta(x)$ and the transverse deflection $w_0(x)$ are the primary kinematic variables of the underlying equivalent single-layer Timoshenko beam theory. In Eq. (1b) function $\phi^k(z)$ denotes *a piecewise linear zigzag function*, yet to be established, and $\Psi(x)$ is a primary kinematic variable that defines the *amplitude of the zigzag function* along the beam. Collectively, the interfacial axial displacement field has a zigzag distribution, as shown in Fig. 1c.

The strain–displacement relations are derived by substituting Eq. (1a) into the expressions of classical Timoshenko beam theory, i.e.

$$\varepsilon_x^k = \frac{\partial u^k}{\partial x} = \frac{\partial u_0}{\partial x} - z\frac{\partial \theta}{\partial x} + \phi^k \frac{\partial \Psi}{\partial x} = [1, -z, \phi^k] \left\{ \begin{matrix} \frac{\partial u_0}{\partial x} \\ \frac{\partial \theta}{\partial x} \\ \frac{\partial \Psi}{\partial x} \end{matrix} \right\} = \mathbf{S}_p \hat{\boldsymbol{\varepsilon}}_p, \tag{2a}$$

$$\gamma_{xz}^k = \frac{\partial u^k}{\partial z} + \frac{\partial w}{\partial x} = \frac{\partial w_0}{\partial x} - \theta + \frac{\partial \phi^k}{\partial z}\Psi = \gamma + \beta^k \Psi = [1, \beta^k] \left\{ \begin{matrix} \gamma \\ \Psi \end{matrix} \right\} = \mathbf{S}_t \hat{\boldsymbol{\varepsilon}}_t. \tag{2b}$$

In Eqs. (2a) and (2b)

$$\begin{aligned} &\mathbf{S}_p = [1, -z, \phi^k], \quad \hat{\boldsymbol{\varepsilon}}_p = \left[\frac{\partial u_0}{\partial x}, \frac{\partial \theta}{\partial x}, \frac{\partial \Psi}{\partial x}\right]^T, \\ &\mathbf{S}_t = [1, \beta^k], \quad \hat{\boldsymbol{\varepsilon}}_t = [\gamma, \Psi]^T, \end{aligned} \tag{2c}$$

where $\hat{\boldsymbol{\varepsilon}}_p$ and $\hat{\boldsymbol{\varepsilon}}_t$ are the generalized in-plane and transverse shear strain vectors, respectively. Vector $\hat{\boldsymbol{\varepsilon}}_p$ contains the axial elongation $\left(\frac{\partial u_0}{\partial x}\right)$, the pseudo-curvature $\left(\frac{\partial \theta}{\partial x}\right)$ and the derivatives of the amplitude of the zigzag function $\left(\frac{\partial \Psi}{\partial x}\right)$. In $\hat{\boldsymbol{\varepsilon}}_t$, $\gamma = \frac{\partial w_0}{\partial x} - \theta$ is the average transverse shear strain of Timoshenko beam theory and $\beta^k = \frac{\partial \phi^k}{\partial z}$. Note that since $\phi^k(z)$ is piecewise linear, β^k is constant across each layer.

For major principal material axes that are coincident with the beam x-axis, Hooke stress–strain relations for the kth orthotropic layer have the standard form

$$\sigma_x^k = E^k \varepsilon_x^k = E^k \mathbf{S}_p \hat{\boldsymbol{\varepsilon}}_p, \tag{3a}$$

$$\tau_{xz}^k = G^k \gamma_{xz}^k = G^k \mathbf{S}_t \hat{\boldsymbol{\varepsilon}}_t, \tag{3b}$$

where E^k and G^k are the axial and shear moduli for the kth layer, respectively.

In the above equations we have distinguished all variables within a layer with superscript k.

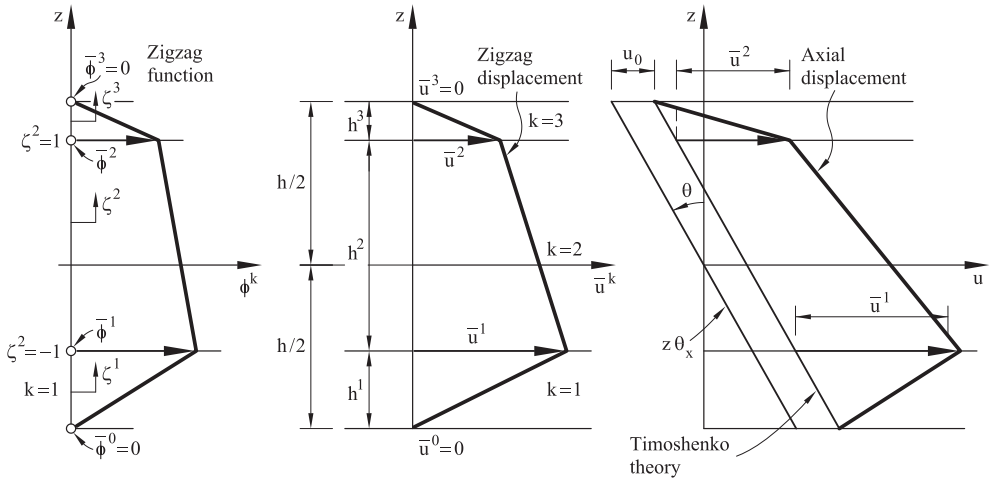

Fig. 1. Thickness distribution of the zigzag function ϕ^k (a), the zigzag displacement function $\bar{u}^k$ (b), and the axial displacement (c) in refined zigzag beam theory.

3. Refined zigzag theory

3.1. Zigzag kinematics

The key attributes of the refined zigzag (RZ) theory proposed by Tessler et al. [22] are, first, *the zigzag function vanishes at the top and bottom surfaces of the beam* section and does not require full shear-stress continuity across the laminated-beam depth. Second, all boundary conditions can be modeled adequately. And third, C^0 continuity is only required for the FEM approximation of the kinematic variables.

Within each layer the zigzag function is expressed as

$$\phi^k = \frac{1}{2}(1-\zeta^k)\bar{\phi}^{k-1} + \frac{1}{2}(1+\zeta^k)\bar{\phi}^k = \frac{\bar{\phi}^k + \bar{\phi}^{k-1}}{2} + \frac{\bar{\phi}^k - \bar{\phi}^{k-1}}{2}\zeta^k, \quad (4)$$

where $\bar{\phi}^k$ and $\bar{\phi}^{k-1}$ are the zigzag function values of the k and $k-1$ interface, respectively with $\bar{\phi}^0 = \bar{\phi}^N = 0$ and $\zeta^k = \frac{2(z-z^{k-1})}{h^k} - 1$.

Collectively, function ϕ^k has the zigzag distribution shown in Fig. 1a. Due to the dependence between the zigzag displacement function $\tilde{u}^k$ and $\bar{\phi}^k$ (see Eq. (1b)), $\tilde{u}^k$ also vanishes at the top and bottom layers. The axial displacement field is plotted in Fig. 1c.

The above form of ϕ^k gives the constant value of β^k for each layer as

$$\beta^k = \frac{\partial \phi^k}{\partial z} = \frac{\bar{\phi}^k - \bar{\phi}^{k-1}}{h^k} \quad (5a)$$

and

$$\iint_A \beta^k dA = 0. \quad (5b)$$

The β^k parameter is useful for computing the zigzag function as explained in the next section.

3.2. Computation of the zigzag function

Integrating Eq. (2b) over the cross section and using Eq. (5b) and the fact that Ψ is independent of z yields

$$\gamma = \frac{1}{A}\iint_A \gamma_{xz}^k dA \quad (6)$$

i.e. γ represents the average shear strain of the cross section, as expected.

The shear strain–shear stress relationship of Eq. (3b) is written as

$$\tau_{xz}^k = G^k \eta + G^k(1+\beta^k)\Psi, \quad (7)$$

where $\eta = \gamma - \Psi$ is a difference function.

Remark 1. Function Ψ can be interpreted as a weighted-average shear strain angle [22]. The value of Ψ should be prescribed to zero at a clamped edge and left unprescribed at free and simply supported edges.

Eq. (7) shows that the distribution of τ_{xz}^k within each layer is constant, as η is independent of the zigzag function and β^k is constant.

The distribution of τ_{xz}^k is now *enforced to be independent of the zigzag function*. This can be achieved by constraining the term multiplying Ψ in Eq. (7) to be constant, i.e.

$$G^k(1+\beta^k) = G^{k+1}(1+\beta^{k+1}) = G, \quad \text{constant}. \quad (8)$$

This is equivalent to enforcing the interfacial continuity of the second term in the r.h.s. of Eq. (7).

Remark 2. We emphasize that this zigzag theory does not enforce the continuity of the transverse shear stresses across the section. This is consistent with the kinematic freedom inherent in the lower order kinematic approximation of the underlying beam theory. An accurate continuous distribution of the transverse shear stress across the thickness of the laminate can be obtained "a posteriori" in terms of axial stresses by integrating the equilibrium equations as explained in Section 7.3.

From Eq. (8) we deduce

$$\beta^k = \frac{G}{G^k} - 1. \quad (9)$$

Substituting β^k in the integral of Eq. (5b) gives

$$G = \left[\frac{1}{A}\iint_A \frac{dA}{G^k}\right]^{-1} = \left[h\sum_{k=1}^{N}\frac{h^k}{G^k}\right]^{-1}, \quad (10)$$

where h is the section depth. Substituting Eq. (9) into Eq. (5a) gives the following recursion relation for the zigzag displacement function values at the layer interfaces

$$\bar{u}_k = \sum_{i=1}^{k} h^i \beta^i \quad \text{with} \quad u^0 = u^N = 0. \quad (11)$$

Introducing Eq. (11) into (4) gives the expression for the zigzag function as

$$\phi^k = \frac{h^k \beta^k}{2}(\zeta^k - 1) + \sum_{i=1}^{k} h^i \beta^i. \quad (12)$$

Recall that superindex k denotes the number of each material layer.

Remark 3. For homogeneous material $G^k = G$ and $\beta^k = 0$. Hence, the zigzag function ϕ^k vanishes and we recover the kinematics and constitutive expressions of the standard Timoshenko composite laminated beam theory. This is a particular feature of this zigzag theory.

Remark 4. Note that differently from standard Timoshenko beam theory, a shear correction parameter is not needed in the RZ theory.

3.3. Constitutive relationship

The in-plane bending and transverse shear resultant stresses are defined as

$$\hat{\boldsymbol{\sigma}}_p = \left\{ \begin{array}{c} N \\ M \\ M_\phi \end{array} \right\} = \iint_A \mathbf{S}_p^T \sigma_x^k dA = \left(\iint_A \mathbf{S}_p^T \mathbf{S}_p E^k dA \right) \hat{\boldsymbol{\varepsilon}}_p = \widehat{\mathbf{D}}_p \hat{\boldsymbol{\varepsilon}}_p, \tag{13}$$

$$\hat{\boldsymbol{\sigma}}_t = \left\{ \begin{array}{c} Q \\ Q_\phi \end{array} \right\} = \iint_A \mathbf{S}_t^T \tau_{xz}^k dA = \left(\iint_A \mathbf{S}_t^T \mathbf{S}_t G^k dA \right) \hat{\boldsymbol{\varepsilon}}_t = \widehat{\mathbf{D}}_t \hat{\boldsymbol{\varepsilon}}_t. \tag{14}$$

In vectors $\hat{\boldsymbol{\sigma}}_p$ and $\hat{\boldsymbol{\sigma}}_t$, N, M and Q are respectively the axial force, the bending moment and the transverse shear force of standard beam theory, whereas M_ϕ and Q_ϕ are an additional bending moment and an additional shear force which are conjugate to the new generalized strains $\frac{\partial \Psi}{\partial x}$ and Ψ, respectively.

The generalized constitutive matrices $\widehat{\mathbf{D}}_p$ and $\widehat{\mathbf{D}}_t$ are

$$\widehat{\mathbf{D}}_p = \iint_A E^k \begin{bmatrix} 1 & -z & \phi^k \\ -z & z^2 & -z\phi^k \\ \phi^k & -z\phi^k & (\phi^k)^2 \end{bmatrix} dA, \quad \widehat{\mathbf{D}}_t = \begin{bmatrix} D_s & -g \\ -g & g \end{bmatrix} \tag{15a}$$

with

$$D_s = \iint_A G^k dA, \quad g = D_s - GA. \tag{15b}$$

In the derivation of the expression for $\widehat{\mathbf{D}}_t$ we have used the definition of β^k of Eq. (9).

The generalized constitutive equation can be written as

$$\hat{\boldsymbol{\sigma}} = \left\{ \begin{array}{c} \hat{\boldsymbol{\sigma}}_p \\ \hat{\boldsymbol{\sigma}}_t \end{array} \right\} = \widehat{\mathbf{D}} \hat{\boldsymbol{\varepsilon}} = \widehat{\mathbf{D}} \left\{ \begin{array}{c} \hat{\boldsymbol{\varepsilon}}_p \\ \hat{\boldsymbol{\varepsilon}}_t \end{array} \right\} \quad \text{with} \quad \widehat{\mathbf{D}} = \begin{bmatrix} \widehat{\mathbf{D}}_p & \mathbf{0} \\ \mathbf{0} & \widehat{\mathbf{D}}_t \end{bmatrix}. \tag{16}$$

3.4. Virtual work expression

The virtual work expression for a distributed load q is

$$\iiint_V (\delta \varepsilon_x^k \sigma_x^k + \delta \gamma_{xz}^k \tau_{xz}^k) dV - \int_l \delta w q dA = 0. \tag{17}$$

The l.h.s. of Eq. (17) contains the internal virtual work performed by the axial and tangential stresses and the r.h.s. is the external virtual work carried out by the distributed load. V and l are the volume and length of the beam, respectively.

Substituting Eqs. (3) into the expression for the virtual internal work and using Eqs. (13) and (14) gives

$$\begin{aligned} \iiint_V (\delta \varepsilon_x^k \sigma_x^k + \delta \gamma_{xz}^k \tau_{xz}^k) dV &= \iiint_V \left(\delta \hat{\boldsymbol{\varepsilon}}_p^T \mathbf{S}_p^T \sigma_x^k + \delta \hat{\boldsymbol{\varepsilon}}_t^T \mathbf{S}_t^T \tau_{xz}^k \right) dV \\ &= \int_l \left(\delta \hat{\boldsymbol{\varepsilon}}_p^T \hat{\boldsymbol{\sigma}}_p + \delta \hat{\boldsymbol{\varepsilon}}_t^T \hat{\boldsymbol{\sigma}}_t \right) dx. \end{aligned} \tag{18}$$

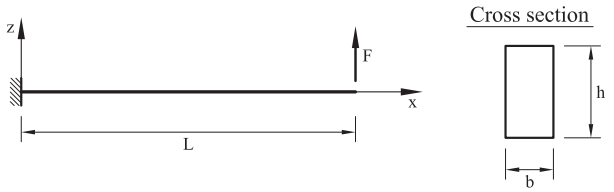

Fig. 2. Cantilever beam under point load.

Table 1
Symmetric 3-layered cantilever beam. Material properties for shear locking study.

	Composite material properties		
	Layer 1 (bottom)	Layer 2 (core)	Layer 3 (top)
h [mm]	6.6667	6.6667	6.6667
E [MPa]	2.19E5	2.19E3	2.19E5
G [MPa]	0.876E5	8.80E2	0.876E5

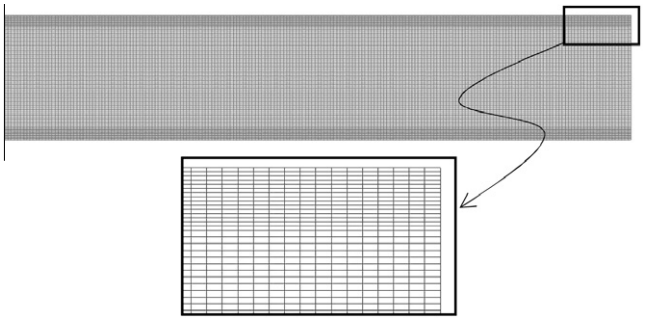

Fig. 3. Mesh of 27,000 4-noded plane stress rectangular elements for analysis of cantilever and simple supported beams.

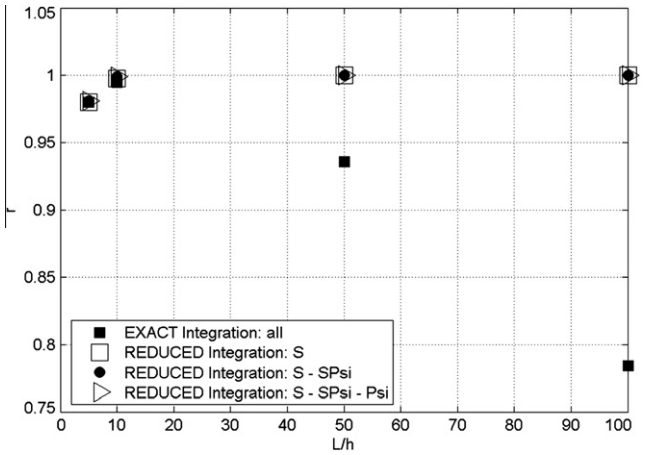

Fig. 4. r Ratio $\left(r = \frac{w_{zz}}{w_{ps}}\right)$ versus L/h for cantilever under point load analyzed with the LRZ element. Labels "*all*", *S*, *SPsi* and *Psi* refer to matrices $\mathbf{K}_t^e$, $\mathbf{K}_s^e$, $\mathbf{K}_{s\psi}^e$ and $\mathbf{K}_\psi^e$, respectively.

The virtual work is therefore written as

$$\int_l \left(\delta \hat{\boldsymbol{\varepsilon}}_p^T \hat{\boldsymbol{\sigma}}_p + \delta \hat{\boldsymbol{\varepsilon}}_t^T \hat{\boldsymbol{\sigma}}_t \right) dx - \int_l \delta w q dx = 0. \tag{19}$$

4. Two-noded LRZ beam element

The four kinematic variables are u_0, w_0, θ and Ψ. They can be discretized using 2-noded linear C^0 beam elements of length l^e in the standard form as

$$\mathbf{u} = \begin{Bmatrix} u_0 \\ w_0 \\ \theta \\ \Psi \end{Bmatrix} = \sum_{i=1}^{2} N_i \mathbf{a}_i = \mathbf{N}\mathbf{a}^e \tag{20}$$

with

$$\mathbf{N} = [N_1\mathbf{I}_4, N_2\mathbf{I}_4], \quad \mathbf{a}^e = \begin{Bmatrix} \mathbf{a}_1 \\ \mathbf{a}_2 \end{Bmatrix}, \quad \mathbf{a}_i = \begin{Bmatrix} u_{0_i} \\ w_{0_i} \\ \theta_i \\ \Psi_i \end{Bmatrix}, \tag{21}$$

where $N_i = \frac{1}{2}(1 + \xi\xi_i)$ with $\xi = 1 - \frac{2x}{l^e}$ are the standard one-dimensional linear shape functions, $\mathbf{a}_i$ is the vector of nodal kinematic variables and $\mathbf{I}_4$ is the 4×4 unit matrix.

Substituting Eq. (20) into the generalized strain vectors in Eq. (2c) gives

$$\hat{\boldsymbol{\varepsilon}}_p = \mathbf{B}_p\mathbf{a}^e, \quad \hat{\boldsymbol{\varepsilon}}_t = \mathbf{B}_t\mathbf{a}^e. \tag{22}$$

The generalized strain matrices $\mathbf{B}_p$ and $\mathbf{B}_t$ are

$$\mathbf{B}_p = [\mathbf{B}_{p_1}, \mathbf{B}_{p_2}], \quad \mathbf{B}_t = [\mathbf{B}_{t_1}, \mathbf{B}_{t_2}] \tag{23a}$$

with

$$\mathbf{B}_{p_i} = \begin{bmatrix} \frac{\partial N_i}{\partial x} & 0 & 0 & 0 \\ 0 & 0 & \frac{\partial N_i}{\partial x} & 0 \\ 0 & 0 & 0 & \frac{\partial N_i}{\partial x} \end{bmatrix}, \tag{23b}$$

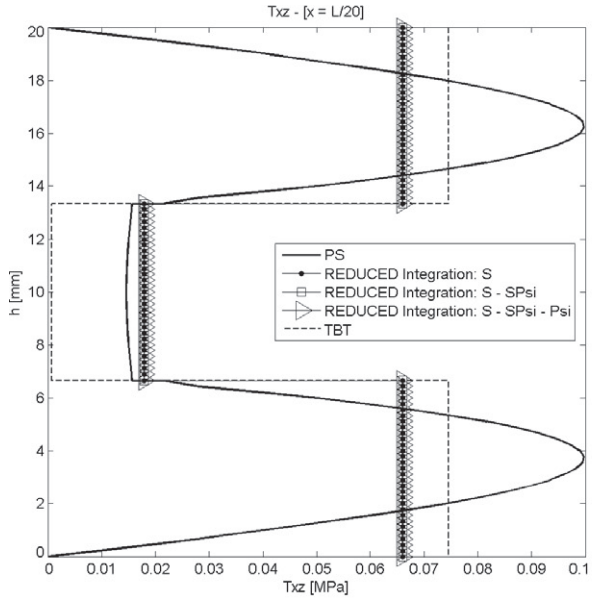

(a) $\tau_{xz}, \lambda = 5, L/20$

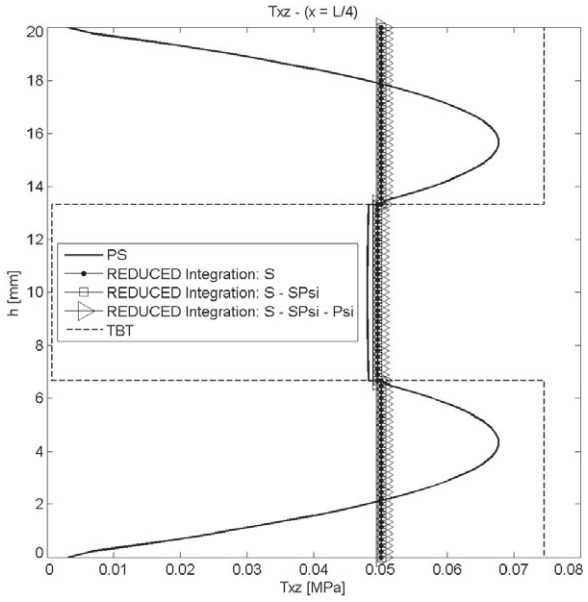

(b) $\tau_{xz}, \lambda = 5, L/4$

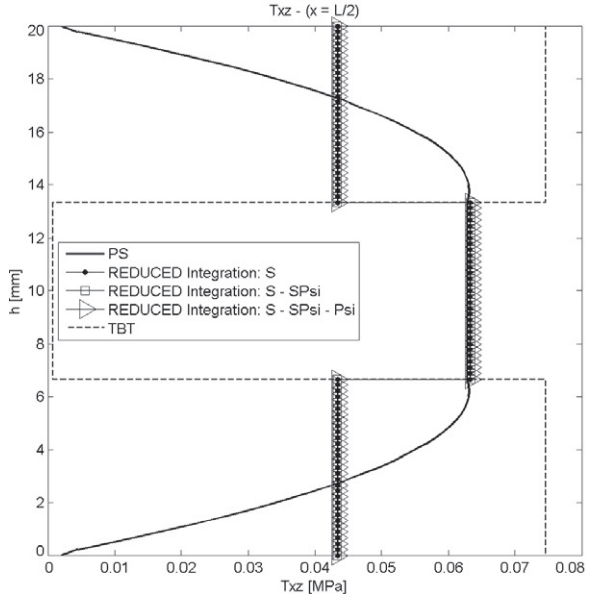

(c) $\tau_{xz}, \lambda = 5, L/2$

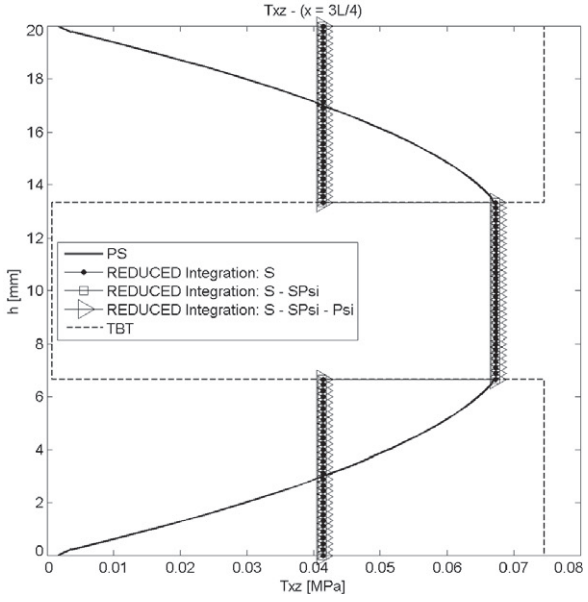

(d) $\tau_{xz}, \lambda = 5, 3L/4$

Fig. 5. Symmetric 3-layered cantilever thick beam under end point load. Thickness distribution of shear stress for $\lambda = 5$ at different sections.

$$\mathbf{B}_{t_i} = \begin{bmatrix} 0 & \frac{\partial N_i}{\partial x} & -N_i & 0 \\ -- & -- & -- & -- \\ 0 & 0 & 0 & N_i \end{bmatrix} = \begin{bmatrix} \mathbf{B}_{s_i} \\ -- \\ \mathbf{B}_{\psi_i} \end{bmatrix}, \tag{23c}$$

where $\mathbf{B}_{p_i}$ and $\mathbf{B}_{t_i}$ are the in-plane and transverse shear strain matrices for node *i*.

The virtual displacement and generalized strain fields are expressed in terms of the virtual nodal kinematic variables as

$$\delta\mathbf{u} = \mathbf{N}\delta\mathbf{a}^e, \quad \delta\hat{\boldsymbol{\varepsilon}}_p = \mathbf{B}_p\delta\mathbf{a}^e, \quad \delta\hat{\boldsymbol{\varepsilon}}_t = \mathbf{B}_t\delta\mathbf{a}^e. \tag{24}$$

The discretized equilibrium equations are obtained by substituting Eqs. (13), (14), (20), (22) and (24) into the virtual work expression (19). After simplification of the virtual nodal kinematic variables, the following standard matrix equation is obtained

$$\mathbf{K}\mathbf{a} - \mathbf{f} = 0, \tag{25}$$

where $\mathbf{a}$ is the vector of nodal kinematic variables for the whole mesh.

The stiffness matrix $\mathbf{K}$ and the equivalent nodal force vector $\mathbf{f}$ are obtained by assembling the element contributions $\mathbf{K}^e$ and $\mathbf{f}^e$ given by

$$\mathbf{K}^e = \mathbf{K}_p^e + \mathbf{K}_t^e \tag{26}$$

with

$$\mathbf{K}_{p_{ij}}^e = \int_{l^e} \mathbf{B}_{p_i}^T \widehat{\mathbf{D}}_p \mathbf{B}_{p_j} dx, \mathbf{K}_{t_{ij}}^e = \int_{l^e} \mathbf{B}_{t_i}^T \widehat{\mathbf{D}}_t \mathbf{B}_{t_j} dx \tag{27}$$

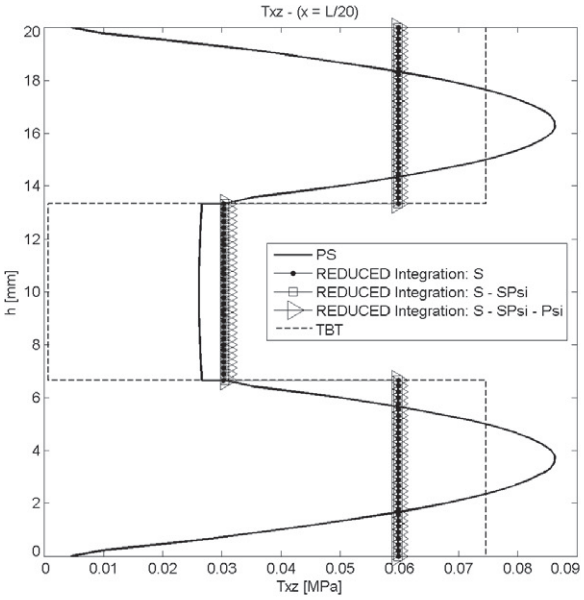

(a) $\tau_{xz}, \lambda = 10, L/20$

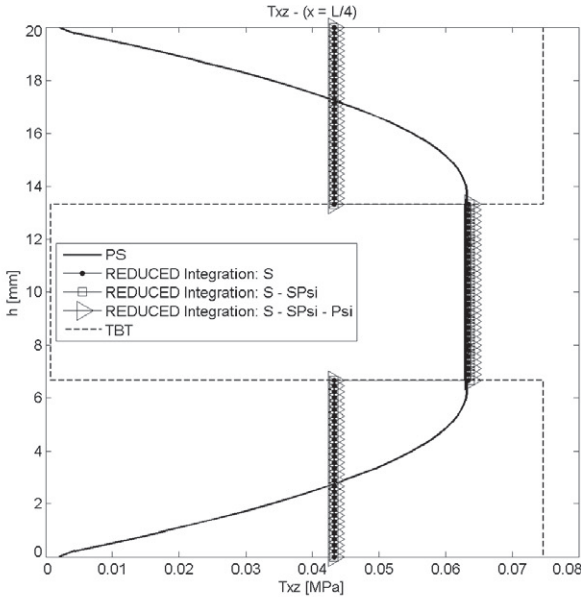

(b) $\tau_{xz}, \lambda = 10, L/4$

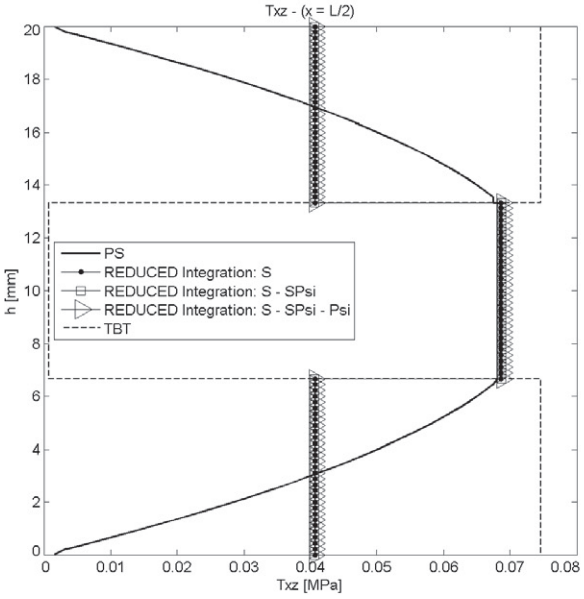

(c) $\tau_{xz}, \lambda = 10, L/2$

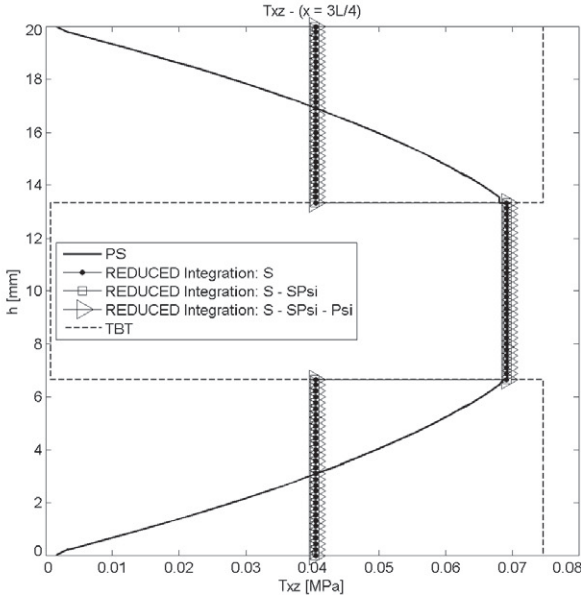

(d) $\tau_{xz}, \lambda = 10, 3L/4$

Fig. 6. Symmetric 3-layered cantilever thick beam under end point load. Thickness distribution of shear stress for $\lambda = 10$ at different sections.

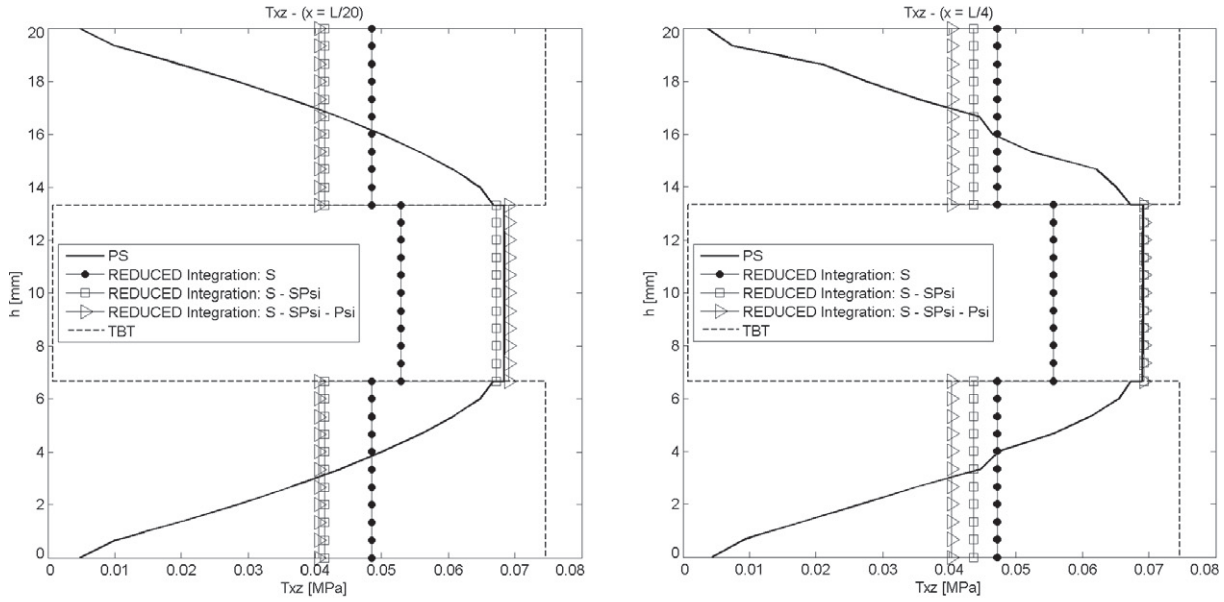

(a) $\tau_{xz}, \lambda = 100, L/20$ (b) $\tau_{xz}, \lambda = 100, L/4$

(c) $\tau_{xz}, \lambda = 100, L/2$ (d) $\tau_{xz}, \lambda = 100, 3L/4$

Fig. 7. Symmetric 3-layered cantilever thick beam under end point load. Thickness distribution of transverse shear stress for $\lambda = 100$ at different sections.

Table 2
Non symmetric 3-layered cantilever beams. Material properties for convergence analysis.

		Material properties		
		Layer 1(bottom)	Layer 2 (core)	Layer 3 (top)
Composite A	h [mm]	6.66	6.66	6.66
	E [MPa]	4.40E5	2.19E4	2.19E5
	G [MPa]	2.00E5	8.80E3	8.76E4
Composite B	h [mm]	6.66	6.66	6.66
	E [MPa]	2.19E5	2.19E3	2.19E5
	G [MPa]	8.76E4	8.80E2	8.76E4
Composite C	h [mm]	2	16	2
	E [MPa]	7.30E5	7.30E2	2.19E5
	G [MPa]	2.92E5	2.20E2	8.76E4

Table 3
Non symmetric 3-layered cantilever thick beams under end point load ($\lambda = 5$). Relative error for w at $x = L$.

Number of elements	Composites		
	A	B	C
$e_r\% - w$ at $x = L$			
5	1.800	9.588	42.289
10	0.506	2.901	19.277
25	0.0860	0.499	4.913
50	0.0191	0.123	1.406
100	0.0048	0.031	0.339
300	0.0000	0.0000	0.0000

and

$$\mathbf{f}_i^e = \int_{l^e} N_i q[1,0,0,0]^T dx. \tag{28}$$

Matrix $\mathbf{K}_p^e$ is integrated with a one-point numerical quadrature which is exact in this case. Full integration of matrix $\mathbf{K}_t^e$ requires a two-point Gauss quadrature. This however leads to shear locking for slender composite laminated beams (Section 5).

In order to asses the influence of the reduced integration of matrix $\mathbf{K}_t^e$ for overcoming the shear locking problem we split $\mathbf{K}_t^e$ as follows:

$$\mathbf{K}_t^e = \mathbf{K}_s^e + \mathbf{K}_\psi^e + \mathbf{K}_{s\psi}^e + [\mathbf{K}_{s\psi}^e]^T \tag{29a}$$

with

$$\mathbf{K}_{s_{ij}}^e = \int_{l^e} D_s \mathbf{B}_{s_i}^T \mathbf{B}_{s_j} dx, \quad \mathbf{K}_{\psi_{ij}}^e = \int_{l^e} g \mathbf{B}_{\psi_i}^T \mathbf{B}_{\psi_j} dx, \tag{29b}$$

$$\mathbf{K}_{s\psi_{ij}}^e = \int_{l^e} (-g) \mathbf{B}_{s_i}^T \mathbf{B}_{\psi_j} dx,$$

where $\mathbf{B}_{s_i}$ and $\mathbf{B}_{\psi_i}$ are defined in Eq. (23c) and D_s and g are given in Eq. (15b).

The new linear beam element based on the RZ theory is termed LRZ.

A study of the accuracy of the LRZ beam element for analysis of slender laminated beams using one and two-point quadratures for integrating matrices $\mathbf{K}_s^e$, $\mathbf{K}_\psi^e$ and $\mathbf{K}_{s\psi}^e$ is presented in the next section.

5. Study of shear locking for the LRZ beam element

We study the performance of the LRZ beam element for the analysis of a cantilever beam of length L under an end point load of value $F = 1$ (Fig. 2). The beam is formed by a symmetric three-layered material whose properties are listed on Table 1. The analysis is performed for four span-to-thickness ratios: $\lambda = 5$, 10, 50, 100 ($\lambda = L/h$) using a mesh of 100 LRZ beam elements. Results for the LRZ element are labeled "ZZ" in the figures.

The same beam was analyzed using a mesh of 27,000 four-noded plane stress rectangles for comparison purposes (Fig. 3). Results for the plane stress analysis are labeled "PS" in the figures.

Fig. 4 shows the ratio r between the end node deflection obtained with the LRZ element (w_{zz}) and with the plane stress quadrilateral (w_{ps}) (i.e. $r = \frac{w_{zz}}{w_{ps}}$) versus the beam span-to-thickness ratio $d = \frac{L}{h}$. Results for the LRZ element have been obtained using *exact* two-point integration for all terms of matrix $\mathbf{K}_t^e$ (Eq. (27)) and a one-point *reduced* integration for the following three groups of matrices: $\mathbf{K}_s^e$; $\mathbf{K}_s^e$ and $\mathbf{K}_{s\psi}^e$; and $\mathbf{K}_s$, $\mathbf{K}_{s\psi}^e$ and $\mathbf{K}_\psi^e$ (Eqs. (29b)).

Labels "*all*", "*S*", "*SPsi*" and "*Psi*" in Figs. 4–7 refer to matrices $\mathbf{K}_t^e$, $\mathbf{K}_s^e$, $\mathbf{K}_{s\psi}^e$ and $\mathbf{K}_\psi^e$ of Eq. (29a), respectively.

Results in Fig. 4 clearly show that the exact integration of $\mathbf{K}_t^e$ leads to shear locking as expected. Good (locking-free) results are obtained by one-point reduced integration of the three groups of matrices.

The influence of reduced integration in the distribution of the transverse shear stress was studied next for the three groups of matrices. Figs. 5–7 show the thickness distribution of τ_{xz} in sections located at distances $\frac{L}{20}$, $\frac{L}{4}$, $\frac{L}{2}$ and $\frac{3}{4}L$ from the clamped end for span-to-thickness ratios of $\lambda = 5$, 10 and 100. Results are compared with the plane stress solution and also with results obtained with a mesh of 300 standard 2-noded elements based on laminated Timoshenko beam theory (labeled TBT in the figures). All TBT results presented in the paper have been used with a simple shear correction factor of $\frac{5}{6}$. Indeed a more accurate value of the shear correction factor in TBT can be used for laminated sections [28].

The conclusion is that for small values of λ the reduced or exact reduced integration of matrix $\mathbf{K}_t^e$ leads to similar results. For slender beams, however, results obtained using reduced integration for $\mathbf{K}_s^e$; $\mathbf{K}_s^e$ and $\mathbf{K}_{s\psi}^e$; and $\mathbf{K}_s^e$, $\mathbf{K}_{s\psi}^e$ and $\mathbf{K}_\psi^e$ are different. Slightly more accurate results are obtained with the second choice for the section at $x = L/4$ and $\lambda = 100$ (Fig. 7b).

In conclusion, we recommend using a reduced one-point integration for matrices $\mathbf{K}_s^e$ and $\mathbf{K}_{s\psi}^e$, while matrix $\mathbf{K}_\psi^e$ should be integrated with a 2-point quadrature.

6. Convergence study

The same three-layered cantilever beam of Fig. 2 was studied next for three different set of thickness and material properties for the three layers as listed in Table 2. Material A is the more homogeneous one, while material C is clearly the more heterogeneous.

The problem was studied with six meshes of LRZ elements ranging from 5 to 300 elements. Tables 3–5 show the convergence with the number of elements for the deflection and function Ψ at the beam end, the maximum axial stress σ_x at the end section and the maximum shear stress τ_{xz} at the mid section.

Convergence is measured by the relative error defined (in absolute value) as

$$e_r = \left| \frac{v_6 - v_i}{v_6} \right|, \tag{30}$$

Table 4
Non symmetric 3-layered cantilever thick beams under end point load ($\lambda = 5$). Convergence study. Relative error for Ψ at $x = L$.

Number of elements	Composites		
	A	B	C
$e_r\% - \Psi$ *at* $x = L$			
5	0.040	8.563	36.113
10	0.003	1.814	8.042
25	0.000	0.259	0.328
50	0.000	0.063	0.033
100	0.000	0.016	0.007
300	0.000	0.000	0.000

Table 5
Non symmetric 3-layered cantilever thick beams under end point load ($\lambda = 5$). Convergence study. (a) Relative error for the maximum value of σ_x at $x = L$ and (b) idem for τ_{xz} at $x = L/2$.

Number of elements	Composites		
	A	B	C
(a) $e_r\% - (\sigma_x)_{\max}$ *at* $x = L$			
5	0.568	6.923	18.239
10	0.076	2.704	12.437
25	0.013	0.568	4.266
50	0.003	0.131	1.095
100	0.001	0.029	0.250
300	0.000	0.000	0.000
(b) $e_r\% - (\tau_{xz})_{\max}$ *at* $\frac{L}{2}$			
5	7.020	19.283	50.938
10	0.352	5.176	20.602
25	0.052	0.888	3.408
50	0.010	0.210	0.707
100	0.003	0.049	0.147
300	0.000	0.000	0.000

where v_6 and v_i are the values of the magnitude of interest obtained using the finest grid (300 elements) and the ith mesh ($i = 1,2,\ldots,5$), respectively.

Results clearly show that convergence is always slower for the heterogeneous material case, as expected.

For a mesh of 25 elements the errors for all the magnitudes considered are less than 1% for materials A and B. For material C the maximum error does not exceed 5% (Table 5). For the 50 element mesh errors of the order of 1% or less were obtained in all cases.

Results for a 10 element mesh are good for material A (errors less than 0.4%), relatively good for material B (errors less than around 5%) and unacceptable for material C (errors ranging from around 8–20%).

7. Examples of application

7.1. Three-layered thick cantilever beam with non symmetric material properties

We present results for a laminated thick cantilever beam under an end point load. The material properties are those of Composite C in Table 2. The span-to-thickness ratio is $\lambda = 5$.

For the laminated sandwich considered the core is eight times thicker than the face sheets. In addition, the core is three orders of magnitude more compliant than the bottom face sheet. Moreover, the top face sheet has the same thickness as the bottom face sheet, but is about three times stiffer. Note that this laminate does not possess material symmetry with respect to the mid-depth reference axis. The high heterogeneity of this stacking sequence is very challenging for the beam theories considered herein to model adequately.

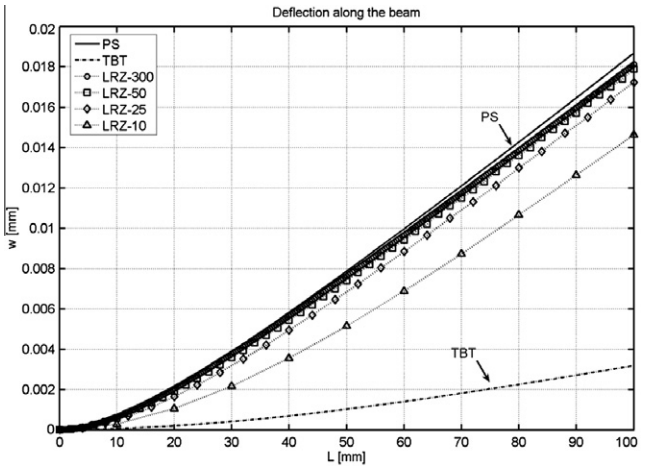

Fig. 8. Non symmetric 3-layered cantilever thick beam under end point load ($\lambda = 5$). Distribution of the vertical deflection w for different theories and meshes.

As in previous section, the legend caption PS denotes the *reference* solution obtained with the structured mesh of 27,000 four-noded plane stress quadrilaterals shown in Fig. 3. TBT denotes the solution obtained with a mesh of 300 2-noded beam elements based on standard laminated Timoshenko beam theory. LRZ-300, LRZ-50, LRZ-25, LRZ-10 refer to the solution obtained with the LRZ beam element using meshes of 300, 50, 25 and 10 elements, respectively.

Fig. 8 shows the deflection values along the beam length. Very good agreement with the plane stress solution is obtained already for the LRZ-50 mesh as expected from the conclusions of the previous section.

TBT results are considerable stiffer. The difference with the reference solution is about *six times stiffer* for the end deflection value.

Fig. 9 shows the distribution of the axial displacements at the upper and lower surfaces of layer 3 (top layer) along the beam length. Excellent results are again obtained with the 50 element mesh. The TBT results are far from the correct ones.

Fig. 10 shows the thickness distribution for the axial displacement at sections located at distances $\frac{L}{4}$, $\frac{L}{2}$ and $\frac{3L}{4}$ from the clamped end. Results for the LRZ element (LRZ-25, LRZ-50 and LRZ-300) are in good agreement with the reference solution. The TBT results have the standard linear distribution which is far from the correct zigzag results.

Fig. 11 shows the distribution along the beam length of the axial stress σ_x at the top and bottom surfaces of the beam cross section. Very good agreement between the reference PS solution and the LRZ-50 and LRZ-300 results is obtained. Results for the LRZ-25 mesh compare reasonably well with the PS solution except in the vicinity of the clamped edge. This error is corrected for the LRZ-50 and LRZ-300 meshes. The TBT results yield a linear distribution of the axial stress along the beam, as expected. This introduces large errors in the axial stress values in the vicinity of the clamped edge, as clearly shown in Fig. 11.

Figs. 12 and 13 show the thickness distribution for the axial stress σ_x at the clamped section and at the center of the beam. LRZ results agree quite well with those of the reference solution.

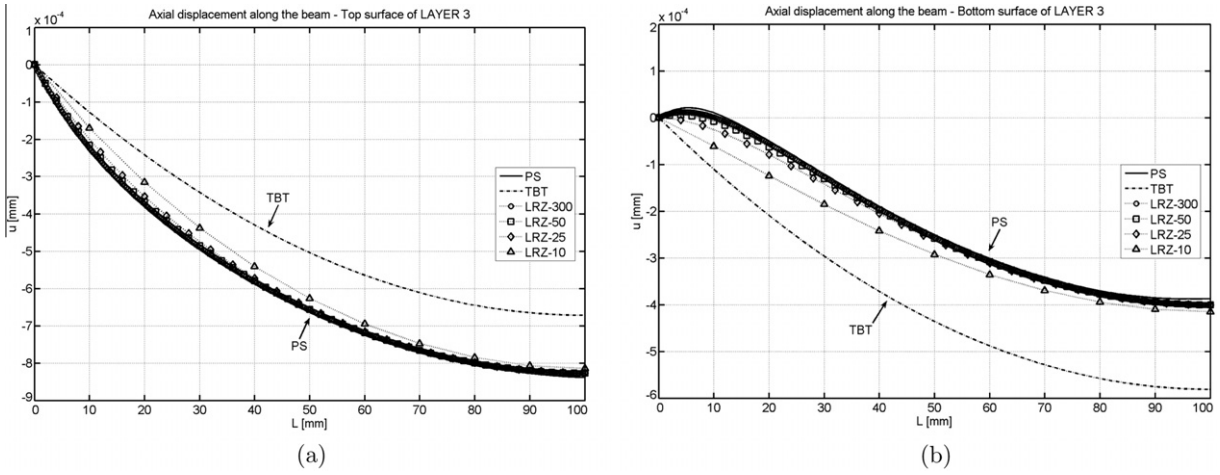

Fig. 9. Non symmetric 3-layered cantilever thick beam under end point load ($\lambda = 5$). Axial displacement u at the upper and lower surfaces of the top layer (layer 3).

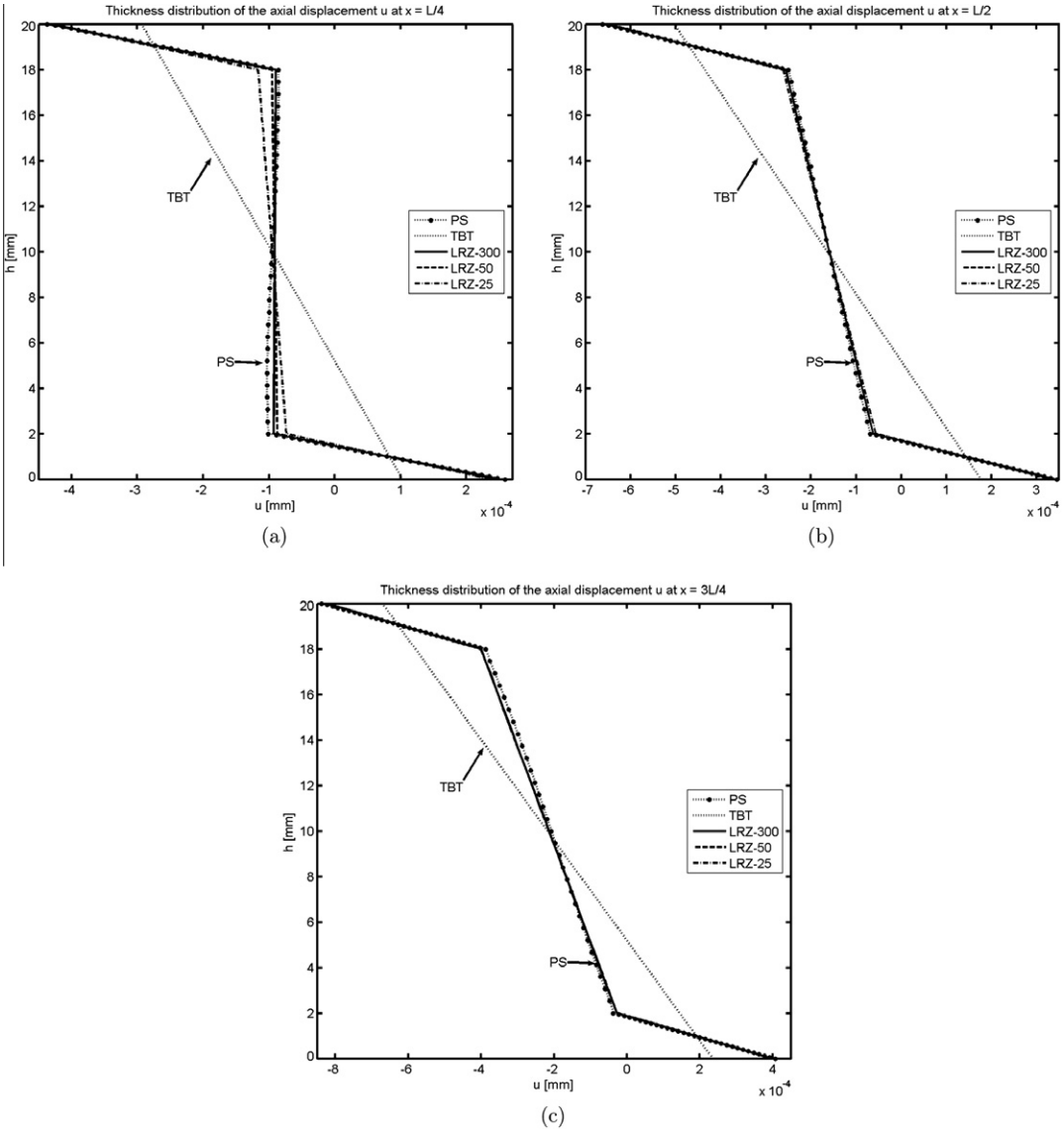

Fig. 10. Non symmetric 3-layered cantilever thick beam under end point load ($\lambda = 5$). Thickness distribution of the axial displacement u at $x = L/4$ (a), $x = L/2$ (b) and $x = L$ (c).

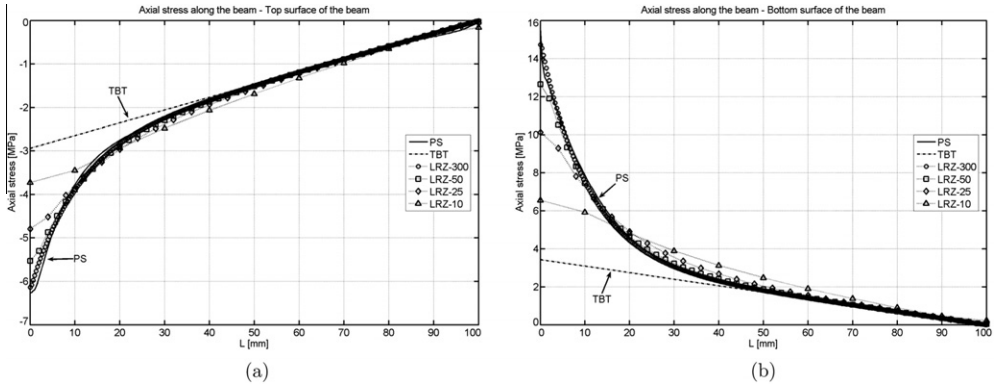

Fig. 11. Non symmetric 3-layered cantilever thick beam under end point load ($\lambda = 5$). Axial stress σ_x at upper (a) and lower (b) surfaces of the cross section along the beam length.

TBT results have an erroneous stress distribution for the top and bottom layers at the clamped end. These differences are less important for the central section.

Fig. 14 shows the thickness distribution for the transverse shear stress τ_{xz} at different sections ($\frac{L}{20}$, $\frac{L}{4}$, $\frac{L}{2}$ and $\frac{3L}{4}$). LRZ results provide an accurate estimate of the average transverse shear stress value

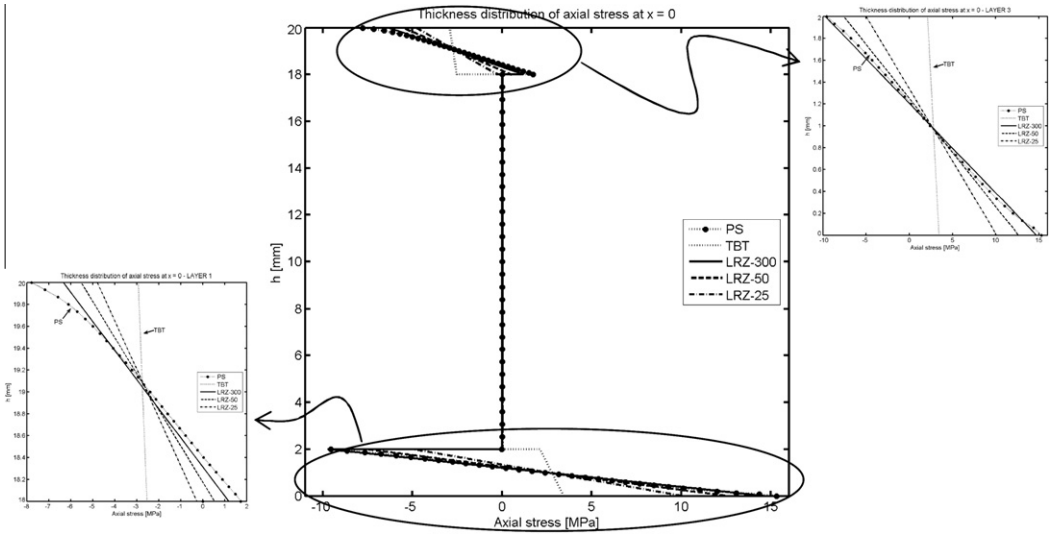

Fig. 12. Non symmetric 3-layered cantilever thick beam under end point load ($\lambda = 5$). Thickness distribution of the axial stress σ_x at $x = 0$.

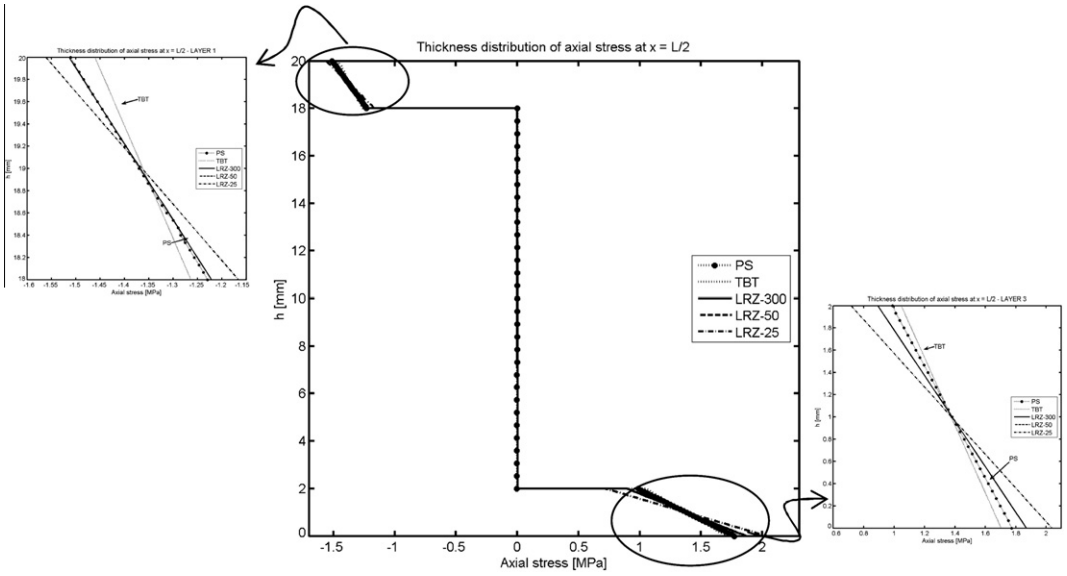

Fig. 13. Non symmetric 3-layered cantilever thick beam under end point load ($\lambda = 5$). Thickness distribution of the axial stress σ_x at $x = L/2$.

for each layer. The distribution of τ_{xz} across the thickness can be substantially improved by using the equilibrium equations for computing τ_{xz} "a posteriori" as explained in Section 7.3.

TBT results are acceptable for the central layer and clearly overestimate the transverse shear stress in sections far from the clamped end.

LRZ and TBT results for the distribution of the (constant) tangential shear stress τ_{xz} for each of the three layers along the beam length are shown in Fig. 15. TBT results are clearly inaccurate (except for the values at the clamped edge).

7.2. Three-layered simple supported (SS) thick beams under uniform load

The next example is the analysis of a three-layered simple supported thick beam under a uniformly distributed load of unit value ($q = 1$). The material properties and the thickness for the three layers are shown in Table 6. *The material has a non symmetric distribution* with respect to the beam axis. An unusually low value for the shear modulus of the core layer has been taken, thus reproducing the effect of a damaged material in this zone. The span-to-thickness ratio is $\lambda = 5$. Results obtained with the LRZ element are once more compared with those obtained with a mesh of 300 2-noded TBT elements and with the mesh of 27,000 4-noded plane stress (PS) rectangles shown in Fig. 3. The PS solution has been obtained by fixing the vertical displacement of all nodes at the end sections and the horizontal displacement of the mid-line node at $x = 0$ and $x = L$ to a zero value. This way of approximating a simple support condition leads to some discrepancies between the PS results and those obtained with beam theory.

No advantage of the symmetry of the problem for the discretization has been taken.

Fig. 16 shows the distribution of the vertical deflection for the different methods. The error in the "best" maximum central deflection value versus the "exact" PS solution is $\simeq$12%. The discrepancy is due to the difference in the way the simple support condition is

modeled in beam and PS theories, as well as to the limitations of beam theory to model accurately very thick beams. TBT results are inaccurate, as expected.

Fig. 17 shows the distribution of the axial stress σ_x along the beam for the top surface of the second and third layer.

The accuracy of the LRZ results is remarkable with a maximum error of 10% despite the modeling limitations mentioned above. TBT results are incorrect.

Fig. 18 shows the thickness distribution of the axial displacement at the left end section and at $x = \frac{L}{4}$. The LRZ element captures very well the zigzag shape of the axial displacement field even for a coarse mesh of 10 elements. The TBT element yields an unrealistic linear distribution.

Figs. 19 and 20 show the thickness distribution of the axial stress and the transverse shear stress at the left end and mid sections. The accuracy of the LRZ results is again noticeable (even for the coarse 10 element mesh). The TBT element fails to capture the zigzag distribution of the axial stress (Fig. 19) and gives a wrong value of almost zero shear stress at the core layer for the two sections chosen (Fig. 20).

Fig. 21 shows the distribution of the shear stress τ_{xz} along the beam for each of the three layers obtained with the LRZ and TBT elements. TBT results are accurate for the first and third layer but are wrong for the core layer.

Fig. 22 shows a similar set of results for a moderately thick SS beam ($\lambda = 10$) and the same material properties. Results shown

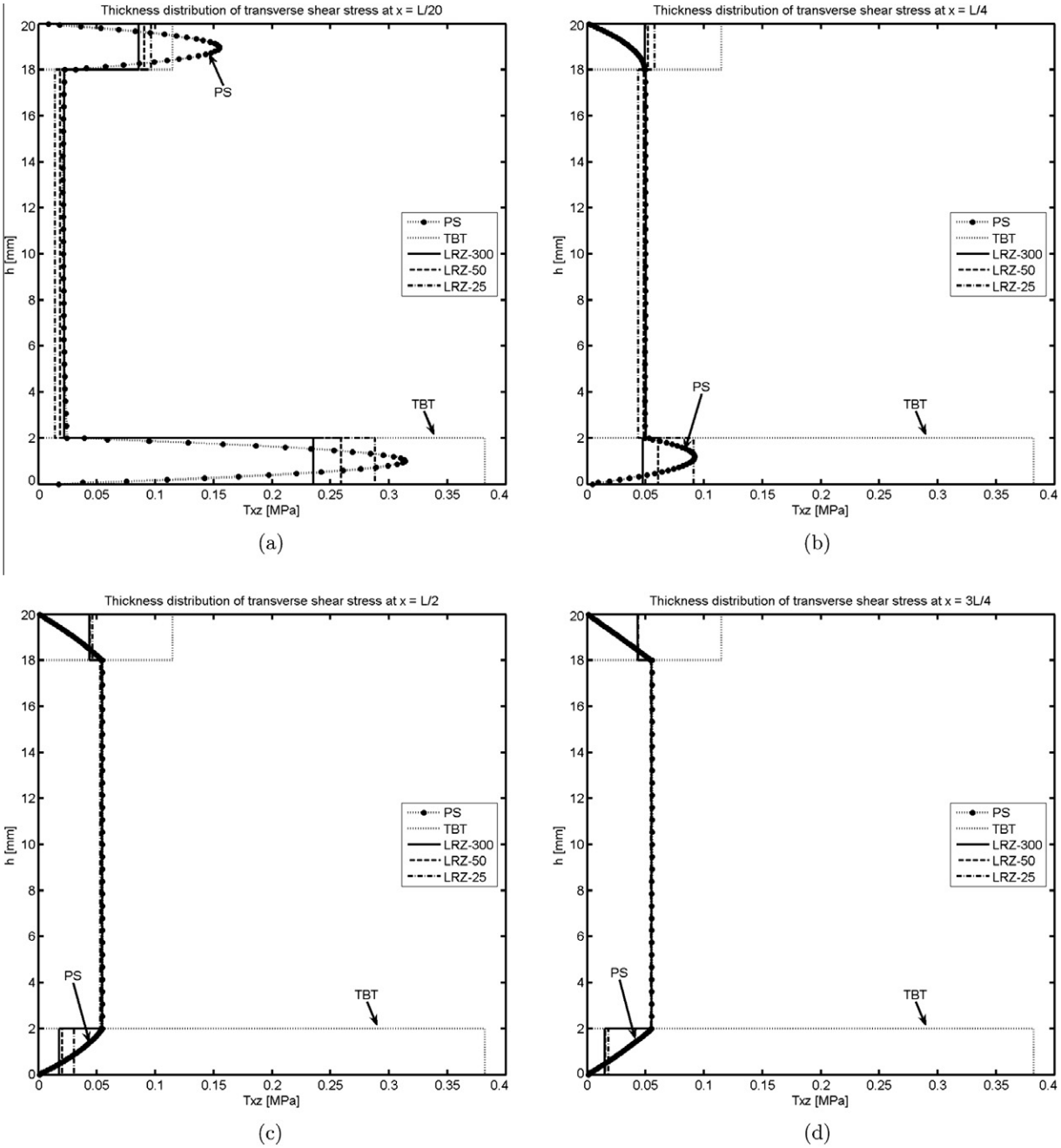

Fig. 14. Non symmetric 3-layered cantilever thick beam under end point load ($\lambda = 5$). Thickness distribution of transverse shear stress τ_{xz} at $L/20$ (a), $L/4$ (b), $L/2$ (c) and $3L/4$ (d).

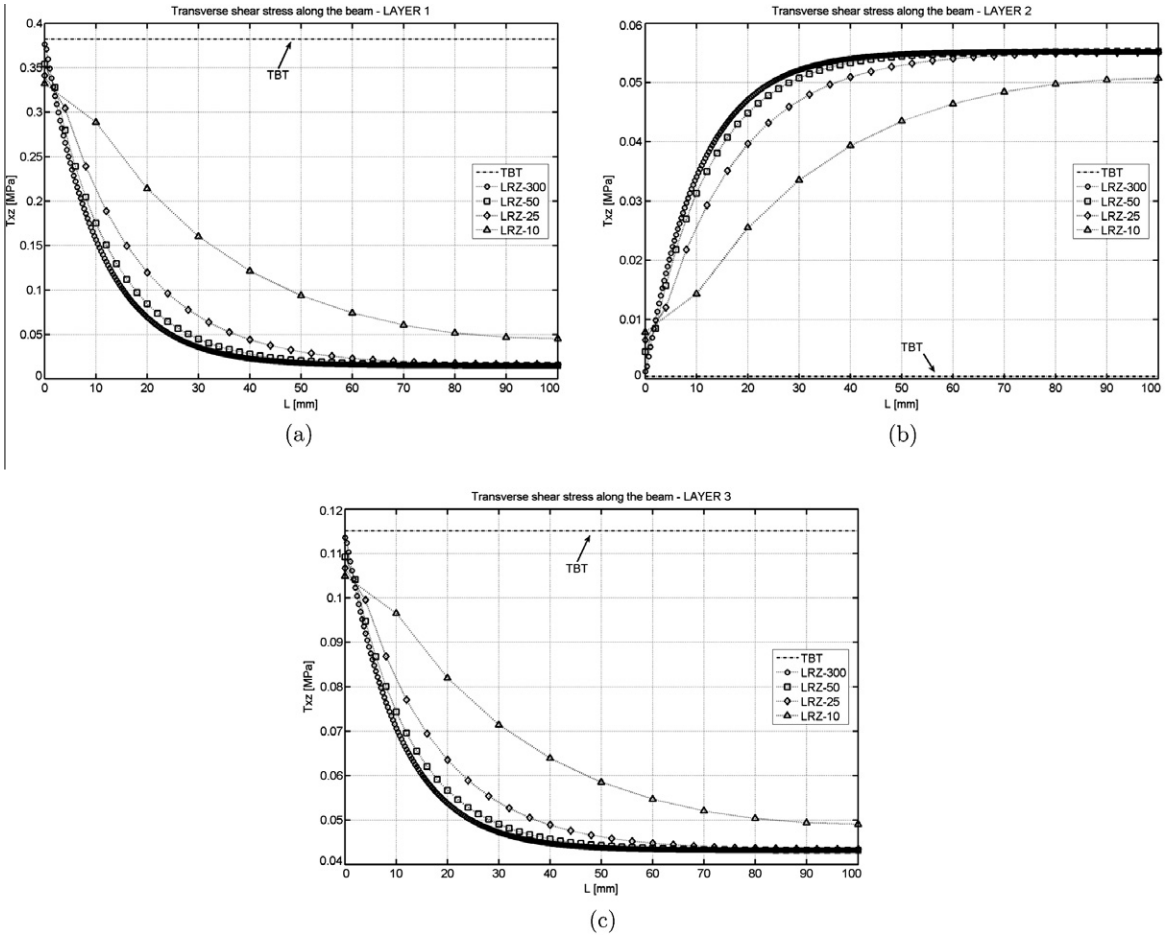

Fig. 15. Non symmetric 3-layered cantilever thick beam under end point load ($\lambda = 5$). LRZ and TBT results for the transverse shear stress τ_{xz} along the beam. Layer 1 (a), layer 2 (b) and layer 3(c).

Table 6
Thickness and material properties for 3-layered non-symmetric simple supported (SS) beam.

	Thickness and material properties		
	Layer 1 (bottom)	Layer 2 (core)	Layer 3 (top)
h [mm]	6.6666	6.6666	6.6666
E [MPa]	$2.19E^5$	$5.30E^5$	$7.30E^5$
G [MPa]	$8.76E^4$	$2.90E^2$	$2.92E^5$

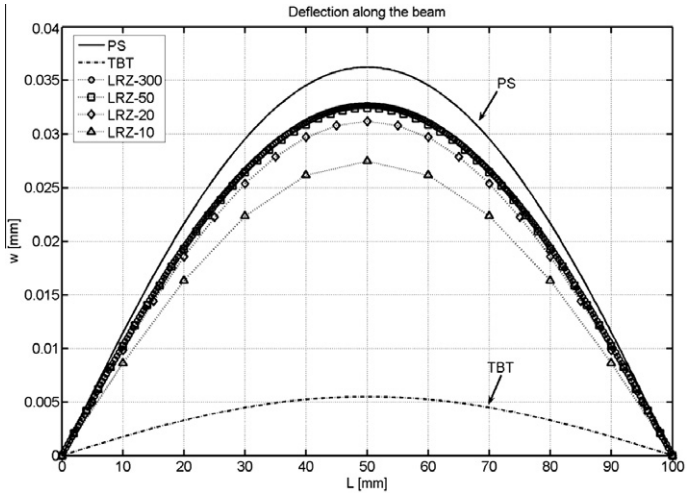

Fig. 16. Non symmetric 3-layered SS thick beam under uniformly distributed load ($\lambda = 5$). Distribution of vertical deflection w along the beam length.

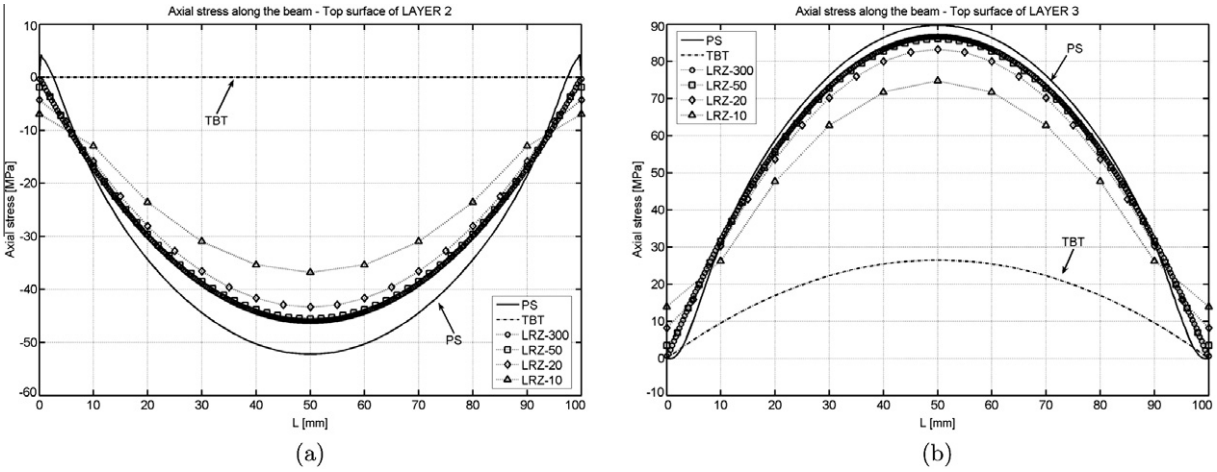

Fig. 17. Non symmetric 3-layered SS thick beam under uniformly distributed load ($\lambda = 5$). Distribution of axial stress σ_x at upper surface of layer 2 (a) and layer 3 (b).

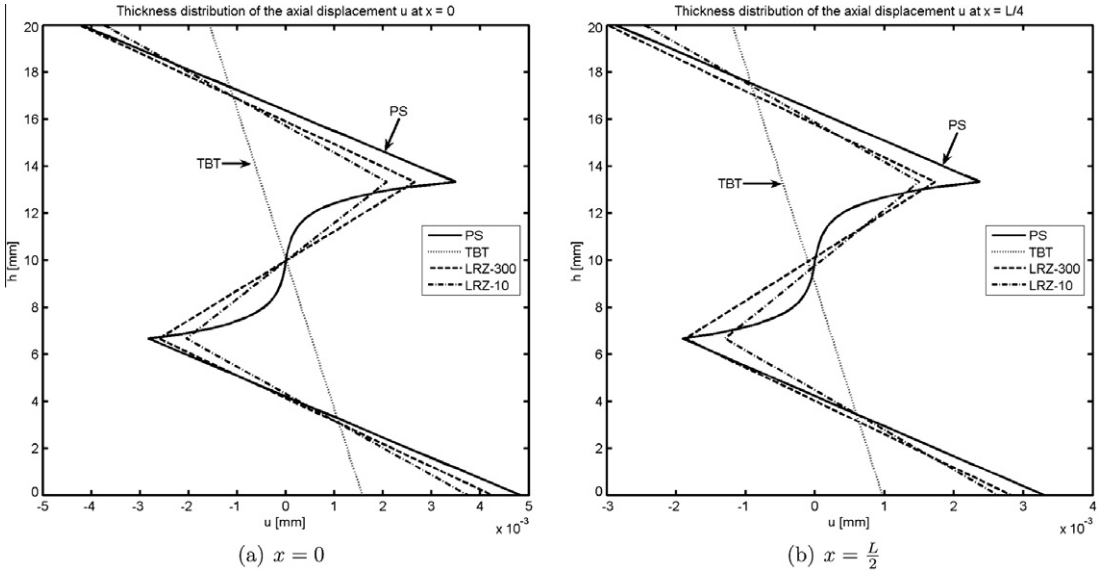

Fig. 18. Non symmetric 3-layered SS thick beam under uniformly distributed load ($\lambda = 5$). Thickness distribution of axial displacement at $x = 0$ (a) and at $x = L/2$ (b).

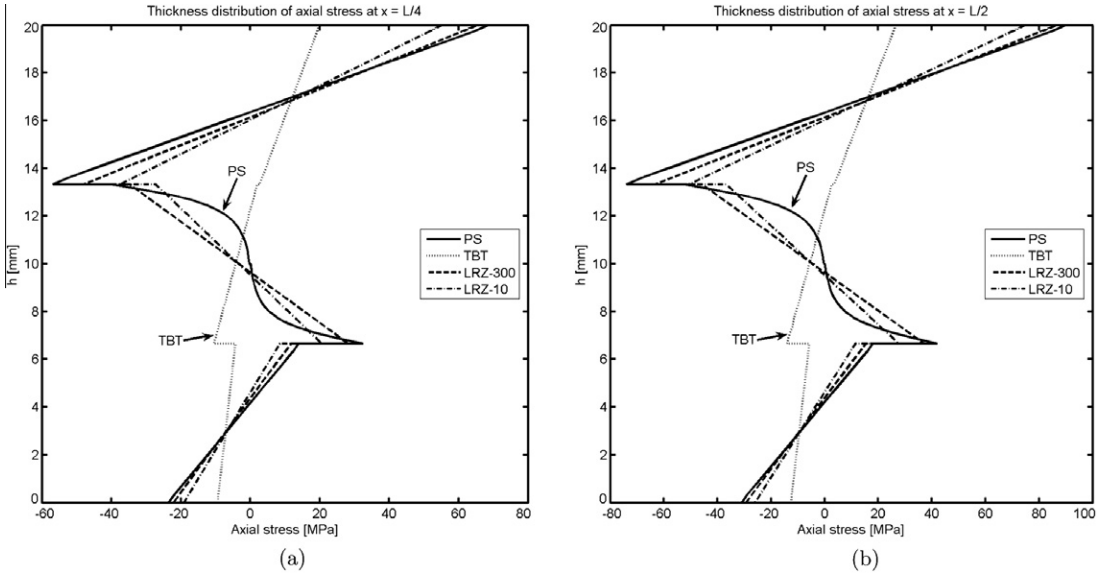

Fig. 19. Non symmetric 3-layered SS thick beam under uniformly distributed load ($\lambda = 5$). Thickness distribution of axial stress σ_x at $x = 0$ (a) and at $x = L/2$ (b).

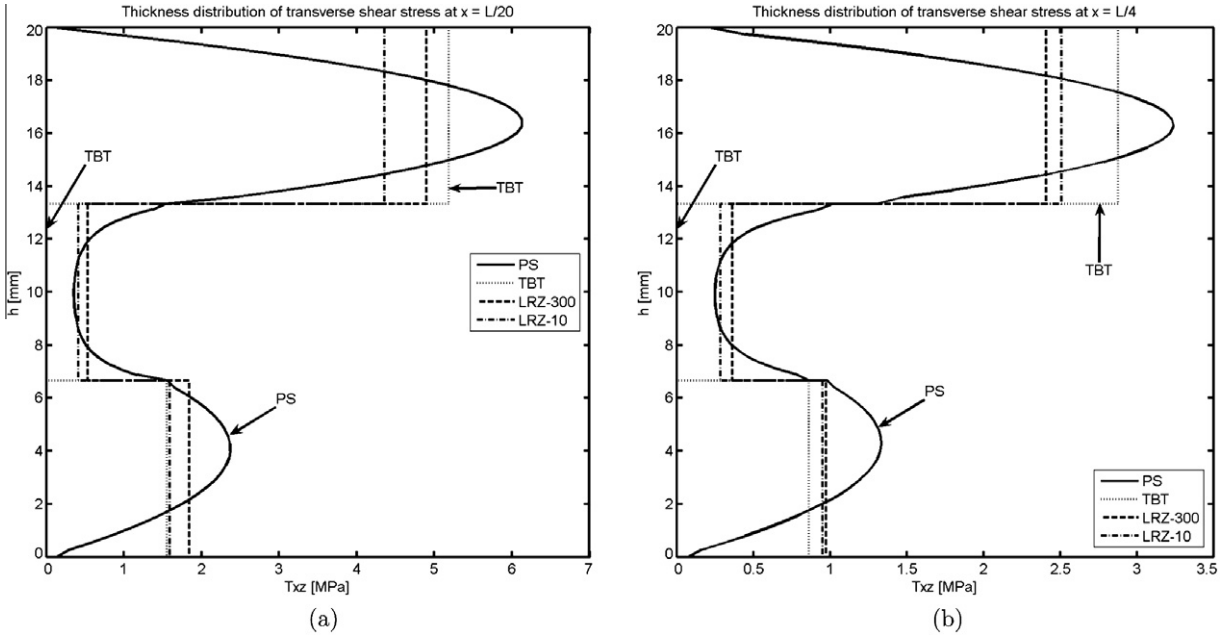

Fig. 20. Non symmetric 3-layered SS thick beam under uniformly distributed load ($\lambda = 5$). Thickness distribution of the shear stress at $x = L/20$ (a) and at $x = L/4$ (b).

are the distribution along the beam of the deflection and the axial stress at the top surface of layer 2. The accuracy of the LRZ element is again noticeable.

7.3. Non-symmetric ten-layered clamped slender beam under uniformly distributed loading

We present results for a ten-layered clamped slender rectangular beam ($L = 100$ mm, $h = 5$ mm, $b = 1$ mm, $\lambda = 20$) under uniformly distributed loading ($q = 1$ kN/mm). The composite material has the non-symmetric distribution across the thickness shown in Table 7.

Fig. 23 shows results for the deflection along the beam for LRZ meshes with 10 and 300 elements (LRZ-10 and LRZ-300). Results obtained with a mesh of 27.000 4-noded plane stress quadrilaterals and with a mesh of 300 TBT elements are also shown for comparison. Note the accuracy of the coarse LRZ-10 mesh and the erroneous results of the TBT solution.

Fig. 24 shows the thickness distribution of the axial displacement and the axial stress (σ_x) for the section at $x = \frac{L}{4}$. The accuracy of the LRZ results is once more remarkable.

Fig. 25 shows the thickness distribution of the transverse shear stress at $x = \frac{L}{4}$. Results in Fig. 25a show the values directly obtained with the LRZ-10 and LRZ-300 meshes. These results are clearly better than those obtained with the TBT element but only coincide in an average sense with the plane stress FEM solution.

LRZ results for the thickness distribution of τ_{xz} can be much improved by computing τ_{xz} "a posteriori" from the axial stress field using the equilibrium equation

$$\frac{\partial \sigma_x}{\partial x} + \frac{\partial \tau_{xz}}{\partial z} = 0. \tag{31}$$

The transverse shear stress at a point across the thickness with coordinate z is computed by integrating Eq. (31) as

$$\tau_{xz}(z) = -\int_{-\frac{h}{2}}^{z} \frac{\partial \sigma_x}{\partial x} dz = -\frac{\partial N_z}{\partial x}, \tag{32}$$

where

$$N_z = \int_{-\frac{h}{2}}^{z} \sigma_x dz \tag{33}$$

is the axial force (per unit width) resulting from the thickness integration of σ_x between the coordinates $-\frac{h}{2}$ and z.

The space derivative of N_z in Eq. (32) is computed *at a node i* as

$$\frac{\partial N_z}{\partial x} = \frac{2}{l^e + l^{e-1}} \left(N_z^e - N_z^{e-1} \right), \tag{34}$$

where (l^e, N_z^e) and $\left(l^{e-1}, N_z^{e-1}\right)$ are the element length and the value of N_z at elements e and $e-1$ adjacent to node i, respectively. A value of $\tau_{xz}(-\frac{h}{2}) = 0$ is taken. It is remarkable that the method yields automatically $\tau_{xz}(\frac{h}{2}) \simeq 0$.

Results for τ_{xz} obtained with this procedure are termed LRZ-10-N_z and LRZ-300-N_z in Fig. 25. We note the accuracy of the "recovered" thickness distribution for τ_{xz}, even for the coarse mesh of 10 LRZ elements.

7.4. Modeling of delamination with the LRZ element

Prediction of delamination in composite laminated beams is a challenge for all beam models. A method for predicting delamination in beams using a Hermitian zigzag theory was presented in [26,27]. A sub-laminate approach is used for which the number of kinematic unknowns depends of the number of physical layers. This increases the number of variables but it yields the correct an accurate transverse shear stress distribution without integrating the equilibrium equations.

Delamination effects in composite laminated beams can be effectively reproduced with the LRZ element *without introducing additional kinematic variables*. The delamination model simply implies *introducing a very thin "interface layer" between adjacent material layers* in the actual composite laminated section. Delamination is produced when the material properties of the interface layer are drastically reduced to almost a zero value in comparison with those of the adjacent layers due to interlamina failure. This simple delamination model allows the LRZ element to take into account the reduction of the overall beam stiffness due to the failure of

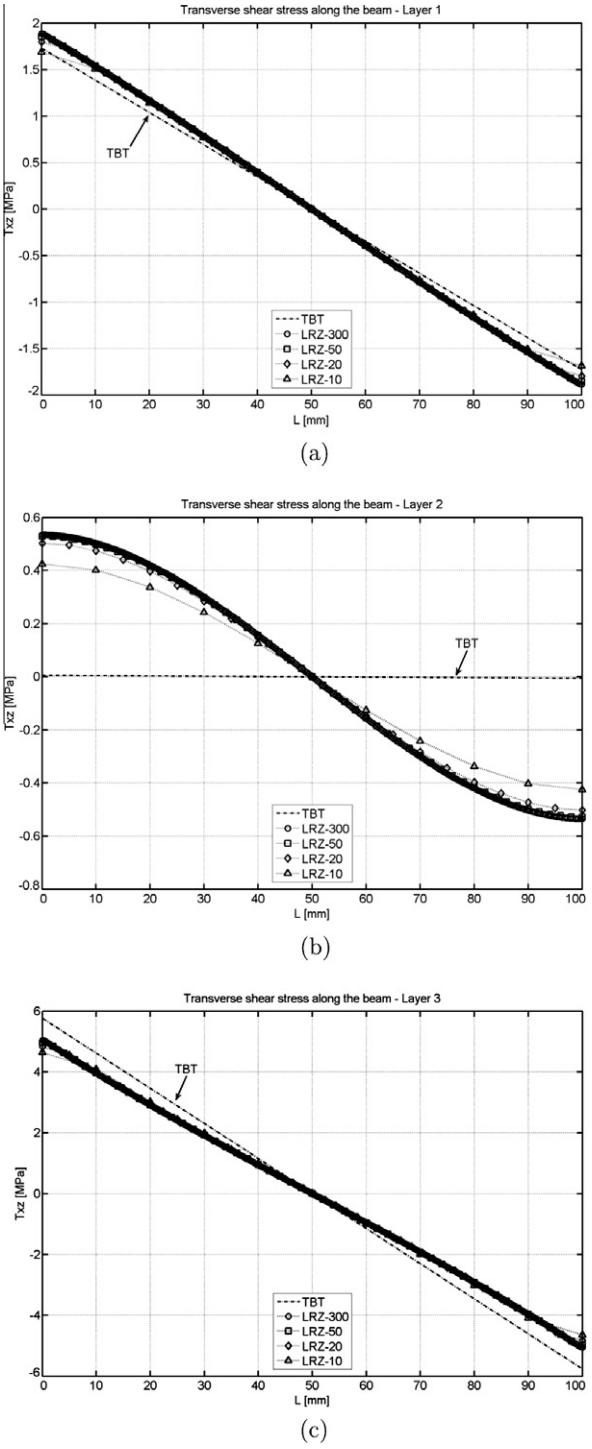

Fig. 21. Non symmetric 3-layered SS thick beam under uniformly distributed load ($\lambda = 5$). LRZ and TBT results for the distribution of τ_{xz} along the beam for layer 1 (a), layer 2 (b) and layer 3 (c).

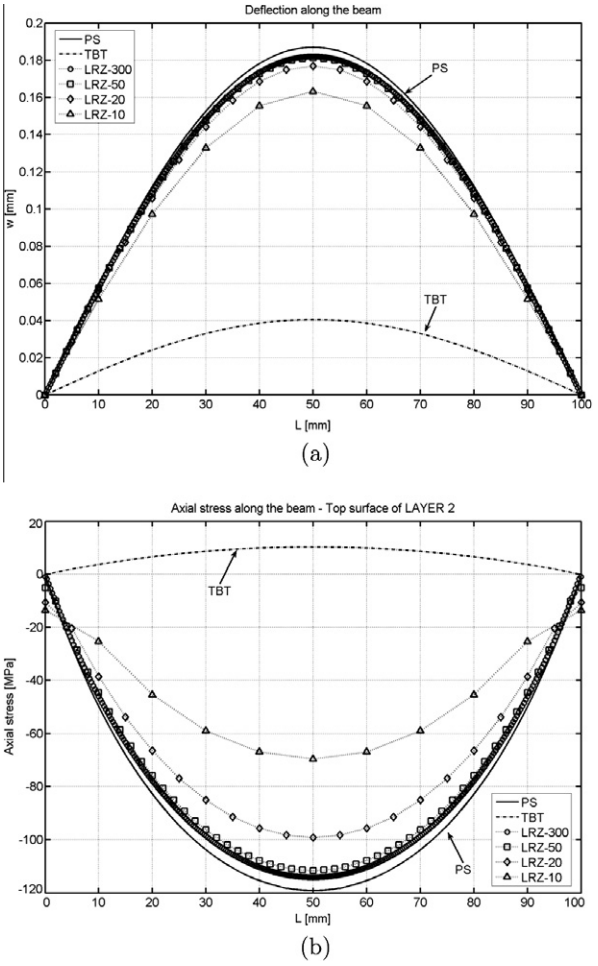

Fig. 22. Non symmetric 3-layered SS moderately thick beam under uniformly distributed load ($\lambda = 10$). Distribution along the beam length of the vertical deflection w (a) and the axial stress σ_x at the upper of layer 2 (b).

Table 7
Ten-layered clamped slender rectangular beam under uniformly distributed loading. (a) Thickness and material number for each of the 10 layers. (b) Properties of each material.

Layer	h_i	Material
(a)		
1	0.5	IV
2	0.6	I
3	0.5	V
4	0.4	III
5	0.7	IV
6	0.1	III
7	0.4	II
8	0.5	V
9	0.3	I
10	1	II
Material	E [MPa]	G [MPa]
(b)		
I	2.19e5	0.876e5
II	7.3e5	2.92e5
III	0.0073e5	0.0029e5
IV	5.3e5	2.12e5
V	0.82e5	0.328e5

the interface layer leading to an increase in the deflection and rotation field. Moreover, the LRZ element can also accurately represent the jump in the axial displacement field across the interface layer and the change in the axial and tangential stress distributions over the beam sections as delamination progresses.

Figs. 26–30 show an example of the capabilities of the LRZ beam element to model delamination. The problem represents the analysis of a cantilever thick rectangular beam ($\lambda = 5$) under an end point load. The beam section has three layers of composite material with properties shown in Table 8. Delamination between the upper and core layers has been modeled by introducing a very thin interface layer ($h = 0.01$ mm) between these two layers (Fig. 26).

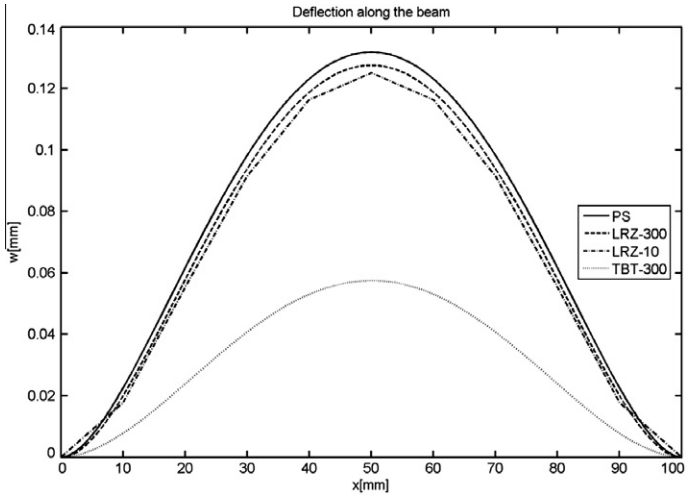

Fig. 23. Ten-layered clamped slender beam under uniform loading. Distribution of the deflection along the beam.

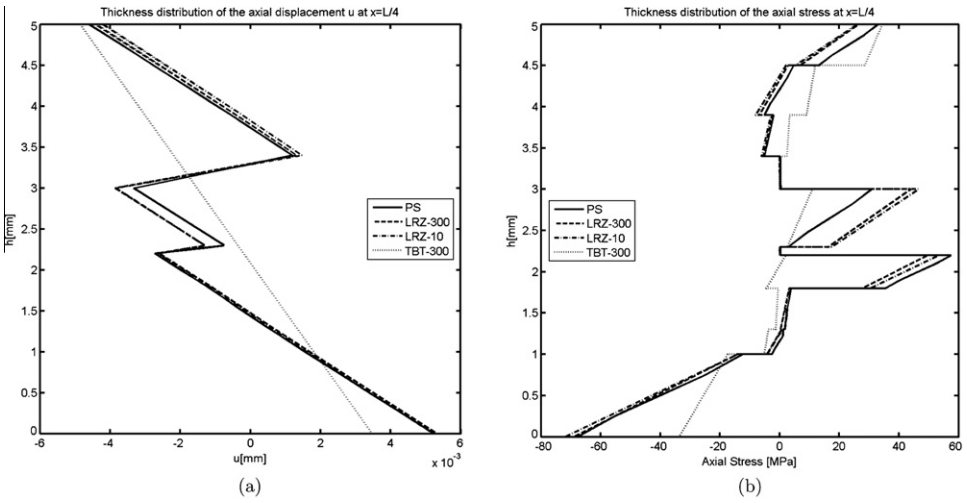

Fig. 24. Ten-layered clamped slender beam under uniform loading. Thickness distribution of axial displacement (a) and axial stress σ_x (b) for $x = \frac{L}{4}$.

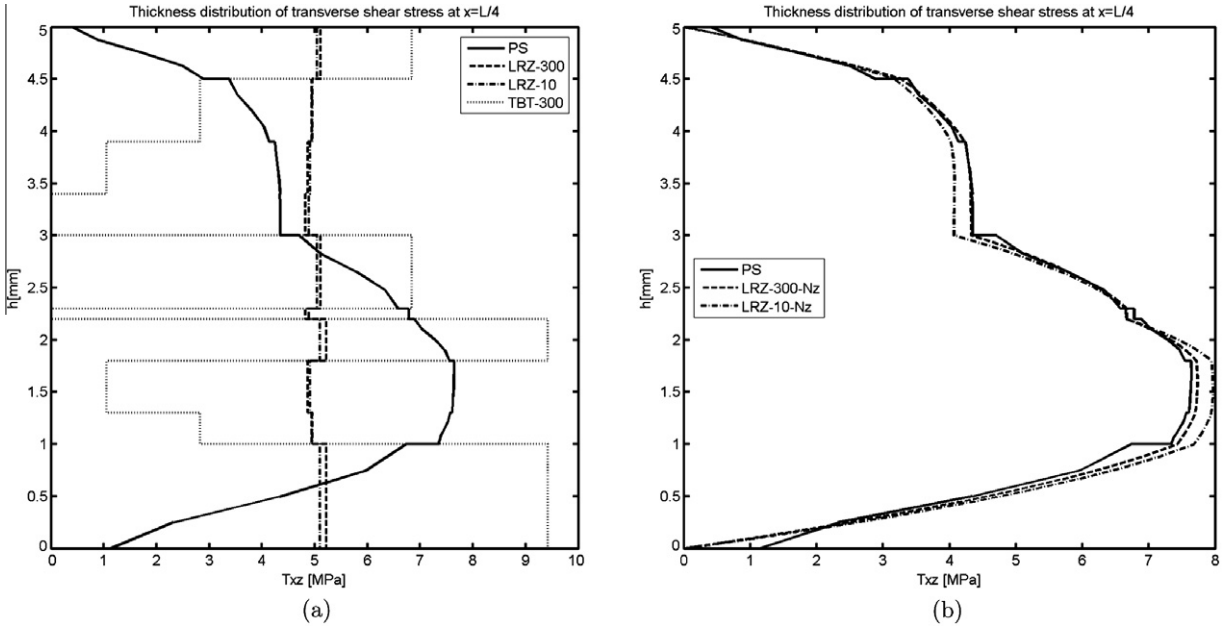

Fig. 25. Ten-layered clamped slender beam under uniform loading. Thickness distribution of τ_{xz} at $x = \frac{L}{4}$. (a) Comparison of LRZ-10 and LRZ-300 results with plane stress (PS) and TBT solutions. (b) PS solution and LRZ-10-N_z and LRZ-300-N_z results for τ_{xz} obtained by thickness integration of the equilibrium equation using the LRZ-10 and LRZ-300 results (Eq. (32)).

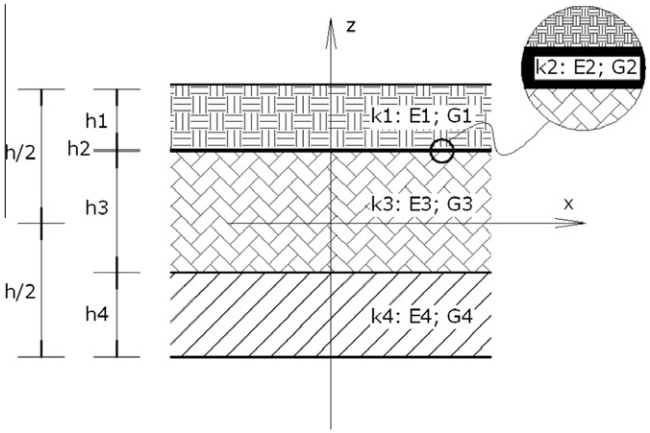

Fig. 26. Modeling of interface layer for delamination study in 3-layered thick cantilever beam ($\lambda = 5$) under end point load.

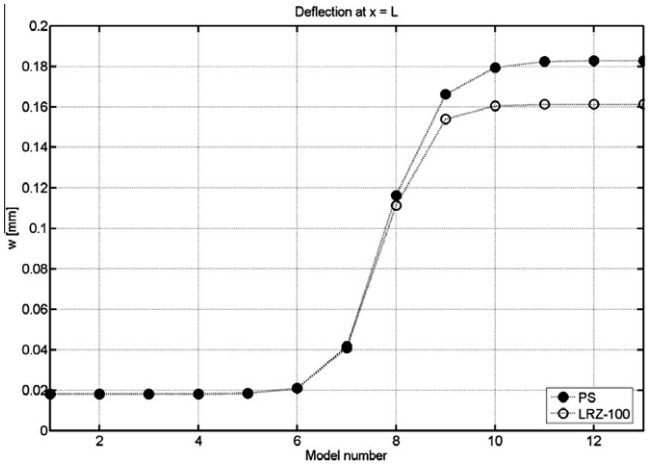

Fig. 27. Delamination study in 3-layered cantilever beam under end point load. Evolution of end deflection with the shear modulus value for the interface layer LRZ-100 results and PS solution.

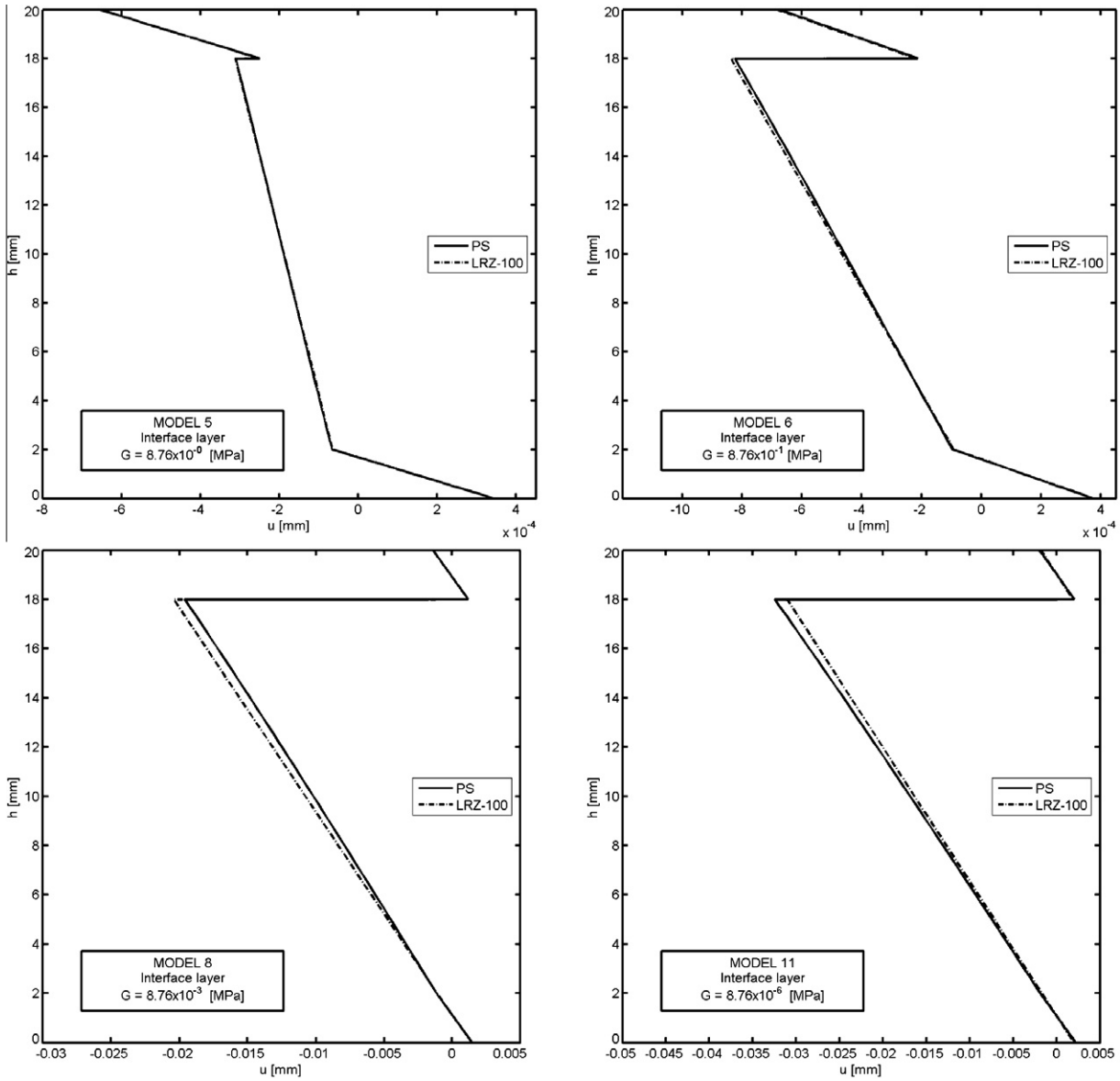

Fig. 28. Delamination study in 3-layered cantilever beam under end point load. Thickness distribution of axial displacement at $x = \frac{L}{2}$ for four decreasing values of the shear modulus at the interface layer (Models 5, 6, 8 and 11, Table 9).

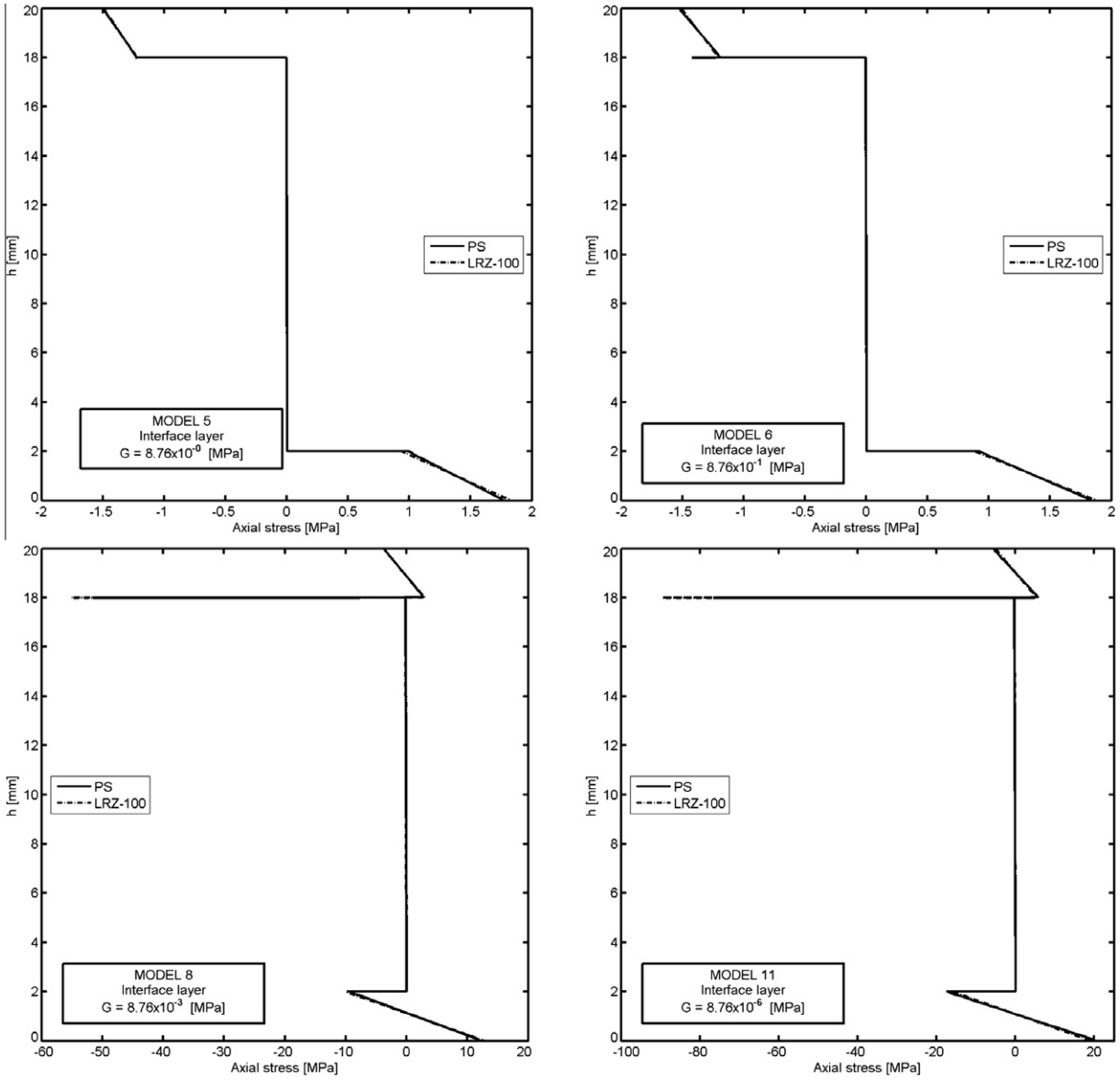

Fig. 29. Delamination study in 3-layered cantilever beam under end point load. Thickness distribution of σ_x at $x = \frac{L}{2}$ for four decreasing values of the shear modulus at the interface layer (Models 5, 6, 8 and 11, Table 9).

The initial properties of the interface layer coincide with those of the upper layer. Next, the shear modulus value for the interface layer has been progressively reduced up to 11 orders of magnitude from $G2 = 8.76 \times 10^4$ MPa (Model 1) to $G2 = 8.76 \times 10^{-7}$ MPa (Model 12) (Table 9).

We note that the reduction of the shear modulus has been applied over the whole beam length in this case. However it can applied in selected beam regions as appropriate.

Fig. 27 shows results for the end deflection in terms of the shear modulus value of the interface layer for the LRZ-100 mesh. Note that the deflection increases one order of magnitude versus the non-delaminated case. It is also interesting that the end deflection does not change after the shear modulus of the interface layer is reduced beyond eight orders of magnitude (results for Model 9 in Fig. 27). Results agree reasonably well (error $\simeq 10\%$) with those obtained with the plane stress model of Fig. 3 introducing a similar reduction in the shear modulus of an *ad hoc* interface layer.

Fig. 28 shows the thickness distribution for the axial displacement at the mid section for four decreasing values of the shear modulus at the interface layer: $G2 = 8.76$, 8.76×10^{-1}, 8.76×10^{-3} and 8.76×10^{-6} MPa. The jump of the axial displacement across the thickness at the interface layer during delamination is well captured. We again note that the displacement jump at the interface layer remains stationary after a reduction of the material properties in that layer of six orders of magnitude. Results agree well with the plane stress solution also shown in the figure.

Fig. 29 shows the thickness distribution of the axial stress (σ_x) for the same four decreasing values of the shear modulus at the interface layer. The effect of delamination in the stress distribution is clearly visible. Once again the LRZ-100 results agree well with the plane stress solution.

Fig. 30 finally shows the thickness distribution for the transverse shear stress at $x = \frac{L}{2}$ for the same four values of the shear modulus at the interface layer. The three graphs show the PS results, the LRZ-100 results and the solution obtained by inte-

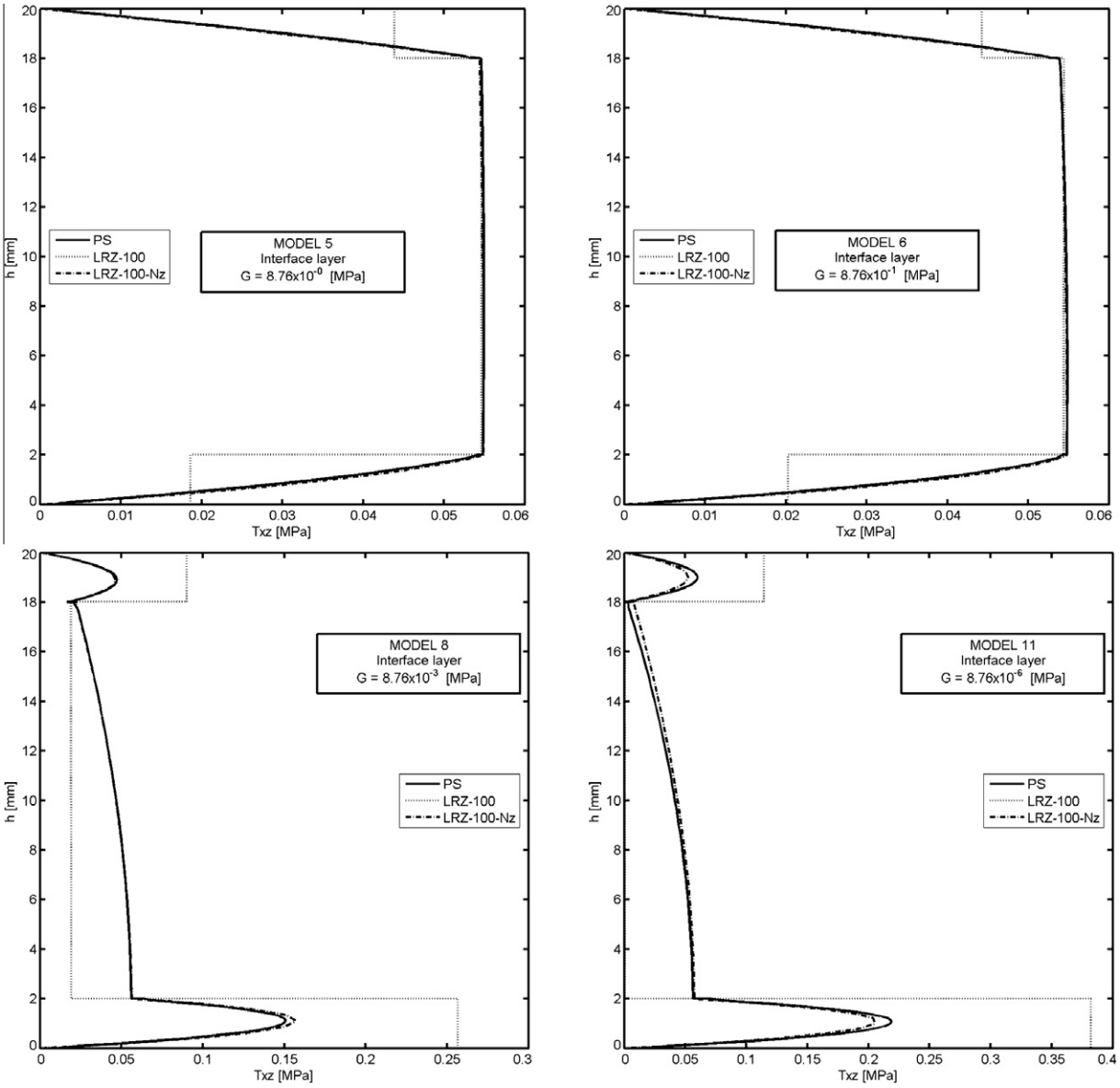

Fig. 30. Delamination study in 3-layered cantilever beam under end point load. Thickness distribution of τ_{xz} at $x = \frac{l}{2}$ for four values of G at the interface layer (Models 5, 6, 8 and 11, Table 9). LRZ-100 results, plane stress (PS) solution and LRZ-100-Sx results obtained by integrating the equilibrium equation (Eq. (32)) using the LRZ-100 results.

Table 8
Thickness and layer properties for delamination study in a 3-layered cantilever beam under end point load. Layer 2 is the interface layer. $G2$ values are given in Table 9.

	Composite material			
	Layer 1	Layer 2	Layer 3	Layer 4
h [mm]	2	0.01	16	2
E [MPa]	2.19E5	2.19E5	0.0073E5	7.30E5
G [MPa]	0.876E5	$G2$	0.0029E5	2.92E5

Table 9
Shear modulus values for the interface layer for delamination study in a 3-layered cantilever beam. Values of $G2$ in MPa.

Model	$G2$	Model	$G2$	Model	$G2$
1	8.76E+004	5	8.76E+000	9	8.76E−004
2	8.76E+003	6	8.76E−001	10	8.76E−005
3	8.76E+002	7	8.76E−002	11	8.76E−006
4	8.76E+001	8	8.76E−003	12	8.76E−007

grating the equilibrium equation (via Eqs. (31)–(34)) using the LRZ-100 results. Note the accuracy of the later solution versus the standard LRZ-100 results as delamination develops and the transverse shear stress progressively vanishes at the interface layer.

Similar good results for predicting the delamination and the thickness distribution of the axial and transverse shear stresses are obtained over the entire beam length.

The example shows clearly the capability of the LRZ element to model a complex phenomenon such as delamination in composite laminated beams *without introducing additional kinematic variables*. More evidence of the good behavior of the LRZ beam element for predicting delamination in beams are reported in [29].

8. Conclusions

We have presented a simple and accurate 2-noded beam element based on the refined zigzag beam theory proposed by Tessler et al. [22]. The element has four degrees of freedom per

node (the axial displacement, the deflection, the rotation and the amplitude of the zigzag function). A standard C^0 linear interpolation is used for all variables. The resulting LRZ beam element is shear locking-free and has shown an excellent behavior for analysis of thick and thin composite laminated beams with clamped and simple supported conditions. Numerical results agree in practically all cases with those obtained with a two-dimensional plane-stress FEM using a far larger number of degrees of freedom. It is remarkable that the zigzag distribution of the axial displacement and the axial stress across the thickness, typical of composite laminated beams, is very accurately captured with the basic approximation chosen. The possibilities of the new LRZ beam element for predicting delamination effects has been demonstrated in a simple but representative example of application.

Acknowledgements

This research was partially supported by project SEDUREC of the Consolider Programme of the Ministerio de Educación y Ciencia of Spain.

References

[1] S.P. Timoshenko, S. Woinowsky-Krieger, Theory of Plates and Shells, third ed., McGraw-Hill, New York, 1959.
[2] S. Timoshenko, On the correction for shear of differential equations for transverse vibrations of prismatic bars, Philos. Mag. Ser. 41 (1921) 744–746.
[3] D. Liu, X. Li, An overall view of laminate theories based on displacement hypothesis, J. Compos. Mater. 30 (14) (1996) 1539–1561.
[4] J.N. Reddy, Mechanics of Laminated Composite Plates and Shells. Theory and Analysis, second ed., CRC Press, Boca Raton, 2004.
[5] D.R.J. Owen, Z.H. Li, A refined analysis of laminated plates by finite element displacement methods. Part I. Fundamentals and static analysis. II Vibration and stability, Comput. Struct. 26 (1987) 907–923.
[6] S. Botello, E. Oñate, J.M. Canet, A layer-wise triangle for analysis of laminated composite plates and shells, Comput. Struct. 70 (1999) 635–646.
[7] M. Di Sciuva, Bending, vibration and buckling of simply supported thick multilayered orthotropic plates: an evaluation of a new displacement model, J. Sound Vibr. 105 (1986) 425–442.
[8] H. Murakami, Laminated composite plate theory with improved in-plane responses, ASME J. Appl. Mech. 53 (1986) 661–666.
[9] V.R. Aitharaju, R.C. Averill, An assessment of zig-zag kinematic displacement models for the analysis of laminated composites, Mech. Compos. Mater. Struct. 6 (1999) 1–26.
[10] V.R. Aitharaju, R.C. Averill, C^0 zig-zag finite element for analysis of laminated composite beams, J. Engrg. Mech. ASCE (1999) 323–330.
[11] X. Li, D. Liu, An interlaminar shear stress continuity theory for both thin and thick composite laminates, J. Appl. Mech. 59 (1992) 502–509.
[12] M. Di Sciuva, An improved shear-deformation theory for moderately thick multilayered anisotropic shells and plates, J. Appl. Mech. 54 (1987) 589–594.
[13] A. Toledano, H. Murakami, A higher-order laminate plate theory with improved in-plane response, Int. J. Solids Struct. 23 (1987) 111–131.
[14] M. Cho, R.R. Parmerter, Efficient higher order composite plate theory for general laminations configuration, AIAA J. 31 (1993) 1299–1306.
[15] S. Kapuria, P.C. Dumir, A. Ahmed, N. Alam, Finite element model of efficient zigzag theory for static analysis of hybrid piezoelectric beams, Comput. Mech. 34 (6) (2004) 475–483.
[16] R.C. Averill, Static and dynamic response of moderately thick laminated beams with damage, Compos. Engrg. 4 (4) (1994) 381–395.
[17] R.C. Averill, Yip Yuen Cheong, Development of simple, robust finite elements based on refined theories for thick laminated beams, Comput. Struct. 59 (3) (1996) 529–546.
[18] N.M. Alam, N.Kr. Upadhyay, Finite element analysis of laminated composite beams for zigzag theory using MATLAB, Int. J. Mech. Solids 5 (1) (2010) 1–14.
[19] M. Savoia, On the accuracy of one-dimensional models for multilayered composite beams, Int. J. Solids Struct. 33 (1996) 521–544.
[20] S. Kapuria, P.C. Dumir, N.K. Jain, Assessment of zigzag theory for static loading, buckling, free and forced response of composite and sandwich beams, Compos. Struct. 64 (2004) 317–327.
[21] E. Carrera, Historical review of zigzag theories for multilayered plate and shell, Appl. Mech. Rev. 56 (3) (2003) 287–308.
[22] A. Tessler, M. Di Sciuva, M. Gherlone, A refined zigzag beam theory for composite and sandwich beams, J. Compos. Mater. 43 (2009) 1051–1081.
[23] A. Tessler, M. Di Sciuva, M. Gherlone, A consistent refinement of first-order shear-deformation theory for laminated composite and sandwich plates using improved zigzag kinematics, J. Mech. Mater. Struct. 5 (2) (2010) 341–367.
[24] M. Gherlone, A. Tessler, M. Di Sciuva, C^0 beam element based on the refined zigzag theory for multilayered composite and sandwich laminates, Compos. Struct. 93 (2011) 2882–2894.
[25] E. Oñate, A. Eijo, S. Oller, Two-noded Beam Element for Composite and Sandwich Beams Using Timoshenko Theory and Refined Zigzag Kinematics, Publication CIMNE PI346, CIMNE, Barcelona, October 2010.
[26] M. Di Sciuva, M. Gherlone, A global/local third-order Hermitian displacement field with damaged interfaces and transverse extensibility: FEM formulation, Compos. Struct. 59 (4) (2003) 433–444.
[27] M. Di Sciuva, M. Gherlone, Quasi-3D static and dynamic analysis of undamaged and damaged sandwich beams, J. Sandwich Struct. Mater. 7 (1) (2005) 31–52.
[28] E. Oñate, Structural analysis with the finite element method, Beams, Plates and Shells, vol. 2, CIMNE-Springer, 2012.
[29] E. Oñate,A. Eijo, S. Oller, Modeling of Delamination in Composite Laminated Beams Using a Two-noded Beam Element Based in Refined Zigzag Theory, Publication CIMNE, PI367, November 2011.

INTERNATIONAL JOURNAL FOR NUMERICAL METHODS IN ENGINEERING
Int. J. Numer. Meth. Engng 2013; **95**:631–660
Published online 20 May 2013 in Wiley Online Library (wileyonlinelibrary.com). DOI: 10.1002/nme.4503

A four-noded quadrilateral element for composite laminated plates/shells using the refined zigzag theory

A. Eijo*,†, E. Oñate and S. Oller

International Center for Numerical Methods in Engineering (CIMNE), Universitat Politècnica de Catalunya (UPC), Gran Capitán s/n, 08034 Barcelona, Spain

SUMMARY

A new bilinear four-noded quadrilateral element (called quadrilateral linear refined zigzag) for the analysis of composite laminated and sandwich plates/shells based on the refined zigzag theory is presented. The element has seven kinematic variables per node. Shear locking is avoided by introducing an assumed linear shear strain field. The performance of the element is studied in several examples where the reference solution is the 3D finite element analysis using 20-noded hexahedral elements.

Received 12 June 2012; Revised 12 September 2012; Accepted 11 March 2013

KEY WORDS: composites; finite element methods; plates; shells

1. INTRODUCTION

The classical thin plate theory, known as *Kirchhoff theory* [1], and the more advanced *Reissner–Mindlin* theory (RMT) [2, 3], also called *first order shear deformation theory* (FSDT), were the first simplified theories able to precisely model a plate structure of homogeneous material. However, when applied to highly heterogeneous laminated composite plates, it is known that both theories give poor predictions. The cause of this drawback is because these theories propose a linear thickness distribution of the axial displacement, which is unable to represent the complex real kinematics of a composite laminate.

Three-dimensional finite element analysis is the more appropriate tool to accurately model plates and shells of laminated composite material. However, for composites with hundred of plies, 3D analysis becomes prohibitively expensive.

Improved FSDT models have been obtained by the so-called *higher order shear deformation theory* [4, 5]. In these models, higher order kinematic terms with respect to the plate thickness are added to the expression for the axial displacement. However, these models are not effective for complex cases with localized loads or high transverse anisotropy.

More accurate models are given by the *layerwise theories* (LWT) [4, 6], in which the thickness coordinate is divided into a number of analysis layers (that may be not coincident with the number of laminate physical layers) assuming separate displacement field expansions within each ply. LWT yield high quality predictions. However, the number of unknowns depends on the number of analysis layers, which largely increases the computational cost of the method.

*Correspondence to: A. Eijo, International Center for Numerical Methods in Engineering (CIMNE), Universitat Politècnica de Catalunya (UPC), Gran Capitán s/n, 08034 Barcelona, Spain.

†E-mail: aeijo@cimne.upc.edu

An attractive alternative between the accuracy of LWT and the computational efficiency of FSDT and some higher order shear deformation theory are the *zigzag* (ZZ) *theories* [4, 5, 7]. In ZZ theories, the in-plane displacement is a superposition of a piecewise linear displacement function (the ZZ function) over a linear, a quadratic or a cubic displacement field along the thickness direction. It is important to note that the number of kinematics variables in ZZ theories is independent of the number of layers. Many of the ZZ formulations suffer from their inability to model correctly a clamped boundary condition, which makes it difficult to satisfy equilibrium of forces at a support. In addition, many ZZ theories require C^1 continuity for the deflection field, which is a disadvantage versus simpler C^0 continuity plate theories, such as RMT.

Tessler *et al.* [8–12] have recently developed a *refined zigzag theory* (RZT) for beams and plates that adopt Timoshenko and RMT displacement fields as the baselines for beam and plate analysis, respectively. The key attributes of the RZT are, first, a linear piecewise ZZ function that vanishes at top and bottom surfaces of the beam and the plate section. Second, it does not require full transverse shear stress continuity across the laminated plate depth. Third, C^0 continuity is only required for the FEM approximation of the kinematic variables, and finally, all boundary conditions can be effectively simulated [8, 9, 13, 14].

Oñate *et al.* [13] have taken the RZT as the basis for developing a simple two-noded C^0 beam element named LRZ. The accuracy of the LRZ beam element for analyzing composite laminated beams has been demonstrated for simple support and clamped beams under different loads. The possibility of the LRZ beam element for modeling delamination effects has also been tested [13]. Recently, anisoparametric two-noded and three-noded C^0 beam elements based on the RZT have been presented by Gherlone *et al.* [14]. More recently, a six-node and three-node, C^0-continuous, RZT-based triangular plate finite elements have been developed by Versino *et al.* [15].

In this work, we present the formulation of an isoparametric four-noded C^0 quadrilateral plate element named quadrilateral linear refined zigzag (QLRZ) [16] with seven kinematic variables per node based on the RZT [8]. Shear looking is avoided by using an *assumed linear shear strain field*. The good performance of QLRZ is shown in three different studies: *verification*, *convergence*, and *comparison*. The *verification* section aims at evaluating the performance of this element when the material is homogenous, that is, when the ZZ function vanishes. The influence of composite material on the convergence and the accuracy of the QLRZ element is analyzed in the *convergence* section. Finally, we present several examples of the good performance of the QLRZ element highly heterogeneous materials in the *comparison* section.

2. GENERAL CONCEPTS OF ZIGZAG PLATE THEORY

2.1. Zigzag kinematics

The kinematic field in *ZZ plate theory* is generally written as

$$\begin{aligned} u^k(x,y,z) &= u_0(x,y) - z\cdot\theta_x(x,y) + \bar{u}^k(x,y,z) \\ v^k(x,y,z) &= v_0(x,y) - z\cdot\theta_y(x,y) + \bar{v}^k(x,y,z) \\ w\ (x,y) &= w_0(x,y) \end{aligned} \tag{1a}$$

where the axial displacement functions are

$$\begin{aligned} \bar{u}^k &= \phi_x^k(z)\cdot\psi_x(x,y) \qquad ; \qquad k=1,N \\ \bar{v}^k &= \phi_y^k(z)\cdot\psi_y(x,y) \end{aligned} \tag{1b}$$

and superscript k indicates quantities within the kth layer with $z_k \leqslant z \leqslant z_{k+1}$, z_k is the vertical coordinate of the kth interface and N is the number of layers. The *uniform axial displacements* along the coordinate directions x and y are u_0 and v_0, respectively; θ_x and θ_y represent the *average bending rotation* of the transverse normal about the negative y and positive x directions and w_0 is the *transverse deflection*. ϕ_i^k $(i = x, y)$ denotes a known piecewise linear *ZZ function*, and ψ_i is a

DOI: 10.1002/nme

primary kinematic variable defining the *amplitude of the ZZ function* on the plate. Summarizing, the kinematic variables are

$$\mathrm{a} = \left[\begin{array}{ccccccc} u_0 & v_0 & w_0 & \theta_x & \theta_y & \psi_x & \psi_y \end{array} \right]^T \tag{1c}$$

The ZZ displacement field of Equation (1a) is a superposition between the standard kinematics of the first order RMT and the linear piecewise ZZ functions (Equation (1b)). Note that the ZZ displacement vanishes for homogeneous materials leading to the displacement field of the RMT.

The in-plane $\left(\varepsilon_p^k\right)$ and transverse shear $\left(\varepsilon_t^k\right)$ strains are defined as

$$\begin{aligned} \varepsilon^k = \left[\begin{array}{c} \varepsilon_p \\ \hline \varepsilon_t \end{array} \right]^k = \left[\begin{array}{c} \varepsilon_x \\ \varepsilon_y \\ \gamma_{xy} \\ \hline \gamma_{xz} \\ \gamma_{yz} \end{array} \right]^k = \left[\begin{array}{c} \dfrac{\partial u^k}{\partial x} \\ \dfrac{\partial v^k}{\partial y} \\ \dfrac{\partial u^k}{\partial y} + \dfrac{\partial v^k}{\partial x} \\ \hline \dfrac{\partial u^k}{\partial z} + \dfrac{\partial w}{\partial x} \\ \dfrac{\partial v^k}{\partial z} + \dfrac{\partial w}{\partial y} \end{array} \right] \\ = \left[\begin{array}{c} \dfrac{\partial u_0}{\partial x} \\ \dfrac{\partial v_0}{\partial y} \\ \dfrac{\partial u_0}{\partial y} + \dfrac{\partial v_0}{\partial x} \\ \hline 0 \\ 0 \end{array} \right] + \left[\begin{array}{c} -z\dfrac{\partial \theta_x}{\partial x} \\ -z\dfrac{\partial \theta_y}{\partial y} \\ -z\left(\dfrac{\partial \theta_x}{\partial y} + \dfrac{\partial \theta_y}{\partial x}\right) \\ \hline \dfrac{\partial w_0}{\partial x} - \theta_x \\ \dfrac{\partial w_0}{\partial y} - \theta_y \end{array} \right] + \left[\begin{array}{c} \phi_x^k(z)\dfrac{\partial \psi_x}{\partial x} \\ \phi_y^k(z)\dfrac{\partial \psi_y}{\partial y} \\ \phi_x^k(z)\dfrac{\partial \psi_x}{\partial y} + \phi_y^k(z)\dfrac{\partial \psi_y}{\partial x} \\ \hline \dfrac{\partial \phi_x^k}{\partial z}\psi_x \\ \dfrac{\partial \phi_y^k}{\partial z}\psi_y \end{array} \right] = \\ = \left[\begin{array}{c} \varepsilon_m \\ \hline 0 \end{array} \right] + \left[\begin{array}{c} \varepsilon_b \\ \hline \varepsilon_s \end{array} \right] + \left[\begin{array}{c} \varepsilon_{mb\phi} \\ \hline \varepsilon_{s\phi} \end{array} \right]^k = \left[\begin{array}{cc} S_p & 0 \\ 0 & S_t \end{array} \right]^k \cdot \left[\begin{array}{c} \hat{\varepsilon}_p \\ \hline \hat{\varepsilon}_t \end{array} \right] \end{aligned} \tag{2a}$$

where ε_m, ε_b, and ε_s are the strain vectors duo to membrane, bending, and transverse shear effects of the RMT, respectively. The in-plane and the transverse shear strain vectors emanating from the RZT are denoted by $\varepsilon_{mb\phi}$ and $\varepsilon_{s\phi}$, and $\hat{\varepsilon}_p$ and $\hat{\varepsilon}_t$ are the generalized in-plane and the transverse shear strain vectors defined as

$$\begin{aligned} \hat{\varepsilon}_p = \left[\begin{array}{c} \hat{\varepsilon}_m \\ \hat{\varepsilon}_b \\ \hat{\varepsilon}_{mb\phi} \end{array} \right]; \hat{\varepsilon}_t = \left[\begin{array}{c} \hat{\varepsilon}_s \\ \hat{\varepsilon}_{s\phi} \end{array} \right] \\ S_p^k = \left[\begin{array}{ccc} S_m & S_b & S_{mb\phi}^k \end{array} \right]; S_t^k = \left[\begin{array}{cc} S_s & S_{s\phi}^k \end{array} \right] \end{aligned} \tag{2b}$$

DOI: 10.1002/nme

where $\widehat{(.)}$ denotes the generalized strain vectors given by

$$\begin{aligned}
\hat{\varepsilon}_m &= \left[\begin{array}{cccc} \frac{\partial u_0}{\partial x} & \frac{\partial v_0}{\partial y} & \frac{\partial u_0}{\partial y}+\frac{\partial v_0}{\partial x} \end{array}\right]^T;\ \hat{\varepsilon}_s = \left[\begin{array}{c} \frac{\partial w_0}{\partial x}-\theta_x \\ \frac{\partial w_0}{\partial y}-\theta_y \end{array}\right] = \left[\begin{array}{c} \gamma_{xz} \\ \gamma_{yz} \end{array}\right] \\
\hat{\varepsilon}_b &= \left[\begin{array}{cccc} \frac{\partial \theta_x}{\partial x} & \frac{\partial \theta_y}{\partial y} & \frac{\partial \theta_x}{\partial y}+\frac{\partial \theta_y}{\partial x} \end{array}\right]^T; \hat{\varepsilon}_{s\phi} = \left[\begin{array}{c} \psi_x \\ \psi_y \end{array}\right] \\
\hat{\varepsilon}_{mb\phi} &= \left[\begin{array}{cccc} \frac{\partial \psi_x}{\partial x} & \frac{\partial \psi_y}{\partial y} & \frac{\partial \psi_x}{\partial y} & \frac{\partial \psi_y}{\partial x} \end{array}\right]^T
\end{aligned} \tag{2c}$$

$$\begin{aligned}
S_m &= \left[\begin{array}{ccc} 1 & 0 & 0 \\ 0 & 1 & 0 \\ 0 & 0 & 1 \end{array}\right] = \mathrm{I}_3;\ S_b = -z\ \mathrm{I}_3;\ S_s = \left[\begin{array}{cc} 1 & 0 \\ 0 & 1 \end{array}\right] = \mathrm{I}_2 \\
S^k_{mb\phi} &= \left[\begin{array}{cccc} \phi^k_x(z) & 0 & 0 & 0 \\ 0 & \phi^k_y(z) & 0 & 0 \\ 0 & 0 & \phi^k_x(z) & \phi^k_y(z) \end{array}\right];\ S^k_{s\phi} = \left[\begin{array}{cc} \frac{\partial \phi^k_x}{\partial z} & 0 \\ 0 & \frac{\partial \phi^k_y}{\partial z} \end{array}\right]
\end{aligned} \tag{2d}$$

where γ_{iz} $(i = x, y)$ is the average transverse shear strain of RMT. Note that ϕ^k_i is piecewise linear; hence, its derivative $\left(\frac{\partial \phi^k_i}{\partial z} = \beta^k_i\right)$ is constant within each layer.

2.2. Constitutive relationships

The relationship between the in-plane and the transverse shear stresses and the strains for the kth layer are expressed in matrix form as

$$\sigma^k = \left[\begin{array}{c} \sigma_p \\ \sigma_t \end{array}\right]^k = \left[\begin{array}{c} \sigma_x \\ \sigma_y \\ \tau_{xy} \\ \tau_{xz} \\ \tau_{yz} \end{array}\right]^k = \left[\begin{array}{cc} \mathrm{D}_p & 0 \\ 0 & \mathrm{D}_t \end{array}\right]^k \cdot \left[\begin{array}{c} \varepsilon_p \\ \varepsilon_t \end{array}\right]^k = \mathrm{D}^k \varepsilon^k \tag{3a}$$

with

$$\begin{aligned}
\mathrm{D}^k_p &= \frac{1}{1-\upsilon_{xy}\upsilon_{yx}} \left[\begin{array}{ccc} E_x & \upsilon_{xy}E_x & 0 \\ \upsilon_{yx}E_x & E_y & 0 \\ 0 & 0 & (1-\upsilon_{xy}\upsilon_{yx})G_{xy} \end{array}\right] \\
\mathrm{D}^k_t &= \left[\begin{array}{cc} G_{xz} & 0 \\ 0 & G_{yz} \end{array}\right]
\end{aligned} \tag{3b}$$

Note that the constitutive matrix D (Equation (3b)) is valid for homogeneous isotropic/orthotropic materials only. For anisotropic composed materials, created by two or more substances, it should be necessary to use other more advanced theories [17, 18].

DOI: 10.1002/nme

The resultant stress vectors are defined as

Membrane forces

$$\hat{\sigma}_m = \begin{bmatrix} N_x \\ N_y \\ N_{xy} \end{bmatrix} = \int_z {S_m}^T \sigma_p^k dz$$

$$\hat{\sigma}_m = \left(\int_z {S_m}^T D_p^k S_m dz \right) \hat{\varepsilon}_m + \left(\int_z {S_m}^T D_p^k S_b dz \right) \hat{\varepsilon}_b + \left(\int_z {S_m}^T D_p^k S_{mb\phi}^k dz \right) \hat{\varepsilon}_{mb\phi}$$

$$\hat{\sigma}_m = \hat{D}_m \hat{\varepsilon}_m + \hat{D}_{mb} \hat{\varepsilon}_b + \hat{D}_{mmb\phi} \hat{\varepsilon}_{mb\phi} \tag{3c}$$

$$\hat{D}_m = \int_z {S_m}^T D_p^k S_m dz$$

$$\hat{D}_{mb} = \int_z {S_m}^T D_p^k S_b dz$$

$$\hat{D}_{mmb\phi} = \int_z {S_m}^T D_p^k S_{mb\phi}^k dz$$

Bending moments

$$\hat{\sigma}_b = \begin{bmatrix} M_x \\ M_y \\ M_{xy} \end{bmatrix} = \int_z {S_b}^T \sigma_p^k dz$$

$$\hat{\sigma}_b = \left(\int_z {S_b}^T D_p^k S_m dz \right) \hat{\varepsilon}_m + \left(\int_z {S_b}^T D_p^k S_b dz \right) \hat{\varepsilon}_b + \left(\int_z {S_b}^T D_p^k S_{mb\phi}^k dz \right) \hat{\varepsilon}_{mb\phi} \tag{3d}$$

$$\hat{\sigma}_b = \hat{D}_{bm} \hat{\varepsilon}_m + \hat{D}_b \hat{\varepsilon}_b + \hat{D}_{bmb\phi} \hat{\varepsilon}_{mb\phi}$$

$$\hat{D}_{bm} = \int_z {S_b}^T D_p^k S_m dz$$

$$\hat{D}_b = \int_z {S_b}^T D_p^k S_b dz$$

$$\hat{D}_{bmb\phi} = \int_z {S_b}^T D_p^k S_{mb\phi}^k dz$$

Transverse shear forces

$$\hat{\sigma}_s = \begin{bmatrix} Q_{xz} \\ Q_{yz} \end{bmatrix} = \int_z {S_s}^T \sigma_t^k dz$$

$$\hat{\sigma}_s = \left(\int_z {S_s}^T D_t^k S_s dz \right) \hat{\varepsilon}_s + \left(\int_z {S_s}^T D_t^k S_{s\phi}^k dz \right) \hat{\varepsilon}_{s\phi}$$

$$\hat{\sigma}_s = \hat{D}_s \hat{\varepsilon}_s + \hat{D}_{ss\phi} \hat{\varepsilon}_{s\phi} \tag{3e}$$

$$\hat{D}_s = \int_z {S_s}^T D_t^k S_s dz$$

$$\hat{D}_{ss\phi} = \int_z {S_s}^T D_t^k S_{s\phi}^k dz$$

Next, we define the additional pseudo-bending moments and the pseudo-shear forces emanating from the RZT, which are conjugate to the new generalized strains $\frac{\partial \psi_i}{\partial j}$ $(i, j = x, y)$ and the variable ψ_i, respectively.

DOI: 10.1002/nme

The *pseudo-bending* moments are defined by

$$\hat{\sigma}_{mb\phi} = \begin{bmatrix} M_{x\phi_x} \\ M_{y\phi_y} \\ M_{xy\phi_x} \\ M_{xy\phi_y} \end{bmatrix} = \int_z {S^k_{mb\phi}}^T \sigma^k_p dz$$

$$\hat{\sigma}_{mb\phi} = \left(\int_z {S^k_{mb\phi}}^T D^k_p S_m dz \right) \hat{\varepsilon}_m + \left(\int_z {S^k_{mb\phi}}^T D^k_p S_b dz \right) \hat{\varepsilon}_b + \left(\int_z {S^k_{mb\phi}}^T D^k_p S^k_{mb\phi} dz \right) \hat{\varepsilon}_{mb\phi}$$

$$\hat{\sigma}_{mb\phi} = \hat{D}_{mb\phi m} \hat{\varepsilon}_m + \hat{D}_{mb\phi b} \hat{\varepsilon}_b + \hat{D}_{mb\phi} \hat{\varepsilon}_{mb\phi} \tag{3f}$$

$$\hat{D}_{mb\phi m} = \int_z {S^k_{mb\phi}}^T D^k_p S_m dz$$

$$\hat{D}_{mb\phi b} = \int_z {S^k_{mb\phi}}^T D^k_p S_b dz$$

$$\hat{D}_{mb\phi} = \int_z {S^k_{mb\phi}}^T D^k_p S^k_{mb\phi} dz$$

and the *pseudo-shear forces* by

$$\hat{\sigma}_s = \begin{bmatrix} Q_{xz\psi_x} \\ Q_{yz\psi_y} \end{bmatrix} = \int_z {S^k_{s\phi}}^T \sigma^k_t dz$$

$$\hat{\sigma}_{s\phi} = \left(\int_z {S^k_{s\phi}}^T D^k_t S_s dz \right) \hat{\varepsilon}_s + \left(\int_z {S^k_{s\phi}}^T D^k_t S^k_{s\phi} dz \right) \hat{\varepsilon}_{s\phi}$$

$$\hat{\sigma}_{s\phi} = \hat{D}_{s\phi s} \hat{\varepsilon}_s + \hat{D}_{s\phi} \hat{\varepsilon}_{s\phi} \tag{3g}$$

$$\hat{D}_{s\phi s} = \int_z {S^k_{s\phi}}^T D^k_t S_s dz$$

$$\hat{D}_{s\phi} = \int_z {S^k_{s\phi}}^T D^k_t S^k_{s\phi} dz$$

The overall constitutive expression for the resultant stresses can be written in matrix form as

$$\hat{\sigma} = \begin{bmatrix} \hat{\sigma}_p \\ \hat{\sigma}_t \end{bmatrix} = \begin{bmatrix} \tilde{D}_p & 0 \\ 0 & \tilde{D}_t \end{bmatrix} \cdot \begin{bmatrix} \hat{\varepsilon}_p \\ \hat{\varepsilon}_t \end{bmatrix} \tag{3h}$$

where $\hat{\sigma}_p$ and $\hat{\sigma}_t$ contain the in-plane and the transverse shear resultant stresses, respectively,

$$\hat{\sigma}_p = \begin{bmatrix} \hat{\sigma}_m \\ \hat{\sigma}_b \\ \hat{\sigma}_{mb\phi} \end{bmatrix}; \hat{\sigma}_t = \begin{bmatrix} \hat{\sigma}_s \\ \hat{\sigma}_{s\phi} \end{bmatrix} \tag{3i}$$

that is, the in-plane and the transverse shear generalized constitutive matrices, $\tilde{D}_p$ and $\tilde{D}_t$, are given by

$$\tilde{D}_p = \begin{bmatrix} \hat{D}_m & \hat{D}_{mb} & \hat{D}_{mmb\phi} \\ \hat{D}_{bm} & \hat{D}_b & \hat{D}_{bmb\phi} \\ \hat{D}_{mb\phi m} & \hat{D}_{mb\phi b} & \hat{D}_{mb\phi} \end{bmatrix}; \tilde{D}_t = \begin{bmatrix} \hat{D}_s & \hat{D}_{ss\phi} \\ \hat{D}_{s\phi s} & \hat{D}_{s\phi} \end{bmatrix}$$

2.3. Principle of virtual work

The virtual work principle for a distributed load q and point loads $\mathbf{f}_i$ can be stated as

$$\iiint_V \delta\varepsilon^{k\,T} \sigma^k dV = \iint_A \delta a^T q dA + \sum_{i=1}^{npl} \delta a_i{}^T f_i \tag{4a}$$

DOI: 10.1002/nme

where the l.h.s. of Equation (4a) expresses the internal virtual work performed by the stresses and the r.h.s. is the external virtual work of the distributed and point loads. V is the volume of the plate, A is the area of application of the distributed load, and npl is the number of point loads. Substituting Equation (2a) into Equation (4a) gives

$$\begin{aligned}\iiint_V \delta\varepsilon^{kT}\sigma^k\,dV &= \iiint_V \left(\delta\hat{\varepsilon}_m{}^T \mathrm{S}_m{}^T + \delta\hat{\varepsilon}_b{}^T \mathrm{S}_b{}^T + \delta\hat{\varepsilon}^T_{mb\phi}\mathrm{S}^k_{mb\phi}{}^T\right)\sigma_p^k\,dV + \\ &\quad + \iiint_V \left(\delta\hat{\varepsilon}_s{}^T \mathrm{S}_s{}^T + \delta\hat{\varepsilon}_{s\phi}{}^T \mathrm{S}^k_{s\phi}{}^T\right)\sigma_t^k\,dV \\ &= \iiint_V \left(\delta\hat{\varepsilon}_m{}^T \mathrm{S}_m{}^T\sigma_p^k + \delta\hat{\varepsilon}_b{}^T \mathrm{S}_b{}^T\sigma_p^k + \delta\hat{\varepsilon}^T_{mb\phi}\mathrm{S}^k_{mb\phi}{}^T\sigma_p^k\right)dV + \\ &\quad + \iiint_V \left(\delta\hat{\varepsilon}_s{}^T \mathrm{S}_s{}^T\sigma_t^k + \delta\hat{\varepsilon}_{s\phi}{}^T \mathrm{S}^k_{s\phi}{}^T\sigma_t^k\right)dV\end{aligned}$$

By using Equations (3c), (3d), (3e), (3f), and (3g) yields

$$\iiint_V \delta\varepsilon^{kT}\sigma^k\,dV = \iint_A \left(\delta\hat{\varepsilon}_m{}^T\hat{\sigma}_m + \delta\hat{\varepsilon}_b{}^T\hat{\sigma}_b + \delta\hat{\varepsilon}_{mb\phi}{}^T\hat{\sigma}_{mb\phi}\right)\,dA + \iint_A \left(\delta\hat{\varepsilon}_s{}^T\hat{\sigma}_s + \delta\hat{\varepsilon}_{s\phi}{}^T\hat{\sigma}_{s\phi}\right)\,dA$$

The virtual work can be therefore written as

$$\iint_A \left(\delta\hat{\varepsilon}_p{}^T\hat{\sigma}_p + \delta\hat{\varepsilon}_t{}^T\hat{\sigma}_t\right) = \iint_A \delta\mathrm{a}^T\mathrm{q}dA + \sum_{i=1}^{npl}\delta\mathrm{a}_i{}^T\mathrm{f}_i \tag{4b}$$

The integrands in Equation (4b) contain kinematic variable derivatives up to first order only, which allows us to use C^0 continuous elements.

3. DERIVATION OF THE ZIGZAG FUNCTION

The ZZ function is defined within each layer by

$$\phi_i^k = \frac{1}{2}(1-\xi)\bar{\phi}_i^{k-1} + \frac{1}{2}(1+\xi)\bar{\phi}_i^k = \frac{\bar{\phi}_i^k + \bar{\phi}_i^{k-1}}{2} + \frac{\bar{\phi}_i^k - \bar{\phi}_i^{k-1}}{2}\xi^k \qquad i = x, y \tag{5}$$

where $\bar{\phi}_i^k$ and $\bar{\phi}_i^{k-1}$ is the ZZ function valued at k and $k-1$ interface, respectively with $\bar{\phi}_i^0 = \bar{\phi}_i^N = 0$ and $\xi^k = 2\frac{(z-z^{k-1})}{h^k} - 1$.

Figure 1 shows the *ZZ function* ϕ_x^k, the *ZZ displacements* $\bar{u}^k$, and the *axial displacements* u^k, for the x direction. A similar distribution is found for the ZZ function ϕ_y^k.

The slope of the ZZ function (Equation (5)) gives a constant value for each layer defined as

$$\beta_i^k = \frac{\partial\phi_i^k}{\partial z} = \frac{\left(\bar{\phi}_i^k - \bar{\phi}_i^{k-1}\right)}{h^k} \tag{6a}$$

Because the ZZ function vanishes on the top and bottom surfaces, the through-the-thickness integrals of the slope functions β_i^k is equal to zero, that is,

$$\int_z \beta_i^k\,dz = 0 \tag{6b}$$

It is convenient to define a new difference function η_i as

$$\eta_i = \gamma_{iz} - \psi_i \tag{7}$$

which leads to the following expression for the kth layer transverse shear strains and stresses as

$$\gamma_{iz}^k = \left(1 + \beta_i^k\right)\gamma_{iz} - \beta_i^k\eta_i \tag{8a}$$

DOI: 10.1002/nme

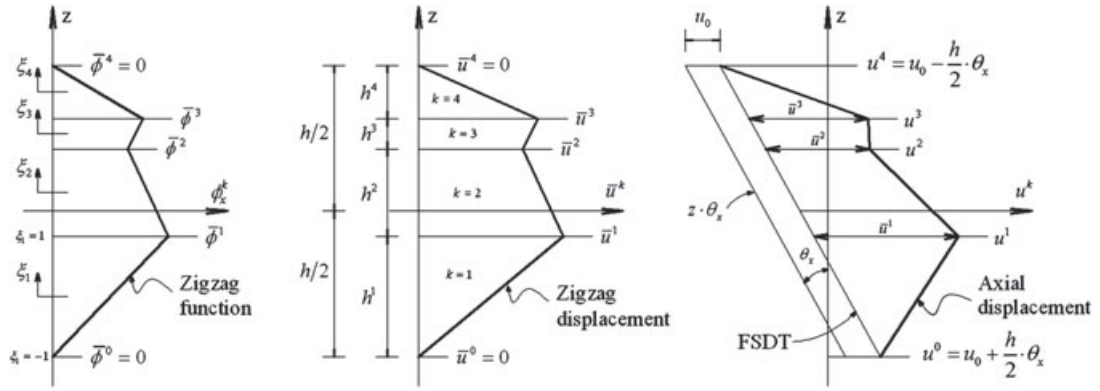

Figure 1. Thickness distribution of (a) the zigzag function ϕ_x^k; (b) the zigzag displacement $\bar{u}^k$; and (c) the axial displacement u^k in the RZT.

$$\tau_{iz}^k = G_{iz}^k \left(1 + \beta_i^k\right) \gamma_{iz} - G_{iz}^k \beta_i^k \eta_i \tag{8b}$$

Equation (8b) is valid for a cross-ply case only.

The average shear strains over the plate thickness are obtained by integrating the transverse shear strains γ_{iz}^k (Equation (8a)) over the thickness and using Equation (6b). This gives

$$\gamma_{iz} = \frac{1}{h} \int_z \gamma_{iz}^k dz \tag{9}$$

The interfacial continuity of the first term, associated with the average shear strain γ_{iz}, is enforced in the transverse shear stress distribution (Equation (8b)), that is,

$$G_{iz}^k \left(1 + \beta_i^k\right) = G_{iz}^{k+1} \left(1 + \beta_i^{k+1}\right) \tag{10a}$$

which leads to a constant shear modulus across the plate thickness defined by

$$G_{iz} = G_{iz}^k \left(1 + \beta_i^k\right) \tag{10b}$$

Then, from Equation (10b)

$$\beta_i^k = \frac{G_{iz}}{G_{iz}^k} - 1 \tag{11}$$

the explicit form of G_{iz} is obtained by substituting β_i^k in the integral of Equation (6b), that is,

$$G_{iz} = h \left[\sum_{k=1}^{N} \frac{h^k}{G_{iz}^k} \right]^{-1} \tag{12}$$

Finally, the ZZ function is obtained by replacing Equation (6a) into Equation (5) — this gives

$$\phi_i^k = \bar{\phi}_i^{k-1} + \frac{h^k \beta_i^k}{2} \left(\zeta^k + 1\right) \tag{13}$$

with β_i^k defined by Equation (11).

4. QUADRILATERAL LINEAR REFINED ZIGZAG PLATE ELEMENT

The QLRZ element (Figure A.1) is a Lagrangian isoparametric four-noded finite element derived from the RZT described previously.

DOI: 10.1002/nme

4.1. Discretization of the displacement field

The middle surface of a plate is discretized into four-node 2D isoparametric finite elements of quadrilateral shape. The kinematic variables (Equation (1c)) can be interpolated within each element as

$$\mathrm{a} = \begin{bmatrix} u_0 \\ v_0 \\ w_0 \\ \theta_x \\ \theta_y \\ \psi_x \\ \psi_y \end{bmatrix} = \sum_{i=1}^{4} \mathrm{N}_i \mathrm{a}_i^{(e)} = \begin{bmatrix} \mathrm{N}_1 & \mathrm{N}_2 & \mathrm{N}_3 & \mathrm{N}_4 \end{bmatrix} \cdot \begin{bmatrix} \mathrm{a}_1^{(e)} \\ \mathrm{a}_2^{(e)} \\ \mathrm{a}_3^{(e)} \\ \mathrm{a}_4^{(e)} \end{bmatrix} = \mathrm{N}\mathrm{a}^{(e)} \tag{14}$$

where

$$\mathrm{N}_i = N_i \mathrm{I}_7 \quad ; \quad \mathrm{a}_i^{(e)} = \begin{bmatrix} u_0 & v_0 & w_0 & \theta_x & \theta_y & \psi_x & \psi_y \end{bmatrix}_i^T$$

being $N_i(\xi, \eta)$ (Equation (21)) the C^0 continuous shape function of node ith and I_7 is the 7×7 unit matrix.

4.2. Generalized strain field

The generalized in-plane strains are obtained in terms of the nodal kinematic variables by substituting Equation (14) into the generalized in-plane shear strains $\hat{\varepsilon}_p$ (Equation (2b)),

$$\hat{\varepsilon}_p = \begin{bmatrix} \hat{\varepsilon}_m \\ \hat{\varepsilon}_b \\ \hat{\varepsilon}_{mb\phi} \end{bmatrix} = \begin{bmatrix} \dfrac{\partial u_0}{\partial x} \\ \dfrac{\partial v_0}{\partial y} \\ \dfrac{\partial u0}{\partial y} + \dfrac{\partial v0}{\partial x} \\ \hline \dfrac{\partial \theta_x}{\partial x} \\ \dfrac{\partial \theta_y}{\partial y} \\ \dfrac{\partial \theta_x}{\partial y} + \dfrac{\partial \theta_y}{\partial x} \\ \hline \dfrac{\partial \psi_x}{\partial x} \\ \dfrac{\partial \psi_y}{\partial y} \\ \dfrac{\partial \psi_x}{\partial y} \\ \dfrac{\partial \psi_y}{\partial x} \end{bmatrix} = \sum_{i=1}^{4} \begin{bmatrix} \dfrac{\partial N_i}{\partial x} u_0 \\ \dfrac{\partial N_i}{\partial y} v_0 \\ \dfrac{\partial Ni}{\partial y} u_0 + \dfrac{\partial N_i}{\partial x} v0 \\ \hline \dfrac{\partial N_i}{\partial x} \theta_x \\ \dfrac{\partial N_i}{\partial y} \theta_y \\ \dfrac{\partial Ni}{\partial y} \theta_x + \dfrac{\partial Ni}{\partial x} \theta_y \\ \hline \dfrac{\partial N_i}{\partial x} \psi_x \\ \dfrac{\partial N_i}{\partial y} \psi_y \\ \dfrac{\partial N_i}{\partial y} \psi_x \\ \dfrac{\partial N_i}{\partial x} \psi_y \end{bmatrix}_i = \sum_{i=1}^{4} \mathrm{B}_{pi} \mathrm{a}_i^{(e)} = \mathrm{B}_p \mathrm{a}^{(e)} \tag{15a}$$

where B_p and B_{pi} are the in-plane generalized strain matrices for the element and the ith node, respectively. The matrix B_{pi} can be split into membrane (m), bending (b), and ZZ ($mb\phi$) contributions. This leads to

$$\mathrm{B}_{pi} = \begin{bmatrix} \mathrm{B}_m \\ \mathrm{B}_b \\ \mathrm{B}_{mb\phi} \end{bmatrix}_i \tag{15b}$$

DOI: 10.1002/nme

with

$$\mathrm{B}_{mi} = \begin{bmatrix} \frac{\partial N_i}{\partial x} & 0 & 0 & 0 & 0 & 0 & 0 \\ 0 & \frac{\partial N_i}{\partial y} & 0 & 0 & 0 & 0 & 0 \\ \frac{\partial N_i}{\partial y} & \frac{\partial N_i}{\partial x} & 0 & 0 & 0 & 0 & 0 \end{bmatrix} \mathrm{B}_{bi} = \begin{bmatrix} 0 & 0 & 0 & \frac{\partial N_i}{\partial x} & 0 & 0 & 0 \\ 0 & 0 & 0 & 0 & \frac{\partial N_i}{\partial y} & 0 & 0 \\ 0 & 0 & 0 & \frac{\partial N_i}{\partial y} & \frac{\partial N_i}{\partial x} & 0 & 0 \end{bmatrix}$$

$$\mathrm{B}_{mb\phi i} = \begin{bmatrix} 0 & 0 & 0 & 0 & 0 & \frac{\partial N_i}{\partial x} & 0 \\ 0 & 0 & 0 & 0 & 0 & 0 & \frac{\partial N_i}{\partial y} \\ 0 & 0 & 0 & 0 & 0 & \frac{\partial N_i}{\partial y} & 0 \\ 0 & 0 & 0 & 0 & 0 & 0 & \frac{\partial N_i}{\partial x} \end{bmatrix} \tag{15c}$$

Replacing Equation (14) into Equation (2b), the generalized transverse strains are obtained as

$$\hat{\varepsilon}_t = \begin{bmatrix} \hat{\varepsilon}_s \\ \hat{\varepsilon}_{s\phi} \end{bmatrix} = \begin{bmatrix} \frac{\partial w_0}{\partial x} - \theta_x \\ \frac{\partial w_0}{\partial y} - \theta_y \\ \hline \psi_x \\ \psi_y \end{bmatrix} = \sum_{i=1}^{4} \begin{bmatrix} \frac{\partial N_i}{\partial x} w_0 - N_i \theta_x \\ \frac{\partial N i}{\partial y} w_0 - N_i \theta_y \\ \hline N_i \psi_x \\ N_i \psi_y \end{bmatrix}_i = \sum_{i=1}^{4} \mathrm{B}_{ti}\, \mathrm{a}_i^{(e)} = \mathrm{B}_t\, \mathrm{a}^{(e)} \tag{16a}$$

where B_t and B_{ti} are the transverse generalized strain matrices for the e element and the ith node, respectively. Matrix B_{ti} can be split into shear (s) and ZZ ($s\phi$) contributions as

$$\mathrm{B}_{ti} = \begin{bmatrix} \mathrm{B}_s \\ \mathrm{B}_{s\phi} \end{bmatrix}_i \tag{16b}$$

where

$$\mathrm{B}_{si} = \begin{bmatrix} 0 & 0 & \frac{\partial N_i}{\partial x} & -N_i & 0 & 0 & 0 \\ 0 & 0 & \frac{\partial N_i}{\partial y} & 0 & -N_i & 0 & 0 \end{bmatrix}$$

$$\mathrm{B}_{s\phi i} = \begin{bmatrix} 0 & 0 & 0 & 0 & 0 & N_i & 0 \\ 0 & 0 & 0 & 0 & 0 & 0 & N_i \end{bmatrix} \tag{16c}$$

4.3. Element stiffness matrix

The equilibrium equations relating nodal forces and displacements are obtained by substituting the discretized Equations (15a) and (16a) into the virtual work principle

$$\iint_A \left(\delta\hat{\varepsilon}_p{}^T \hat{\sigma}_p + \delta\hat{\varepsilon}_t{}^T \hat{\sigma}_t \right) = \iint_A \delta \mathrm{a}^T \mathrm{q}\, dA + \sum_{i=1}^{npl} \delta \mathrm{a}_i{}^T \mathrm{f}_i \tag{17a}$$

Substituting Equation (3h) into the l.h.s of Equation (17a) gives

$$\iint_A \left(\delta\hat{\varepsilon}_p{}^T \hat{\sigma}_p + \delta\hat{\varepsilon}_t{}^T \hat{\sigma}_t \right) = \iint_A \left(\delta\hat{\varepsilon}_p^T \tilde{\mathrm{D}}_p \hat{\varepsilon}_p + \delta\hat{\varepsilon}_t^T \tilde{\mathrm{D}}_t \hat{\varepsilon}_t\, dA \right) \tag{17b}$$

Considering that

$$\begin{aligned} \delta\hat{\varepsilon}_p{}^T &= \sum_{i=1}^{4} \delta \mathrm{a}_i^{(e)T} \mathrm{B}_{pi}{}^T = \delta \mathrm{a}^{(\mathrm{e})T} \mathrm{B}_p{}^T \\ \delta\hat{\varepsilon}_t{}^T &= \sum_{i=1}^{4} \delta \mathrm{a}_i^{(e)T} \mathrm{B}_{ti}{}^T = \delta \mathrm{a}^{(\mathrm{e})T} \mathrm{B}_t{}^T \end{aligned} \tag{17c}$$

DOI: 10.1002/nme

and substituting Equations (15a), (16a), and (17c) into Equation (17b) yields

$$\begin{aligned}\iint_A \left(\delta\hat{\varepsilon}_p^T \tilde{\mathrm{D}}_p \hat{\varepsilon}_p + \delta\hat{\varepsilon}_t^T \tilde{\mathrm{D}}_t \hat{\varepsilon}_t\right) dA &= \iint_A \left(\delta \mathrm{a}^{(\mathrm{e})T} {\mathrm{B}_p}^T \tilde{\mathrm{D}}_p \mathrm{B}_p \mathrm{a}^{(e)}\right) dA \\ &\quad + \iint_A \left(\delta \mathrm{a}^{(\mathrm{e})T} {\mathrm{B}_t}^T \tilde{\mathrm{D}}_t \mathrm{B}_t \mathrm{a}^{(e)}\right) dA = \\ &= \delta \mathrm{a}^{(\mathrm{e})T} \left[\iint_A \left({\mathrm{B}_p}^T \tilde{\mathrm{D}}_p \mathrm{B}_p + {\mathrm{B}_t}^T \tilde{\mathrm{D}}_t \mathrm{B}_t\right) dA\right] a^{(e)} \\ &= \delta \mathrm{a}^{(\mathrm{e})T} \mathrm{K}^{(e)} \mathrm{a}^{(e)}\end{aligned}$$

Finally, Equation (17a) is reduced to

$$\mathrm{K}^{(e)} \mathrm{a}^{(e)} - \iint_A \mathrm{q} dA - \sum_{i=1}^{npl} \mathrm{f}_i = 0 \tag{18}$$

where $\mathrm{K}^{(e)}$ is the sought element stiffness matrix. This matrix can be expressed as

$$\mathrm{K}^{(e)} = \mathrm{K}_p^{(e)} + \mathrm{K}_t^{(e)} \tag{19a}$$

being $\mathrm{K}_p^{(e)}$ and $\mathrm{K}_t^{(e)}$ the in-plane and transverse stiffness matrices, respectively. These are given by

$$\begin{aligned}\mathrm{K}_p^{(e)} &= \iint_A {\mathrm{B}_p}^T \tilde{\mathrm{D}}_p \mathrm{B}_p dA \\ \mathrm{K}_t^{(e)} &= \iint_A {\mathrm{B}_t}^T \tilde{\mathrm{D}}_t \mathrm{B}_t dA\end{aligned} \tag{19b}$$

To facilitate subsequent shear locking studies, we split matrix $\mathrm{K}_t^{(e)}$ as follows

$$\mathrm{K}_t^{(e)} = \mathrm{K}_s^{(e)} + \mathrm{K}_{s\phi}^{(e)} + \mathrm{K}_{ss\phi}^{(e)} + \left[\mathrm{K}_{ss\phi}^{(e)}\right]^T \tag{20a}$$

with

$$\begin{aligned}\mathrm{K}_s^{(e)} &= \iint_A {\mathrm{B}_s}^T \hat{\mathrm{D}}_s \mathrm{B}_s dA \\ \mathrm{K}_{s\phi}^{(e)} &= \iint_A {\mathrm{B}_{s\phi}}^T \hat{\mathrm{D}}_{s\phi} \mathrm{B}_{s\phi} dA \\ \mathrm{K}_{ss\phi}^{(e)} &= \iint_A {\mathrm{B}_s}^T \hat{\mathrm{D}}_{ss\phi} \mathrm{B}_{s\phi} dA\end{aligned} \tag{20b}$$

4.4. Boundary conditions

The boundary conditions are:

A. Clamped side:

$$\begin{aligned} w &= 0 \\ u = \theta_x &= \psi_x = 0 \\ v = \theta_y &= \psi_y = 0\end{aligned}$$

B. Simply supported (SS) side:

- *Hard support:* $w = u_s = \theta_s = \psi_s = 0$
- *Soft support:* $w = 0$

where 's' is the direction of the side.

DOI: 10.1002/nme

C. Symmetry axis:

$$u_n = \theta_n = \psi_n = 0$$

where 'n' is the orthogonal direction to the symmetry axis.

4.5. Shear locking

The original form of the QLRZ element suffers from *shear locking* for slender composite laminated plates. To remove this defect, we use an *assumed transverse shear strain field* [19].

This technique leads to matrix B_s (Equations (16b) and (A.7c)) being replaced by the *substitute transverse shear strain matrix* $\bar{\mathrm{B}}_s$. The form of this matrix can be found in the Appendix section (Equation (A.9)). Matrices B_{mi}, B_{bi}, $\mathrm{B}_{mb\phi i}$ from Equation (15c) and $\mathrm{B}_{s\phi i}$ (Equation (16c)) are computed using the standard bilinear shape functions (see Figure 2 and Table I).

The bilinear shape functions N_i are

$$N_i = \frac{1}{4}(1 + \xi\xi_i)(1 + \eta\eta_i) \tag{21}$$

The stiffness matrices $\mathrm{K}_s^{(e)}$ and $\mathrm{K}_{ss\phi}^{(e)}$ of $\mathrm{K}_t^{(e)}$ in Equation (20a) are therefore computed as

$$\begin{aligned} \mathrm{K}_s^{(e)} &= \iint_A \bar{\mathrm{B}}_s{}^T \hat{\mathrm{D}}_s \bar{\mathrm{B}}_s \, dA \\ \mathrm{K}_{ss\phi}^{(e)} &= \iint_A \bar{\mathrm{B}}_s{}^T \hat{\mathrm{D}}_{ss\phi} \mathrm{B}_{s\phi} \, dA \end{aligned} \tag{22}$$

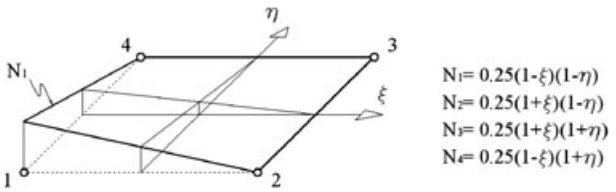

Figure 2. Bilinear shape functions.

Table I. Values of ξ_i and η_i for each node.

Node	ξ_i	η_i
1	-1	-1
2	1	-1
3	1	1
4	-1	1

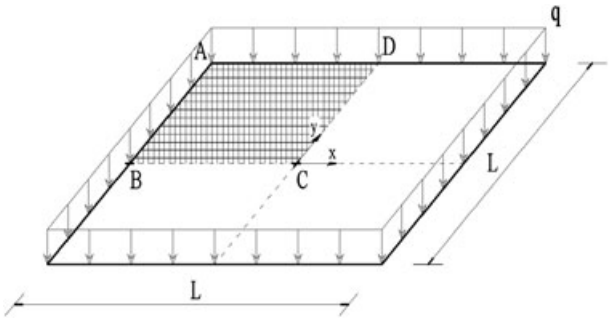

Figure 3. Simply supported square plate under uniformly distributed load.

DOI: 10.1002/nme

Table II. Material properties for shear locking study.

Composite material properties			
Properties	Layer 1 (top)	Layer 2	Layer 3 (bottom)
h	$0.25 \cdot \frac{L}{\lambda}$	$0.50 \cdot \frac{L}{\lambda}$	$0.25 \cdot \frac{L}{\lambda}$
E	2.19E5	2.19E4	4.4E5
G	0.876E5	0.876E4	1.76E5

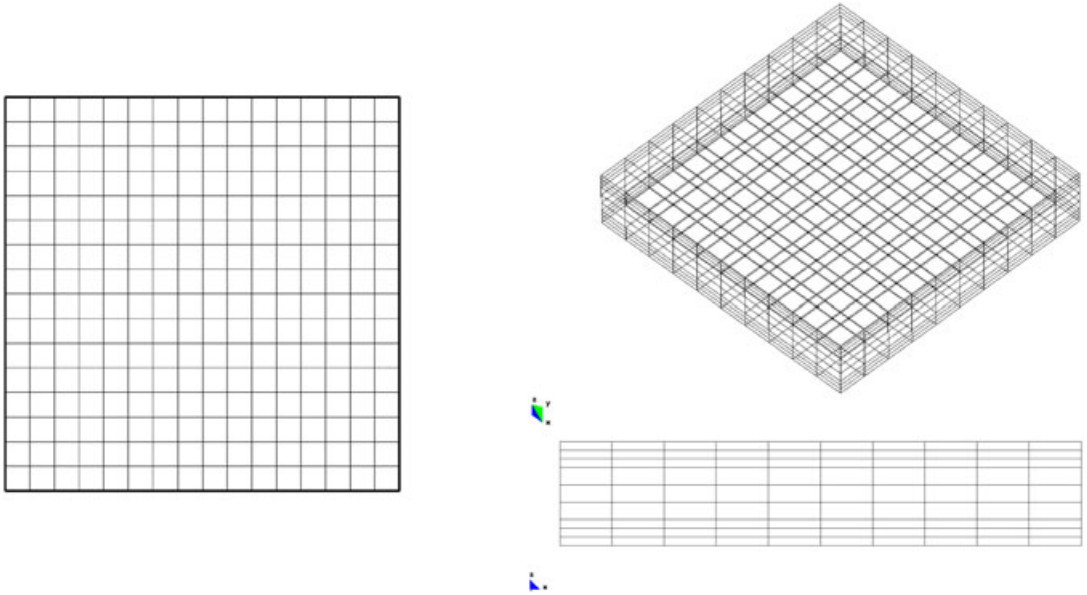

(a) (b)

Figure 4. Meshes used for the analysis of one quarter of the SS plate. (a) 16×16 QLRZ elements and (b) $10 \times 10 \times 9$ HEXA20 elements.

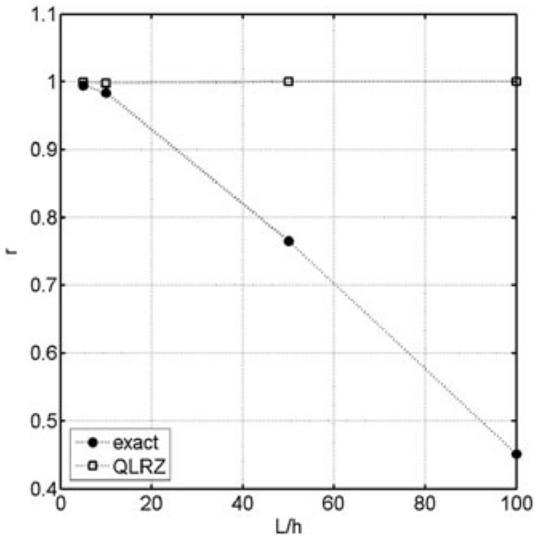

Figure 5. r ratio versus span-to-thickness λ. Simply supported square plate under uniformly distributed load.

DOI: 10.1002/nme

To show the efficiency of this technique, we analyze an SS square plate of length side $L = 2$ under a uniformly distributed load of unit value ($q = 1$) (Figure 3).

The analysis is performed for four span-to-thickness ratios: $\lambda = L/h = 5, 10, 50, 100$. A three-layer composite material is used, whose properties are listed in Table II.

Only one quarter of the plate is studied because of symmetry (Figure 3) by using a mesh of 16×16 QLRZ elements (Figure 4a) with 289 nodes and 1445 DOFs. The reference solution is obtained by a 3D finite element analysis using a mesh of $10\times10\times9$ (3 elements per ply) of 20-noded hexahedral elements (HEXA20) involving 4499 nodes and 13497 DOFs (Figure 4b).

Figure 5 shows the r ratio defined as

$$r = \frac{w_{QLRZ}}{w_{3D}} \tag{23}$$

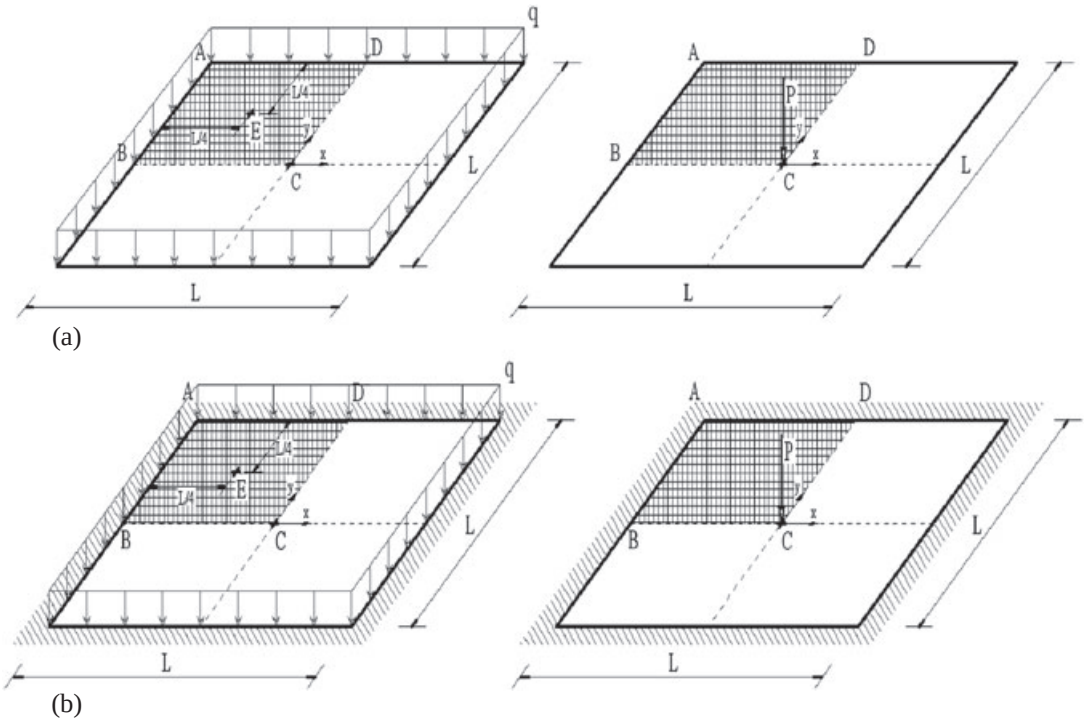

Figure 6. Square plate ($\lambda = 40$) for verification and convergence analysis. (a) SS plate and (b) clamped plate under uniformly distributed load and central point load.

Table III. QLRZ mesh properties.

Meshes properties				
Mesh	N	Elements	Nodes	DOFs
1	2	4	9	45
2	4	16	25	150
3	8	64	81	405
4	16	256	289	1445
5	32	1024	1089	5445

DOI: 10.1002/nme

where w_{QLRZ} and w_{3D} are the middle (z = 0) deflection at the plate center obtained with the QLRZ element and the 3D finite element analysis, respectively. The QLRZ element results have been obtained using *exact* integration of matrix K_t (exact) and with the *assumed transverse shear strain field* technique (QLRZ).

Figure 5 clearly shows the shear locking defect when exact integration of $K_t^{(e)}$ is used. However, this defect disappears by using the assumed transverse shear strain technique.

4.6. *'A posteriori' computation of transverse shear stresses*

Whereas in-plane stresses (σ_x, σ_y and τ_{xy}) are well-predicted by Equation (3a), the transverse shear stresses (τ_{xz} and τ_{yz}) are not. The reason is that the constitutive Equation (3a) yields a constant

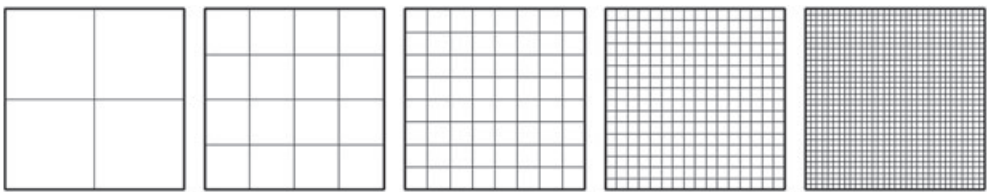

Figure 7. Meshes of N × N QLRZ elements employed for verification and convergence analysis. (a) N = 2; (b) N = 4; (c) N = 8; (d) N = 16; and (e) N = 32.

Table IV. Reissner–Mindlin solutions.

Reissner–Mindlin solutions (32 × 32 four-noded quadrilateral finite element)		
Boundary	Load	w_{RMT}
SS	Distributed	0.02680
	Point	0.07730
Clamped	Distributed	0.00841
	Point	0.03790

Table V. Relative error e_r of w at center point.

Relative error (e_r%) of w at center point					
		SS		Clamped	
Load	Mesh	w	er (%)	w	er (%)
Distributed	2 × 2	0.026150	−2.43	0.0080239	−4.59
	4 × 4	0.026638	−0.60	0.0082998	−1.31
	8 × 8	0.026744	−0.21	0.0083747	−0.42
	16 × 16	0.026770	−0.11	0.0083939	−0.19
	32 × 32	0.026776	−0.09	0.0083988	−0.13
Point	2 × 2	0.076049	−1.62	0.0322470	−14.92
	4 × 4	0.076392	−1.17	0.0360900	− 4.78
	8 × 8	0.076767	−0.69	0.0371910	− 1.87
	16 × 16	0.076966	−0.43	0.0375650	− 0.88
	32 × 32	0.077097	−0.26	0.0377400	− 0.42

DOI: 10.1002/nme

value into each layer, leading to a discontinuous thickness distribution of τ_{xz} and τ_{yz}. A useful alternative is to compute τ_{xz} and τ_{yz} *a posteriori* from the in-plane stresses using the equilibrium equations,

$$\begin{aligned} \frac{\partial \sigma_x}{\partial x} + \frac{\partial \tau_{xy}}{\partial y} + \frac{\partial \tau_{xz}}{\partial z} = 0 \\ \frac{\partial \tau_{xy}}{\partial x} + \frac{\partial \sigma_y}{\partial y} + \frac{\partial \tau_{yz}}{\partial z} = 0 \end{aligned} \tag{24a}$$

from which, the transverse shear stresses at a point 'P' across the thickness coordinates z are computed by

$$\begin{aligned} \tau_{xz}(z)|_P &= -\int_{-\frac{h}{2}}^{z} \left.\frac{\partial \sigma_x}{\partial x}\right|_P dz - \int_{-\frac{h}{2}}^{z} \left.\frac{\partial \tau_{xy}}{\partial y}\right|_P dz \\ \tau_{yz}(z)|_P &= -\int_{-\frac{h}{2}}^{z} \left.\frac{\partial \sigma_y}{\partial y}\right|_P dz - \int_{-\frac{h}{2}}^{z} \left.\frac{\partial \tau_{xy}}{\partial x}\right|_P dz \end{aligned} \tag{25a}$$

The in-plane stresses at point 'P' in the QLRZ element are approximated by the following approximation

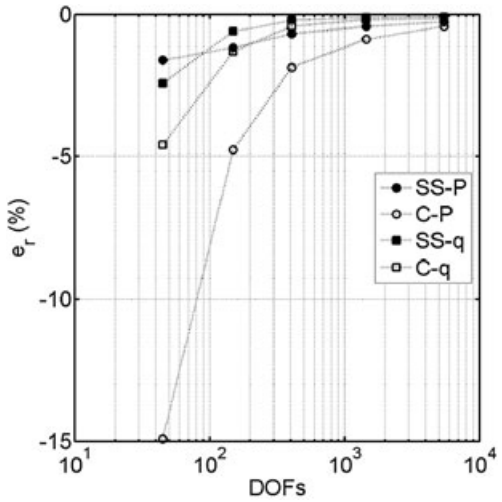

Figure 8. Relative error e_r of central deflection.

Table VI. Composite material properties.

	Properties	Layer 1 (top)	Layer 2	Layer 3 (bottom)
Composite C1	$h\,[m]$	h/3	h/3	h/3
	$E\,[MPa]$	0.219	0.219×10^{-1}	0.44
	μ	0.25	0.25	0.25
Composite C2	$h\,[m]$	h/3	h/3	h/3
	$E\,[MPa]$	0.219	0.219×10^{-2}	0.219
	μ	0.25	0.25	0.25
Composite C3	$h\,[m]$	h/10	h/1.25	h/10
	$E\,[MPa]$	0.219	0.725×10^{-3}	$0.73\text{E} \times 10^{-1}$
	μ	0.25	0.25	0.25

DOI: 10.1002/nme

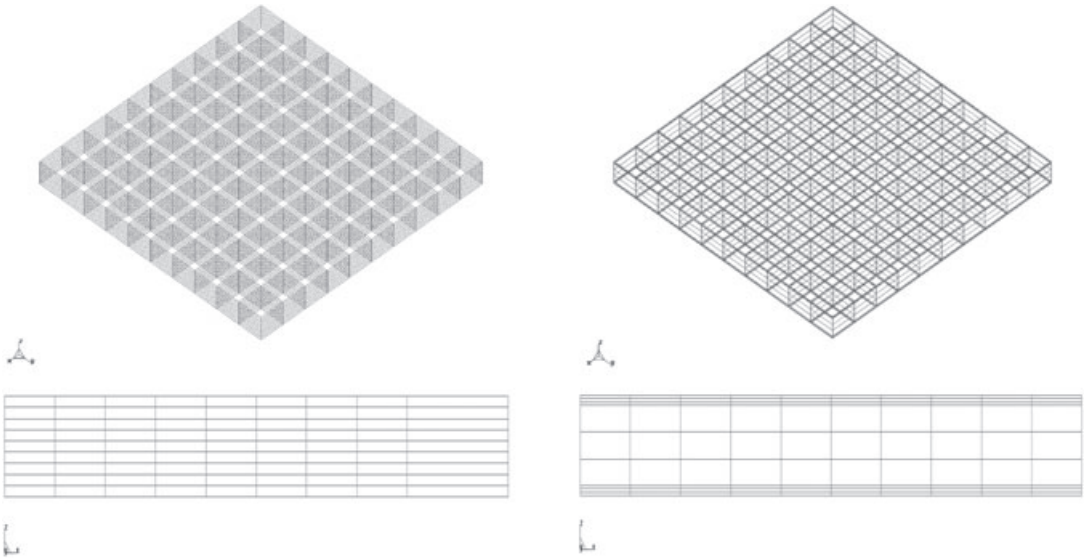

(a) (b)

Figure 9. $10 \times 10 \times 9$ HEXA20 meshes employed to compute the reference solution for (a) composite C1 and C2 and (b) composite C3.

Table VII. Clamped square plate ($\lambda = 20$) under uniformly distributed load. Relative error e_r(%) for w, σ_x, and ψ_x.

Relative error e_r(%) in clamped plate									
	w at point C			$\boldsymbol{\sigma_x}$ at point E			$\boldsymbol{\psi_x}$ at point E		
Mesh	C1	C2	C3	C1	C2	C3	C1	C2	C3
2×2	11.71	50.28	60.99	99.99	100	100	26.13	80.09	86.48
4×4	4.65	30.16	43.47	20.86	44.14	45.53	-6.28	43.34	54.80
8×8	1.60	12.32	22.44	2.90	14.35	17.24	-1.47	13.68	18.58
16×16	0.29	3.67	9.25	-1.21	-0.40	-1.15	-0.30	2.58	2.22
32×32	-0.14	0.69	2.85	-2.22	-4.70	-4.62	0.00	0.00	0.00

Table VIII. SS square plate ($\lambda = 20$) under uniformly distributed load. Relative error e_r(%) for w, σ_x, and ψ_x.

Relative error e_r(%) in SS plate									
	w at point C			$\boldsymbol{\sigma_x}$ at point E			$\boldsymbol{\psi_x}$ at point E		
Mesh	C1	C2	C3	C1	C2	C3	C1	C2	C3
2×2	2.69	19.36	25.83	26.98	32.89	33.24	-9.11	41.06	51.92
4×4	0.68	6.50	10.14	4.86	7.70	9.05	-3.99	8.95	13.67
8×8	0.25	1.54	2.22	-0.30	-0.79	0.44	-0.71	-0.40	-1.84
16×16	0.15	0.38	0.35	-1.55	-3.04	-1.92	0.07	-0.45	-1.44
32×32	0.12	0.12	-0.02	-1.86	-3.49	-2.07	0.00	0.00	0.00

$$\begin{aligned} \sigma_x(z)|_P &= \sum_{i=1}^{4} N_i|_P \cdot \sigma_x^i(z) \\ \sigma_y(z)\big|_P &= \sum_{i=1}^{4} N_i|_P \cdot \sigma_y^i(z) \\ \tau_{xy}(z)\big|_P &= \sum_{i=1}^{4} N_i|_P \cdot \tau_{xy}^i(z) \end{aligned} \tag{26a}$$

DOI: 10.1002/nme

where N_i is the shape function (Equation (21)) and i denotes the ith node. The nodal stresses $\sigma_x^i(z)$, $\sigma_y^i(z)$ and $\tau_{xy}^i(z)$ have been obtained by the averaging of Gauss stresses from neighboring elements

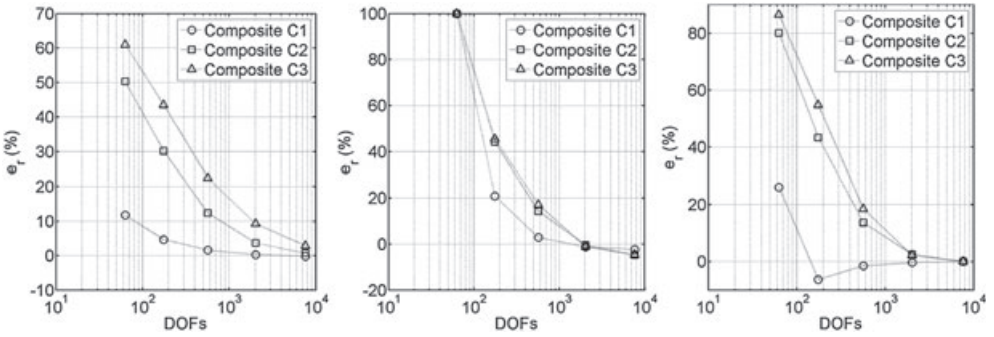

(a) (b) (c)

Figure 10. Clamped square plate ($\lambda = 20$) under uniformly distributed load. Relative error $e_r(\%)$ for (a) w, (b) σ_x, and (c) ψ_x.

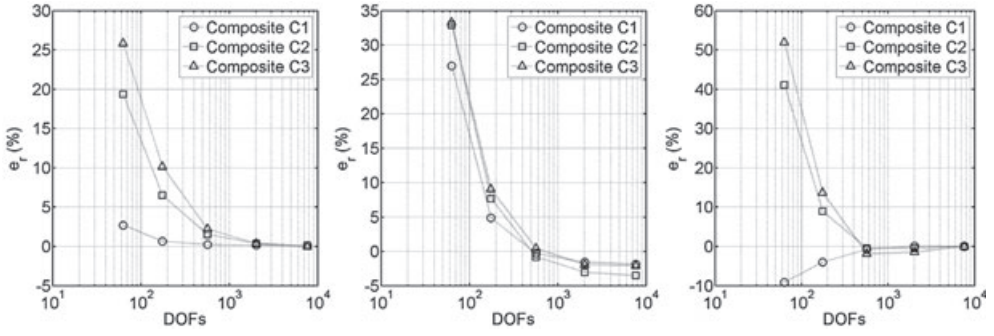

(a) (b) (c)

Figure 11. SS square plate ($\lambda = 20$) under uniformly distributed load. (a) Relative error $e_r(\%)$ for w, (b) σ_x, and (c) ψ_x.

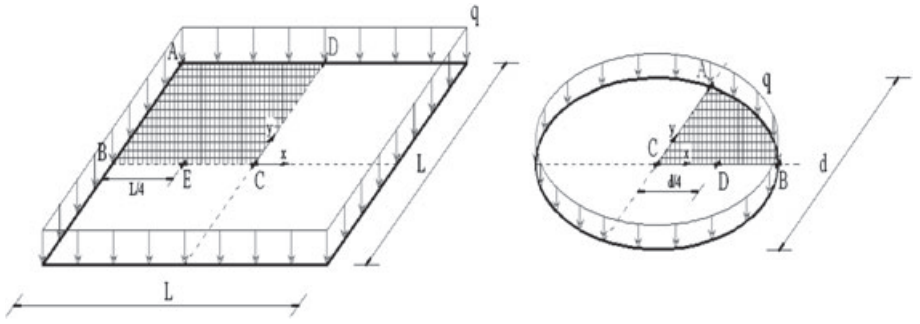

(a) (b)

Figure 12. (a) Square SS plate and (b) circular SS plate under uniformly distributed load.

DOI: 10.1002/nme

at the ith node. Finally, the transverse shear stresses are obtained by replacing Equation (26a) into Equation (25a),

$$\begin{aligned}\tau_{xz}(z)|_P &= -\int_{-h/2}^{z}\left(\sum_{i=1}^{4}\left.\frac{\partial N_i}{\partial x}\right|_P\cdot\sigma_x^i(z)\right)-\int_{-h/2}^{z}\left(\sum_{i=1}^{4}\left.\frac{\partial N_i}{\partial y}\right|_P\cdot\tau_{xy}^i(z)\right)\\ \tau_{yz}(z)|_P &= -\int_{-h/2}^{z}\left(\sum_{i=1}^{4}\left.\frac{\partial N_i}{\partial y}\right|_P\cdot\sigma_y^i(z)\right)-\int_{-h/2}^{z}\left(\sum_{i=1}^{4}\left.\frac{\partial N_i}{\partial x}\right|_P\cdot\tau_{xy}^i(z)\right)\end{aligned} \tag{27}$$

5. VERIFICATION STUDIES

The accuracy of the *QLRZ element* for isotropic homogeneous material is studied in this section. The aim is to evaluate the behavior of the QLRZ element when ϕ_i $(i = x, y)$ vanishes, which leads to $\psi_i = 0$ and the kinematics of Equation (1a) coincide with that of RMT.

This study consists in analyzing an SS and a clamped square plate of side length $L = 2$ and thickness $h = 0.05$ $\left(\lambda = \frac{L}{h} = 40\right)$ under a uniformly distributed load $q = 1$ and a point load $P = 4$ acting at the center (Figure 6). Isotropic homogeneous material properties are assumed with: $E = 0.219$, $\mu = 0.25$, and $G = E/2(1+\mu)$.

Assuming symmetry along both axes, we analyze only one quarter of the plate. Five different meshes of QLRZ elements whose properties are listed in Table III are employed (Figure 7).

The reference solution was obtained by a finite element analysis using a mesh of 32×32 four-noded quadrilateral Reissner–Mindlin (FSDT) element with substitute shear strain fields [20]. A shear correction factor equal to $5/6$ was used.

To assess the element accuracy, we define the following relative error

$$e_{r_i} = \frac{w_i - w_{\mathrm{RMT}}}{w_{\mathrm{RMT}}} \tag{28}$$

where w_i is the vertical deflection at the center point computed with the ith QLRZ mesh ($i = 1, 2, \ldots, 5$) and w_{RMT} is the reference solution. The w_{RMT} values for all cases are show in Table IV.

Table IX. Layer material properties. E and G are given in MPa.

Layer material properties				
	A	B	C	D
E_1	157.9×10^2	19.15		
E_2	9.58×10^2	19.15	0.104×10^2	104.1×10^2
E_3	9.58×10^2	191.5		
μ_{12}	0.32	6.58×10^{-4}		
μ_{13}	0.32	6.43×10^{-8}	0.30	0.31
μ_{23}	0.49	6.43×10^{-8}		
G_{12}	5.93×10^2	42.3×10^{-7}	0.04×10^2	39.73×10^2
G_{13}	5.93×10^2	36.51		
G_{23}	3.23×10^2	124.8		

Table X. Layer distribution of composite materials.

Composite laminated materials		
Composite	Layer distribution	h^k/h
C4	(A/C/A)	(0.1/0.8/0.1)
C5	(A/B)	(0.5/0.5)
C6	(A/B/C/D)	(0.1/0.3/0.5/0.1)
C7	(A/C/A/C/B/C/A/C/A)	(0.1/0.1/0.1/0.1/0.2/0.1/0.1/0.1/0.1)

DOI: 10.1002/nme

The QLRZ solution of the problem and the relative error are presented in Table V. Figure 8 shows the behavior of the error. Labels SS-P, SS-q, C-P, and C-q in Figure 8 refer to SS point load, SS distributed load, clamped point load, and clamped distributed load, respectively.

Figure 8 clearly shows the convergence of the QLRZ solution to the Reissner–Mindlin solution for all cases.

Good accuracy is obtained already for the 4×4 mesh (e_r less than 2.5%) except for the C-p case (e_r approximately equal to 5%). Results for the SS case (error $< 2.5\%$) are better than for the clamped one. The worst result is obtained for the clamped plate under central point load for the 2×2 mesh ($e_r = -14.92\%$).

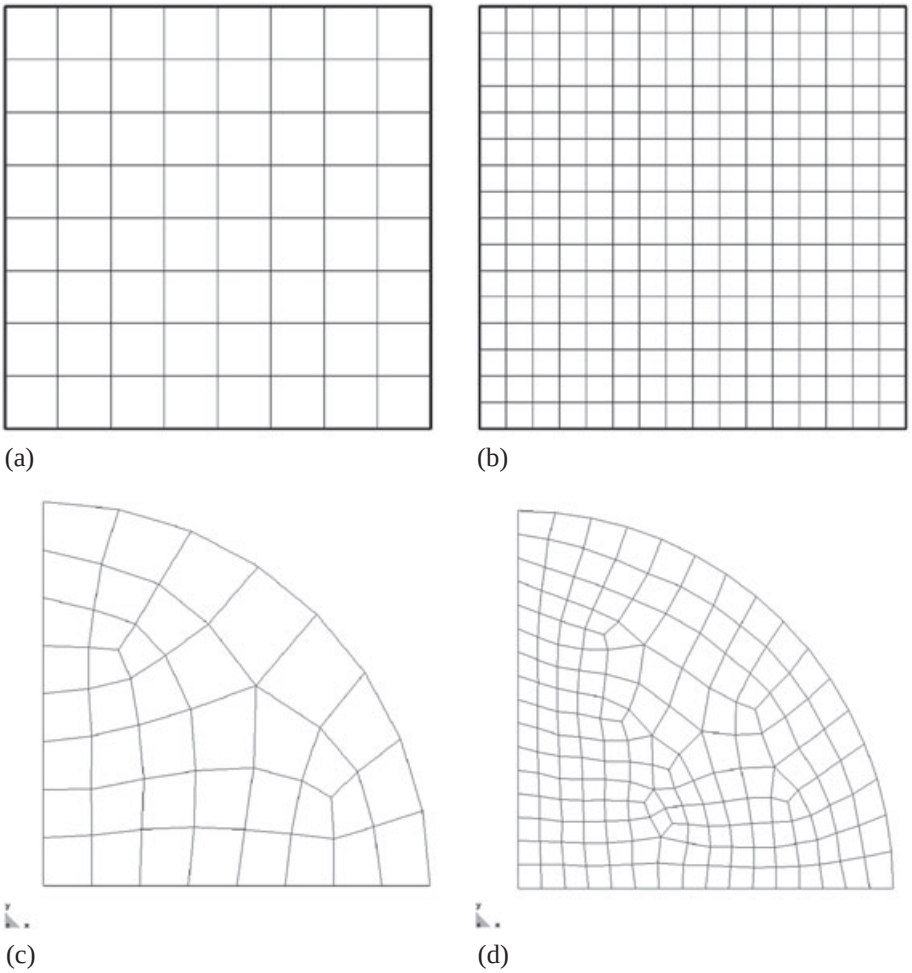

Figure 13. QLRZ meshes. Square plate: (a) 8×8 and (b) 16×16 element. Circular plate: (c) 40 and (d) 168 elements.

Table XI. QLRZ meshes properties.

QLRZ meshes properties				
Meshes (Figure 10)	N × N	Number of elements	Nodes	DOFs
a	8×8	64	81	567
b	16×16	256	289	2023
c	—	40	53	371
d	—	168	193	1351

DOI: 10.1002/nme

6. CONVERGENCE STUDIES

To study the influence of the heterogeneity of the composite material on the convergence and the accuracy of the QLRZ element, we analyze an SS and a clamped square plate of length side $L = 2m$ and thickness $h = 0.1m$ ($\lambda = 20$) under uniformly distributed load $q = 1N/m^2$ (Figures 6a and 6c). Three different composite laminated materials, whose properties are shown in Table VI, are considered for each example. The degree of heterogeneity increases from composite C1 to C3.

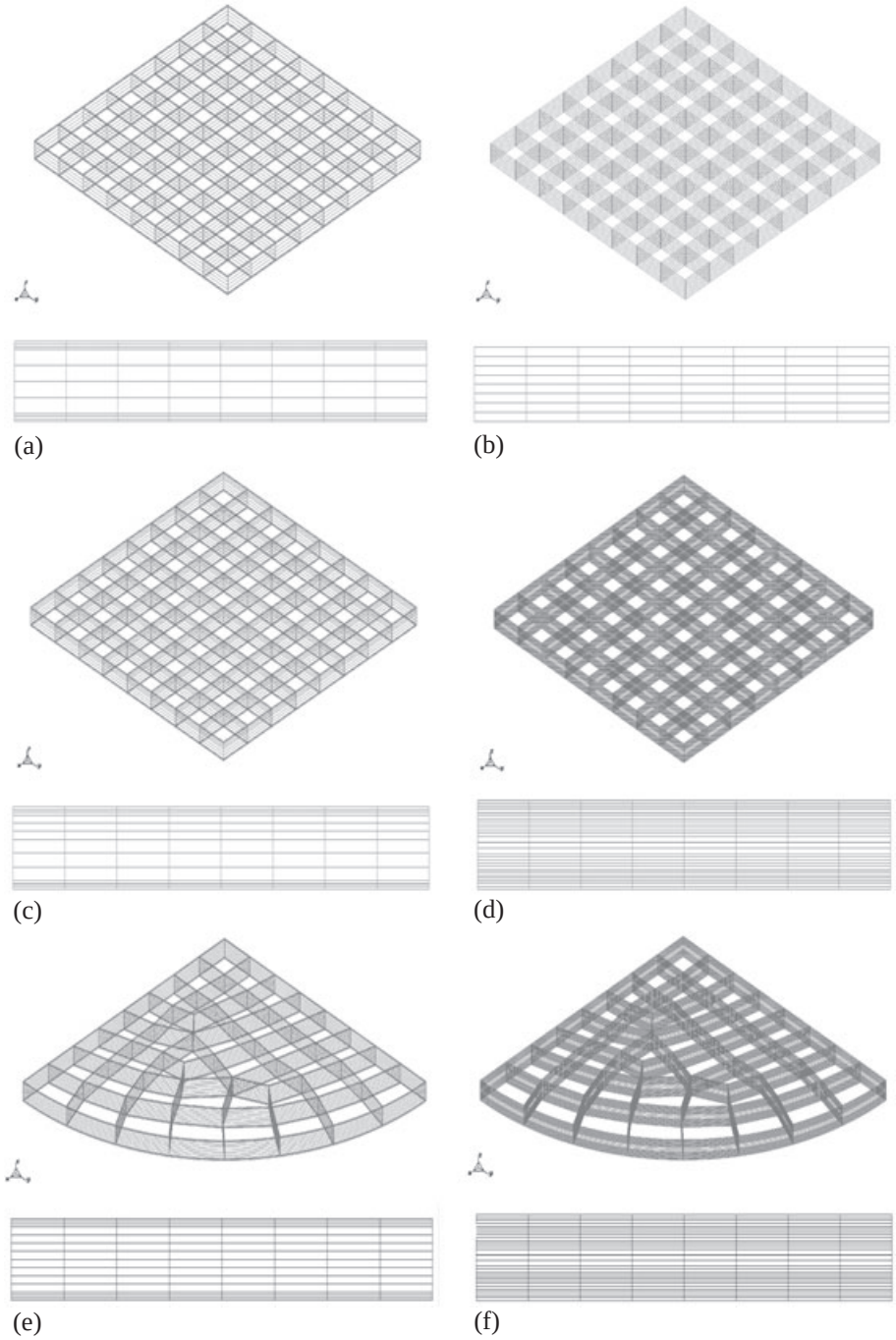

Figure 14. HEXA20 reference meshes. Square meshes for composites (a) C4, (b) C5, (c) C6, (d) C7, and circular meshes for composites (e) C6 and (f) C7.

DOI: 10.1002/nme

Table XII. HEXA20 mesh properties.

HEXA20 mesh properties				
Mesh (Figure 11)	Composite	Number of elements	Nodes	DOFs
a	C4	640	3285	9855
b	C5	512	2673	8019
c	C6	768	3897	11691
d	C7	1728	8487	25461
e	C6	602	3094	9282
f	C7	1161	5824	17472

Taking advantage of symmetry, we analyze only one quarter of plate by using the QLRZ meshes described in Section 5 (Figure 7). The reference solution was obtained by a 3D finite element analysis using a mesh of $10 \times 10 \times 9$ (3 elements per ply) 20-noded hexahedral elements involving 4499 nodes and 13497 DOFs (Figure 9).

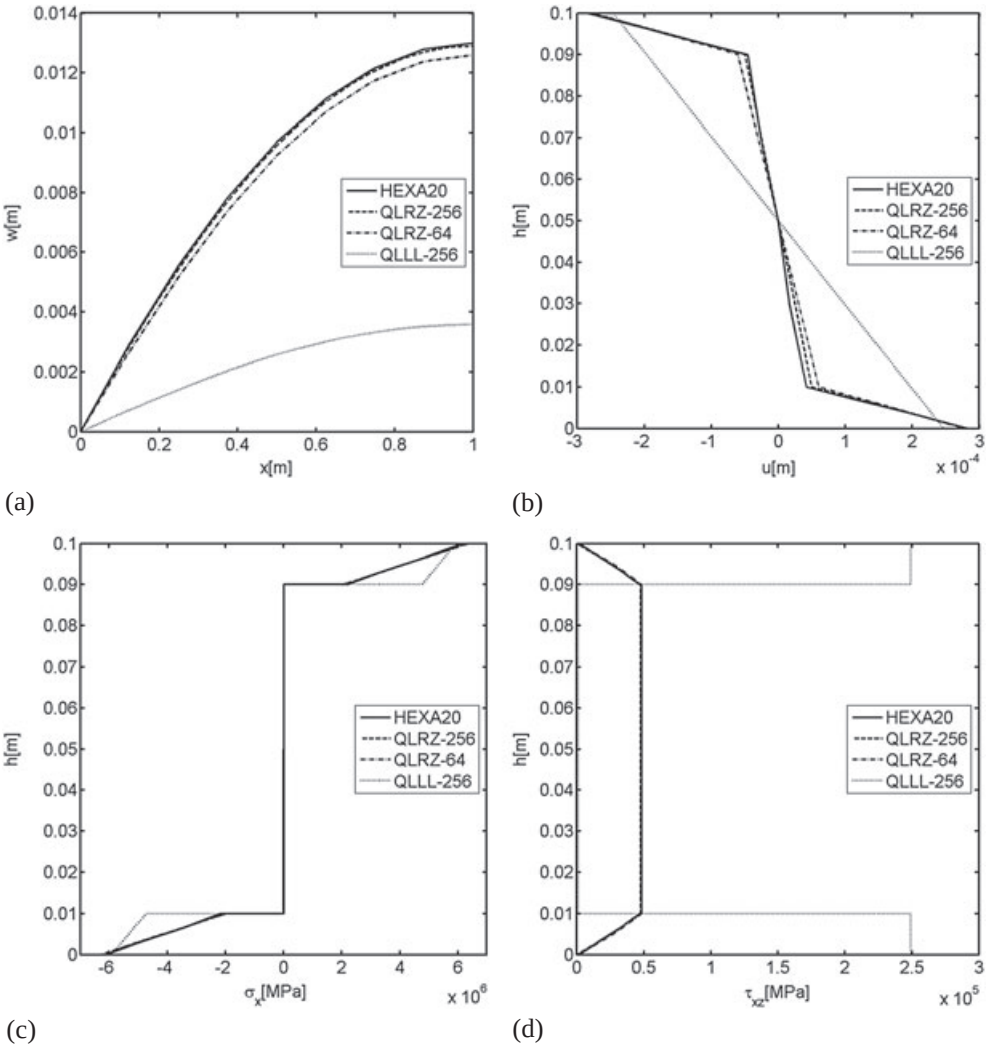

Figure 15. **SS square plate** under uniformly distributed load. **Composite C4**. (a) Vertical deflection along central line BC. Thickness distribution of: (b) axial displacement u at point B; (c) axial stress σ_x at the center point C; and (d) transverse shear stress τ_{xz} at point E.

DOI: 10.1002/nme

Convergence is quantified by the relative error defined as

$$e_r = \frac{m_i - m_{3D}}{m_{3D}} \tag{29}$$

where m_i and m_{3D} are the magnitudes of interest obtained with the ith QLRZ mesh ($i = 1, 2, \ldots, 5$) and the 3D reference solution, respectively. The magnitudes studied m are: the middle (z = 0) vertical deflection w at the center point C (Figure 6); the axial stress σ_x on the top surface of ply 1 at point E; and ψ_x at point E. Because ψ_x does not appear in 3D finite element analysis, m_i and m_{3D} are the values of this magnitude obtained using the ith QLRZ mesh ($i = 1, \ldots, 4$) and the finest mesh (32×32), respectively. The results obtained are shown in Tables VII–VIII, and Figures 10–11.

It is clearly seen that convergence is always slower for the more heterogeneous material and for the clamped plate.

For the clamped plate and the three materials (Table VII), errors are less than 10% for the 16×16 mesh for all variables. For the SS plate (Table VIII), errors are less than 2.3% for the 8×8 mesh in all cases.

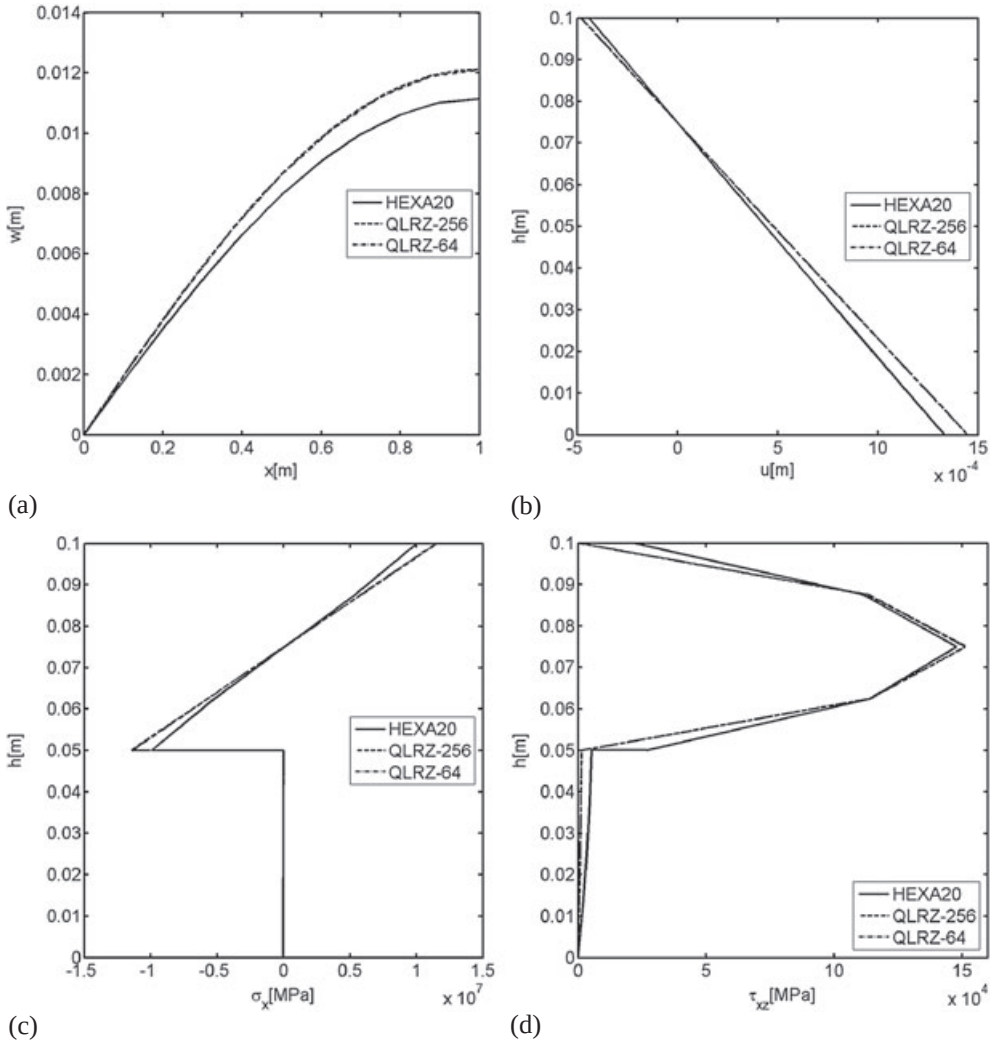

Figure 16. **SS square plate** under uniformly distributed load. **Composite C5**. (a) Vertical deflection along central line BC. Thickness distribution of: (b) axial displacement u at point B; (c) axial stress σ_x at the center point C; and (d) transverse shear stress τ_{xz} at point E.

DOI: 10.1002/nme

For composite C1 (the more homogeneous one), errors are less than 2.9% for the 8×8 mesh in all cases and less than 6.3% for the 4×4 mesh in all cases except for σ_x in the clamped plate.

For the more heterogeneous material (composite C3), the difference in the results between the SS and the clamped plate is larger. For the SS plate (Table VIII), errors are less than 2.3% for the 8×8 mesh in all variables. For the clamped plate (Table VII), errors are less than 23% for the 8×8 mesh and less than 10% for the 16×16 mesh in all cases.

The quality of the results obtained for the composite C2 are between that of composites C1 and C3.

7. COMPARISON STUDIED FOR SS SQUARE AND CIRCULAR COMPOSITE LAMINATED PLATES

To show the performance of the QLRZ element for highly heterogeneous composite material, we study a square SS plate of length $L = 2m$ and thickness $h = 0.1m$, and a circular SS plate of

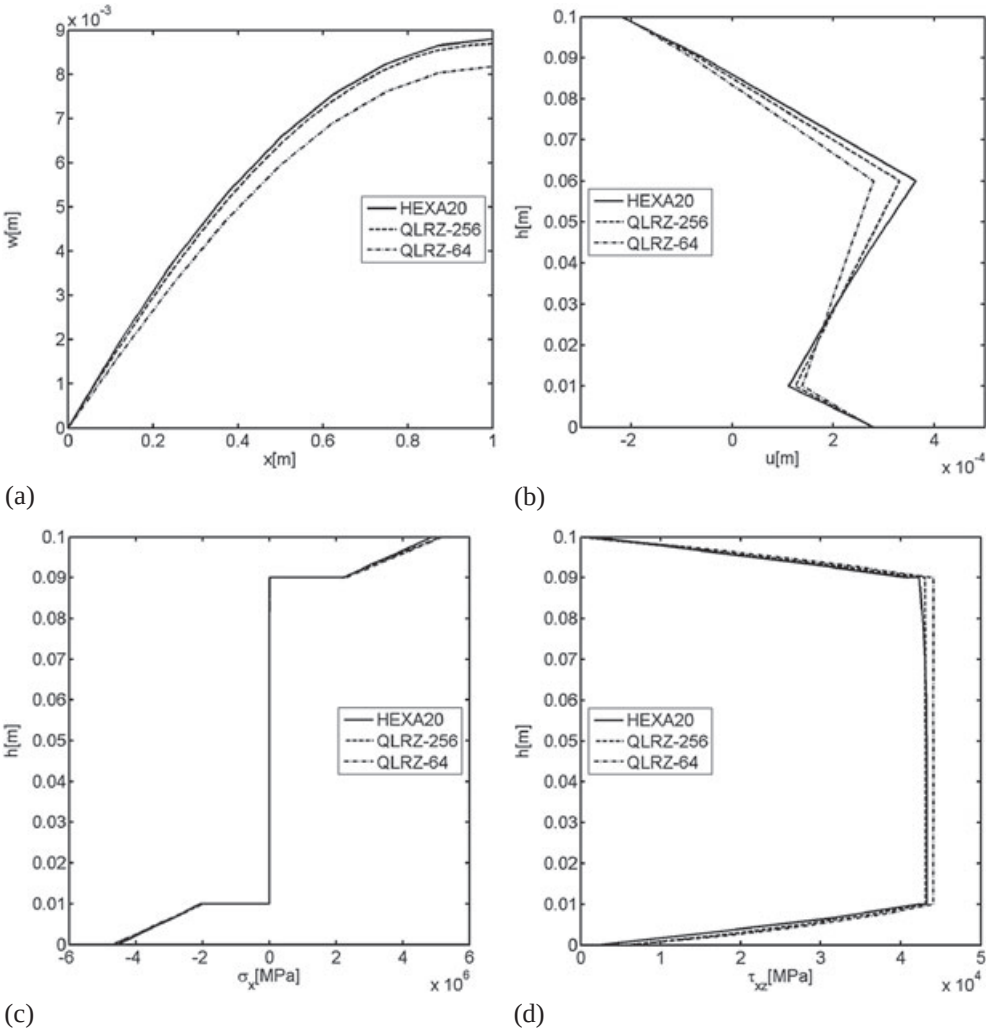

Figure 17. **SS square plate** under uniformly distributed load. **Composite C6**. (a) Vertical deflection along central line BC. Thickness distribution of: (b) axial displacement u at point B; (c) axial stress σ_x at the center point C; and (d) transverse shear stress τ_{xz} at point E.

DOI: 10.1002/nme

diameter $d = 2m$ and thickness $h = 0.1m$. The structures are loaded under a uniformly distributed load, $q = 10000\ N/m^2$ (Figure 12).

Each plate is studied for different composite laminated materials with properties shown in Tables IX and X. The square plate is analyzed for composites C4-7 and the circular plate for composites C6-7.

Because of symmetry, only one quarter of plate is analyzed using the QLRZ meshes shown in Figure 13 whose properties are listed in Table XI. The reference solution is the 3D finite element analysis using HEXA20 elements. The different 3D meshes for each case are shown in Figure 14. Details of each meshes are given in Table XII.

The RMT results for the square plate of composite C4 are also shown in Figure 15. The RMT solution was obtained by using a mesh of 16×16 four-noded QLLL plate element [19, 21].

Figures 15–20 show: (a) the computed vertical deflection w; (b) the thickness distribution of the axial displacement u; (c) the axial stress σ_x; and (d) the transverse shear stress τ_{xz} for each plate under study.

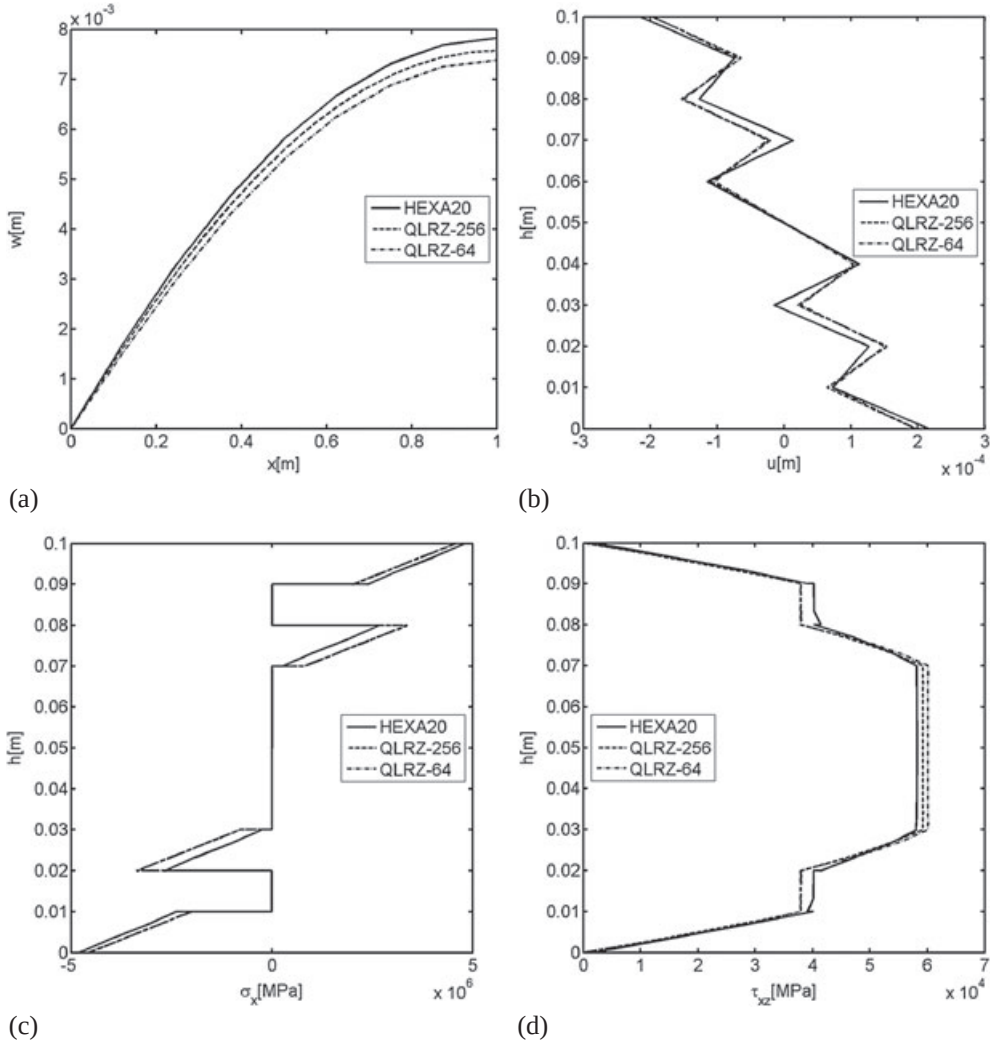

Figure 18. **SS square plate** under uniformly distributed load. **Composite C7**. (a) Vertical deflection along central line BC. Thickness distribution of: (b) axial displacement u at point B; (c) axial stress σ_x at the center point C; and (d) transverse shear stress τ_{xz} at point E.

DOI: 10.1002/nme

The vertical deflection is accurately captured. At the center of plate, the maximum error (14%) is given by the circular plate of composite C6 using the 40-element mesh (Figure 16a). For the finest mesh (168 elements), the computed errors are less than 10%.

The thickness distribution of the axial displacement is accurately predicted in all cases. The ability to capture the complex kinematics of laminated composite materials is a key feature of the QLRZ plate element. The successful axial displacement prediction leads to accurate axial stress values as shown in Figures (c). Figures (d) displays the good results for the thickness distribution of the transverse shear stresses computed *a posteriori* using Equation (27).

Results demonstrate the good performance of the QLRZ element.

Figure 15 shows the inaccurate results when modeling a composite laminated plate using QLLL elements based on RMT. The deflection at the plate center is three times stiffer than the reference solution (Figure 15a). The RMT solution also yields an erroneous linear thickness distribution of the axial displacement (Figure 15b), which leads to a distorted distribution of the axial stress (Figure 15c). Finally, the RMT is unable to capture the correct transverse shear stress distribution (Figure 15d).

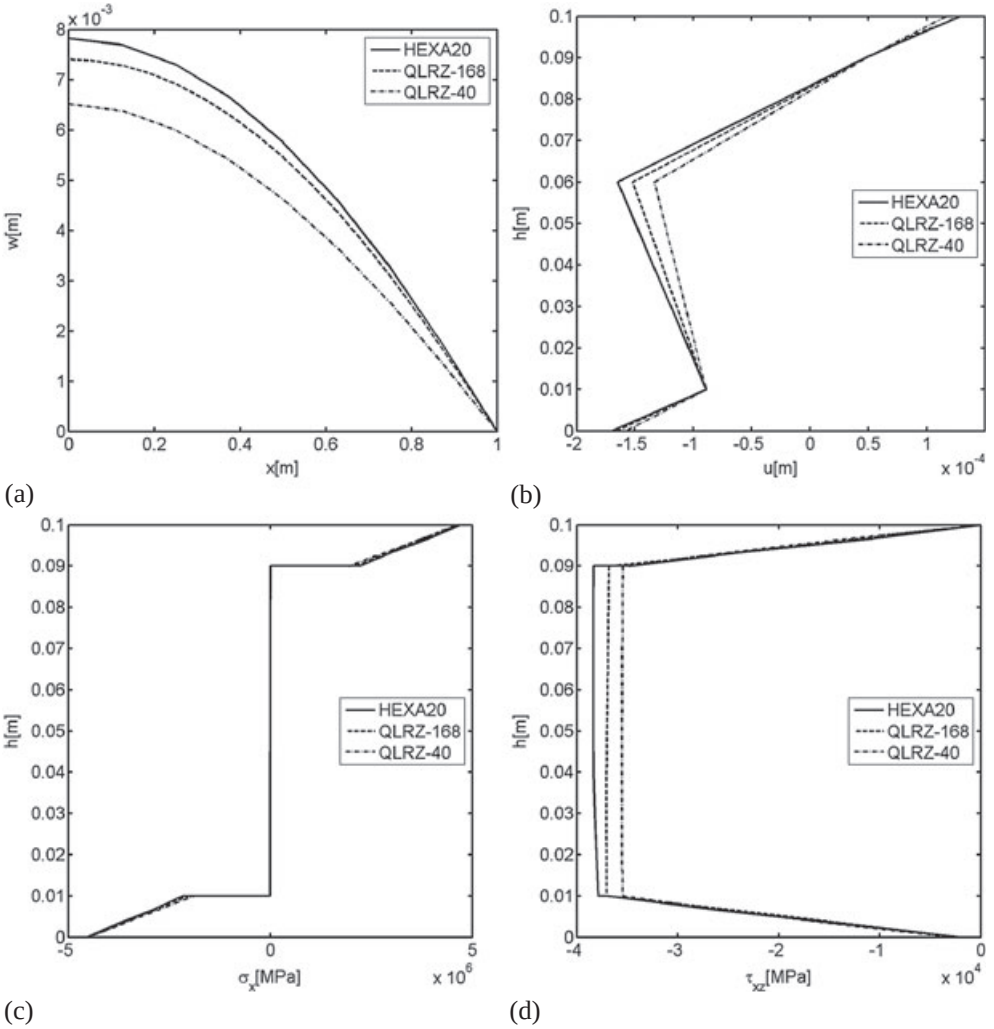

Figure 19. **SS circular plate** under uniformly distributed load. **Composite C6**. (a) Vertical deflection along line BC. Thickness distribution of: (b) axial displacement u at point D; (c) axial stress σ_x at the center point C; and (d) transverse shear stress τ_{xz} at point D.

DOI: 10.1002/nme

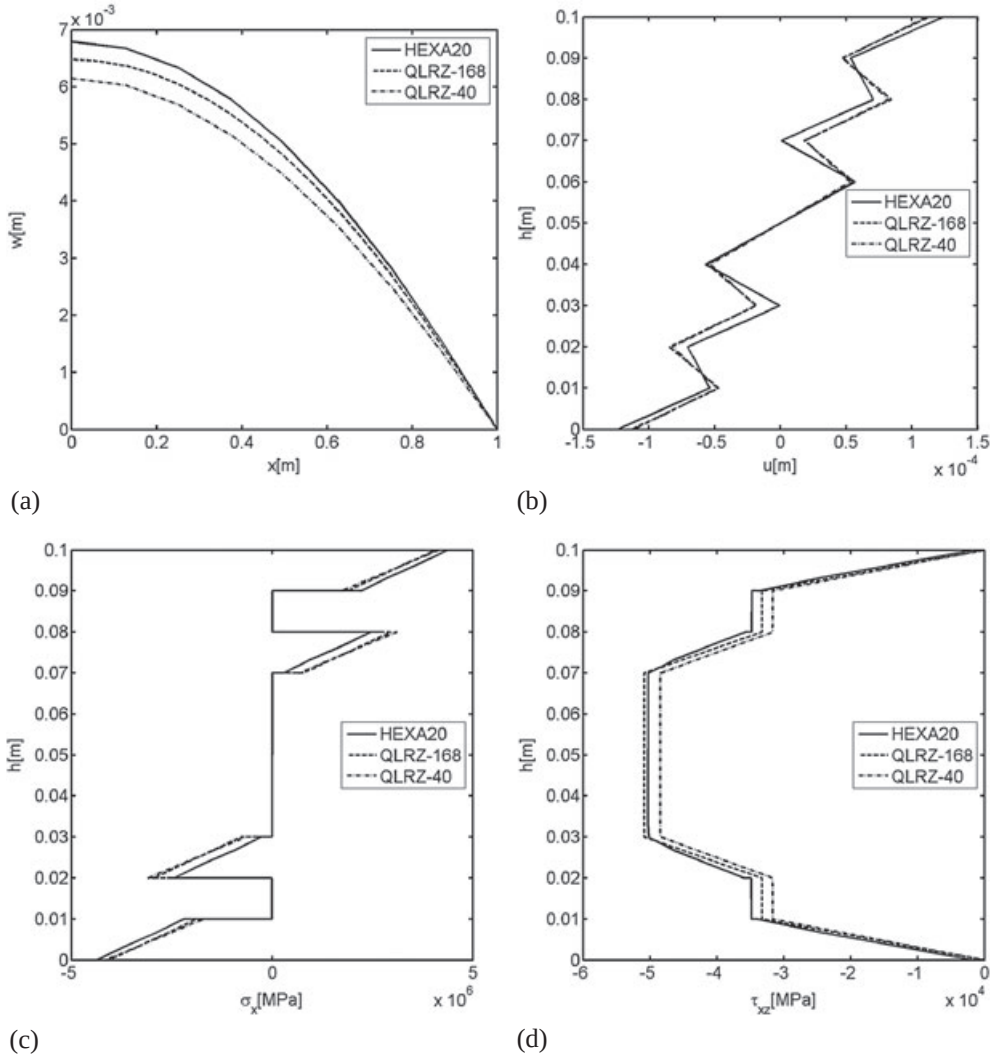

Figure 20. **SS circular plate** under uniformly distributed load. **Composite C7**. (a) Vertical deflection along line BC. Thickness distribution of: (b) axial displacement u at point D; (c) axial stress σ_x at the center point C; and (d) transverse shear stress τ_{xz} at point D.

8. CONCLUSIONS

A simple, robust, shear locking free and accurate four-noded plate element (called QLRZ) based on the *refined ZZ theory* has been presented. The shear locking defect was overcome by introducing an *assumed linear shear strain field*. The element has only seven unknowns per node, which are interpolated by standard C^0 linear shape functions. The thickness distribution of the transverse shear stresses is accurately reproduced by *a posteriori* computational process. The verification analysis has shown that the element is able to accurately model plates of homogeneous material for different loads and boundary conditions. The influence of the heterogeneity of composite laminated material on the convergence and the accuracy of QLRZ solution has been studied. An important feature of the QLRZ element is its ability to capture the ZZ distribution of axial displacement and the subsequent complex strain and stress distribution across the thickness with the simple approximation chosen.

APPENDIX A

A.1. Computation of substitutive shear strain generalized matrix $\bar{B}_s$

The natural transverse shear strain field is given by [19, 21]

DOI: 10.1002/nme

$$\hat{\varepsilon}'_s = \begin{bmatrix} \gamma_\xi \\ \gamma_\eta \end{bmatrix} = \begin{bmatrix} \alpha_1 + \alpha_2\eta \\ \alpha_3 + \alpha_4\xi \end{bmatrix} = \begin{bmatrix} 1 & \eta & 0 & 0 \\ 0 & 0 & 1 & \xi \end{bmatrix} \cdot \begin{bmatrix} \alpha_1 \\ \alpha_2 \\ \alpha_3 \\ \alpha_4 \end{bmatrix} = \mathrm{A} \cdot \alpha \tag{A.1}$$

The transverse shear strains $\hat{\varepsilon}_s$ in the cartesian coordinate system are expressed as

$$\hat{\varepsilon}_s = \begin{bmatrix} \gamma_{xz} \\ \gamma_{yz} \end{bmatrix} = \mathrm{J}^{-1} \cdot \hat{\varepsilon}'_s \tag{A.2a}$$

where J is the 2D Jacobian matrix

$$\mathrm{J} = \begin{bmatrix} \dfrac{\partial x}{\partial \xi} & \dfrac{\partial y}{\partial \xi} \\ \dfrac{\partial x}{\partial \eta} & \dfrac{\partial y}{\partial \eta} \end{bmatrix} \tag{A.2b}$$

The coefficients α_i are obtained by sampling the natural shear strains (Equation (A.1)) at the four points shown in Figure A.1, with

$$\gamma_{\bar{\xi}_i} = (\alpha_1 + \alpha_2\eta) \cdot \cos\delta_i + (\alpha_3 + \alpha_4\xi) \cdot \sin\delta_i \quad ; \quad i = 1,\ 4 \tag{A.3}$$

where δ_i is the angle between $\bar{\xi}_i$ direction and the natural ξ axis. Combining Equations (A.1) and (A.3) gives

$$\gamma_{\bar{\xi}} = \begin{bmatrix} \gamma_{\bar{\xi}_1} \\ \gamma_{\bar{\xi}_2} \\ \gamma_{\bar{\xi}_3} \\ \gamma_{\bar{\xi}_4} \end{bmatrix} = \begin{bmatrix} 1 & -1 & 0 & 0 \\ 0 & 0 & 1 & 1 \\ 1 & 1 & 0 & 0 \\ 0 & 0 & 1 & -1 \end{bmatrix} \cdot \begin{bmatrix} \alpha_1 \\ \alpha_2 \\ \alpha_3 \\ \alpha_4 \end{bmatrix} = \mathrm{P} \cdot \alpha$$

$$\alpha = \mathrm{P}^{-1} \cdot \gamma_{\bar{\xi}} \tag{A.4}$$

where the strains $\gamma_{\bar{\xi}_i}$ are related to γ_{ξ_i} and γ_{η_i} by

$$\gamma_{\bar{\xi}} = \begin{bmatrix} \gamma_{\bar{\xi}_1} \\ \gamma_{\bar{\xi}_2} \\ \gamma_{\bar{\xi}_3} \\ \gamma_{\bar{\xi}_4} \end{bmatrix} = \begin{bmatrix} 1 & 0 & 0 & 0 & 0 & 0 & 0 & 0 \\ 0 & 0 & 0 & 1 & 0 & 0 & 0 & 0 \\ 0 & 0 & 0 & 0 & 1 & 0 & 0 & 0 \\ 0 & 0 & 0 & 0 & 0 & 0 & 0 & 1 \end{bmatrix} \cdot \begin{bmatrix} \gamma_{\xi_1} \\ \gamma_{\eta_1} \\ \gamma_{\xi_2} \\ \gamma_{\eta_2} \\ \gamma_{\xi_3} \\ \gamma_{\eta_3} \\ \gamma_{\xi_4} \\ \gamma_{\eta_4} \end{bmatrix} = \mathrm{T} \cdot \hat{\gamma}' \tag{A.5}$$

Combining Eqsuations (A.1), (A.4), and (A.5) gives

$$\hat{\varepsilon}'_s = \mathrm{A} \cdot \mathrm{P}^{-1} \cdot \mathrm{T} \cdot \hat{\gamma}' \tag{A.6}$$

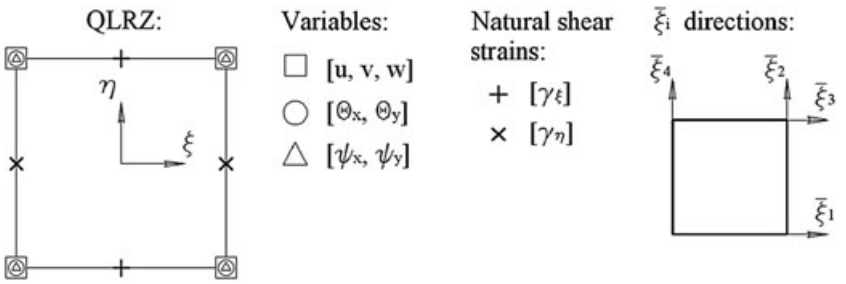

Figure A.1. QLRZ plate element.

DOI: 10.1002/nme

The cartesian transverse shear strains $\hat{\gamma}$ at the sampling points are related to the natural transverse shear strains $\hat{\gamma}'$ by

$$\hat{\gamma}' = \begin{bmatrix} J^1 & 0 & 0 & 0 \\ 0 & J^2 & 0 & 0 \\ 0 & 0 & J^3 & 0 \\ 0 & 0 & 0 & J^4 \end{bmatrix} \cdot \begin{bmatrix} \hat{\gamma}_1 \\ \hat{\gamma}_2 \\ \hat{\gamma}_3 \\ \hat{\gamma}_4 \end{bmatrix} = C \cdot \hat{\gamma} \qquad ; \qquad \hat{\gamma}_i = \begin{bmatrix} \gamma_{xz} \\ \gamma_{yz} \end{bmatrix}_i \tag{A.7}$$

The relationship between the cartesian shear strains $\hat{\gamma}$ at the four sampling points (Figure A.1) and the nodal displacements $a^{(e)}$ is

$$\hat{\gamma} = B_s \cdot a^{(e)} \tag{A.7b}$$

with

$$B_s = \begin{bmatrix} B_{s1} & B_{s2} & B_{s3} & B_{s4} \end{bmatrix}^T \tag{A.7c}$$

where B_{si} $(i = 1, 2, 3, 4)$ is the original transverse generalized strain matrix (Equation (16c)) at the ith sampling point.

Combining Equations (A.2a), (A.6), (A.7), and (A.7b) gives

$$\hat{\varepsilon}_s = J^{-1} \cdot A \cdot P^{-1} \cdot T \cdot C \cdot B_s \cdot a = \bar{B}_s \cdot a \tag{A.8}$$

where $\bar{B}_s$ is the sought substitute transverse shear strain matrix given by

$$\bar{B}_s = J^{-1} \cdot A \cdot P^{-1} \cdot T \cdot C \cdot B_s \tag{A.9}$$

ACKNOWLEDGEMENT

The first author would like to acknowledge the FPU-UPC scholarship supported by the Universitat Politècnica de Catalunya and the Ministerio de Educación of Spain. This research was partially financially supported by the SAFECON project of the European Research Council (ERC) of the European Commission.

REFERENCES

1. Kirchhoff G. Über das Gleichgewicht und die Bewegung einer elastischen Scheibe. *Journal für die reine und Angewandte Mathematik* 1850; **40**:51–88.
2. Reissner E. The effect of transverse shear deformation on the bending of elastic plates. *Journal of Applied Mechanics* 1945; **12**:69–79.
3. Mindlin RD. Influence of rotatory inertia and shear in flexural motions of isotropic elastic plates. *Journal of Applied Mechanics* 1951; **18**:31–38.
4. Liu D, Li X. An overall view of laminate theories based on displacement hypothesis. *Journal of Composite Materials* 1996; **30**(14):1539–1561.
5. Wanji C, Zhen W. A selective review on recent development of displacement-based laminated plate theories. *Recent Patents on Mechanical Engineering* 2008; **1**:29–44.
6. Reddy JN, Robbins DH, Jr. Theories and computational models for composite laminates. *Applied Mechanics Reviews* 1994; **47**(6):147–165.
7. Carrera E. Historical review of Zig-Zag theories for multilayered plates and shells. *Applied Mechanics Reviews* 2003; **56**(3):287–308.
8. Tessler A, Sciuva MD, Gherlone M. A consistent refinement of first-order shear deformation theory for laminated composite and sandwich plates using improved zigzag kinematics. *Mechanics of Materials and Structures* 2010; **5**(2):341–365.
9. Tessler A, Sciuva MD, Gherlone M. Refinement of Timoshenko beam theory for composite and sandwich beams using zigzag kinematics. *Technical Publication TP-215086*, NASA, 2007.
10. Tessler A, Sciuva MD, Gherlone M. A refined zigzag beam theory for composite and sandwich beams. *Journal of Composite Materials* 2009; **43**(9):1051–1081.
11. Sciuva MD, Gherlone M, Tessler A. A robust and consistent first-order zigzag theory for multilayered beams. In *Advances in Mathematical Modelling and Experimental Methods for Materials and Structures: The Jacob Aboudi Volume*, Gilat R, Banks-Sills L (eds). Springer Dordrecht Heidelberg: London New York, 2010; 255–268.
12. Tessler A, Di Sciuva M, Gherlone M. Refined zigzag theory for homogeneous, laminated composite, and sandwich plates: a homogeneous limit methodology for zigzag function selection. *Numerical Methods for Partial Differential Equations* 2011; **27**(1):208–229.

DOI: 10.1002/nme

13. Oñate E, Eijo A, Oller S. Simple and accurate two-noded beam element for composite laminated beams using a refined zigzag theory. *Computer Methods in Applied Mechanics and Engineering* 2012:362–382.
14. Gherlone M, Tessler A, Di Sciuva M. C^0 beam element based on the refined zigzag theory for multilayered composite and sandwich laminates. *Composite Structures* 2011; **93**:2882–2894.
15. Versino D, Gherlone M, Mattone M, Di Sciuva M, Tessler A. C0 triangular elements based on the refined zigzag theory for multilayer composite and sandwich plates. *Composites Part B: Engineering* 2013; **44**(1):218–230.
16. Eijo A, Oñate E, Oller S. A four-noded quadrilateral element for composite laminated plates/shells using the refined zigzag theory. *Publication N°-378*, CIMNE, June 2012.
17. Car E, Oller S, Oñate E. An anisotropic elastoplastic constitutive model for large strain analysis of fiber reinforced composite materials. *Computer Methods in Applied Mechanics and Engineering* 2000; **185**(2–4):245–277.
18. Rastellini F. Numerical modelling of the constitutive non-linearity of composite laminates. *Ph.D. Thesis*, Departament de Resistència de Materials i Estructures a l'Enginyeria (RMEE), Universitat Politècnica de Catalunya, Advisors:, Oller, S., and Oñate, E, 2006.
19. Oñate E. *Structural Analysis by the Finite Element Method*, Vol. 2: Beams, plates and shells. CIMNE-Springer: Barcelona, 2012.
20. Hinton E, Huang HC. A family of quadrilateral Mindlin plate elements with substitute shear strain fields. *Computers & Structures* 1986; **23**(3):409–431.
21. Oñate E, Zienkiewicz O, Suárez B, Taylor RL. A general methodology for deriving shear constrained Reissner-Mindlin plate elements. *International Journal for Numerical Methods in Engineering* 1992; **33**(2):345–367.

DOI: 10.1002/nme

Composite Structures 104 (2013) 270–280

Contents lists available at SciVerse ScienceDirect

Composite Structures

journal homepage: www.elsevier.com/locate/compstruct

A numerical model of delamination in composite laminated beams using the LRZ beam element based on the refined zigzag theory

A. Eijo *, E. Oñate, S. Oller

International Center for Numerical Methods in Engineering (CIMNE), Universitat Politècnica de Catalunya (UPC), Campus Norte UPC, 08034 Barcelona, Spain

ARTICLE INFO

Article history:
Available online 13 May 2013

Keywords:
Laminated beams
Delamination
LRZ beam element
Refined zigzag theory

ABSTRACT

A method based on the Refined Zigzag Theory (RZT) to model delamination in composite laminated beam structures is presented. The novelty of this method is the use of one-dimensional finite elements to discretize the geometry of the beam. The key property of this beam element, named LRZ [1], is the possibility to capture the relative displacement between consecutive layers which occurs during delamination. The fracture mode that the LRZ element is capable to predict is mode II. In order to capture the relative displacement using the LRZ element it is necessary to adapt the RZT theory as presented in this paper. The mechanical properties of the layers are modeled using a continuum isotropic damage model [2]. The modified Newton–Raphson method is used for solving the non-linear problem.

The RZT theory, the LRZ finite element and the isotropic damage model are described in the paper. Also, the implicit integrations algorithm is presented. The performance of the LRZ element is analyzed by studying the delamination in a beam for two different laminates, using the plane stress solution as a reference.

1. Introduction

Delamination, i.e. interlaminar cracks, is a common and dangerous source of damage in laminated composite materials [3] characterized by the loss of adherence between the different plies of the laminate. This phenomenon can occur during the fabrication stage or during the transportation, storage and service phases. Imperfection of various natures and thermal and chemical shrinkage of components may produce delamination during the manufacturing process. Many causes such as local forces, thermal actions and low energy impacts may serve as sources of delamination during the transportation, storage or service period. Geometry discontinuities such as access holes, notches, free edges or bonded and bolted joints can also produce delamination due to high stress gradients. Once delamination occurs, the structural member considerably reduces its original stiffness, which leads to its failure in conjunction with other mechanic phenomena, e.g. buckling, excessive vibration or loss of fatigue life.

Within the framework of numerical simulation, delamination is usually modeled using fracture or damage mechanics procedures. In fracture mechanics, the virtual crack closure technique (VCCT) [4,5] is the most widely used approach, which is based on the assumption that the energy necessary to open the crack is the same to close it. Damage mechanics is based on the concept of a cohesive damage zone developed near the crack front, where the stresses are limited by the yield stress and a thin plastic zone is generated in front of the crack. This technique can easily be implemented in the finite element method leading to cohesive finite elements [6–10].

Each of these techniques has their own drawbacks. One of the most significant is that it is necessary to place interface cohesive or fracture finite elements between the plies where delamination is expected to occur. If the delamination path is unknown, interface finite elements must be placed between all plies. This typically leads to an unbearable computational cost depending on the number of physical composite layers and on the structure size. In order to overcome this problem, Martinez et al. [11] proposed to study delamination under the continuum mechanics setting using a 3D finite element method and an isotropic damage model which manages material degradation.

The efficacy of all above mentioned techniques is undisputed. However, the use of 3D finite elements for discretizing the geometry considerably increases the computational costs and storage, specially for non-linear problems. Surely, there are several cases, for instance: delamination in bonded joints, where 3D finite element analysis is indispensable. However, it is practically impossible to use these methods in large laminated composite structures with tens of layers, e.g. wind turbine blades or aircraft fuselage in composite materials, where simpler models should be used.

Classical thin beam/plate theory [12,13] and the more advanced First Order Shear Deformation Theory (FSDT) [14–16] were the first simplified theories capable to precisely model a plate structure of

* Corresponding author. Tel.: +34 934010808.
E-mail address: aeijo@cimne.upc.edu (A. Eijo).

0263-8223/$ - see front matter © 2013 Elsevier Ltd. All rights reserved.
http://dx.doi.org/10.1016/j.compstruct.2013.04.035

homogeneous material. However, when applied to highly heterogeneous laminated composite materials it is known that both theories give poor predictions. The cause of this drawback is that these theories propose a linear thickness distribution of the axial displacement, which is unable to represent the complex real kinematics of a laminated composite. Because of the same reason, both theories are unable to predict delamination, as they cannot capture the relative displacement between two consecutive layers.

More accurate models are based on Layer–Wise theories (LWTs) [17–19] in which the thickness coordinate is divided into a number of analysis sublayers (that may be not coincident with the number of physical layers), assuming a separate displacement field within each ply and forcing displacement constraints and stress contact conditions at the interfaces. LWT are able to capture accurately interlaminar stresses directly from the constitutive equations. Also, these theories are capable to simulate the delamination phenomenon [20–24] due to the high level of refinement of the displacement field. However, since the number of unknowns is proportional to the number of analysis sublayers, the computational cost increases with the number of subdivisions.

ZigZag (ZZ) theories are an attractive compromise between the high accuracy of LWT and the computational efficiency of FSDT [19,25,26]. In ZZ theories the in-plane displacement is modeled by a superposition of a piecewise linear displacement functions (the zigzag function) over a linear, quadratic or cubic displacement field along the thickness direction. An important property of ZZ theories is that the number of kinematics variables is independent of the number of layers. Although many ZZ theories require C^1 continuity for the deflection field, which is a disadvantage versus simpler C^0 continuity plate theories, some evolved ZZ techniques [27,28] have been developed to overcome this shortcoming. However, several C^0 continuous ZZ formulations for beams suffer from their inability to model correctly a clamped boundary condition, which makes it difficult to satisfy equilibrium of forces at a support. So far, the use of the ZZ theories to model delamination in beams and plates has been quite limited. A C^0 plate element for delamination analysis based on a ZZ model has been developed by Icardi and Zardo [29].

Tessler et al. [30–32] have developed an improved ZZ model for beams and plates, called *Refined ZigZag Theory* (RZT), that adopt FSDT displacement fields as the baselines. The key attributes of the RZT are, first, the proposed linear piecewise zigzag function vanishes at top and bottom surfaces of the structural section. Second, it does not require full transverse shear stress continuity across the laminated. Third, C^0 continuity is only required for the *finite element method* (FEM) approximation of the kinematic variables and finally, all boundary conditions, including the fully clamped condition, can be simulated effectively. Oñate et al. [1] have taken the RZT as the basis for developing a simple two-noded linear C^0 beam element named LRZ. The accuracy of the LRZ beam element for analyzing composite laminated beams has been demonstrated for simple support and clamped boundary conditions under different loads. Oñate et al. [1] have also shown that the LRZ element is capable to capture the relative displacement between layers, typical of a delamination process. It is necessary to mention however that this element can only model the fracture mode II.

In this paper we exploit the capabilities of the RZT element to model delamination (mode II) in laminated beams using an isotropic damage model [2,33] for modeling the nonlinear material behavior. The paper layout is the following. A brief description of the RZT theory, the LRZ finite elements and the isotropic damage model are presented first. Then, the implicit integration algorithm is shown. The non-linear problem is solved by the modified Newton–Raphson method. Finally, the performance of the LRZ element is shown by modeling delamination in a beam for two different laminates, where the reference solution is a plane stress analysis.

2. Refined Zigzag Theory (RZT) for beams and LRZ beam element

2.1. RZT kinematics

Consider a composite laminated beam of depth b, thickness h, and length L, formed by N layer of thickness h^k. The reference coordinate system is the 2D Cartesian system (x,z), where x is set as the in-plane coordinate and z is the thickness coordinate.

The displacement field assumed in the linear piecewise zigzag RZT is written as

$$\begin{aligned} u^k(x,z) &= u_0(x) - z\cdot\theta(x) + \bar{u}^k(x,z) \\ w(x) &= w_0(x) \end{aligned} \tag{1a}$$

In Eq. (1a) the zigzag displacement function $\bar{u}^k$ is expressed as

$$\bar{u}^k = \phi^k(z)\cdot\psi(x); \quad k = 1, N \tag{1b}$$

where superscript k indicates quantities within the kth layer with $z_k \leqslant z \leqslant z_{k+1}$, and z_k is the vertical coordinate of the kth interface; ψ is a primary kinematic variable defining the amplitude of the zigzag function on the beam and ϕ^k is a known piecewise linear zigzag function. u_0 is the uniform axial displacement along the beam axis direction x; θ represents the anticlockwise rotation of the normal and w_0 is the *deflection*.

The kinematics variables are

$$\mathbf{a} = [\,u_0 \quad w_0 \quad \theta \quad \psi\,]^T \tag{2}$$

The in-plane ε^k and the transverse shear γ^k strains are defined as

$$\begin{aligned} \varepsilon^k &= \frac{\partial u^k}{\partial x} = \frac{\partial u_0}{\partial x} - z\cdot\frac{\partial\theta}{\partial x} + \phi^k(z)\cdot\frac{\partial\psi}{\partial x} \\ \gamma^k &= \frac{\partial u^k}{\partial z} + \frac{\partial w}{\partial x} = \gamma(x) + \beta^k\cdot\psi(x) \end{aligned} \tag{3}$$

which can be written in matrix form as

$$\boldsymbol{\varepsilon}^k = \begin{bmatrix} \varepsilon^k \\ \gamma^k \end{bmatrix} = \begin{bmatrix} 1 & -z & \phi^k & 0 & 0 \\ 0 & 0 & 0 & 1 & \beta^k \end{bmatrix} \cdot \begin{bmatrix} \frac{\partial u_0}{\partial x} \\ \frac{\partial\theta}{\partial x} \\ \frac{\partial\psi}{\partial x} \\ \gamma \\ \psi \end{bmatrix} = \mathbf{S}^k\hat{\boldsymbol{\varepsilon}} \tag{4}$$

where $\hat{\boldsymbol{\varepsilon}}$ is the generalized stain vector. This vector contains the axial elongation $\frac{\partial u_0}{\partial x}$, the pseudo-curvature $\frac{\partial\theta}{\partial x}$, the derivative of the amplitude of the zigzag function $\frac{\partial\psi}{\partial x}$, the average transverse shear strain $\gamma(\frac{\partial w_0}{\partial x} - \theta)$ and the variable ψ.

2.2. Derivation of the zigzag function ϕ^k

The zigzag function is defined within each layer as

$$\phi^k = \bar{\phi}^{k-1} + \frac{h^k\beta^k}{2}(\zeta^k + 1) \tag{5}$$

where $\bar{\phi}^{k-1}$ is the zigzag function value at the $k-1$ interface, with $\bar{\phi}^0 = \bar{\phi}^N = 0$ and $\zeta^k = 2\frac{(z-z^{k-1})}{h^k} - 1$. The slope $\beta^k = \frac{\partial\phi^k}{\partial z}$ of the zigzag function within each layer is expressed as

$$\beta^k = \frac{G}{G^k} - 1 \tag{6}$$

where G is an average shear modulus that can be expressed in terms of the shear modulus (G^k) and the thickness (h^k) of each layer as

$$G = h\left[\sum_{k=1}^{N}\frac{h^k}{G^k}\right]^{-1} \tag{7}$$

For a more detailed description of the RZT for beams, the readers are referred to Tessler et al. [30].

2.3. Stresses and resultant stresses

The relation between the stresses and the strains for the kth layer is expressed in matrix form as

$$\boldsymbol{\sigma}^k = \begin{bmatrix} \sigma^k \\ \tau^k \end{bmatrix} = \begin{bmatrix} E^k & 0 \\ 0 & G^k \end{bmatrix} \cdot \begin{bmatrix} \varepsilon^k \\ \gamma^k \end{bmatrix} = \mathbf{D}^k \cdot \boldsymbol{\varepsilon}^k \tag{8}$$

where E^k, G^k and $\mathbf{D}^k$ are the Young modulus, the shear modulus and the constitutive matrix for the kth layer, respectively.The resultant stresses are computed by integrating the stresses over the beam section with area A as

$$\hat{\boldsymbol{\sigma}} = \int_A \mathbf{S}^k \boldsymbol{\sigma}^k dA \tag{9}$$

2.4. LRZ beam element

The kinematics variables of Eq. (2) are discretized using 2-noded C^0 beam elements of length l^e as

$$\mathbf{a} = \begin{bmatrix} u_0 \\ w_0 \\ \theta \\ \psi \end{bmatrix} = \sum_{i=1}^{2} \mathbf{N}_i \cdot \mathbf{a}_i^{(e)} = \mathbf{N} \cdot \mathbf{a}^{(e)} \tag{10}$$

with

$$\mathbf{N}_i = N_i \mathbf{I}_4 \text{ and } \mathbf{a}_i^{(e)} = [\, u_{0i} \quad w_{0i} \quad \theta_i \quad \psi_i \,]^T$$

being N_i the linear C^0 continuous shape function of node ith.

The generalized strains $\hat{\boldsymbol{\varepsilon}}$ of Eq. (4) are expressed in term of the nodal degrees of freedom (DOF) using Eq. (10) as

$$\hat{\boldsymbol{\varepsilon}} = \begin{bmatrix} \frac{\partial u_0}{\partial x} \\ \frac{\partial \theta}{\partial x} \\ \frac{\partial \psi}{\partial x} \\ \gamma \\ \psi \end{bmatrix} = \sum_{i=1}^{2} \begin{bmatrix} \frac{\partial N_i}{\partial x} u_{0i} \\ \frac{\partial N_i}{\partial x} \theta_i \\ \frac{\partial N_i}{\partial x} \psi_i \\ N_i \gamma_i \\ N_i \psi_i \end{bmatrix} = \sum_{i=1}^{2} \mathbf{B}_i \cdot \mathbf{a}_i^{(e)} = \mathbf{B} \cdot \mathbf{a}^{(e)} \tag{11}$$

being $\mathbf{B}_i$ the generalized strain matrix defined as

$$\mathbf{B}_i = \begin{bmatrix} \frac{\partial N_i}{\partial x} & 0 & 0 & 0 \\ 0 & 0 & \frac{\partial N_i}{\partial x} & 0 \\ 0 & 0 & 0 & \frac{\partial N_i}{\partial x} \\ 0 & \frac{\partial N_i}{\partial x} & -N_i & 0 \\ 0 & 0 & 0 & N_i \end{bmatrix} \tag{12}$$

Using the virtual work principle and Eqs. (8), (9), and (11), we can obtain the element stiffness matrix $\mathbf{K}^e$ and the equivalent nodal forces $\mathbf{F}^e$ for the LRZ linear beam elements as

$$\mathbf{K}^e = \int_l \mathbf{B}^T \widehat{\mathbf{D}} \mathbf{B} dl; \quad \mathbf{F}^e = \int_l N_i q [1,0,0,0]^T dl \tag{13}$$

where l is the element length, q is the distributive load and $\widehat{\mathbf{D}}$ is the constitutive generalized matrix defined as

$$\widehat{\mathbf{D}} = \int_A [\mathbf{S}^k]^T \mathbf{D}^k \mathbf{S}^k dA \tag{14}$$

Full integration of matrix $\mathbf{K}^e$ requires a two-point Gauss quadrature. This however leads to shear locking for slender beams. This problem is eliminated by using reduced integration (one-point Gauss quadrature) for all term of $\mathbf{K}^e$ [1].

Details of the formulation of the 2-noded LRZ beam element can be found in [1].

3. Isotropic damage model

The non-linear behavior of material is modeled with an isotropic damage model [2] in which the level of damage or degradation is monitored through a single internal scalar variable d. This variable takes values ranged between 0 (no damage) and 1 (full damage). The constitutive equation for this model is defined as

$$\boldsymbol{\sigma} = (1-d)\boldsymbol{\sigma}_0 = (1-d)\mathbf{D}_0 \cdot \boldsymbol{\varepsilon} \tag{14}$$

where $\boldsymbol{\sigma}$ and $\boldsymbol{\varepsilon}$ are the stress and strain tensors, respectively, and $\mathbf{D}_0$ is the undamaged constitutive tensor.In order to distinguish between a damage state and an undamaged one, it is necessary to define a damage criterion which is formulated here in the undamaged stress space as

$$F(\boldsymbol{\sigma}_0, d) = f(\boldsymbol{\sigma}_0) - c(d) \leqslant 0 \tag{15}$$

where $f(\boldsymbol{\sigma}_0)$ is a norm used to compare different states of deformation and $c(d)$ is the damage threshold. Damage occurs when the value of $f(\boldsymbol{\sigma}_0)$ is larger than $c(d)$. Damage starts for $f(\boldsymbol{\sigma}_0) > c_0$, being c_0 the initial damage threshold value which depends on the material properties. In our work we have defined c_0 as

$$c_0 = \frac{f_t}{\sqrt{E_0}} \tag{16}$$

where f_t is the tensile strength and E_0 the Young modulus of the undamaged material.

The norm chosen in this work is defined as

$$f(\boldsymbol{\sigma}_0) = \sqrt{\boldsymbol{\varepsilon} : \boldsymbol{\sigma}_0} \tag{17}$$

The evolution law for the damage threshold and the damage variable d is obtained using the damage consistency parameter according to the Kuhn–Tucker conditions. The evolution of these variables can be explicitly integrated [34] to obtain

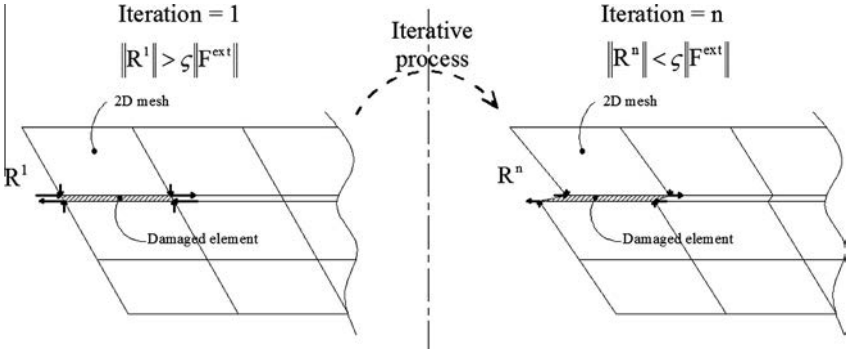

Fig. 1. The delaminated displacement field is achieved by the residual forces (R) in a plane stress analysis (PS).

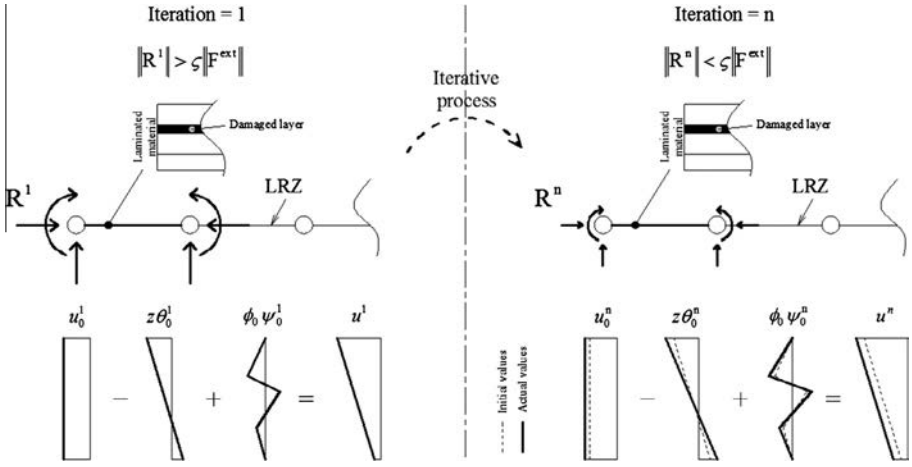

Fig. 2. The residual forces are not capable to induce delamination when the zigzag function ϕ^k is not updated.

$$d = G(f(\boldsymbol{\sigma}_0))$$
$$c(d) = \max\{c_0; \max\{f(\boldsymbol{\sigma}_0)\}\} \tag{18}$$

where $G(\bullet)$ is a monotonic scalar function ranging between 0 and 1 which defines the evolution of the damage variable. In this work an exponential evolution law is adopted for G as

$$G(f(\boldsymbol{\sigma}_0)) = 1 - \frac{f^0(\boldsymbol{\sigma}_0)}{f(\boldsymbol{\sigma}_0)} e^{B\left(1-\frac{f(\boldsymbol{\sigma}_0)}{f^0(\boldsymbol{\sigma}_0)}\right)} \text{ with } f^0(\boldsymbol{\sigma}_0) = c_0 \tag{19}$$

Considering the norm of Eq. (17), the exponential softening of Eq. (19), and the initial damage threshold value c_0 (Eq. (16)), the parameter B is computed as

$$B = \left(\frac{G_f \cdot E_0}{l^* \cdot (f_t)^2} - \frac{1}{2}\right)^{-1} \geqslant 0 \tag{20}$$

being G_f the fracture energy per unit area and l^* a characteristic length. In this paper, l^* is equal to the influence of each Gauss point.

4. Algorithm for the non-linear solution

When a degradation process is considered in the constitutive material model it is necessary to solve a non-linear system of algebraic equations of the form

$$\mathbf{F}^{ext} - \mathbf{F}^{int}(\mathbf{q}) = \mathbf{R}(\mathbf{q}) \tag{21}$$

being $\mathbf{q}$ the discretization parameters, $\mathbf{F}^{\text{ext}}$ and $\mathbf{F}^{\text{int}}(\mathbf{q})$ the external and internal forces, respectively, and $\mathbf{R}(\mathbf{q})$ the residual vector. Note, that the dynamic forces are not considered in this work.In this work, the modified Newton–Raphson method is adopted to solve the nonlinear equation system of Eq. (21). Hence, the following linear problem is solved for each iteration

$$d\mathbf{q} = ({}^{i-1}\mathbf{K}_S)^{-1\,i-1}\mathbf{R} \tag{22}$$

where $d\mathbf{q}$ is the increment of the nodal DOFs at ith iteration. Note that both the damaged stiffness matrix $\mathbf{K}_S$ and the residual vector $\mathbf{R}$ were computed at the previous $i-1$th iteration. For the LRZ element the matrix $\mathbf{K}_S$ is defined as

$${}^{i-1}\mathbf{K}_S = \int_l \mathbf{B}^{T\,i-1}\widehat{\mathbf{D}}_S\mathbf{B}dl \tag{23}$$

with

$${}^{i-1}\widehat{\mathbf{D}}_S = \int_A \left[{}^{i-1}\mathbf{S}^k\right]^{T\,i-1}\mathbf{D}_S^{k\,i-1}\mathbf{S}^k dA \text{ and } {}^{i-1}\mathbf{D}_S^k = \left(1 - {}^{i-1}d^k\right)\mathbf{D}_0^k \tag{24}$$

The updated DOFs are obtained as

$${}^{i}\mathbf{q} = {}^{i-1}\mathbf{q} + d\mathbf{q} \tag{25}$$

This process is repeated until the convergence criterion $\|\mathbf{R}\| \leqslant \varsigma\|\mathbf{F}\|$ is satisfied [35] where ς is a predefined error tolerance.

In 2D finite element analysis, the nodal DOFs $\mathbf{q}$ are the Cartesian displacements $\mathbf{a} = [u_x \quad u_y \quad u_z]$. According to these variables, the

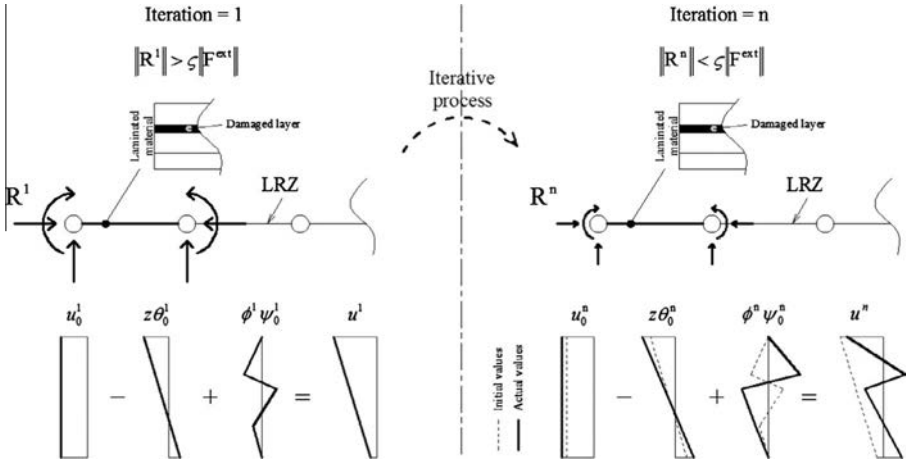

Fig. 3. Delamination can be captured with the LRZ finite element when the zigzag function ϕ^k is updated by reducing the shear modulus of the damaged layer.

 # Loop over load increments

Update external forces $\mathbf{F}^{\text{ext}}$

 # Iterative process

If *i*th iteration = 1

$$^{I}\mathbf{a} = \mathbf{K}_{\text{S}}^{-1} \cdot \mathbf{F}^{\text{ext}}$$

$$^{I}\boldsymbol{\varepsilon}^{k} = \mathbf{S}^{k}\ \mathbf{B}\ ^{I}\mathbf{a}$$

Note that for the first iteration both $\mathbf{K}_{\text{S}}^{-1}$ and $\mathbf{S}^{k}$ were computed at the last iteration of the previous load increment.

Else

$$^{i}d\mathbf{a} = {}^{i-1}\mathbf{K}_{\text{S}} \cdot {}^{i-1}\mathbf{R}$$

$$^{i}\mathbf{a} = {}^{i-1}\mathbf{a} + {}^{i}d\mathbf{a}$$

$$^{i}\boldsymbol{\varepsilon}^{k} = {}^{i-1}\mathbf{S}^{k}\ \mathbf{B}\ ^{i}\mathbf{a}$$

Remember that $^{i-1}\mathbf{S}^{k}$ contains $^{i-1}\phi^{k}$ and $^{i-1}\tilde{\beta}^{k}$ computed at the previous iteration.

End if

Evaluate undamaged stresses

$$^{i}\boldsymbol{\sigma}_{0}^{k} = \mathbf{D}_{0}^{k} \cdot {}^{i}\boldsymbol{\varepsilon}^{k}$$

Update damage variable:

$$^{i}d^{k} = 1 - \frac{c_0}{{}^{i}f} e^{A\left(1 - \frac{{}^{i}f}{c_0}\right)}$$

Update stresses and shear modulus:

$$^{i}\boldsymbol{\sigma}^{k} = \left(1 - {}^{i}d^{k}\right) {}^{i}\boldsymbol{\sigma}_{0}^{k}$$

$$^{i}\tilde{G}^{k} = \left(1 - {}^{i}d^{k}\right) {}^{i}G_{0}^{k}$$

Update zigzag function:

$$^{i}\tilde{G} = h\left[\sum_{k=1}^{N} \frac{h^{k}}{{}^{i}\tilde{G}^{k}}\right]^{-1}$$

$$^{i}\tilde{\beta}^{k} = \frac{{}^{i}\tilde{G}}{{}^{i}\tilde{G}^{k}} - 1$$

$$^{i}\phi^{k} = \bar{\phi}^{k-1} + \frac{h^{k}\ {}^{i}\tilde{\beta}^{k}}{2}\left(\zeta^{k} + 1\right)$$

Computation of the secant stiffness matrix and internal forces:

$$^{i}\mathbf{K}_{\text{S}} = \int_{l} \mathbf{B}^{T}\ {}^{i}\hat{\mathbf{D}}_{\text{S}}\ \mathbf{B}\ dl$$

$$^{i}\mathbf{F}^{\text{int}} = \int_{V} \mathbf{B}^{T}\ {}^{i}\mathbf{S}^{T}\ {}^{i}\boldsymbol{\sigma}^{k}\ dV$$

Verification of convergence criteria

$$\mathbf{F}^{\text{ext}} - {}^{i}\mathbf{F}^{\text{int}} = {}^{i}\mathbf{R}$$

$$\left\| {}^{i}\mathbf{R} \right\| \leq \varsigma \left\| \mathbf{F}^{\text{ext}} \right\|$$

 # END iterative process

 # END loops over load increments

Fig. 4. Algorithm for solving the non-linear problem using the modified Newton–Raphson method. Note that the zigzag function is updated at each iteration.

stress resultants obtained by integrating the stresses on the finite element volume are three forces that induce the movement of the node. So, when a finite element starts to suffer softening ($d > 0$) and its stresses are reduced by Eq. (14), a lack of equilibrium between the external and the internal forces appears which induces residual forces via Eq. (21). These residual forces applied at the nodes of a damaged 2D element generate the relative displacement between layers that occurs during a delamination process. The equilibrium displacement field is achieved using an iterative process such as that of Eqs. (22) and (25). This process is schematized in Fig. 1.

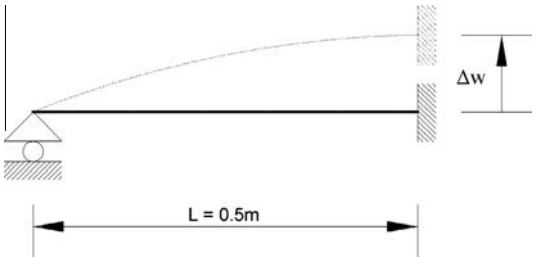

Fig. 5. Boundary conditions of the analyzed beam.

While in 3D finite element analysis, it is possible to generate the relative displacement simply using the residual forces, in the LRZ finite element it is not.

In the LRZ element, the reference surface where the kinematics variables (Eq. (2)) are computed is the middle surface ($z = 0$) of the laminate. The stress resultants computed by integrating the stresses across the beam thickness (Eq. (9)) lead to forces and moments

Table 1
Mechanical properties of linear-elastic layers.

Materials	Young's modulus (E_0)	Shear modulus (G_0)
Mechanical properties of linear-elastic plies (MPa)		
A	157.9×10^4	5.93×10^4
B	104.0×10^1	4.00×10^2
C	5.3×10^1	2.12×10^1
D	2.19×10^1	0.876×10^1
E	0.82×10^1	0.328×10^1
F	0.73×10^{-1}	0.29×10^{-1}
G	7.3×10^1	2.92×10^1

Table 2
Mechanical properties of cohesive layers (cl).

Materials	Young's modulus (E_0) (MPa)	Shear modulus (G_0) (MPa)	Tensile strength (f_t) (MPa)	Fracture energy (G_f) (kN/m)	
				Ductile (G_f^D)	Fragile (G_f^F)
Mechanical properties of cohesive plies (cl)					
H^{cl}	104.0×10^1	4.0×10^2	6.5	5.0×10^4	1.0×10^{-2}
I^{cl}	0.73×10^{-1}	0.29×10^{-1}	0.02	5.0×10^4	1.0×10^{-3}

Table 3
Layer distribution of laminated materials.

Laminate	Layer distribution	h^k/h	h (mm)
Laminated materials			
L1	(A/B/A/H^{cl}/A/B/A/B/A)	(0.11/0.11/0.11/0.01/0.22/0.11/0.11/0.11/0.11)	9.1
L2	(C/D/E/F/C/I^{cl}/G/E/D/G)	(1.0/0.12/0.1/0.08/0.14/0.02/0.08/0.1/0.06/0.2)	25.0

applied at the beam element nodes on the reference surface. Consequently, there are no forces within the laminate capable of producing the relative displacement between plies. For this reason, in the RZT theory, the reduced value of stresses by Eq. (14) in an iterative process gives as result an amplification of the initial kinematics of the laminate, instead of an update of the delamination kinematics. That is so, because the variables of Eq. (2) are not capable to modify by themselves the zigzag form of the axial displacement, but they can only vary the scale of the original zigzag distribution. Fig. 2 outlines the above-mentioned problem.

In summary, the form of the zigzag axial displacement is governed by the zigzag function ϕ^k (Eq. (5)). Therefore, in order to modify the zigzag form of the laminated kinematics (Eq. (1a)) during a delamination process, it is essential to update function ϕ^k depending on the value of damage variable d. Since ϕ^k depends on the shear modulus, the update of ϕ^k is obtained by reducing the initial elastic shear modulus G_0^k at the damaged layer k by

$$\widetilde{G}^k = (1 - d^k) G_0^k \tag{26}$$

Thus, function ϕ^k is expressed in term of the damaged shear modulus as

$$\phi^k = \bar{\phi}^{k-1} + \frac{h^k \tilde{\beta}^k}{2}(\zeta^k + 1) \tag{27}$$

with

$$\tilde{\beta}^k = \frac{\widetilde{G}}{\widetilde{G}^k} - 1 \text{ and } \widetilde{G} = h\left[\sum_{k=1}^{N} \frac{h^k}{\widetilde{G}^k}\right]^{-1} \tag{28}$$

This simple but effective update of the zigzag function ϕ^k allows us to capture the relative displacement between two layers in a delamination process. A scheme of this process is shown in Fig. 3.

Fig. 4 shows the integration algorithm for solving Eq. (21) using the modified Newton–Raphson iterative scheme (Eqs. (22)–(25)), the isotropic damage model and the adapted zigzag function computed by Eq. (27).

5. Numerical simulations

The validity of the algorithm for capturing the relative in-plane displacement (Mode II) between layers is studied by modeling a beam of length $L = 0.5$ m supported as shown in Fig. 5. A vertical displacement Δw at the clamped support is imposed. The beam is analyzed for two laminates (L1 and L2) with properties shown in Tables 1–3.

The proposed method allows damage to occur at any layer of the laminate, so is not necessary to predefine the path of the crack. However since the objective of this work is to demonstrate the capability of the LRZ element for predicting relative displacement between layers, the interface where delamination will take place is defined at the onset of the analysis. Therefore, there is only one layer for each laminate, called "cohesive layer" (cl) henceforth (Fig. 7), whose mechanical behavior is modeled by the isotropic damage model, while the other plies are treated as linear-elastic. Consequently, delamination occurs when damage starts at the cohesive layer, which leads to a loss of its previous stiffness and induces the relative displacement between the adjacent layers to it.

In order to show the influence of the fracture energy G_f^{cl} in the delamination process, two values of this parameter (a larger one and a smaller one) are adopted for the cohesive layer in each laminate. For clarity, in the followings the largest value (G_f^D) is associated to a "ductile" material while the smallest (G_f^F) to a "fragile" material.

LRZ meshes of 2, 16, 128 finite elements are used in the analysis.

The reference solution is obtained by the plane stress analysis (PS) using 4-noded quadrilateral finite elements and the isotropic damage model presented in Section 4. The iterative process uses the modified Newton–Rhapson method explained in Section 5. The beam length, the thickness of the elastic layers and the thickness of the cohesive ply are discretized using 100, 2 and 1 finite elements, respectively. The discretization chosen leads to meshes of 1700 and 1900 4-noded quadrilateral PS elements for the lami-

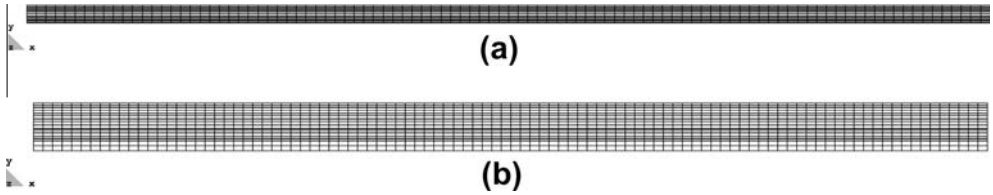

Fig. 6. Four-noded quadrilateral finite element meshes for laminate L1 (a), and laminate L2 (b).

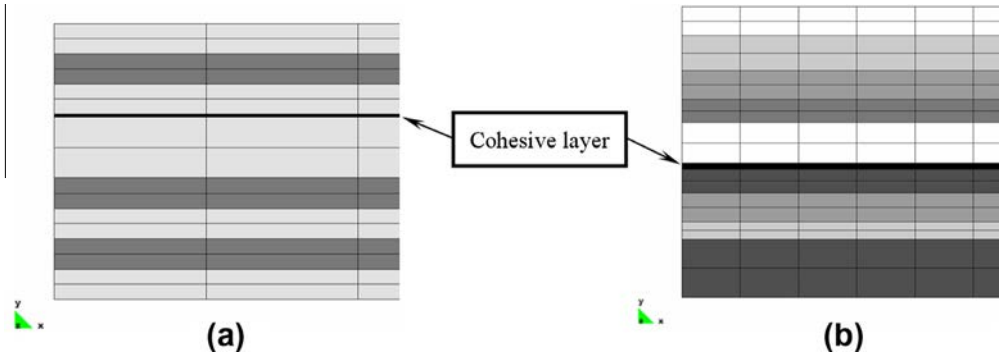

Fig. 7. Cohesive layer in laminate L1 (a), and laminate L2 (b).

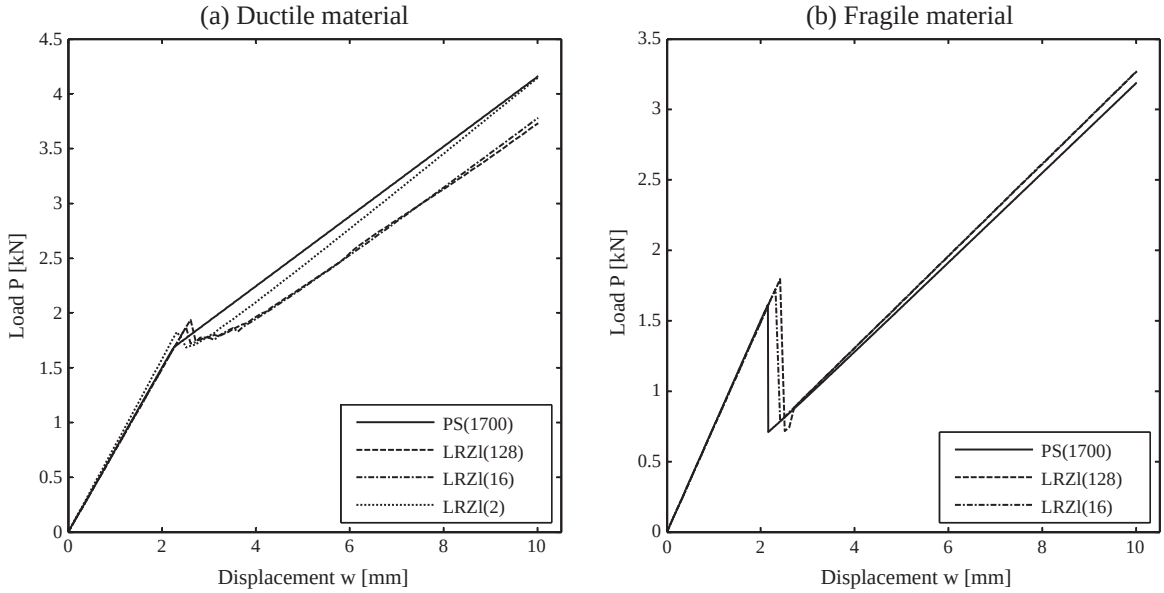

Fig. 8. Load versus displacement curves for laminate L1 with ductile (a) and fragile (b) fracture energy.

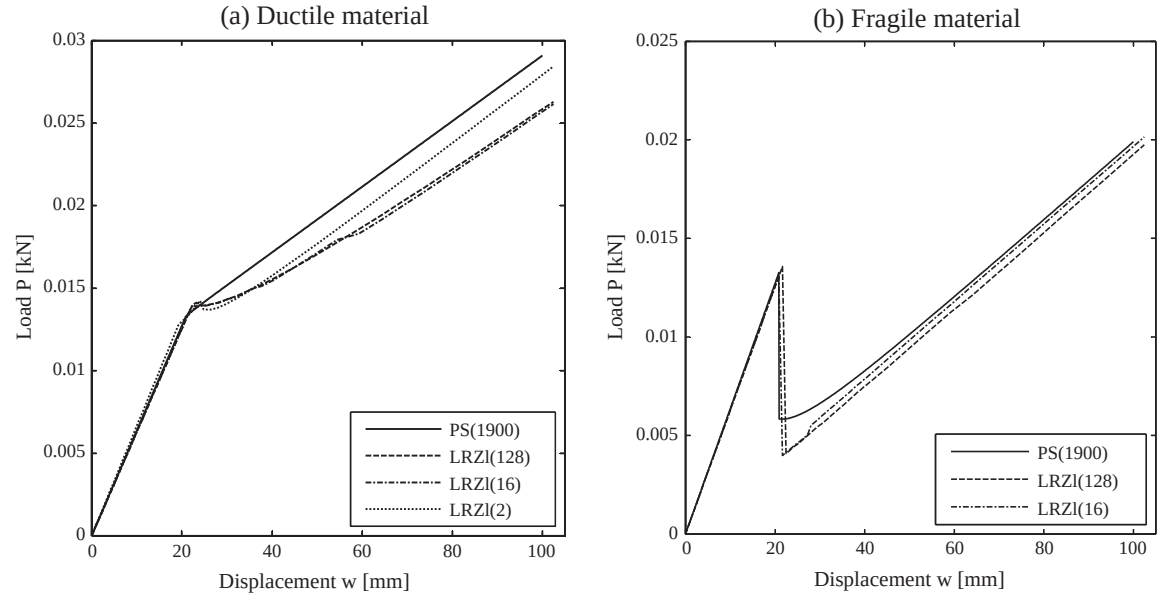

Fig. 9. Load versus displacement curves for laminate L2 with ductile (a) and fragile (b) fracture energy.

nates L1 and L2, respectively. The 2D meshes for each laminate are shown in Figs. 6 and 7.

The simulation is made under the following considerations: quasi-static application of vertical displacement at the clamped support, geometrically linear problem and small deformation.

Figs. 8 and 9 show the load–displacement graph for the laminates L1 and L2, respectively, where the curves are obtained by the PS analysis and the LRZ beam element. The load corresponds to the vertical reaction at the clamped support. The displacement corresponds to the incremental displacement Δw applied to the clamped support (Fig. 5). The curves shown in Figures a are obtained when the "ductile" (G_f^D) fracture energy is considered. The response of the beam when the "fragile" (G_f^F) fracture energy is used is shown in Figures b. The fracture energy values are noted in Table 2.

The results reveal an admissible agreement between the results obtained using PS analysis and LRZ beam elements. The errors for the finest LRZ meshes, at the end of simulation, for the cases L1-G_f^D (Fig. 8a), L1-G_f^F (Fig. 8b), L2 – G_f^D (Fig. 9a) and L2 – G_f^F (Fig. 9b) are less than 11.0%, 2.5%, 7.5% and 2.9%, respectively. The LRZ solution exhibits small drops of load for the case $L1 - G_f^D$ (Fig. 8a), which are not present in the PS solution. The cause of each drop is that the cohesive layer of some finite elements is totally damage at the same increment, which produces a discontinuous loss of stiffness during the simulation. The number of simultaneously delaminated elements, involved on each drop, depends on the longitudinal distribution of the transverse shear stress of the cohesive layer.

When the "fragile" value of the fracture energy (G_f^F) is used, the cohesive layer completely loses its energy at the delamination onset, which provokes the sharp drop in the sample resistance, as shown in Figures b. The loss of resistance computed by the PS solution is around 56% for both laminates, while the LRZ solution gives 60% and 70% for L1 and L2, respectively.

In all cases, both the initial stiffness and the stiffness once delamination process has started are very close to the stiffness obtained by 2D analysis. Also, is shown that delamination starts for the same values of displacement and load.

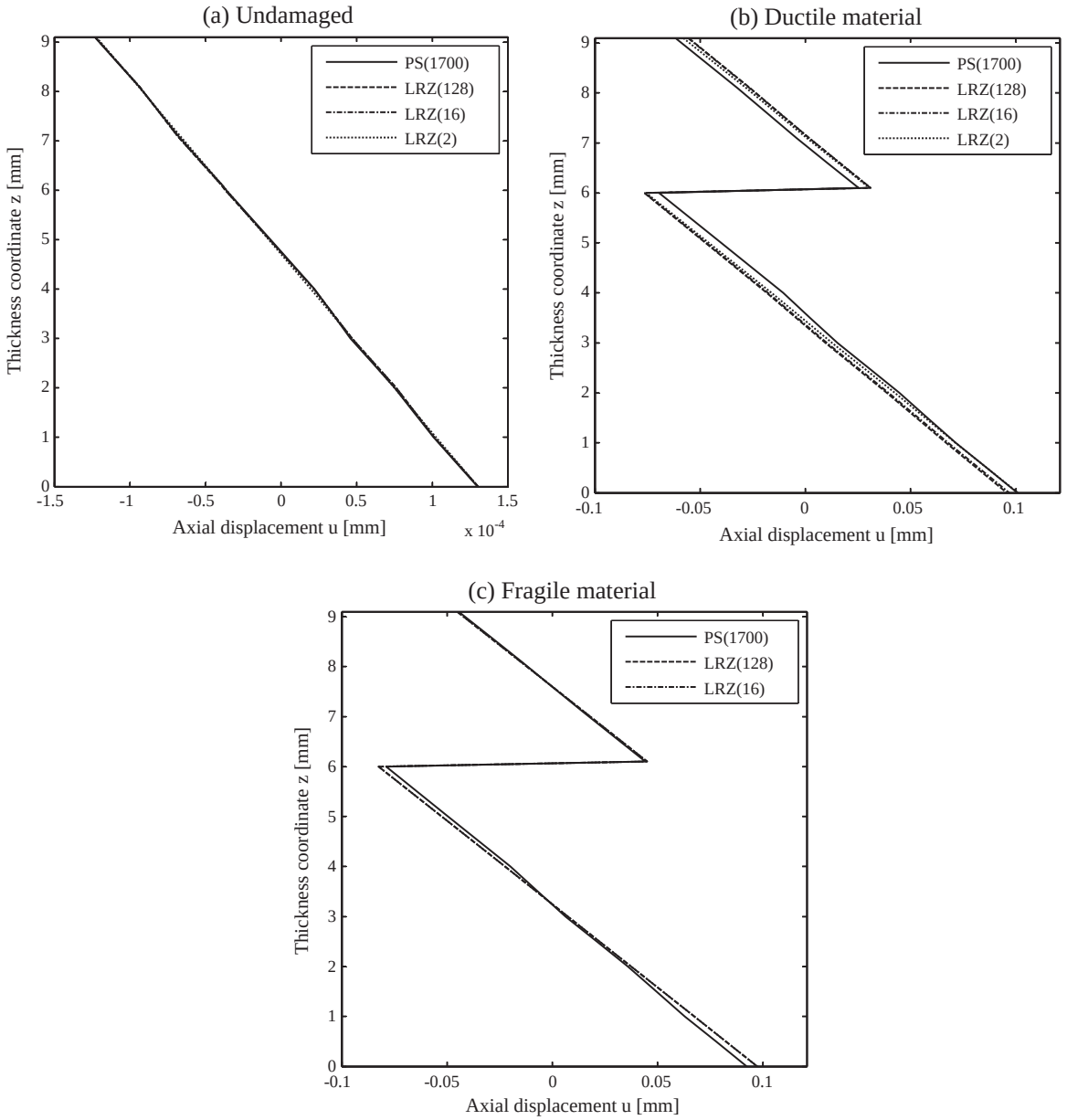

Fig. 10. Thickness distribution of the axial displacement u at the simply supported end for laminate L1. This Fig. shows the undamaged kinematics (a) and the damaged kinematics when the "ductile" (b) and the "fragile" (c) fracture energy is used.

The thickness distribution of the axial displacement u at the simply supported end, before and after delamination onset, is shown in Figs. 10 and 11 for laminates L1 and L2, respectively.

The undamaged kinematics is shown in Figures a, in which the very good match between PS and LRZ kinematics is evident.

Figs. 10 and 11b and c show the delaminated kinematics at the end of simulation when the "ductile" and the "fragile" fracture energy values are used, respectively. In the "ductile" case (Figures b), the LRZ elements are capable to capture the relative displacement with errors around 11% and 16% for laminates L1 and L2, respectively. In the "fragile" case (Figures c), the errors are less than 3.3% for both laminates.

Almost identical results are obtained with the quadratic LRZ beam element.

Fig. 12 shows the thickness distribution of the zigzag function ϕ for laminate L1 (Fig. 12a) and laminate L2 (Fig. 12b). The solid line represents the initial zigzag function (undamaged), whereas that the dashed line and the dash-dot line correspond to the damaged zigzag function when the damage variable of cohesive layer is equal to 0.9 and 1, respectively. As is mentioned in Section 5, the ability of the LRZ element to capture the relative displacement between plies during a delamination process lies in updating the zigzag function as the layers are damaged.

In order to compare the performance of the PS and the LRZ analyses, both the total increment numbers and incremental displacement values as well as the tolerance value ($\varsigma = 1 \times 10^{-4}$) are the same for both methods. The total increment numbers are equal to 1000 and 7000 for laminates L1 and L2, respectively. The incremental displacement value applied in each increment is 1×10^{-3} mm and 4×10^{-3} mm for L1 and L2, respectively. Tables 4 and 5 show the total number of iterations, the maximum number of iteration needed for achieving convergence in any increment and the total CPU time used in the simulation for L1 and L2, respectively.

As expected, the computation time needed for the PS analysis is several times greater than that required for the LRZ solutions.

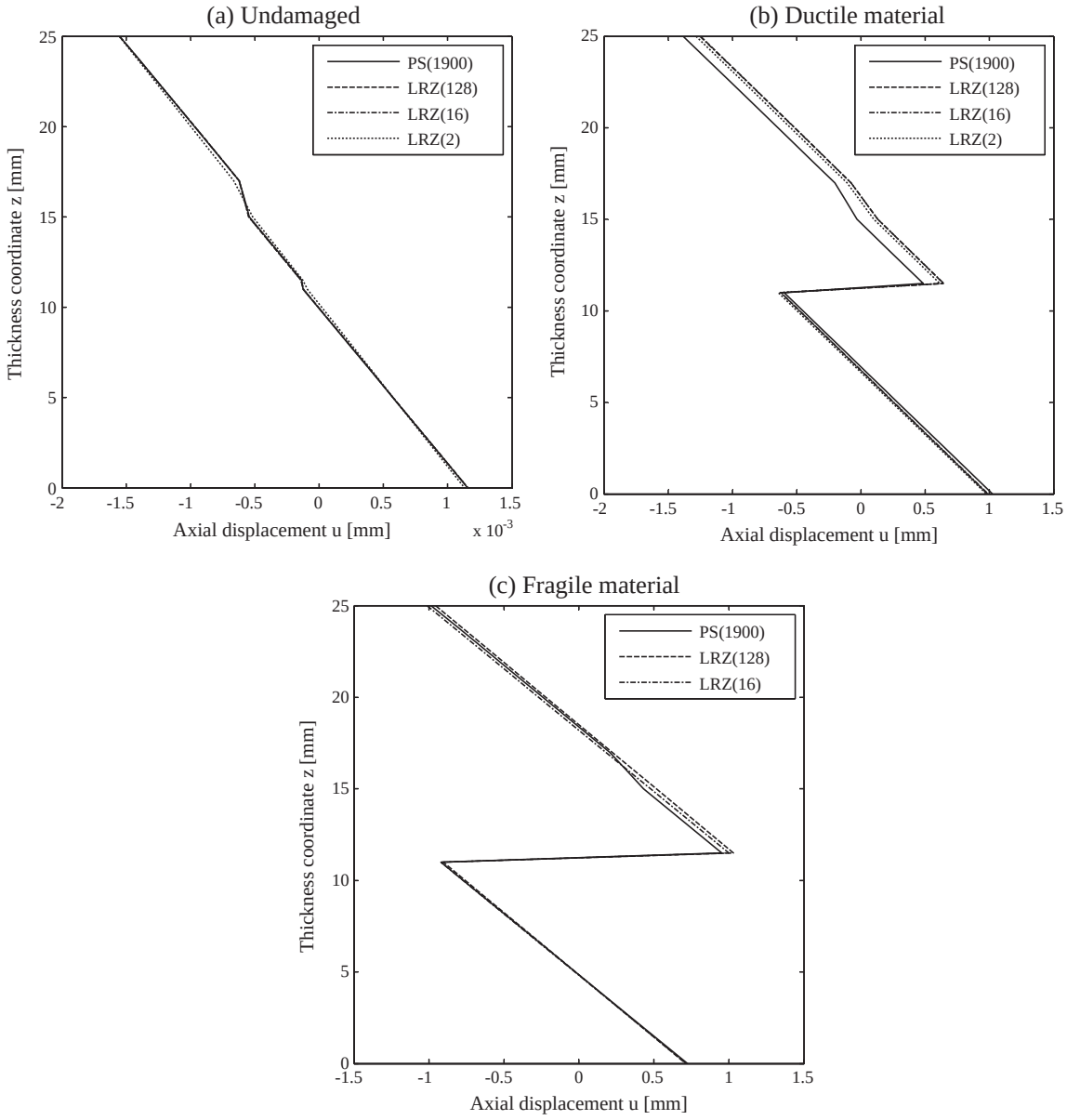

Fig. 11. Thickness distribution of the axial displacement u at the simply supported end for laminate L2. This Fig. shows the undamaged kinematics (a) and the damaged kinematics when the "ductile" (b) and the "fragile" (c) fracture energy is used.

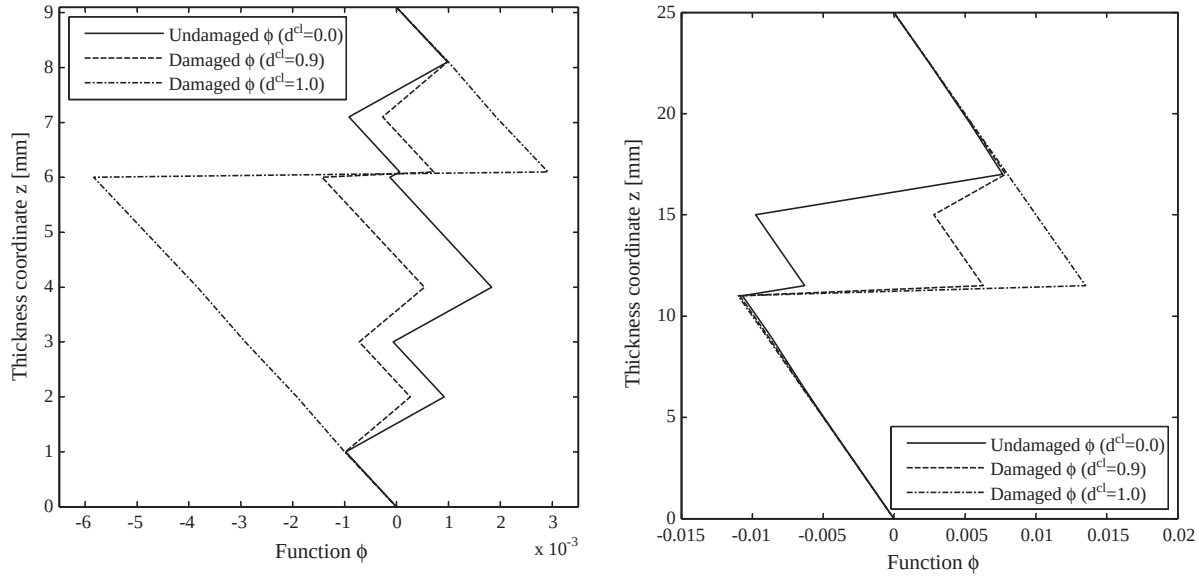

Fig. 12. Undamaged and damaged zigzag function for laminate L1 (a) and laminate L2 (b).

Table 4
Computational cost of the iterative process for laminate L1.

Finite elements		$G_f^D = 5.0 \times 10^4$ (Ductile)			$G_f^F = 1.0 \times 10^{-2}$ (Fragile)		
		Total iter.	Max. iter.	Time (seg)	Total iter.	Max. iter.	Time (seg)
Computational cost of the iterative process for laminate L1							
2D	1700	9308	485	3069.0	3465	254	1127.0
LRZ	2	1543	166	1.52	–	–	–
	16	1286	81	1.57	1009	9	1.27
	128	2291	225	19.61	1036	23	9.45

Table 5
Computational cost of the iterative process for laminate L2.

Finite elements		$G_f^D = 5.0 \times 10^4$ (Ductile)			$G_f^F = 1.0 \times 10^{-3}$ (Fragile)		
		Total iter.	Max. iter.	Time (seg)	Total iter.	Max. iter.	Time (seg)
Computational cost of the iterative process for laminate L2							
2D	1900	18,374	88	6967.0	10,141	144	4223.0
LRZ	2	7298	76	8.10	–	–	–
	16	7131	53	8.11	7016	11	7.96
	128	7072	71	64.51	7372	101	65.46

Comparing with the finest 128-LRZ mesh, PS uses at best around 67 times the time used by LRZ solution for laminate L2 and $G_f^F = 1.0 \times 10^{-3}$ (Table 5). At worst, the time used by PS is 156 times greater than that required by the LRZ solution for laminate L1 and $G_f^D = 5.0 \times 10^4$ (Table 4). If the comparison is made versus the 16-LRZ mesh, the time used by the PS solution is 530 and 1954 times of that needed by the LRZ solution at best and at worst scenarios, respectively.

6. Conclusions

We have presented a promising numerical method based on the RZT for simulating the delamination process (mode II) in laminated beams. This method uses LRZ beam elements for modeling the beam kinematic and an isotropic damage model for modeling the material behavior.

Results show that in order to capture the relative displacement between layers during delamination, the zigzag function has to be updated according as the layers are damaged. Therefore, both the stresses and the zigzag function are degraded by the damage variable during the iterative process.

The ability of this formulation to capture the relative displacement has been proved by the study of delamination in a beam for two different laminates. The comparison of the LRZ solution with the plane stress plate elements analysis revels that the technique presented is capable to predict both the onset and the propagation of delamination. Also, the updating of zigzag function has proven to be essential for reproducing the delaminated kinematics.

A comparison of the computational time between both adopted techniques has shown that, as expected, the computation time and the memory space needed by the LRZ beam element is several times less than that required by a 2D PS analysis.

The extension of the proposed formulation to plate and shells is possible since the RZT plate theory has the same basic features as the RZT beam theory. Because of the kinematics of the RZT plate theory, the extended formulation is able to model not only the fracture mode II but also the mode III. However, this methodology is unable to simulate the fracture mode I since the vertical displacement is defined constant through the thickness of the laminate.

Acknowledgements

The first author would like to acknowledge the FPU-UPC scholarship supported by the Universitat Politècnica de Catalunya and the Ministerio de Educación of Spain.

This research was partially financial supported by the SAFECON project of the European Research Council (ERC) of the European Commission.

References

[1] Oñate E, Eijo A, Oller S. Simple and accurate two-noded beam element for composite laminated beams using a refined zigzag theory. Comput Method Appl Mech Eng 2012:362–82.
[2] Oliver J, Cervera M, Oller S, Lubliner J. Isotropic damage models and smeared crack analysis of concret. In: Second international conference on computer aided analysis and design of concrete structures Zell am See, Austria; 1990.
[3] Bolotin VV. Delaminations in composite structures: its origin, buckling, growth and stability. Compos: Part B 1996;27B:129–45.

[4] Krueger R. The virtual crack closure technique: history, approach and applications. Appl Mech Rev 2002;57(2):109–43.
[5] Mabson G. Fracture analysis for bondlines and interfaces of composite structures. In: 4th International conference on composites testing and model identification (Comptest2008). Dayton (OH); 2008.
[6] Borg R, Nilsson L, Simonsson K. Modeling of delamination using a discretized cohesive zone and damage formulation. Compos Sci Technol 2002;62(10–11):1299–314.
[7] Turon A, Camanho PP, Costa J, Dávila CG. A damage model for the simulation of delamination in advanced composites under variable-mode loading. Mech Mater 2006;38(11):1072–89.
[8] Balzani C, Wagner W. An interface element for the simulation of delamination in unidirectional fiber-reinforced composite laminates. Eng Fract Mech 2008;75(9):2597–615.
[9] Turon A, Camanho PP, Costa J, Renart J. Accurate simulation of delamination growth under mixed-mode loading using cohesive elements: definition of interlaminar strengths and elastic stiffness. Compos Struct 2010;92:1857–64.
[10] Wagner W, Balzani C. Simulation of delamination in stringer stiffened fiber-reinforced composite shells. Comput Struct 2008;86(9):930–9.
[11] Martinez X, Rastellini F, Oller S, Flores F, Oñate E. Computationally optimized formulation for the simulation of composite materials and delamination failures. Compos: Part B 2011;47(–):134–44.
[12] Timoshenko SP, Woinowsky-Krieger S. Theory of plates ans shells. 3rd ed. New York: McGraw-Hill; 1959.
[13] Kirchhoff G. Über das Gleichgewicht und die Bewegung einer elastishen Scheibe. J Angew Math 1850;40:51–88.
[14] Timoshenko SP. On the correction for shear of differential equations for transverse vibrations of prismatic bars. Philos Mag Ser 1921;41:744–6.
[15] Reissner E. The effect of transverse shear deformation on the bending of elastic plates. Appl Mech 1945;12:69–79.
[16] Mindlin RD. Influence of rotatory inertia and shear in flexural motions of isotropic elastic plates. Appl Mech 1951;18:31–8.
[17] Reddy JN. A generalization of two-dimensional theories of laminated plates. Commun Appl Numer Method 1987;3(3):173–80.
[18] Reddy JN, Robbins DH. Theories and computational models for composite laminates. Appl Mech Rev 1994;47(6):147–65.
[19] Liu D, Li X. An overall view of laminate theories based on displacement hypothesis. J Compos Mater 1996;30(14):1539–61.
[20] Barbero EJ, Reddy JN. Modeling of delamination in laminates using a layer-wise plate theory. Int J Solids Struct 1991;28(3):373–88.
[21] Thornburgh R, Chattopadhyay A. Unified approach to modeling matrix cracking and delamination in laminated composite structures. AIAA 2001;39(1):153–60.
[22] Williams TO, Addessio FL. A general theory for laminated plates with delaminations. Int J Solids Struct 1997;34(16):2003–24.
[23] Hosseini-Toudeshky H, Hosseini S, Mohammadi B. Delamination buckling growth in laminated composites using layerwise-interface element. Compos Struct 2010;92(8):1846–56.
[24] Na WJ, Reddy JN. Delamination in cross-ply laminated beams using the layerwise theory. Asian J Civil Eng 2009;10:451–80.
[25] Wanji C, Zhen W. A selective review on recent development of displacement-based laminated plate theories. Recent Pat Mech Eng 2008;1:29–44.
[26] Carrera E. Historical review of Zig-Zag theories for multilayered plates and shells. Appl Mech Rev 2003;56(3):287–308.
[27] Averill RC, Yip YC. Development of simple, robust finite elements based on refined theories for thick laminated beams. Comput Struct 1996;59(3):529–46.
[28] Aitharaju VR, Averill RC. C_0 zig-zag finite element for analysis of laminated composite beams. ASCE 1999;59:502–9.
[29] Icardi U, Zardo G. C^0 plate element for delamination damage analysis, based on a zig-zag model and strain energy updating. Int J Impact Eng 2005;31(5):579–606.
[30] Tessler A, Sciuva MD, Gherlone M. A refined zigzag beam theory for composite and sandwich beams. J Compos Mater 2009;43(9):1051–81.
[31] Tessler A, Sciuva MD, Gherlone M. A consistent refinement of first-order shear deformation theory for laminated composite and sandwich plates using improved zigzag kinematics. Mech Mater Struct 2010;5(2):341–65.
[32] Tessler A, Sciuva MD, Gherlone M. Refined zigzag theory for homogeneous, laminated composite, and sandwich plates: a homogeneous limit methodology for zigzag function selection. Numer Meth Part Diff Eq 2011;27(1):208–29.
[33] Lemaitre J, Chaboche JL. Mechanics of solid materials. Cambridge: Press Syndicate of the University of Cambridge; 1990.
[34] Oller S. Fractura mecánica. Un enfoque global., 1ra ed., CIMNE, Barcelona, España; 2001 [ISBN: 84-89925-76-3].
[35] Zienkiewicz OC, Taylor RL. El método de los elementos finitos, vol. 2, 5 ed. CIMNE, Barcelona; 2004 [ISBN: 84-95999-53-6].

Composite Structures 108 (2014) 456–471

Contents lists available at ScienceDirect

Composite Structures

journal homepage: www.elsevier.com/locate/compstruct

Delamination in laminated plates using the 4-noded quadrilateral QLRZ plate element based on the refined zigzag theory

A. Eijo *, E. Oñate, S. Oller

International Center for Numerical Methods in Engineering (CIMNE), Universitat Politècnica de Catalunya (UPC), Campus Norte UPC, 08034 Barcelona, Spain

ARTICLE INFO

Article history:
Available online 3 October 2013

Keywords:
Laminated plates
Delamination
QLRZ plate element

ABSTRACT

A numerical method based on the Refined Zigzag Theory (RZT) to model delamination in composite laminated plate/shell structures is presented. The originality of this method is the use of 4-noded quadrilateral plate finite elements whit only seven variables per node to discretize the plate/shell geometry. The ability to capture the relative displacement between consecutive layers in fracture mode II and III is the more important advantage of this element, denoted QLRZ [1].

A continuum isotropic damage model [2] is used to model the mechanical behavior of the plies. The material non-lineal problem is solved with the modified Newton–Raphson method.

The RZT plate theory, the QLRZ finite element and the isotropic damage model are described in this work. Also, the implicit integration algorithm is presented. The performance of the numerical model is analyzed by studying the delamination in a rectangular plate for two different laminates, using the 3D analysis as the reference solution.

1. Introduction

Delamination [3] is a dangerous failure mode in laminated composite materials and is normally characterized by a relative displacement between layers due to a loss of adherence. Local forces, thermal actions and low energy impacts may serve as sources of delamination during the transportation, storage or service life of the structural member. In addition, geometry discontinuities such as access holes, notches, free edges or bonded and bolted joints can also induce delamination due to high stress gradients. Once delamination has occurred, the initial stiffness of the structure could be considerably reduced which can induce the structural failure by other phenomena as buckling, excessive vibration or fatigue.

During the design phases of laminated structures, it is important to know how the global response of the structure will be affected by delamination. Thus, much effort and time is been invested to develop numerical tools that can predict delamination in an effective and efficient manner.

The more common procedures to model delamination are based on the fracture mechanics or the damage mechanics. The virtual crack closure technique (VCCT) [4–6] and the cohesive finite elements [7–11] are some typical examples. Each of these techniques has their own drawbacks, but they share one of the most inefficient features: the need to place interface fracture or cohesive finite elements between the plies where delamination is expected to occur. Because of the delamination path is normally unknown, it is necessary to place interface elements between all layers, which leads to an increase of computational resources needed to carry out the simulation, specially in laminates with many plies. In order to avoid the above-mentioned disadvantage, Martinez et al. [12] have studied delamination under the continuum mechanics using a 3D finite element method and an isotropic damage model to manage material degradation.

The capabilities of 3D models are well known. However, the computational resources needed for modeling non-linear problems grow significantly when 3D finite elements are used to discretize the structure. Although there are several cases where a 3D analysis is indispensable, for instance for studying the delamination in bonded joints, it is almost computationally impossible to use them for large laminated composite structures with tens of layers such as wind turbine blades or aircraft fuselage. For these kinds of structures, more simplified models should be used.

Some examples of simple models used to simulate laminated composite plate/shell structures are the First Order Shear Deformation Theory (FSDT) [13,14], the Layer-Wise theories (LWT) [15–18], the ZigZag (ZZ) theories [17,19–21] and the *Refined ZigZag Theory* (RZT) [22–26].

Despite the simplicity of the FSDT theory, it is well documented [1,27] that this model gives wrong predictions for highly heterogeneous laminates. In addition, the FSDT is unable to capture delamination because of its linear kinematics assumptions.

* Corresponding author. Tel.: +34 934010808.
E-mail address: aeijo@cimne.upc.edu (A. Eijo).

0263-8223/$ - see front matter © 2013 Elsevier Ltd. All rights reserved.
http://dx.doi.org/10.1016/j.compstruct.2013.09.052

LWT models describe separately the displacement field within each ply, which leads to a high level of refinement of the kinematics. Because of that, they can reproduce with high precision the complex kinematics of highly heterogeneous laminates, and also simulate the delamination phenomenon [28,29]. However, since the number of unknowns is proportional to the number of analysis sublayers (that may be not coincident with the number of physical layers), the computational cost increases with the number of subdivisions.

ZZ theories are an attractive compromise between the high accuracy of LWT and the computational efficiency of FSDT. The kinematics is defined as a superposition of a piecewise linear displacement functions over a linear, quadratic or cubic displacement field along the thickness direction. The number of kinematics variables is independent of the number of layers, which favors the efficiency. Despite its good performance, they present some difficulties to model correctly some boundary condition. So far, the use of the ZZ theories to model delamination in beams and plates has been quite limited. A ZZ model to simulate delamination has been developed by Icardi and Zardo [30].

The kinematics proposed by the RZT theory is defined by a superposition of a linear piecewise zigzag function over the FSDT displacement fields. Since RZT is an improvement of the ZZ theories, the number of variables is also independent of the number of plies. However, unlike the ZZ, all boundary conditions, including the fully clamped condition, can be simulated effectively as it was demonstrated in the original paper [23,24]. Oñate et al. [25,27] and Eijo et al. [1] have taken the RZT as the basis for developing linear beam (LRZ) and quadrilateral plate (QLRZ) finite elements, respectively.

Eijo et al. [31] have extended the LRZ element to simulate delamination in laminated beams. Since the vertical displacement is defined constant along the thickness and the transversal in-plane displacement is not considered for the RZT beam theory, the proposed methodology is limited to model only the fracture mode II. In addition, delamination in highly heterogeneous laminates, i.e. laminates where the shear modulus of the laminae differ from each other in many orders of magnitude can not be correctly simulated employing this technique. However, that is not the case of composite laminates where the shear modulus of laminae does not differ generally in more than one order of magnitude [32]. For this model, delamination can happen at any place within the laminate, thus, it is not necessary to predefine the path where crack is expected to occur. An isotropic damage model was used to manage the non-linear material behavior. It was demonstrated that, in order to be able for capturing relative displacements between layers, the piecewise zigzag function must be updated in terms of the damage level of the material. In [31] it was shown not only the ability to capture the relative displacement between layers, but also the efficiency of the numerical model based on the RZT theory.

In this paper, we present the extension of the beam delamination model of [31] to plate/shell structures using the QLRZ element. Unlike the beam theory, the transversal in-plane displacement is taken into account for the plate theory, which allows simulating not only the fracture mode II but also mode III. For the same reason as in beams, it is not possible to predict the opening fracture mode. The non-linear material behavior is modeled using an isotropic damage model. The non-linear problem is solved by the modified Newton–Raphson method. The paper describes the RZT plate theory, the formulation of the QLRZ finite elements and the isotropic damage model. Also, the implicit integration algorithm is described. Finally, the performance of the proposed numerical model is shown by modeling delamination in a simply supported rectangular plate with a center hole for two different laminates. The reference solution is a 3D analysis using eight-noded hexahedral elements.

2. Refined Zigzag Theory (RZT) for plate and QLRZ plate/shell element

2.1. RZT plate kinematics

A laminated plate formed by N analysis layers of thickness h^k is considered. The number of analysis layer may be not coincident with the number of physical layers. The reference coordinate system is the 3D Cartesian system (x,y,z), where x–y are set as the in-plane coordinates and z is the thickness coordinate.

The plate displacement field proposed by the RZT is defined as (Fig. 1)

$$\begin{aligned} u^k(x,y,z) &= u_0(x,y) - z\cdot\theta_x(x,y) + \bar{u}^k(x,y,z)\\ v^k(x,y,z) &= v_0(x,y) - z\cdot\theta_y(x,y) + \bar{v}^k(x,y,z)\\ w(x,y) &= w_0(x,y) \end{aligned} \tag{1a}$$

where the linear piecewise zigzag functions are

$$\begin{aligned} \bar{u}^k &= \phi_x^k(z)\cdot\psi_x(x,y); \quad k=1,N\\ \bar{v}^k &= \phi_y^k(z)\cdot\psi_y(x,y) \end{aligned} \tag{1b}$$

and superscript k indicates quantities within the kth layer with $z_k \leqslant z \leqslant z_{k+1}$, and z_k is the vertical coordinate of the kth interface. The *uniform axial displacements* along the coordinate directions x and y are u_0 and v_0, respectively; θ_x and θ_y represent the *average bending rotation* of the transverse normal about the negative y and positive x directions; and w_0 is the *transverse deflection*.

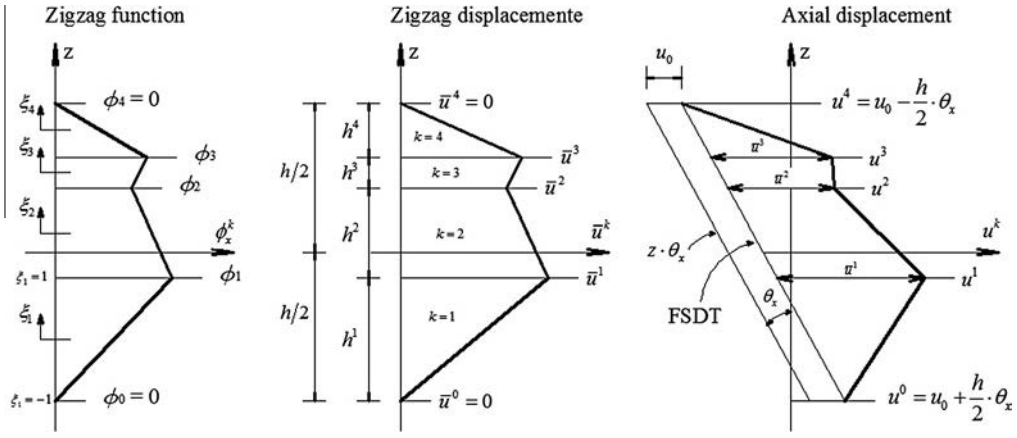

Fig. 1. RZT kinematics.

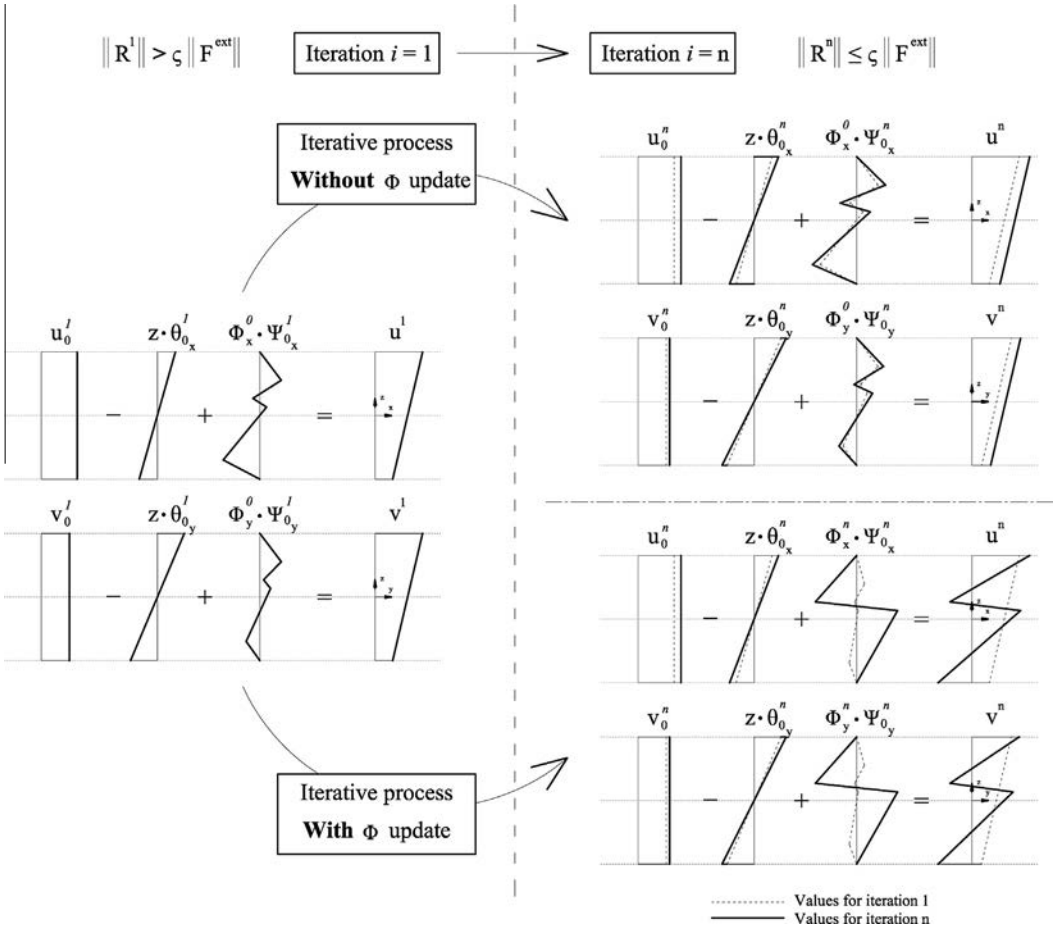

Fig. 2. Iterative process with and without update of ϕ_i ($i = x,y$). Delamination can be captured using the QLRZ finite element when the zigzag function ϕ_i is updated by reducing the shear modulus of the damaged layer.

$\phi_i^k(i = x, y)$ denotes a known piecewise linear *zigzag function*, and ψ_i is a primary kinematic variable defining the *amplitude of the zigzag function* on the plate.

Summarizing, the kinematic variables are

$$\mathbf{a} = \begin{bmatrix} u_0 & v_0 & w_0 & \theta_x & \theta_y & \psi_x & \psi_y \end{bmatrix}^T \tag{2}$$

The in-plane $\boldsymbol{\varepsilon}_p^k$ and the transverse shear $\boldsymbol{\varepsilon}_t^k$ strains are defined as

$$\boldsymbol{\varepsilon}^k = \begin{bmatrix} \boldsymbol{\varepsilon}_p \\ \boldsymbol{\varepsilon}_t \end{bmatrix}^k = \begin{bmatrix} \varepsilon_x \\ \varepsilon_y \\ \gamma_{xy} \\ \gamma_{xz} \\ \gamma_{yz} \end{bmatrix}^k = \begin{bmatrix} \frac{\partial u^k}{\partial x} \\ \frac{\partial v^k}{\partial y} \\ \frac{\partial u^k}{\partial y} + \frac{\partial v^k}{\partial x} \\ \frac{\partial u^k}{\partial z} + \frac{\partial w}{\partial x} \\ \frac{\partial v^k}{\partial z} + \frac{\partial w}{\partial y} \end{bmatrix}$$

$$= \begin{bmatrix} \frac{\partial u_0}{\partial x} \\ \frac{\partial v_0}{\partial y} \\ \frac{\partial u_0}{\partial y} + \frac{\partial v_0}{\partial x} \\ 0 \\ 0 \end{bmatrix} + \begin{bmatrix} -z\frac{\partial \theta_x}{\partial x} \\ -z\frac{\partial \theta_y}{\partial y} \\ -z\left(\frac{\partial \theta_x}{\partial y} + \frac{\partial \theta_y}{\partial x}\right) \\ \frac{\partial w_0}{\partial x} - \theta_x \\ \frac{\partial w_0}{\partial y} - \theta_y \end{bmatrix} + \begin{bmatrix} \phi_x^k(z)\frac{\partial \psi_x}{\partial x} \\ \phi_y^k(z)\frac{\partial \psi_y}{\partial y} \\ \phi_x^k(z)\frac{\partial \psi_x}{\partial y} + \phi_y^k(z)\frac{\partial \psi_y}{\partial x} \\ \frac{\partial \phi_x^k}{\partial z}\psi_x \\ \frac{\partial \phi_y^k}{\partial z}\psi_y \end{bmatrix} \tag{3}$$

which can be written in matrix form as

$$\boldsymbol{\varepsilon}^k = \begin{bmatrix} \boldsymbol{\varepsilon}_p^k \\ \boldsymbol{\varepsilon}_t^k \end{bmatrix} = \begin{bmatrix} \mathbf{S}_p & \mathbf{0} \\ \mathbf{0} & \mathbf{S}_t \end{bmatrix}^k \cdot \begin{bmatrix} \hat{\boldsymbol{\varepsilon}}_p \\ \hat{\boldsymbol{\varepsilon}}_t \end{bmatrix} = S^k \hat{\boldsymbol{\varepsilon}} \tag{4}$$

where $\hat{\boldsymbol{\varepsilon}}$ is the generalized stain vector.

2.2. Derivation of the zigzag function ϕ

The zigzag function is defined within each layer as

$$\phi_i^k = \bar{\phi}_i^{k-1} + \frac{h^k \beta_i^k}{2}(\zeta^k + 1) \quad i = x, y \tag{5}$$

where $\bar{\phi}_i^k$ and $\bar{\phi}_i^{k-1}$ are the zigzag function valued at k and $k-1$ interface, respectively with $\bar{\phi}_i^0 = \bar{\phi}_i^N = 0$ and $\zeta^k = 2\frac{(z - z^{k-1})}{h^k} - 1$. The slope $\beta_i^k = \frac{\partial \phi_i^k}{\partial z}$ of the zigzag function within each layer is expressed as

$$\beta_i^k = \frac{G_{iz}}{G_{iz}^k} - 1 \tag{6}$$

where G_{iz} is an average shear modulus that can be expressed in terms of the shear modulus $\left(G_{iz}^k\right)$ and the thickness (h^k) of each layer as

$$G_{iz} = h\left[\sum_{k=1}^{N} \frac{h^k}{G_{iz}^k}\right]^{-1} \tag{7}$$

For a more detailed description of the RZT for plates, the readers are referred to Tessler et al. [23].

2.3. Stresses and resultant stresses

The relationship between the stresses and the strains for the kth layer are expressed in matrix form as

 # Loop over load increments

Update external forces $\mathbf{F}^{\text{ext}}$

 # Iterative process

If *i*th iteration = 1

$${}^{1}\mathbf{a} = \mathbf{K}_{\text{d}}{}^{-1} \cdot \mathbf{F}^{\text{ext}}$$

$${}^{1}\boldsymbol{\varepsilon}^{k} = \mathbf{S}^{k}\ \mathbf{B}\ {}^{1}\mathbf{a}$$

Note that for the first iteration both $\mathbf{K}_{\text{d}}{}^{-1}$ and $\mathbf{S}^{k}$ were computed at the last iteration of the previous load increment.

Else

$${}^{i}d\mathbf{a} = {}^{i-1}\mathbf{K}_{\text{d}} \cdot {}^{i-1}\mathbf{R}$$

$${}^{i}\mathbf{a} = {}^{i-1}\mathbf{a} + {}^{i}d\mathbf{a}$$

$${}^{i}\boldsymbol{\varepsilon}^{k} = {}^{i-1}\mathbf{S}^{k}\ \mathbf{B}\ {}^{i}\mathbf{a}$$

Remember that ${}^{i-1}\mathbf{S}^{k}$ contains ${}^{i-1}\phi_x^k$, ${}^{i-1}\phi_y^k$, ${}^{i-1}\tilde{\beta}_x^k$ and ${}^{i-1}\tilde{\beta}_y^k$ computed at the previous iteration.

End if

Evaluate undamaged stresses

$${}^{i}\boldsymbol{\sigma}_0^k = \mathbf{D}_0^k \cdot {}^{i}\boldsymbol{\varepsilon}^k$$

Compute damage variable:

$${}^{i}d^k = 1 - \frac{c_0}{{}^{i}f} e^{B\left(1-\frac{{}^{i}f}{c_0}\right)} \qquad \text{with} \qquad {}^{i}f = \sqrt{{}^{i}\boldsymbol{\varepsilon}^k : {}^{i}\boldsymbol{\sigma}_0^k}$$

Update stresses and shear modulus:

$${}^{i}\boldsymbol{\sigma}^k = \left(1 - {}^{i}d^k\right){}^{i}\boldsymbol{\sigma}_0^k$$

$${}^{i}\tilde{G}_{xz}^k = \left(1 - {}^{i}d^k\right){}^{i}G_{xz0}^k \quad ; \quad {}^{i}\tilde{G}_{yz}^k = \left(1 - {}^{i}d^k\right){}^{i}G_{yz0}^k$$

Update zigzag function:

$${}^{i}\tilde{G}_{xz} = h\left[\sum_{k=1}^{N} \frac{h^k}{{}^{i}\tilde{G}_{xz}^k}\right]^{-1} \quad ; \quad {}^{i}\tilde{G}_{yz} = h\left[\sum_{k=1}^{N} \frac{h^k}{{}^{i}\tilde{G}_{yz}^k}\right]^{-1}$$

$${}^{i}\tilde{\beta}_x^k = \frac{{}^{i}\tilde{G}_{xz}}{{}^{i}\tilde{G}_{xz}^k} - 1 \quad ; \quad {}^{i}\tilde{\beta}_y^k = \frac{{}^{i}\tilde{G}_{yz}}{{}^{i}\tilde{G}_{yz}^k} - 1$$

$${}^{i}\phi_x^k = \bar{\phi}_x^{k-1} + \frac{h^k\,{}^{i}\tilde{\beta}_x^k}{2}\left(\zeta^k + 1\right) \quad ; \quad {}^{i}\phi_y^k = \bar{\phi}_y^{k-1} + \frac{h^k\,{}^{i}\tilde{\beta}_y^k}{2}\left(\zeta^k + 1\right)$$

Computation of the secant stiffness matrix and internal forces:

$${}^{i}\mathbf{K}_{\text{d}} = \int_l \mathbf{B}^T\ {}^{i}\hat{\mathbf{D}}_{\text{d}}\ \mathbf{B}\ dl$$

$${}^{i}\mathbf{F}^{\text{int}} = \int_V \mathbf{B}^T\ {}^{i}\mathbf{S}^T\ {}^{i}\boldsymbol{\sigma}^k dV$$

Verification of convergence criteria

$$\mathbf{F}^{\text{ext}} - {}^{i}\mathbf{F}^{\text{int}} = {}^{i}\mathbf{R}$$

$$\left\| {}^{i}\mathbf{R} \right\| \le \varsigma \left\| \mathbf{F}^{\text{ext}} \right\|$$

 # END iterative process

 # END loops over load increments

Fig. 3. Algorithm for solving the non-linear problem using the modified Newton–Raphson method. Note that the zigzag function is updated at each iteration.

$$\boldsymbol{\sigma}^k = \begin{bmatrix} \boldsymbol{\sigma}_p \\ \boldsymbol{\sigma}_t \end{bmatrix}^k = \begin{bmatrix} \sigma_x \\ \sigma_y \\ \tau_{xy} \\ \tau_{xz} \\ \tau_{yz} \end{bmatrix}^k = \begin{bmatrix} \mathbf{D}_p & \mathbf{0} \\ \mathbf{0} & \mathbf{D}_t \end{bmatrix}^k \cdot \begin{bmatrix} \boldsymbol{\varepsilon}_p \\ \boldsymbol{\varepsilon}_t \end{bmatrix}^k = \mathbf{D}^k \boldsymbol{\varepsilon}^k \tag{8}$$

with

$$\mathbf{D}_p^k = \frac{1}{1 - \upsilon_{xy}\upsilon_{yx}} \begin{bmatrix} E_x & \upsilon_{xy}E_x & 0 \\ \upsilon_{yx}E_x & E_y & 0 \\ 0 & 0 & (1 - \upsilon_{xy}\upsilon_{yx})G_{xy} \end{bmatrix}$$

$$\mathbf{D}_t^k = \begin{bmatrix} G_{xz} & 0 \\ 0 & G_{yz} \end{bmatrix} \tag{9}$$

where E, G, υ and $\mathbf{D}$ are the Young modulus, the shear modulus, the Poisson's ratio and the constitutive matrix for the kth layer, respectively.

The stress resultants are computed by integrating the stresses over the plate thickness as

$$\hat{\boldsymbol{\sigma}} = \int_z \mathbf{S}^k \boldsymbol{\sigma}^k dz \tag{10}$$

2.4. QLRZ plate/shell element

The middle surface of the plate is discretized using quadrilateral 4-noded C^0 finite elements. Thus, the kinematics variables of Eq. (2) are interpolated within each element e as

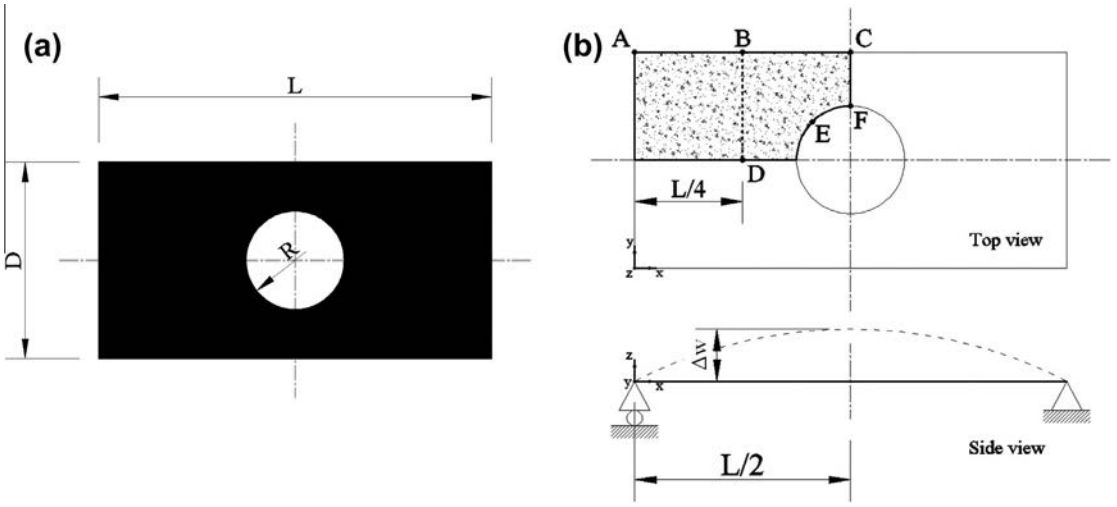

Fig. 4. Simply supported rectangular plate with a center hole. Whole structure dimensions (a), quarter of plate under study with boundary conditions (b).

Table 1
Mechanical properties of linear-elastic layers.

Materials	Young's modulus			Shear modulus			Poisson
	E_x	E_y	E_z	G_{xy}	G_{xz}	G_{yz}	μ
Mechanical properties of linear-elastic plies (MPa)							
A	157.9×10^4	9.584×10^4	9.584×10^4	5.93×10^4	5.93×10^4	3.227×10^4	0.32
B	19.15×10^2	19.15×10^2	19.15×10^3	42.3×10^{-5}	36.51×10^2	124.8×10^2	6.58×10^{-4}
C		104.0×10^1			4.00×10^2		0.30
D		5.30×10^1			2.12×10^1		0.25
E		2.19×10^1			0.876×10^1		0.25
F		0.82×10^1			0.328×10^1		0.25
G		0.73×10^{-1}			0.29×10^{-1}		0.25
H		7.3×10^1			2.92×10^1		0.25

Table 2
Mechanical properties of cohesive layers (cl).

Materials	Young's modulus (E_0) (MPa)	Shear modulus (G_0) (MPa)	Tensile strength (f_t) (MPa)	Fracture energy (G_f) (kN/m)
Mechanical properties of cohesive plies (cl)				
I^{cl}	104.0×10^1	4.0×10^2	2.0×10^1	5.0×10^4
J^{cl}	0.73×10^{-1}	0.29×10^{-1}	3.0×10^{-4}	5.0×10^4

Table 3
Layer distribution of laminated materials.

Laminate	Layer distribution	h^k/h	h (mm)
Laminated materials			
L1	(A/C/A/C/B/I^{cl}/C/A/C/A)	(1.0/0.12/0.1/0.08/0.14/0.02/0.08/0.1/0.06/0.2)	25.0
L2	(D/E/F/G/D/J^{cl}/H/F/E/H)	(1.0/0.12/0.1/0.08/0.14/0.02/0.08/0.1/0.06/0.2)	25.0

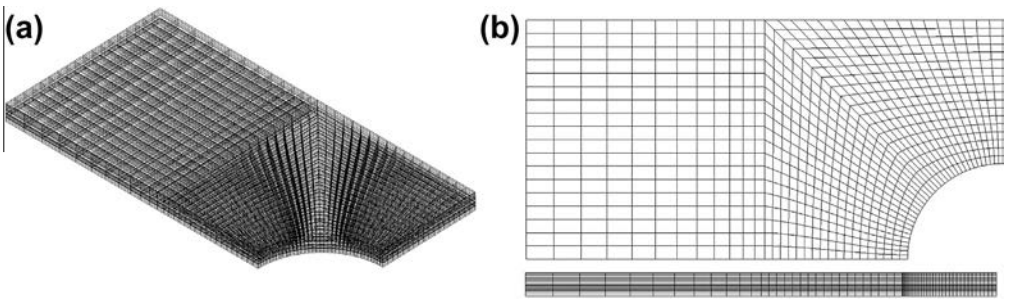

Fig. 5. HEXA8 mesh for both laminates. Isometric view (a), top and side view (b).

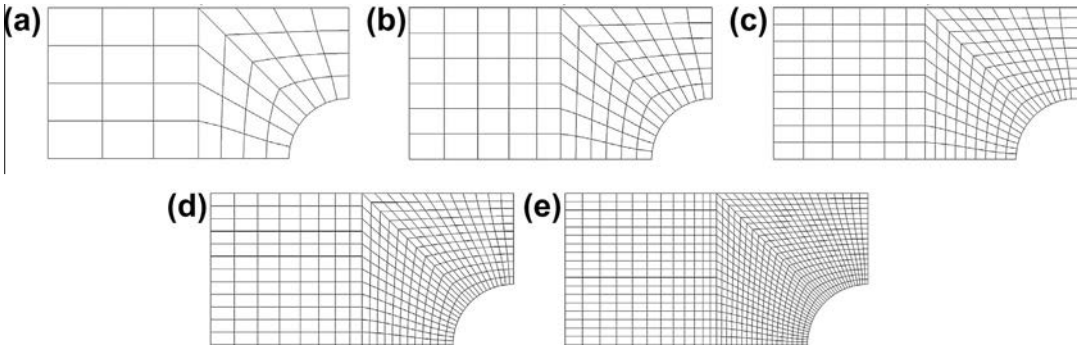

Fig. 6. QLRZ meshes of 44 (a), 102 (b), 216 (c), 384 (d) and 964 (e) finite elements.

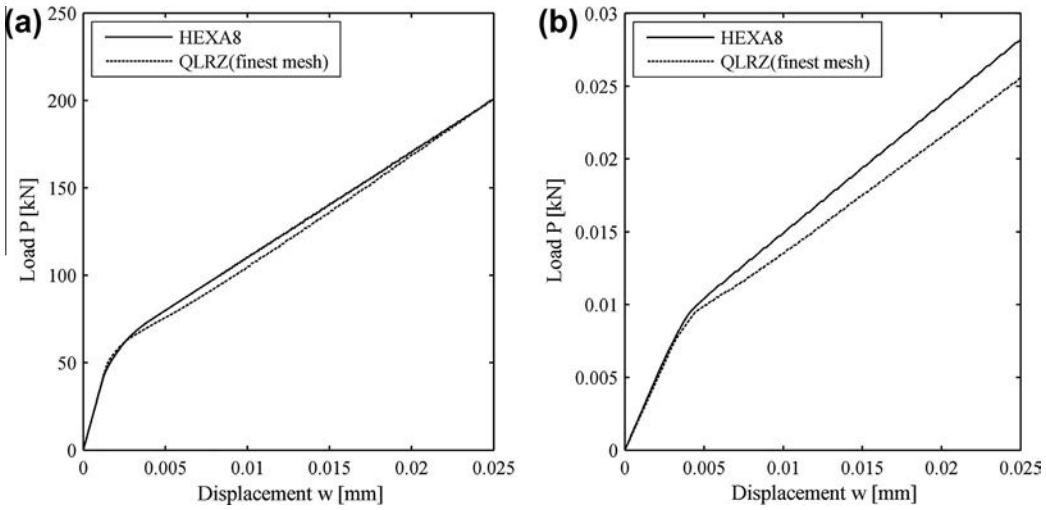

Fig. 7. Load vs vertical displacement for laminate **L1** (a) and **L2** (b).

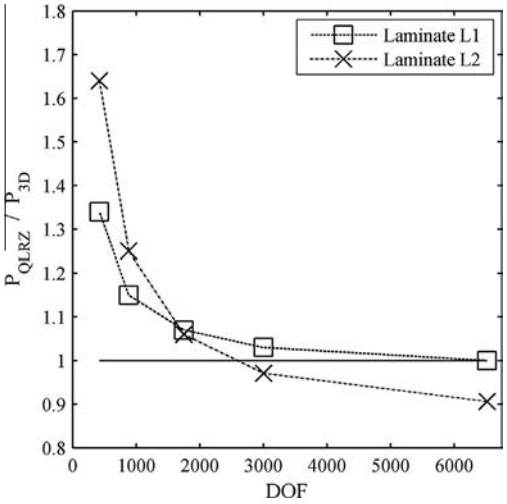

Fig. 8. Mesh convergence. Normalized load value for both laminates and all meshes.

$$\mathrm{a}^{(e)} = \sum_{i=1}^{4} \mathbf{N}_i \mathbf{a}_i^{(e)} \tag{11}$$

with

$$\mathbf{N}_i = N_i \mathbf{I}_7 \quad \text{and} \quad \mathbf{a}_i^{(e)} = \begin{bmatrix} u_0 & v_0 & w_0 & \theta_x & \theta_y & \psi_x & \psi_y \end{bmatrix}_i^T$$

being N_i the linear C^0 continuous shape function of node ith.

The generalized strains $\hat{\boldsymbol{\varepsilon}}$ of Eq. (4) are expressed in term of the nodal degrees of freedom (DOF) using Eq. (11) as

$$\hat{\boldsymbol{\varepsilon}} = \sum_{i=1}^{4} \mathbf{B}_i \cdot \mathbf{a}_i^{(e)} = \mathbf{B} \cdot \mathbf{a}^{(e)} \tag{12}$$

being $\mathbf{B}_i$ the generalized strain matrix defined as

$$\mathbf{B}_i = \begin{bmatrix} \mathbf{B}1 \\ \mathbf{B}2 \\ \mathbf{B}3 \\ \mathbf{B}4 \end{bmatrix}_i \tag{13}$$

with

$$\mathbf{B}1_i = \begin{bmatrix} \frac{\partial N_i}{\partial x} & 0 & 0 & 0 & 0 & 0 & 0 \\ 0 & \frac{\partial N_i}{\partial y} & 0 & 0 & 0 & 0 & 0 \\ \frac{\partial N_i}{\partial y} & \frac{\partial N_i}{\partial x} & 0 & 0 & 0 & 0 & 0 \end{bmatrix} \quad \mathbf{B}2_i = \begin{bmatrix} 0 & 0 & 0 & \frac{\partial N_i}{\partial x} & 0 & 0 & 0 \\ 0 & 0 & 0 & 0 & \frac{\partial N_i}{\partial y} & 0 & 0 \\ 0 & 0 & 0 & \frac{\partial N_i}{\partial y} & \frac{\partial N_i}{\partial x} & 0 & 0 \end{bmatrix}$$

$$\mathbf{B}3_i = \begin{bmatrix} 0 & 0 & 0 & 0 & 0 & \frac{\partial N_i}{\partial x} & 0 \\ 0 & 0 & 0 & 0 & 0 & 0 & \frac{\partial N_i}{\partial y} \\ 0 & 0 & 0 & 0 & 0 & \frac{\partial N_i}{\partial y} & 0 \\ 0 & 0 & 0 & 0 & 0 & 0 & \frac{\partial N_i}{\partial x} \end{bmatrix} \quad \mathbf{B}3_i = \begin{bmatrix} 0 & 0 & \frac{\partial N_i}{\partial x} & -N_i & 0 & 0 & 0 \\ 0 & 0 & \frac{\partial N_i}{\partial y} & 0 & -N_i & 0 & 0 \\ 0 & 0 & 0 & 0 & 0 & N_i & 0 \\ 0 & 0 & 0 & 0 & 0 & 0 & N_i \end{bmatrix} \tag{14}$$

The element stiffness matrix $\mathbf{K}^e$ and the external forces are obtained by using the virtual work principle and Eqs. (8), (10) and (12)

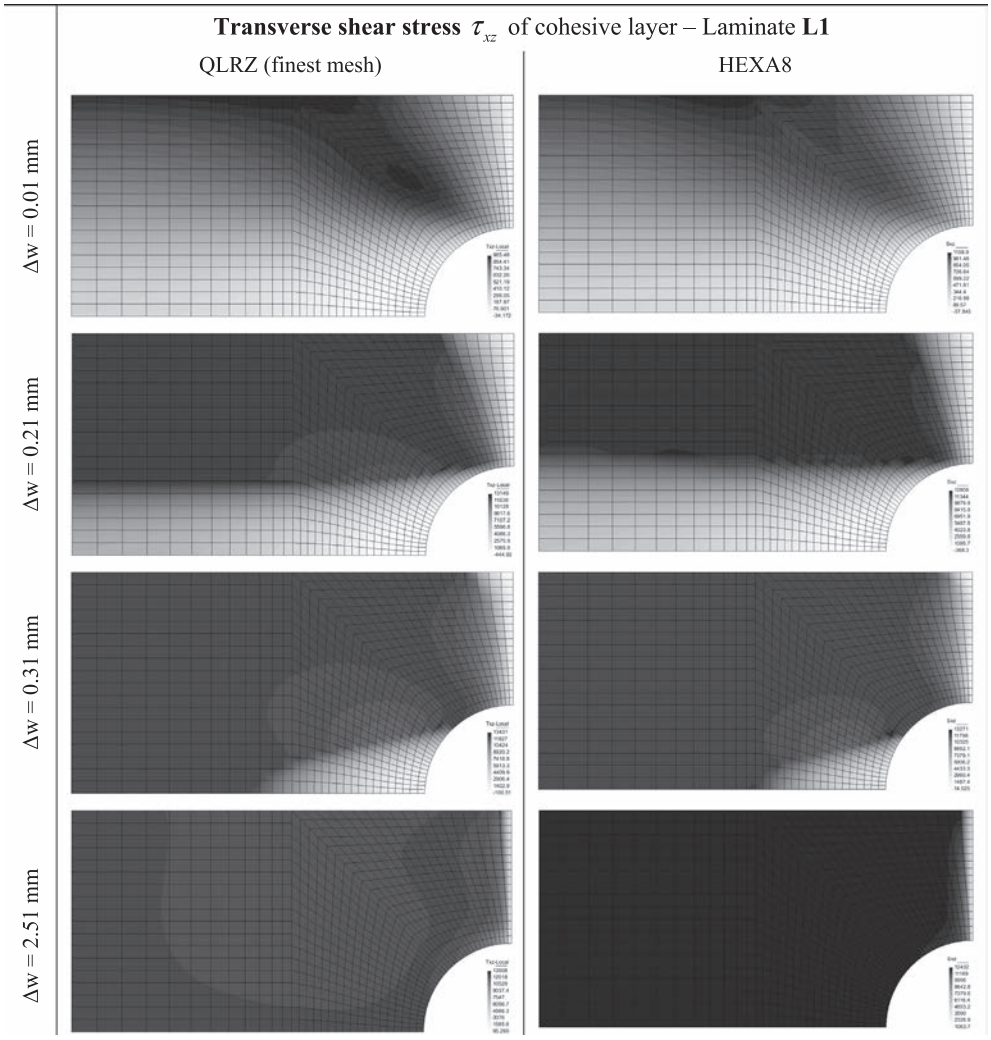

Fig. 9. Transverse shear distribution τ_{xz} of cohesive layer for laminate **L1** computed by using the finest QLRZ mesh (left) and the HEXA8 mesh (right) observed at four different Δw increments.

$$\mathbf{K}^e = \iint_A \mathbf{B}^T \widehat{\mathbf{D}} \mathbf{B}\, dA; \quad \mathbf{F}^e = \iint_A \mathbf{q}\, dA + \sum_{i=1}^{npl} \mathbf{f}_i \tag{15}$$

where A is the in-plane area of the finite element, q is the distributive load, f is the nodal force and $\widehat{\mathbf{D}}$ is the constitutive generalized matrix defined as

$$\widehat{\mathbf{D}} = \int_z [\mathbf{S}^k]^T \mathbf{D}^k \mathbf{S}^k\, dz \tag{16}$$

Full integration of matrix $\mathbf{K}^e$ by Gauss quadrature leads to shear locking for slender plates. In order to avoid this defect an *assumed transverse shear strain field*..[25] is used. Details of the formulation of the 4-noded QLRZ plate finite element can be found in [1,25].

3. Isotropic damage model

The non-linear behavior of material is managed by an isotropic damage model [2]. The level of damage is measured by a single internal scalar variable d, which takes values ranged between 0 (no damage) and 1 (full damage). The relationship between stresses and strains is written as

$$\boldsymbol{\sigma} = (1-d)\boldsymbol{\sigma}_0 = (1-d)\mathbf{D}_0 \cdot \boldsymbol{\varepsilon} \tag{17}$$

being $\boldsymbol{\sigma}$, $\boldsymbol{\varepsilon}$ and $\mathbf{D}_0$ the stress, the strain and the undamaged constitutive tensors, respectively.

The damage criterion, which is used to distinguish between a damage state and an undamaged one, is defined as

$$F(\boldsymbol{\sigma}_0, d) = f(\boldsymbol{\sigma}_0) - c(d) \leqslant 0 \tag{18}$$

where $f(\boldsymbol{\sigma}_0)$ is a norm used to compare different states of deformation and $c(d)$ is the damage threshold. Damage occurs when the value of $f(\boldsymbol{\sigma}_0)$ is larger than $c(d)$. Damage starts for $f(\boldsymbol{\sigma}_0) > c_0$, being c_0 the initial damage threshold value which depends on the material properties.

In this work, c_0 is defined as

$$c_0 = \frac{f_t}{\sqrt{E_0}} \tag{19}$$

where f_t is the tensile strength and E_0 the Young modulus of the undamaged material.

The proposed norm is

$$f(\boldsymbol{\sigma}_0) = \sqrt{\boldsymbol{\varepsilon} : \boldsymbol{\sigma}_0} \tag{20}$$

The evolution law for the damage threshold and the damage variable d are obtained using the damage consistency parameter according to the Kuhn–Tucker conditions. The evolution of these variables can be explicitly integrated [33] to obtain

$$\begin{aligned} d &= \Omega(f(\boldsymbol{\sigma}_0)) \\ c(d) &= \max\{c_0; \max\{f(\boldsymbol{\sigma}_0)\}\} \end{aligned} \tag{21}$$

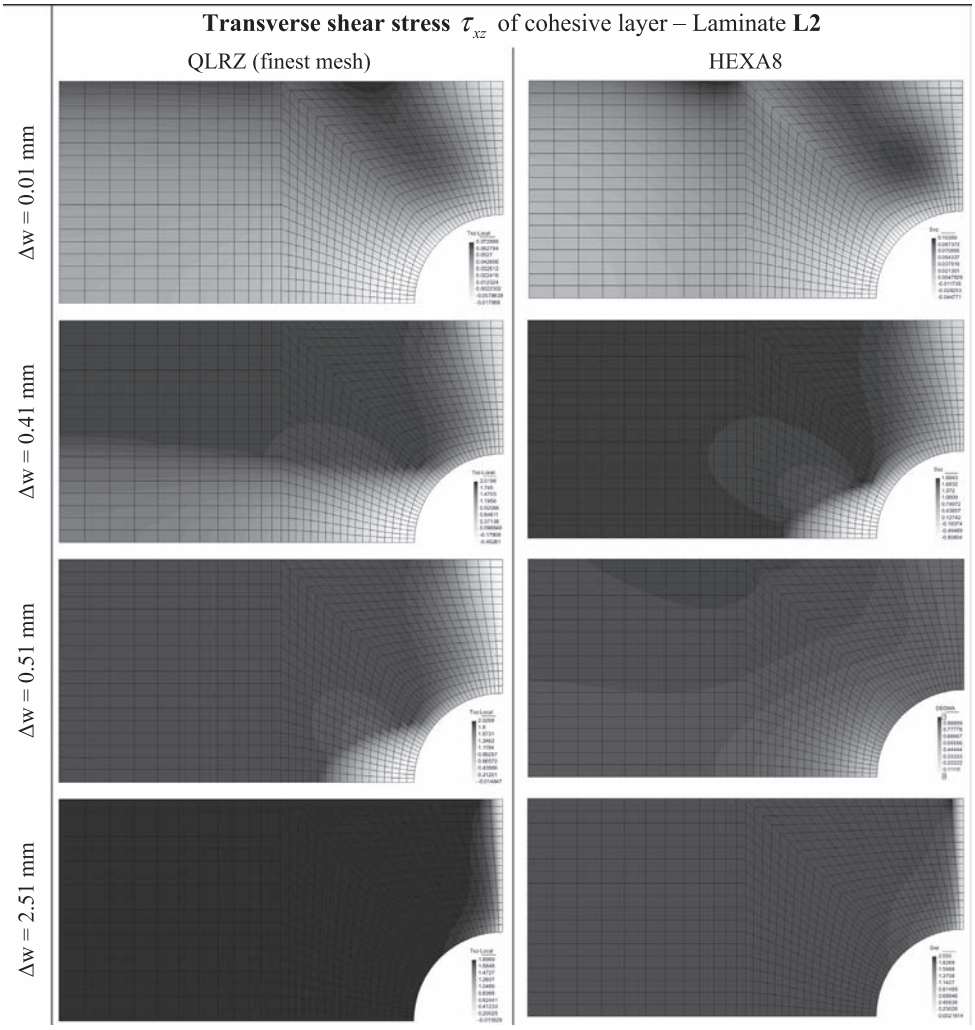

Fig. 10. Transverse shear distribution τ_{xz} of cohesive layer for laminate **L2** computed by using the finest QLRZ mesh (left) and the HEXA8 mesh (right) observed at four different Δw increments.

where $\Omega(\bullet)$ is a monotonic scalar function ranging between 0 and 1 which defines the evolution of the damage variable. In this work, an exponential evolution law is adopted for Ω as

$$\Omega(f(\boldsymbol{\sigma}_0)) = 1 - \frac{f^0(\boldsymbol{\sigma}_0)}{f(\boldsymbol{\sigma}_0)} e^{B\left(1-\frac{f(\boldsymbol{\sigma}_0)}{f^0(\boldsymbol{\sigma}_0)}\right)} \quad \text{with} \quad f^0(\boldsymbol{\sigma}_0) = c_0 \tag{22}$$

Considering the norm of Eq. (20), the exponential softening function of Eq. (22), and the initial damage threshold value c_0 (Eq. (19)), the parameter B in Eq. (22) is computed as

$$B = \left(\frac{G_f \cdot E_0}{l^* \cdot (f_t)^2} - \frac{1}{2}\right)^{-1} \geqslant 0 \tag{23}$$

being G_f the fracture energy per unit area and l^* a characteristic length. In this paper, l^* is defined as the square root of the influence area of each Gauss point.

Finally, the evolution equation of the variable d is written as

$$d = 1 - \frac{c_0}{\sqrt{\boldsymbol{\varepsilon} : \boldsymbol{\sigma}_0}} e^{B\left(1-\frac{\sqrt{\boldsymbol{\varepsilon}:\boldsymbol{\sigma}_0}}{c_0}\right)} \tag{24}$$

4. Update of the zigzag function ϕ to simulate delamination

During a material degradation process, the structure stiffness suffers changes that induce a non-linear response of the structure. The resulting non-linear set of equilibrium equations can be schematically written as

$$\mathbf{F}^{\text{ext}} - \mathbf{F}^{\text{int}}(\mathbf{q}) = \mathbf{R}(\mathbf{q}) \tag{25}$$

where $\mathbf{q}$, $\mathbf{F}^{\text{ext}}$ and $\mathbf{F}^{\text{int}}$ $(\mathbf{q})$ are the discretization parameters, the external and the internal forces vectors, respectively. $\mathbf{R}(\mathbf{q})$ is the residual forces vector. In this work, dynamic forces are not considered.

The non-linear equation system of Eq. (25) is solved whit a modified Newton–Raphson method. Hence, the following linear problem is solved for each iteration i

$$d\mathbf{q} = ({}^{i-1}\mathbf{K}_{\text{d}})^{-1}\, {}^{i-1}\mathbf{R} \tag{26}$$

where $d\mathbf{q}$ is the increment of the nodal DOF at ith iteration. $\mathbf{K}_{\text{d}}$ and $\mathbf{R}$ are the damaged stiffness matrix and the residual vector, respectively, which are computed at the previous $i-1$th iteration. For the QLRZ element matrix $\mathbf{K}_{\text{d}}$ is defined as

$${}^{i-1}K_d = \iint_A \mathbf{B}^T\, {}^{i-1}\widehat{\mathbf{D}}_d \mathbf{B}\, dA \tag{27}$$

with

$${}^{i-1}\widehat{\mathbf{D}}_{\text{d}} = \int_z \left[{}^{i-1}\mathbf{S}^k\right]^T {}^{i-1}\mathbf{D}_{\text{d}}^k\, {}^{i-1}\mathbf{S}^k\, dz \quad \text{and} \quad {}^{i-1}\mathbf{D}_{\text{d}}^k = (1 - {}^{i-1}d^k)\, \mathbf{D}_0^k \tag{28}$$

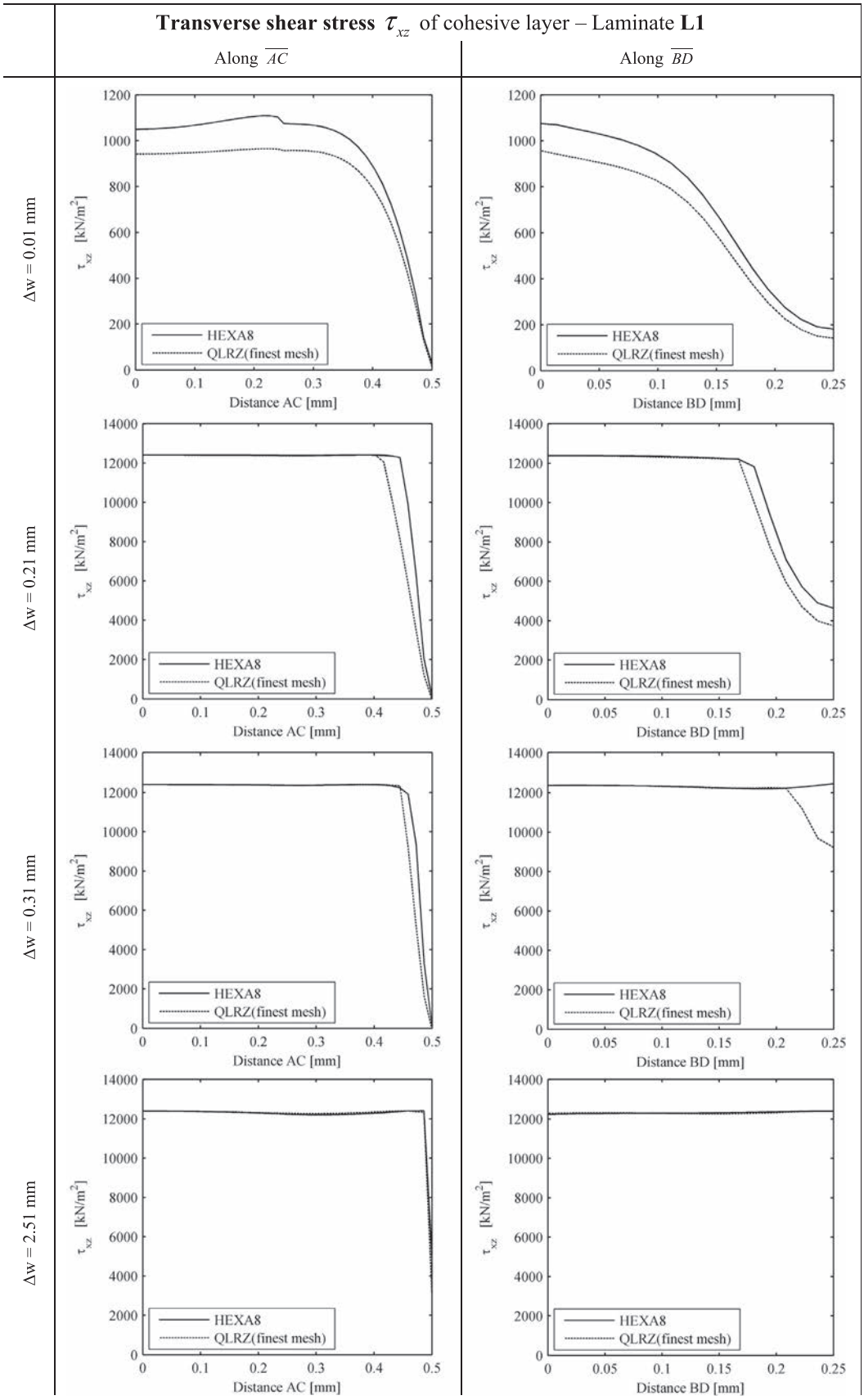

Fig. 11. Transverse shear distribution τ_{xz} of cohesive layer for laminate **L1** along the segments $\overline{AC}$ (left) and $\overline{BD}$ (right), which were observed at four different Δw increments.

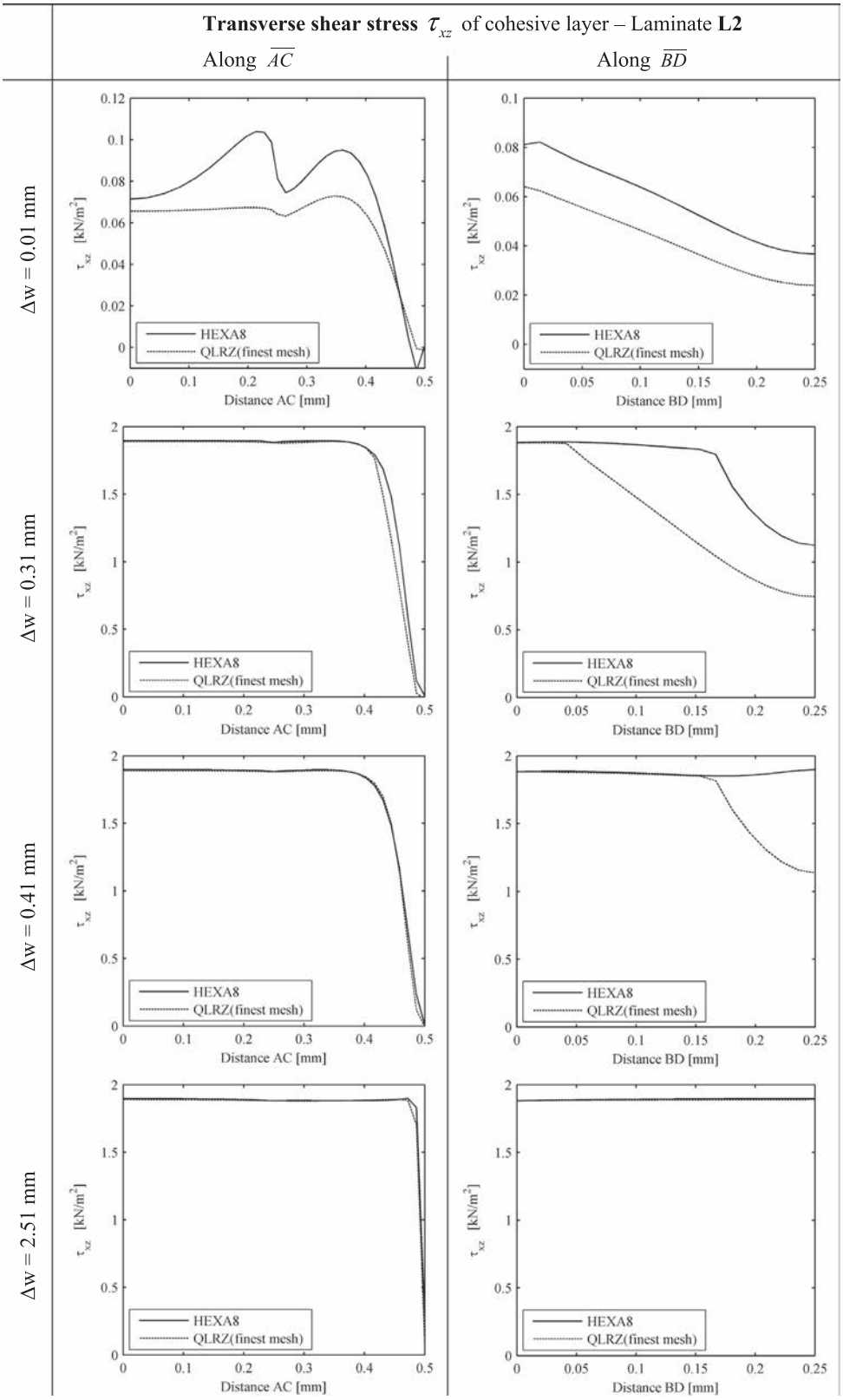

Fig. 12. Transverse shear distribution τ_{xz} of cohesive layer for laminate **L2** along the segments $\overline{AC}$ (left) and $\overline{BD}$ (right), which were observed at four different Δw increments.

where d^k is the scalar damage variable for the kth computed by equation Eq. (24) at the previous $i-1$th iteration.

The nodal DOFs are updated by

$$^{i}\mathbf{q} = {}^{i-1}\mathbf{q} + d\mathbf{q} \tag{29}$$

The process is repeated until the convergence criterion $\|\mathbf{R}\| \leqslant \varsigma\|\mathbf{F}^{ext}\|$ is satisfied where ς is a predefined error tolerance [34].

In 3D finite element analysis, the nodal internal forces are obtained by integrating the stresses on the finite element volume. When any finite element exceeds the damage threshold and suffers

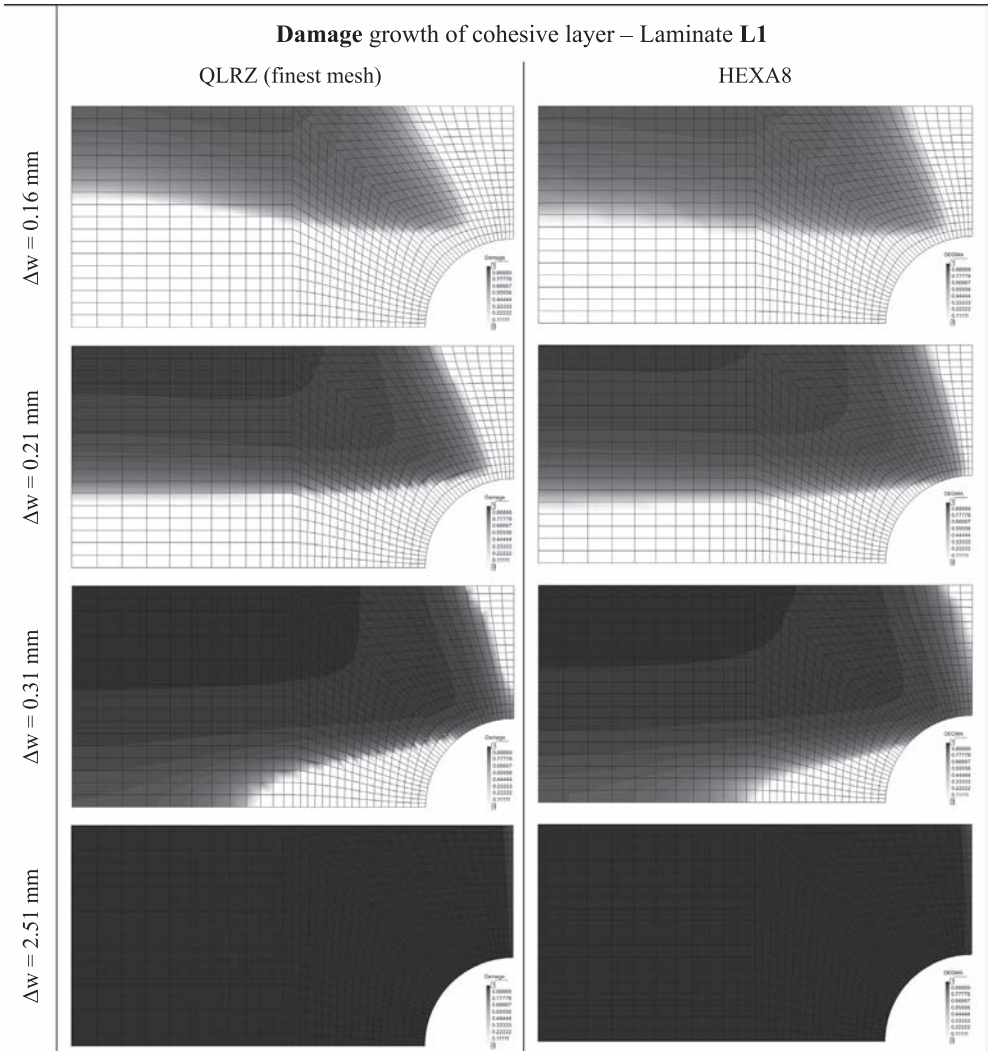

Fig. 13. Damage level of cohesive layer for laminate **L1** computed by using the finest QLRZ mesh (left) and the HEXA8 mesh (right) observed at four different Δw increments. White color is a sing of non-damage and black color indicates full damage.

softening ($d > 0$), its stresses are reduced by Eq. (17). Thus, a lack of internal force equilibrium between the damaged element and its neighbors appears which induces residual forces (**R**). These residual forces generate the relative displacement between layers that typically occurs during a delamination process. Equilibrium is achieved using an iterative process such as that of Eqs. (26) and (29).

For the QLRZ finite element, the kinematic variables (Eq. (2)) and the stress resultants (Eq. (10)) are computed at the in-plane middle surface of the plate ($z = 0$). Because of that, unlike the 3D analysis, there are no forces within the laminate capable of inducing a relative displacement between plies. Thus, it is not possible to predict delamination with QLRZ element by only reducing the stresses using Eq. (17). Therefore, if the stresses are reduced only, the iterative process (Eqs. (26) and (29)) gives as result an amplification of the initial kinematics of the laminate, instead of an update of the delaminated kinematics. That is so, because the variables of Eq. (2) are not capable to modify by themselves the zigzag form of the axial displacement, but they can only vary the scale of the original zigzag distribution.

The kinematics of the RZT theory is defined by a superposition of a linear piecewise zigzag function over the linear FSDT displacement fields (Fig. 1). As a result, the zigzag shape of the laminate kinematics is governed by only the zigzag function ϕ. Comprehensibly, in order for capturing the relative displacement using the QLRZ element, it is indispensable to update the zigzag function. In this work, the update of ϕ is expressed as a function of the damage variable d. The zigzag function ϕ depends on the shear modulus, thus, it is updated by reducing the initial elastic shear modulus G^k_{iz} at the damaged kth layer as

$$\widetilde{G}^k_{iz} = (1 - d^k) G^k_{iz} \tag{30}$$

which leads to the definition of ϕ in term of the damaged shear modulus as

$$\phi^k_i = \bar{\phi}^{k-1}_i + \frac{h^k \tilde{\beta}^k_i}{2}(\zeta^k + 1) \tag{31}$$

with

$$\tilde{\beta}^k_i = \frac{\widetilde{G}_{iz}}{\widetilde{G}^k_{iz}} - 1 \quad \text{and} \quad \widetilde{G}_{iz} = h\left[\sum_{k=1}^{N} \frac{h^k}{\widetilde{G}^k_{iz}}\right]^{-1} \tag{32}$$

This simple update procedure of the zigzag function ϕ allows us to capture the relative displacement in a delamination process. All above-mentioned steps are schematized in Fig. 2.

The algorithm to solve the non-linear equilibrium problem of Eq. (25) is shown in Fig. 3.

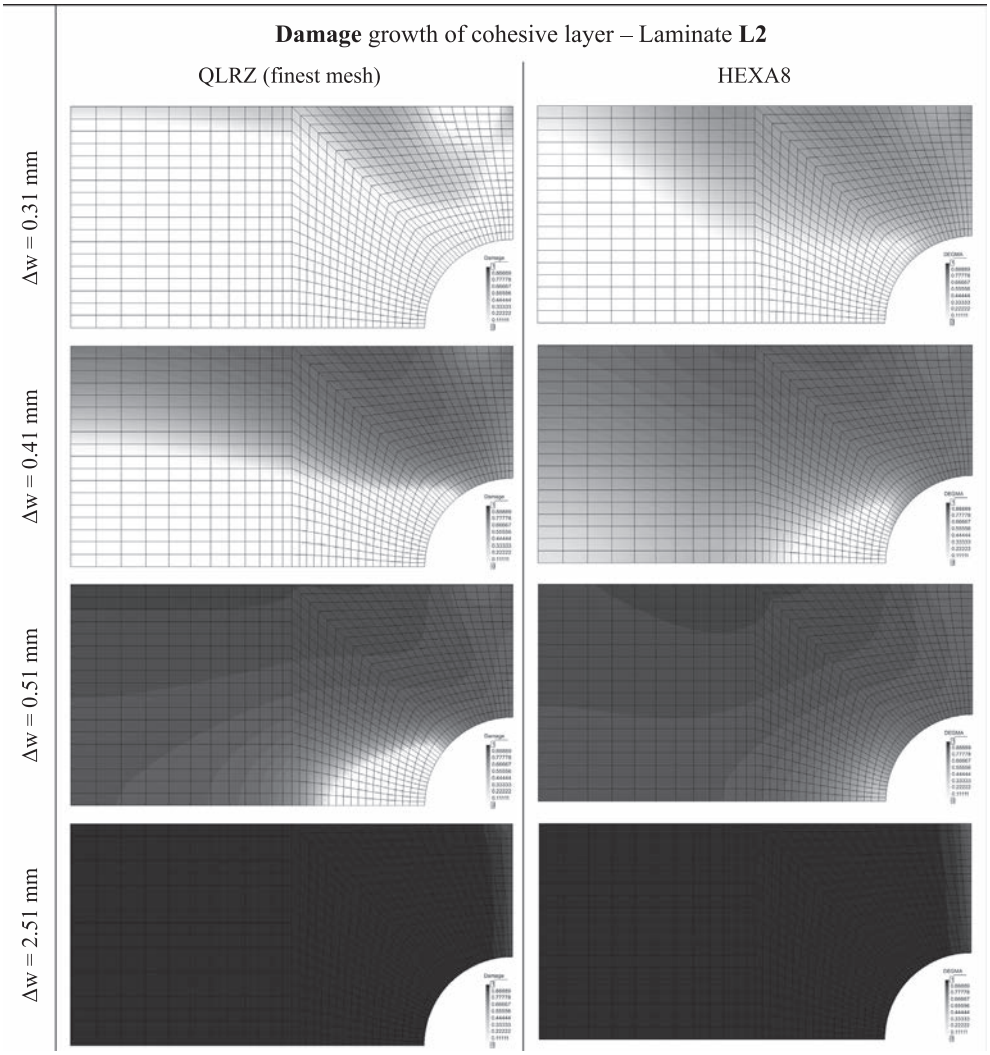

Fig. 14. Damage level of cohesive layer for laminate **L2** computed by using the finest QLRZ mesh (left) and the HEXA8 mesh (right) observed at four different Δw increments. White color is a sing of non-damage and black color indicates full damage.

5. Numerical simulations

The capability of the proposed method for capturing the relative in-plane displacements (Mode II and III) between plies is studied by modeling a simply supported rectangular plate of length $L = 1.0$ m, depth $D = 0.5$ m and thickness $h = 0.025$ m with a center hole of radius $R = 0.0125$ m (Fig. 4a). Taking advantage of symmetry, only one quarter of plate is studied (Fig. 4b). The structure is subjected to bending by imposing a uniform vertical displacement Δw along the line $\overline{CF}$ (Fig. 4b). The plate is analyzed for two laminates (L1 and L2) with properties shown in Tables 1–3.

As any laminate ply is capable to suffer damage, it is not necessary to predefine the delamination path. However, in order to show the capability of the QLRZ element to capture relative displacement between plies, in this work delamination is forced to take place at only one predefined interface within each laminate. This interface is modeled by a ply, called "cohesive layer" (cl) henceforth, whose mechanical behavior is modeled by the isotropic damage model of Section 3. Thus, delamination occurs when the cohesive layer starts to be damaged. The other plies are treated as linear-elastic.

The analysis was carried out under the following considerations: quasi-static application of vertical displacement, geometrically linear conditions and small deformations.

The reference solution was obtained via a 3D finite element analysis using a mesh of 16,416 8-noded hexahedral elements (HEXA8) involving 18,620 nodes and 55,860 DOFs (Fig. 5). One and two finite elements are used to discretize the thickness of the cohesive layer and the thickness of the elastic layers, respectively. This mesh was used for both laminates as they share the same geometry.

Mesh convergence is studied using five QLRZ meshes of 44, 102, 216, 384 and 964 finite elements with 60, 126, 250, 429, 931 nodes and 420, 882, 1750, 3003, 6517 DOF, respectively, as shown in Fig. 6.

The load–displacement plot for laminates L1 and L2 is shown in Figs. 7a and 6b, respectively. The curves are obtained with the HEXA8 element (solid line) and the finest QLRZ mesh (dashed lines). The load corresponds to the total vertical reaction computed at the simply supported end and an imposed vertical displacement Δw (Fig. 4b). Results show a good agreement between both solution techniques. In all cases, the lineal-elastic QLRZ stiffness is very close to that computed using 3D analysis. Also, it is shown that delamination starts approximately at the same values of displacement and load.

Fig. 8 shows the convergence of the normalized load value at the end of the simulation as the number of DOF is increased. The error for the coarser QLRZ mesh reaches almost 35% and 65% for

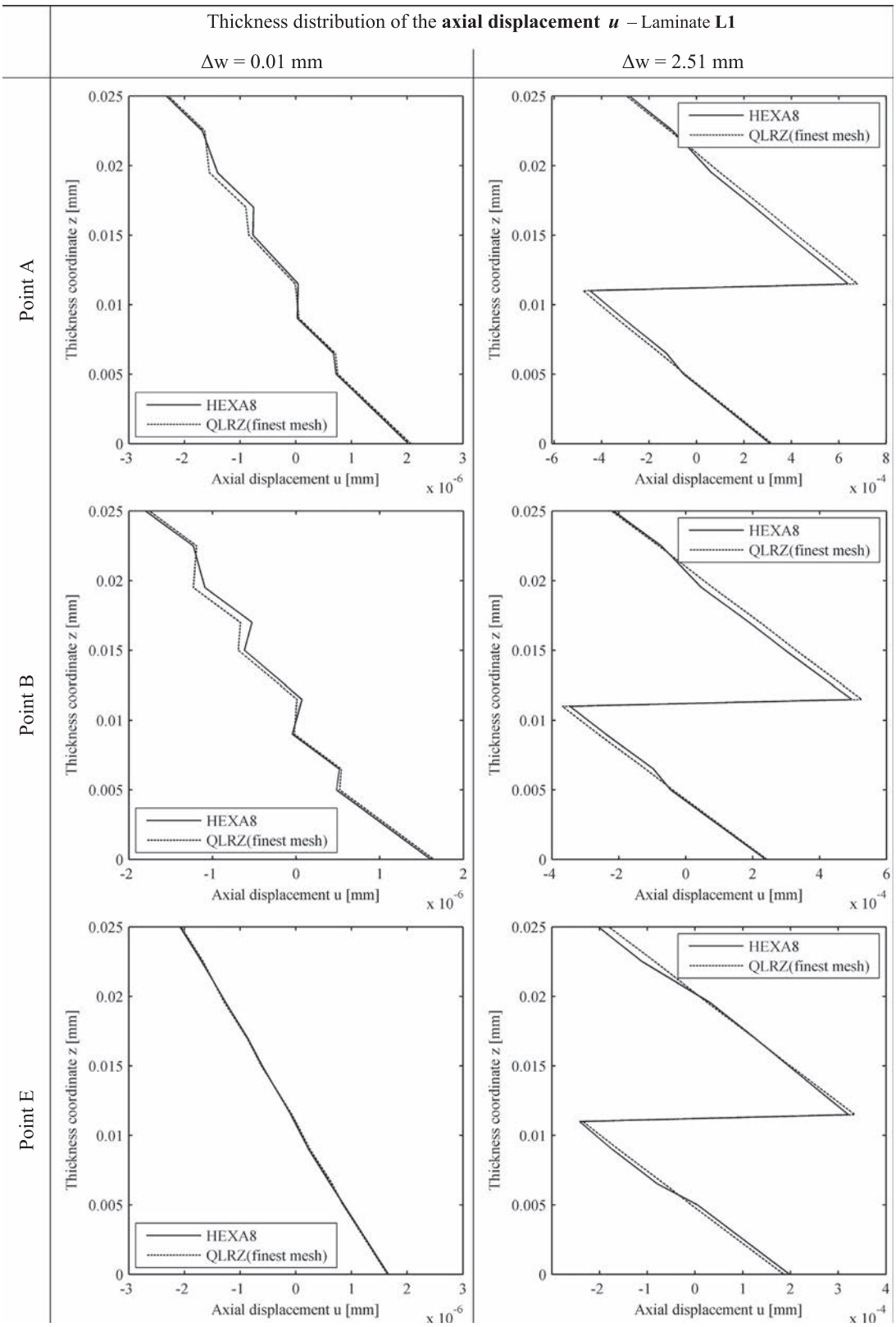

Fig. 15. Thickness distribution of the axial displacement u at three different points for laminate **L1**. Figures show the undamaged kinematics (left – $\Delta w = 0.01$ mm) and the delaminated kinematics at the end of simulation (right – $\Delta w = 2.51$ mm).

laminates L1 and L2, respectively. However, the error is around 1% (L1) and 10% (L2) for the finest QLRZ mesh.

The evolution of the transverse shear stress τ_{xz} for the cohesive layer for laminates L1 and L2 is shown in Figs. 9 and 10, respectively. For the linear-elastic state, the HEXA8 solution gives about 12% (L1) and 30% (L2) higher maximum value of τ_{xz} as appreciated for $\Delta w = 0.01$ mm. Because of that, damage starts a little later for the QLRZ solution. This mismatch between both solutions is more

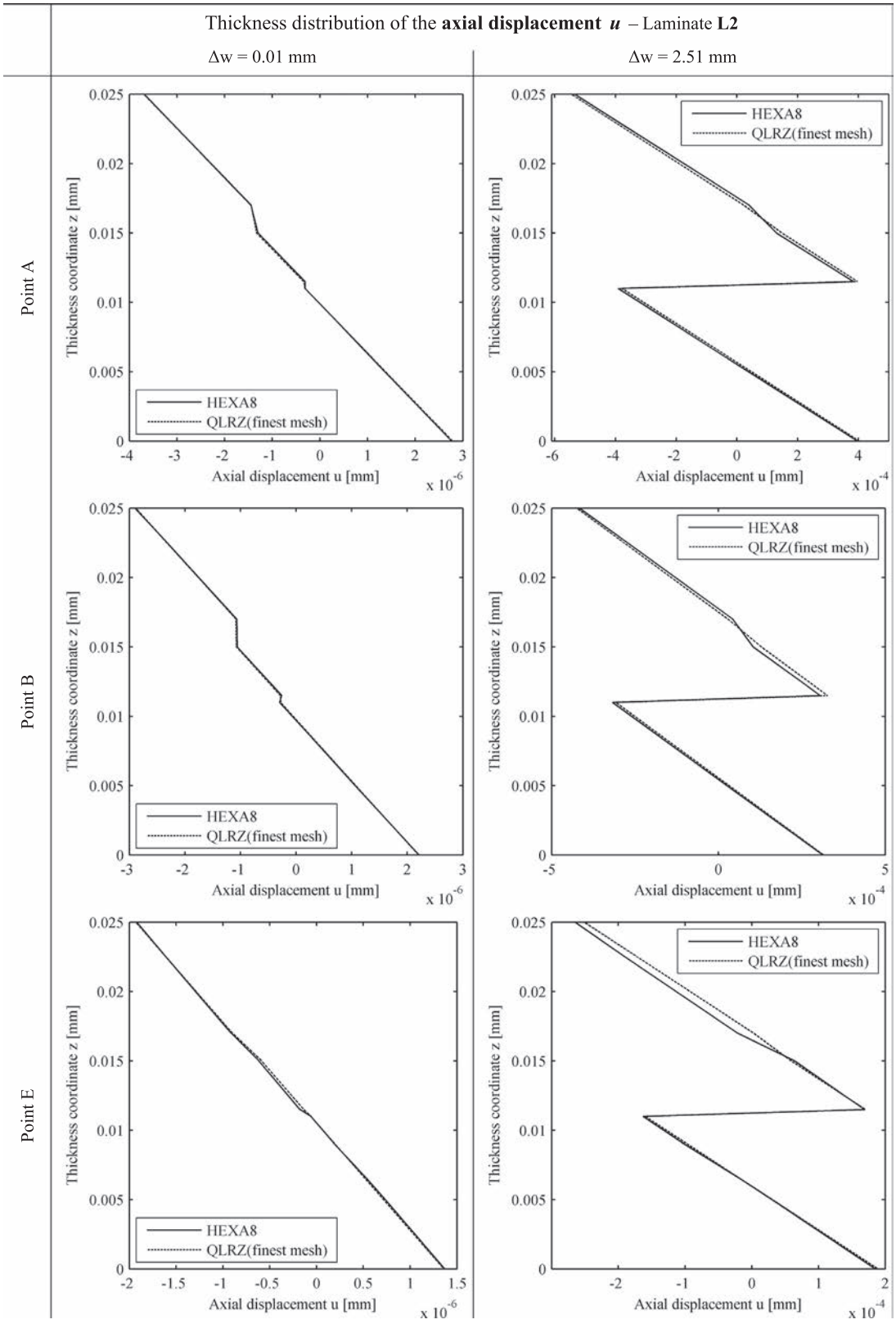

Fig. 16. Thickness distribution of the axial displacement u at three different points for laminate **L2**. Figures show the undamaged kinematics (left – $\Delta w = 0.01$ mm) and the delaminated kinematics at the end of simulation (right – $\Delta w = 2.51$ mm).

evident for the L2 laminate where the τ_{xz} distribution obtained with the HEXA8 mesh for $\Delta w = 0.41$ mm is similar to that computed using the QLRZ mesh for $\Delta w = 0.51$ mm. For the L1 laminate, no great differences are observed between both solutions. In all cases, approximately the same values of τ_{xz} are predicted at the end of the simulation ($\Delta w = 2.51$ mm). In order to clarify theses situations the distribution of τ_{xz} along segments $\overline{AC}$ and $\overline{BD}$ (Fig. 4b) for different increment steps is presented in Figs. 11(L1) and 12

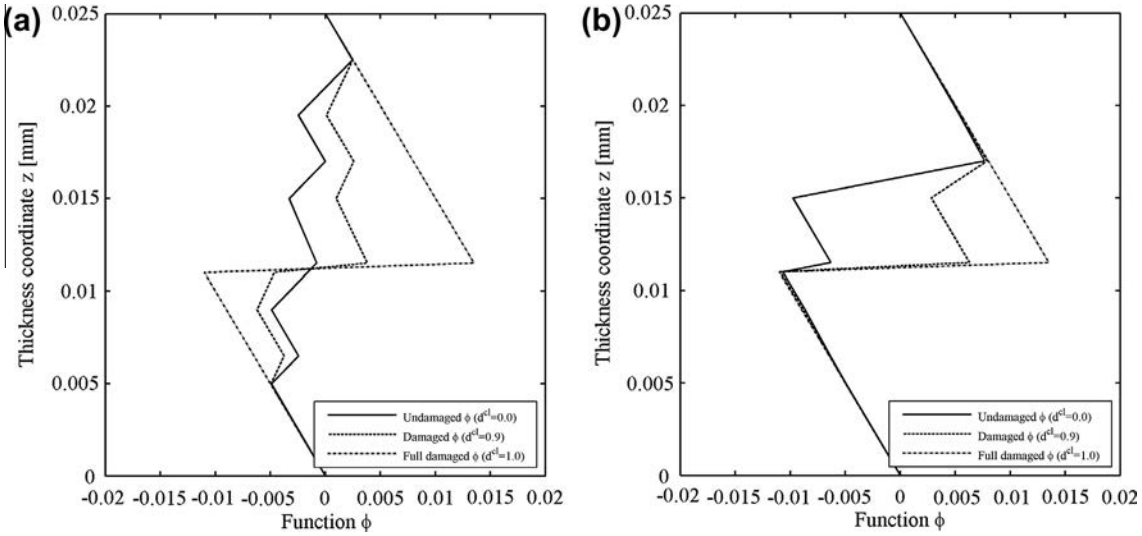

Fig. 17. Undamaged and damaged zigzag function ϕ_x for laminate L1 (a) and L2 (b).

(L2). Results are influenced by the mesh topology specially for laminate L2 as is shown in Fig. 12 for $\Delta w = 0.01$ mm. However, this mesh dependence disappears once delamination has started.

The greyscale images shown in Figs. 13 and 14 illustrate the damage growth of the cohesive ply for laminates L1 and L2, respectively. The black color denotes a full damage state ($d = 1$). These images confirm that damage starts earlier when the HEXA8 finite elements are used, especially for the L2 laminate. However, the global response of the structure (Fig. 7) is similar for both finite elements.

Although the cohesive layer seems to be full damaged at the last step ($\Delta w = 2.51$ mm), the damage variable just reaches at most a value of 0.997. For this reason, the transverse shear stress τ_{xz} did not decrease as expected in a softening process. Surely, if the test continues until the ply is full damaged, the stresses will be reduced to zero.

The thickness distribution of the axial displacement u at points A, B and E (Fig. 4b), before ($\Delta w = 0.01$ mm) and after ($\Delta w = 2.51$ mm) delamination, is plotted in Figs. 15 (L1) and 16 (L2), respectively. The QLRZ element captures the relative displacement with errors less than 6% and 2% for laminates L1 and L2, respectively. For all cases, a very good match between 3D and QLRZ kinematics was found.

To emphasize the importance of the zigzag function update to capture relative displacement between layers during a delamination process, Fig. 17 shows the change of the zigzag thickness distribution from an undamaged to a full damaged state for laminates L1 (Fig. 17a) and L2 (Fig. 17b).

In order to compare the performance of the 3D solution and the QLRZ analysis, both the total increment numbers and incremental displacement values as well as the error tolerance value are the same for both methods. As expected, the computation time needed for the QLRZ solution is several times less than that required for the 3D analysis. The time used by the finest QLRZ mesh is approximately 20 and 12 times less than that required by the HEXA8 mesh for laminates L1 and L2, respectively. In addition, the computation storage space during the simulation is much greater for the 3D analysis as expected.

6. Conclusions

We have presented a promising numerical method based on the refined zigzag theory for modeling delamination in laminated plate/shell structures. The proposed method uses the quadrilateral QLRZ finite element for predicting the laminate kinematics and an isotropic damage model for managing the non-linear material behavior. The proposed formulation can model the fracture modes II and III. However, this methodology is unable to simulate the fracture mode I as the vertical displacement is constant through the laminate thickness. In addition, the use of this technique is limited to laminates where the shear modulus of the laminae does not differ from each other in many orders of magnitude, which occurs generally in laminated composite materials.

We have shown the need of updating the zigzag function so that it can capture the relative displacement between plies. The proposed update depends on the level of degradation. Therefore, both the stresses and the zigzag function are influenced by the damage variable during the iterative process.

The performance of the QLRZ element has been studied by simulating delamination in a simply supported rectangular plate with a center hole subjected to bending. The reference solution was obtained whit a 3D finite element analysis. Results show that both the onset and the evolution of delamination are accurately predicted by the QLRZ element. Also, the delaminated kinematics at the end of simulation is well predicted whit the new plate element.

Acknowledgements

The first author acknowledges the FPU-UPC scholarship from the Universitat Politècnica de Catalunya and the Ministerio de Educación of Spain.

This research was partially financial supported by the SAFECON project of the European Research Council (ERC) of the European Commission.

References

[1] Eijo A, Oñate E, Oller S. A four-noded quadrilateral element for composite laminated plates/shells using the refined zigzag theory. Int J Numer Methods Eng 2013. <http://dx.doi.org/10.1002/nme.4503>.
[2] Oliver J, Cervera M, Oller S, Lubliner J. Isotropic damage models and smeared crack analysis of concret. In: Second international conference on computer aided analysis and design of concrete structures. Zell am See, Austria; 1990.
[3] Bolotin VV. Delaminations in composite structures: its origin, buckling, growth and stability. Composites: Part B 1996;27B:129–45.
[4] Krueger R. The virtual crack closure technique: history, approach and applications. Appl Mech Rev 2002;57(2):109–43.
[5] Mabson G. Fracture analysis for bondlines and interfaces of composite structures. In: 4th international conference on composites testing and model identification (Comptest2008), Dayton (OH); October 2008.
[6] Liu PF, Hou SJ, Chu JK, Hu XY, Zhou CL, Liu YL, et al. Finite element analysis of postbuckling and delamination of composite laminates using virtual crack closure technique. Compos Struct 2011;93(6):1549–60.

[7] Balzani C, Wagner W. An interface element for the simulation of delamination in unidirectional fiber-reinforced composite laminates. Eng Fract Mech 2008;75(9):2597–615.
[8] Wagner W, Balzani C. Simulation of delamination in stringer stiffened fiber-reinforced composite shells. Comput Struct 2008;86(9):930–9.
[9] Turon A, Camanho PP, Costa J, Renart J. Accurate simulation of delamination growth under mixed-mode loading using cohesive elements: definition of interlaminar strengths and elastic stiffness. Compos Struct 2010;92(8):1857–64.
[10] Borg R, Nilsson L, Simonsson K. Modeling of delamination using a discretized cohesive zone and damage formulation. Compos Sci Technol 2002;62(10–11):1299–314.
[11] Liu PF, Islam MM. A nonlinear cohesive model for mixed-mode delamination of composite laminates. Compos Struct 2013;106:47–56.
[12] Martinez X, Rastellini F, Oller S, Flores F, Oñate E. Computationally optimized formulation for the simulation of composite materials and delamination failures. Composites: Part B 2011;47:134–44.
[13] Reissner E. The effect of transverse shear deformation on the bending of elastic plates. Appl Mech 1945;12:69–79.
[14] Mindlin RD. Influence of rotatory inertia and shear in flexural motions of isotropic elastic plates. Appl Mech 1951;18:1–38.
[15] Reddy JN, Robbins DH. Theories and computational models for composite laminates. Appl Mech Rev 1994;47(6):147–69.
[16] Reddy JN. A generalization of two-dimensional theories of laminated plates. Commun Appl Numer Methods 1987;3(3):173–80.
[17] Liu D, Li X. An overall view of laminate theories based on displacement hypothesis. J Compos Mater 1996;30(14):1539–61.
[18] Carrera E. Mixed layer-wise models for multilayered plates analysis. Compos Struct 1998;43(1):57–70.
[19] Wanji C, Zhen W. A selective review on recent development of displacement-based laminated plate theories. Recent Patents Mech Eng 2008;1:29–44.
[20] Carrera E. Historical review of zig–zag theories for multilayered plates and shells. Appl Mech Rev 2003;56(3):287–308.
[21] Kumar A, Chakrabarti A, Bhargava P. Finite element analysis of laminated composite and sandwich shells using higher order zigzag theory. Compos Struct 2013;106:270–81.
[22] Tessler A, Sciuva MD, Gherlone M. Refined zigzag theory for homogeneous, laminated composite, and sandwich plates: a homogeneous limit methodology for zigzag function selection. Numer Methods Part Diff Eq 2011;27(1):208–29.
[23] Tessler A, Sciuva MD, Gherlone M. A consistent refinement of first-order shear deformation theory for laminated composite and sandwich plates using improved zigzag kinematics. Mech Mater Struct 2010;5(2):341–65.
[24] Tessler A, Sciuva MD, Gherlone M. A refined zigzag beam theory for composite and sandwich beams. J Compos Mater 2009;43(9):1051–81.
[25] Oñate E. Structural analysis by the finite element method. Beams, plates and shells, vol. 2. Barcelona: Springer-CIMNE; 2013.
[26] Gherlone M, Tessler A, Di Sciuva M. C^0 beam element based on the refined zigzag theory for multilayered composite and sandwich laminates. Compos Struct 2011;93:2882–94.
[27] Oñate E, Eijo A, Oller S. Simple and accurate two-noded beam element for composite laminated beams using a refined zigzag theory. Comput Methods Appl Mech Eng 2012:362–82.
[28] Barbero EJ, Reddy JN. Modeling of delamination in laminates using a layer-wise plate theory. Int J Solids Struct 1991;28(3):373–88.
[29] Na WJ, Reddy JN. Delamination in cross-ply laminated beams using the layerwise theory. Asian J Civ Eng 2009;10:451–80.
[30] Icardi U, Zardo G. C0 Plate element for delamination damage analysis, based on a zig–zag model and strain energy updating. Int J Impact Eng 2005;31(5):579–606.
[31] Eijo A, Oñate E, Oller S. A numerical model of delamination in composite laminated beams using the LRZ beam element based on the refined zigzag theory. Compos Struct 2013:270–80. http://dx.doi.org/10.1016/j.compstruct.2013.04.035.
[32] Soden PD, Hinton MJ, Kaddour AS. Lamina properties, lay-up configurations and loading conditions for a range of fibre-reinforced composite laminates. Compos Sci Technol 1998;58:1011–22.
[33] Oller S. Fractura mecánica. Un enfoque global. Barcelona, España: CIMNE; 2001. ISBN: 84-89925-76-3.
[34] Zienkiewicz OC, Taylor RL. El método de los elementos finitos, 5th ed., vol. 2. Barcelona: CIMNE; 2004. ISBN: 84-95999-53-6.